N73-26843

NASA TECHNICAL NOTE

NASA TN D-7263

NASA TN D-7263

CASE FILE COPY

A STUDY OF ZODIACAL LIGHT MODELS

by G. A. Gary and P. D. Craven

George C. Marshall Space Flight Center
Marshall Space Flight Center, Ala. 35812

NATIONAL AERONAUTICS AND SPACE ADMINISTRATION • WASHINGTON, D. C. • JUNE 1973

1. REPORT NO.	2. GOVERNMENT ACCESSION NO.	3. RECIPIENT'S CATALOG NO.
NASA TN D-7263		

4. TITLE AND SUBTITLE	5. REPORT DATE
A Study of Zodiacal Light Models	June 1973
	6. PERFORMING ORGANIZATION CODE
7. AUTHOR(S)	8. PERFORMING ORGANIZATION REPORT #
G. A. Gary and P. D. Craven	M-454
9. PERFORMING ORGANIZATION NAME AND ADDRESS	10. WORK UNIT NO.
George C. Marshall Space Flight Center Marshall Space Flight Center, Alabama 35812	11. CONTRACT OR GRANT NO.
	13. TYPE OF REPORT & PERIOD COVERED
12. SPONSORING AGENCY NAME AND ADDRESS National Aeronautics and Space Administration Washington, D. C. 20546	Technical Note
	14. SPONSORING AGENCY CODE

15. SUPPLEMENTARY NOTES

Prepared by Space Sciences Laboratory,
Science and Engineering

16. ABSTRACT

This report presents a review of the basic equations used in the analysis of photometric observations of zodiacal light. A survey of the methods used to model the zodiacal light in and out of the ecliptic is given. Results and comparison of various models are presented, as well as recent results by the authors.

17. KEY WORDS	18. DISTRIBUTION STATEMENT

19. SECURITY CLASSIF. (of this report)	20. SECURITY CLASSIF. (of this page)	21. NO. OF PAGES	22. PRICE
Unclassified	Unclassified	302	$3.00

For sale by National Technical Information Service, Springfield, Virginia 22151

Page Intentionally Left Blank

TABLE OF CONTENTS

Page

SUMMARY 1

SECTION I. INTRODUCTION. 3

SECTION II. SCATTERING THEORY 9

A. Introduction 9
B. General Scattering Theory 9
C. Differential Scattering Cross Section 12
D. Size Distributions 15

SECTION III. MODEL CALCULATIONS. 28

A. Introduction 28
B. Cloud Radiance Integral 29
C. Particle Size Distribution 33
D. Heliocentric Distribution of Scattering Particles 34
E. Gillett Models 42
F. Exponential Model. 53
G. Belt Model 56
H. Ellipsoidal Symmetry Model 58
I. Meteor Model 64
J. Generalized Method For Meteor Models 71

SECTION IV. INVERSE FUNCTION ANALYSIS 79

A. Integral Inversion 79
B. Numerical Approximation Methods 80
C. The Method of Collocation 81
D. The Methods of Least Squares. 82
E. Liouville Solution 88
F. Southworth Analysis 89
G. Cumulative Function 90

SECTION V. OBSERVATIONAL RESULTS 97

SECTION VI. COMPARISON AND ANALYSIS OF MODEL CALCULATIONS 114

TABLE OF CONTENTS (Concluded)

Page

A. Model Comparison 114
B. Basic Heliocentric Model 116
C. Basic Heliocentric Model with Spatial Dependence 121
D. Belt Model for Isotropic Scattering 123
E. Approximation 124
F. Diffraction — Reflection Models 133
G. Polarization — Empirical 144
H. Polarization - Single - Particle Scattering 158
I. Scattering from Distributions 170
J. Ecliptic Zodiacal Light Models 189
K. Spectral Dependence and Null Point 226
L. Out-of-the-Ecliptic Model 229
M. Nonspherical Particles 248
N. Areas for Further Research 253

APPENDIX. DYNAMICAL FORCES 255

REFERENCES 266

BIBLIOGRAPHY 276

LIST OF ILLUSTRATIONS

Figure	Title	Page
1.	Representative results of (a) radiance and (b) polarization of the zodiacal light in the plane of the ecliptic	5
2.	The geometry for incident and scattered radiation, and the scattering plane from a different prospective	10
3.	Category I distributions	18
4.	Gaussian particle size distribution for positive radii	20
5.	Category II distributions for some examples of simple powers of the exponential	21
6.	Effect of the shape factor m on the form of the logarithmic distribution	22
7.	Logarithmic normal distribution curves for $\bar{a} = 5.0$ and $\sigma = 0.10$, 0.25, and 0.50	24
8.	The zeroth-order logarithmic distribution (ZOLD) with $\bar{a} = 5.0$ and $\sigma = 0.10$, 0.25, and 0.50	25
9.	Category IV distributions for $k = 2.5$, 3.0, and 4.0	27
10.	The geometry for light scattering from interplanetary medium	31
11.	Modification of Figure 10	36
12.	Scattering angle contributions from ϵ to 180 deg for an elongation of ϵ	38
13.	I_m dependence on ϵ for $m = 0$, 1, and 2	41
14.	Constant thickness model	43
15.	Linear thickness model	44

LIST OF ILLUSTRATIONS (Continued)

Figure	Title	Page
16.	Geometry for constant thickness model	45
17.	Geometry for linear thickness model	47
18.	The double cross of the linear thickness model showing, for a plane perpendicular to the earth-sun line, the contribution from each region of ϵ to θ_{max} and θ'_{max} to π	49
19.	Geometry for the ellipsoid symmetry model	54
20.	Belt model	57
21.	Geometry for the belt model	57
22.	Ellipsoid symmetry model	59
23.	Parameters of an elliptical orbit	65
24.	The meteor model	67
25.	Generalized meteor model geometry	73
26.	Definition of spherical angles a, b, c and A, B, C	74
27.	Collection of representative results between 25 and 110 deg for the radiance of the zodiacal light in the ecliptic	99
28.	Collection of representative results between 20 and 160 deg for the polarization of the zodiacal light	101
29.	Isophotal map of Smith, Roach, and Owen observations of the zodiacal light out-of-the-ecliptic	106
30.	Dumont results for out-of-the-ecliptic	106

LIST OF ILLUSTRATIONS (Continued)

Figure	Title	Page
31.	Relationship between the neutral-point position in elongation and the wavelength in the plane of the ecliptic.	109
32.	Normalized brightness of the gegenschein averaged from the 41 scans made March 12, 13, 18, and 19, 1969	110
33.	Brightness of the gegenschein in the ecliptic plane near 5300 Å, determined by various observers and normalized to unity at opposition	111
34.	The shape parameter Q for various observers	112
35.	Comparison of the basic heliocentric model with Weinberg's data	119
36.	Comparison of a spatially dependent heliocentric model with Weinberg's data.	122
37.	Comparison of a belt model with Weinberg's data.	125
38.	Approximate reflection scattering functions (no diffraction peak)	127
39a.	Approximate scattering functions with a diffraction peak. . .	129
39b.	The scattering functions of Gillett.	130
40.	The differential cross section for a Lambertian sphere, the forward diffraction peak for a sphere, and the sum	135
41.	The differential cross section for an isotropic scatterer, the forward diffraction peak for a sphere, and their sum. . .	136
42.	The scattering dependence $F_d(\epsilon)$ for diffraction of spherical particles for α = 10, 100, and 1000	138

LIST OF ILLUSTRATIONS (Continued)

Figure	Title	Page
43.	Comparison of diffraction model with Weinberg's data for albedo of $\gamma = 0.1$ and $\alpha = 1$, 10, and 100	141
44a.	The asteroidal phase function determined by Gehrels showing the opposition effect	144
44b.	Spatial distribution of numbered asteroids determined by Narin and corrected for selection effects by Kessler	145
44c.	Gegenschein brightnesses for models assuming the material is distributed according to an inverse power law R^{-m} (where R is the heliocentric distance) for an isotropic phase function	146
44d.	Brightness of the gegenschein as calculated using different phase functions and as found by three observers	147
45.	The degree of polarization predicted by Ingham's empirical form for q = 3, 4, 5, 6, and 11	149
46a.	Radiance of powders with micron-size particles for iron, graphite, and quartz	150
46b.	Radiance of 6-cm iron meteorite compared with the Lambertian curve	150
47.	Percent polarization of powders and of a 6-cm iron meteorite for Figure 46	151
48.	The degree of polarization for the zodiacal light for Ingham's empirical model for q = 3, 4, and 5 and m = 0, 1, and 2	155
49.	Total scattering intensity function for spherical ice particles for $\alpha = 1$-5	159

LIST OF ILLUSTRATIONS (Continued)

Figure	Title	Page
50.	Total scattering intensity functions for spherical ice particles for α = 6-10	160
51.	The degree of polarization for particles of Figure 49	161
52.	The degree of polarization for particles of Figure 50	162
53.	The degree of polarization for a spherical ice particle for α = 20	163
54.	The total intensity scattering function for a spherical ice particle for α = 20	163
55.	Total scattering intensity function for spherical particles with various values of the absorptive part of the refractive index	164
56.	Degree of polarization for particles of Figure 55	165
57.	Total scattering intensity functions for various spherical dielectric particles with α = 5.0	166
58.	Degree of polarization for the dielectric particles of Figure 57	167
59.	Total scattering intensity functions for various spherical metallic particles with α = 5.0	168
60.	Degree of polarization for particles of Figure 59	169
61a.	Radiance versus scattering angle for dielectrics	171
61b.	Radiance versus scattering angle for metals	172
62.	Polarization versus scattering angle for dielectrics of Figure 61a	173
63.	Polarization versus scattering angle for metals of Figure 61b	174

LIST OF ILLUSTRATIONS (Continued)

Figure	Title	Page
64.	Radiance versus scattering angle for ice with distributions of particles for which α_{max} = 5, 15, 20, 25, and 30	175
65.	Polarization versus scattering angle for distribution of Figure 64	176
66.	Polarization versus scattering angle for iron with distributions for which α_{max} = 5, 15, and 30	178
67.	Radiance versus scattering angle for iron in distributions for which n $(\alpha) \sim \alpha^{-4}$ and α_{max} = 5, 15, and 30	179
68.	Radiance of water in distributions for which α_{min} = 2, 3, 4, and 10	180
69.	Polarization for water in distributions in which α_{min} = 2, 3, 4, and 10	181
70.	Polarization of 50-50 mixture of water and quartz	182
71.	Radiance of 50-50 mixture of water and quartz	183
72a.	Normalized scattered intensity versus angle for iron with a modified gamma-size distribution (Category I)	184
72b.	Normalized scattered intensity versus angle for ice in a modified gamma distribution (Category I)	185
72c.	Degree of polarization of iron in a modified gamma distribution (Category I)	186
72d.	Degree of polarization for ice in a modified gamma distribution (Category I)	186
72e.	Normalized scattered intensity versus angle for iron in an exponential size distribution (Category II)	187

LIST OF ILLUSTRATIONS (Continued)

Figure	Title	Page
72f.	Normalized scattered intensity versus angle for ice in an exponential size distribution (Category II)	187
72g.	Degree of polarization of iron in an exponential distribution (Category II)	188
72h.	Degree of polarization for ice in an exponential distribution (Category II)	188
72i.	Normalized scattered intensity versus angle for iron with a logarithmic (shape factor m = 0) size distribution (Category III)	190
72j.	Normalized scattered intensity versus angle for ice in a logarithmic (shape factor m = 0) size distribution (Category III)	190
72k.	Degree of polarization of iron in a logarithmic (shape factory m = 0) distribution (Category III)	191
72l.	Degree of polarization for ice in a logarithmic distribution (shape factor m = 0) (Category III)	191
73.	The radiance dependence for very small ice particles	193
74.	Degree of polarization for very small ice particles	195
75.	Radiance for a variation of α_{max} by 96-point Gaussian	196
76.	Degree of polarization for a variation of α_{max} for Figure 75	197
77.	Radiance for a variation of α_{min}	198
78.	Degree of polarization for variation of α_{min} for Figure 77	199
79.	Radiance for a variation of m	200
80.	Degree of polarization for a variation of m for Figure 79	201

LIST OF ILLUSTRATIONS (Continued)

Figure	Title	Page
81.	Giese and Siedentopf's results for m variation	203
82.	Radiance for variation of p	204
83.	Degree of polarization for a variation of p for Figure 82	205
84.	Giese and Siedentopf's results for a variation in p and particle type	206
85.	Radiance for a variation of metallic materials	208
86.	Degree of polarization for a variation of metallic materials	209
87.	Radiance for a variation of dielectric materials	210
88.	Degree of polarization for a variation of metallic materials	211
89.	Variation of N_o^M and N_o^D on $\bar{L}_\lambda$ and $\bar{P}_\lambda$: (a) metal M dominates and the sum $\sum$ resembles a metallic model, (b) dielectric D dominates and the sum $\sum$ resembles a dielectric model, and (c) a dielectric balanced model	214
90.	Radiance values for a combination of quartz, ice, and iron	215
91.	Degree of polarization for combinations of quartz, ice, and iron	216
92.	Giese and Siedentopf's results for various electron-dielectric models	218
93.	Giese and Siedentopf's results for various metallic-dielectric models	219
94.	Giese and Siedentopf's results for an isotropic reflecting dielectric and a hypothetical metal having Ingham's polarization function	220

LIST OF ILLUSTRATIONS (Continued)

Figure	Title	Page
95.	Giese's results for radiance and polarization for three models assuming different electron densities	220
96.	Kovar and Kovar's Models 5 and 7 results for radiance for a combination of iron, ice, and glass	221
97.	Polarization for Kovar and Kovar's Models 5 and 7	222
98.	Gillett's results for a constant thickness model	231
99.	Out-of-the-ecliptic results using the constant thickness model and the basic heliocentric model	232
100.	Out-of-the-ecliptic results using the linear thickness model and the basic heliocentric model	232
101.	Out-of-the-ecliptic results using the constant thickness model for ice; ROW = 1/100 and p = 4	234
102.	Out-of-the-ecliptic results using the constant thickness model for ice; ROW = 1/10 and p = 4	235
103.	Out-of-the-ecliptic results using the constant thickness model for ice; ROW = 1 and p = 4	236
104.	The degree of polarization for the constant thickness models of Figures 101, 102, and 103 for an inclination of 90 deg	237
105.	Out-of-the-ecliptic results using the constant thickness model for dirty ice; ROW = 1/10 and p = 4	238
106.	Out-of-the-ecliptic results using the constant thickness model for zinc; ROW = 1/10 and p = 4	239
107.	Out-of-the-ecliptic results using the constant thickness model for iron; ROW = 1/10 and p = 4	240

LIST OF ILLUSTRATIONS (Concluded)

Figure	Title	Page
108.	Out-of-the-ecliptic results using the constant thickness model for ice; ROW = 1/10 and p = 3	241
109.	Out-of-the-ecliptic results using the constant thickness model for ice; ROW = 1/10 and p = 5	242
110.	Giese and Dziembowski's results for two ellipsoidal symmetry models compared with Smith et al. observations	243
111.	Van Rhijn's ellipsoid results for out-of-the-ecliptic compared with Smith's et al data normalized at $\delta = 0$ and $\epsilon = 80$ deg.	245
112.	Apparent Gaussian distribution of zodiacal light and the zeros of the derivatives	247
113.	The total scattering intensity functions for cylinders perpendicular to the incident beam	250
114.	The degree of polarization for cylinders perpendicular to the incident beam	251
115.	Hanner's results for cylinders with a distribution of the form $n = n_o \exp[-5 (a/ao)^3]$, α = tilt angle	252
A-1.	The magnitude of $1 + \mu$ as a function of the particle radius: water, quartz, titanite, iron, and graphite	260
A-2.	Processes which determine the electric charge on an interplanetary dust particle	262

LIST OF TABLES

Table	Title	Page
1.	A Condensed History of the Zodiacal Light	6
2.	Differential Scattering Cross Sections for Single Scatterers	14
3.	Size Distribution Formulae	16
4.	Parameters for the Modified Gamma Distribution of Figure 3	17
5.	Radiometric Quantitites	30
6.	Elliptical Orbits	66
7.	Collocation and Least Squares Results for Models A and B Using Weinberg's Data	87
8.	Selected Values of $\overline{i(\theta)}$ and s $(\sin\beta)$	90
9.	Values of the Radiance Gradient Exponent κ	100
10.	Observational Results for the Radiance and Degree of Polarization of the Average Zodiacal Light at 530 nm	103
11.	Blackwell and Ingham Data	104
12.	Zodiacal Light in Ecliptic Coordinates	105
13.	Radiance and Polarization of the Zodiacal Light at the Ecliptic Pole	107
14.	Values of the Color Index (CI) of the Zodiacal Light	107
15.	Brightness of the Gegenschein, the Ecliptic Pole, and Their Ratio for Various Observers	113

LIST OF TABLES (Concluded)

Table	Title	Page
16.	Comparison of the Basic Heliocentric Model with Weinberg's Data	120
17.	Heliocentric Model with Spatial Dependence	121
18.	Comparison of a Belt Model with Weinberg's Data	126
19.	Phase Function Approximations	132
20.	$\psi(z)$ Values	138
21.	Diffraction Model Calculations	140
22.	Comparison of Hypotheses	142
23.	Ingham's Polarization Results for the Isotropic Scatters	154
24.	Exponential Gradient (30 to 60 Deg) for Ice	202
25.	Exponential Gradient for Various Materials Between 30 to 60 Deg for the Models Considered	212
26.	Partial Listing of Zodiacal Light Models Which Are in Approximate Agreement with Observations	224
27.	Color Excesses from Zodiacal Light Model F1	228
28.	Gillett's Results	230
29.	Giese-Dziembowski Models	233
A-1.	Efficiency Factor $Q(m, \alpha)$	258
A-2.	Values of $\Phi(m, \alpha)$ or $1 + \mu$ with $\rho = 1\ g \cdot cm^{-3}$	259

A STUDY OF ZODIACAL LIGHT MODELS

SUMMARY

Various interplanetary dust cloud models which were formulated to predict the photometric properties of the zodiacal light are considered. A compilation and analysis of the models in the literature is presented. This study revealed a lack of unified coverage of the zodiacal light models in the literature.

The important points of the present study are as follows:

1. A detailed compilation of most of the models presented in the literature.

2. A correlation of the models and their association with the development of more detail models.

3. The coverage of out-of-the-ecliptic models.

4. An introduction to the inversion formulation.

The authors' own calculations of single particle Mie scattering results, size distribution Mie scattering results, and ecliptic and out-of-the-ecliptic zodiacal light model results are presented to illustrate and extend the presentation for various models.

The conclusion of the study is that at present there is not a unique model for the zodiacal light, although extensive work has been carried out by various authors. However, it is believed that this direction of research is fruitful and, with new observation results, defensive data on the nature of the interplanetary dust cloud can be obtained.

The study makes the following recommendations for better refinement for model calculations and analysis of the zodiacal light by photometry:

1. The size and spatial distribution needs to be based on experimental data. This is particularly true in the case of particle size distributions where a lower cut-off limit is assumed.

2. A set of polynomials needs to be created to form $d\sigma/d\Omega$.

3. The effects of irregularly shaped particles compared to spheres should be better defined to categorize differences.

4. The method of inversion of the photometric observation to find particle sizes and composition needs more definition and study.

5. The complete effects of the physical forces on the dynamics of the interplanetary particles need to be determined for input into models.

6. A Mie theory model which satisfies all the gross properties of the observation data should be found, if possible.

SECTION I. INTRODUCTION

Zodiacal light is produced by sunlight scattered by the interplanetary cloud of particles around the sun. The cloud is concentrated toward the plane of the ecliptic so that the zodiacal light appears as a band along the ecliptic. In the vicinity of the sun, the interplanetary particles merge with the plasma surrounding the sun to form part of the solar corona. In the antisolar direction, a slight increase in brightness occurs; this phenomenon of the zodiacal light is called either gegenschein or counterglow.

Zodiacal light observations have a long history. It is known that zodiacal light was observed by the Egyptians and the Greeks [106]. The first recorded systematic series of observations of zodiacal light was made by Cassini in 1672 [20]. Cassini proposed that the zodiacal light was sunlight scattered by an interplanetary lenticular dust cloud. Searle [1] compiled the notes on the observations of the zodiacal light and gegenschein made at the Harvard University Astronomical Observatory during the period from 1840 to 1890. He modeled the zodiacal cloud using different phase functions and spatial densities. He found that the best fit to observational data was given by a phase function approximately proportional to the phase angle and a density inversely proportional to the distance of the scatterers from the sun, although data from asteroids indicated to him that it may fall off faster. To account for the increase in brightness near the sun, an increase in the amount of meteoric matter was suggested. Fessenkoff in 1914 attempted further theoretical models to explain his own observations [106]. He assumed the meteor cloud to be infinite in extent and the density to vary inversely with the distance from the sun. For phase functions, he used Euler, Lambert, and Lommel-Seeliger laws.

As reported by Schoenberg [2], Van Rhijn [3], in the course of attempting to determine the contribution of scattered stellar light to the sky brightness, observed that zodiacal light constituted almost 43 percent of the light in the night sky. Van Rhijn modeled the zodiacal cloud, assuming phase functions for the particles that corresponded to meteor phase functions and assuming that the spatial density was constant over spheroids. His studies and calculations extended outside the ecliptic. Dufay [4] reported a substantial polarization of the zodiacal light through photographic analysis. Elvey and Roach [5] made detailed photoelectric observations. Whipple and Grossner in 1949 [107] used the polarization data of Dufay and the brightness data of Hoffmeister [6,7] and Elvey and Roach [5] to set upper limits on the electron density. However, they concluded that the dust component alone could

probably account for the observed polarization. Behr and Siedentopf [8] made the first accurate measurements of the polarization. From these measurements it was proposed that near the sun ($\epsilon < 35$ deg), almost one-half of the zodiacal light was because of scattering from electrons.

The spectrum of the zodiacal light was observed by Fath [108] in 1909 and found to be like that of the sun. Blackwell and Ingham [9, 10, 11] used the spectrum of the zodiacal light obtained by them to infer an upper limit of the electron density much lower than that predicted by Behr and Seidentopf.

Allen [12] and Van de Hulst [13] independently showed that the increase in brightness of the zodiacal light near the sun was caused by light diffracted by the interplanetary particles. Because of this result the requirement for an increase in spatial density of the particles near the sun could be omitted.

Richter [14] made studies of the scattering of light from dust clouds using scattering functions measured in the laboratory. Walter [15] and Giese and Siedentopf [16] used the Mie theory of scattering from spheres to obtain theoretical scattering functions for use in gegenschein and zodiacal light model calculations.

Detailed radiance and polarization measurements of the zodiacal light were made by Weinberg [17, 18]. Smith, et al. [19] obtained a whole sky radiance map.

It is impossible to include all the research in a condensed history of the zodiacal light as is attempted above and summarized in Table 1. Such abbreviation inevitably omits the works of many important contributors. The above history is presented to give an indication of the work done in the past on zodiacal light. Since about 1960, there has been a great deal of study (theoretical and observational) of the zodiacal light, using modern tools and techniques, which does not show in the condensed history.

Representative results of photometric observations of the radiance and polarization in the ecliptic are shown in Figure 1. Figure 1a presents the range of the results for the radiance of the zodiacal light. The ordinate is radiance in units of the number of 10th magnitude stars per square degree and of the average brightness of the solar disk ($\overline{B}_{\odot}$). The abscissa is the elongation in degrees; elongation is the angle between the earth-sun line and the line of sight. The radiance increases rapidly as the zodiacal light merges with the solar corona. Gegenschein is indicated by a much smaller peak in radiance in

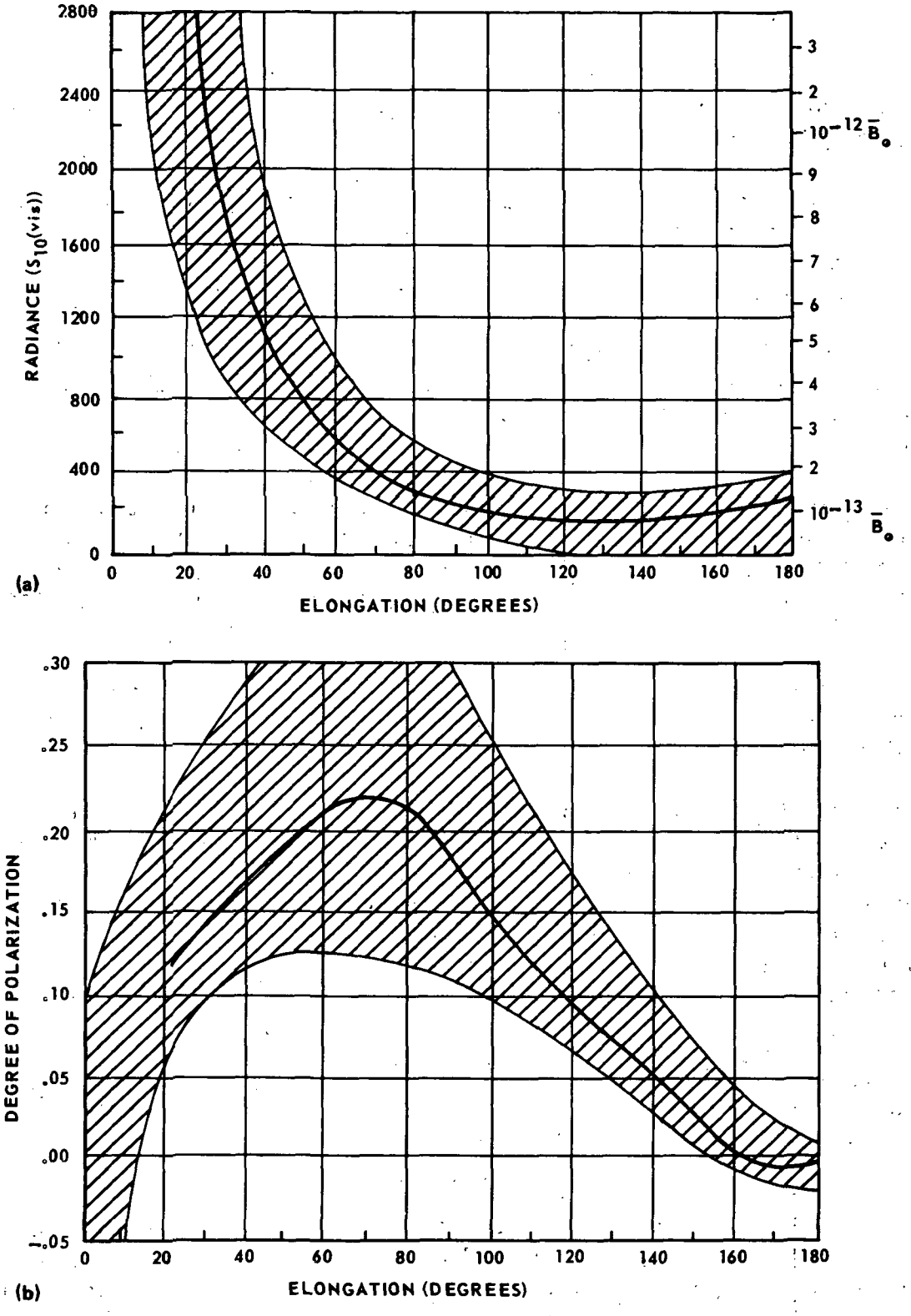

Figure 1. Representative results of (a) radiance and (b) polarization of the zodiacal light in the plane of the ecliptic. (The solid line indicates the average value, and the shaded region indicates the spread in the observational data.)

TABLE 1. A CONDENSED HISTORY OF THE ZODIACAL LIGHT

Egyptians [106]	Observed the zodiacal light and drew pictures of it in the pyramid.
Cassini [20]	Observed the zodiacal light and proposed a lenticular cloud of dust in the ecliptic for its origin.
Brorsen [109]	Observed the gegenschein.
Searle [1]	Calculated the radiance by using asteroidal observations. Compiled observations at HCO.
Fath [108]	Photographed the spectrum of the zodiacal light.
Van Rhijn [3]	Observed the zodiacal light photometrically and calculated out-of-the-ecliptic models for the radiance of the zodiacal light.
Dufay [4]	Found considerable polarization in zodiacal light.
Elvey/Roach [5]	Carried out detail photoelectric observations.
Allen [12] and Van de Hulst [13]	Added diffraction peak contribution to the F-corona calculations.
Richter [14]	Made laboratory studies of the scattering of dust clouds.
Walter [15]	Used the Mie theory in gegenschein model calculations.
Blackwell/Ingham [9, 10, 11]	Used the spectrum of the zodiacal light to set an upper limit of 120 electrons/cm^3 at the earth in interplanetary space.
Giese/Siedentopf [16]	Used the Mie theory to obtain optical properties of the zodiacal light for various models.
Weinberg [17, 18]	Obtained detailed radiance and polarization data.
Smith et al. [19]	Obtained a whole sky radiance map of the zodiacal light.

the antisolar direction. In Figure 1b , the range of the degree of polarization of the zodiacal light versus elongation is presented. The maximum degree of polarization occurs at approximately 70-degree elongation.

The particles which produce the zodiacal light are assumed to range between 0.01 and 10 microns in diameter with a peak frequency distribution near 0.5 micron. The spatial concentration is toward the ecliptic and decreases as a function of radial distance from the sun. This distribution is supported by photometric measurements and by analysis using scattering theory.

A number of hypotheses have been generated to explain the existence of interplanetary dust. These hypotheses include the following [21];

1. Dust injection from comets.

2. Debris from asteroidal collision.

3. Grains from condensation of gas on nucleation centers.

4. The remains of an original and very dense dust cloud.

5. The passing of the solar system through an interstellar dust cloud.

In recent years, there has been renewal of interest in problems concerned with the interplanetary medium, since it is believed that the determination of the correct hypothesis for the existence of the interplanetary medium will be a major step forward in understanding the environment of interplanetary space and, by apocatastasis, the origin of the solar system. Earlier studies of zodiacal light were performed visually or with photographs at unfavorable sites and include uncertain corrections for extinction and extraneous sources. Photoelectric techniques are now being employed to measure the distribution over the celestial sphere of the parameters of the light. Earth-based observations are still hampered by the earth's atmosphere. However, polarimetric observations from spacecraft are now planned. These observations will give better data on the radiance, degree of polarization, color, and orientation of the polarization plane of zodiacal light.

To deduce physical characteristics of zodiacal dust from photometric observations, it is necessary to compare the observed properties with those calculated for several models of the zodiacal cloud. These several models must be used, for there is no unique model for the cloud because of the number of parameters in each model and the lack of sufficiently accurate experimental

data; nonetheless, the models are very informative. The difficulty in obtaining a unique model may be appreciated by considering the following major steps in the calculation of a zodiacal light cloud model [22]:

1. Select a particle size and shape distribution which is consistent with the dynamics that act upon the particles and their physical constraints.

2. Calculate the individual scattering functions for the particles assumed.

3. Calculate the photometric properties, based on the spatial distribution assumed for the model.

4. Analyze the results of varying the parameter to determine the individual uniqueness.

The last two steps are presented in detail later in this report.

SECTION II. SCATTERING THEORY

A. Introduction

To be able to accurately model a cloud of scattering particles, the scattering properties of the individual particles composing the cloud must be known. In this section, the general scattering theory for individual particles will be presented and then extended to a tenuous cloud of such particles. Since the scattering is classical field scattering for electromagnetic radiation, the derivations are omitted since they are available in the literature. This section presents the general treatment for scattering, the forms of some differential scattering cross sections which are used to describe the angular distributions of the scattered field from different scatterers, and a discussion of the size distribution for the scattering centers.

B. General Scattering Theory

To know the scattering properties of the particles, one must know the relation between the electromagnetic fields that are incident on and scattered by the particle. Such a relation depends on the shape and physical properties of the particle and, in general, the relation is very difficult to describe analytically. However, the scattered properties can be described in a general formalism without direct reference to the properties of the particle. Consider the electromagnetic fields at a large distance r from the particle. The field is transverse to the direction of propagation, and the amplitude of the scattered waves is a function of position. The fields are a combination of the incident wave, considered hereafter to be a plane wave with a wave vector $k = 2\pi/\lambda$, and a spherical outgoing wave.

$$\underset{\sim}{E} \rightarrow \underset{\sim}{E}_0 \, e^{i\underset{\sim}{k}\cdot\underset{\sim}{r}} + \underset{\sim}{A}\,(\theta,\ \phi)\,\frac{e^{ikr}}{r} \tag{1}$$

where $|\underset{\sim}{A}\,(\theta,\ \phi)|$ is the amplitude of the scattered wave, e^{ikr} is its phase, and $\frac{1}{r}$ is the geometric attenuation factor. $\underset{\sim}{A}\,(\theta,\ \phi)$ is such that the scattered part contributes nothing to $\underset{\sim}{E}$ before scattering. It is related to the incident

field by a scattering matrix, $\underline{\underline{S}}$, which will be defined shortly. The linear relationship between the incident and scattered waves is a consequence of the linearity of Maxwell's equations and is valid for the cases considered here. Before defining $\underline{\underline{S}}$, consider Figure 2 which shows the coordinate system used to describe both the direction and polarization of the incident and scattered fields.

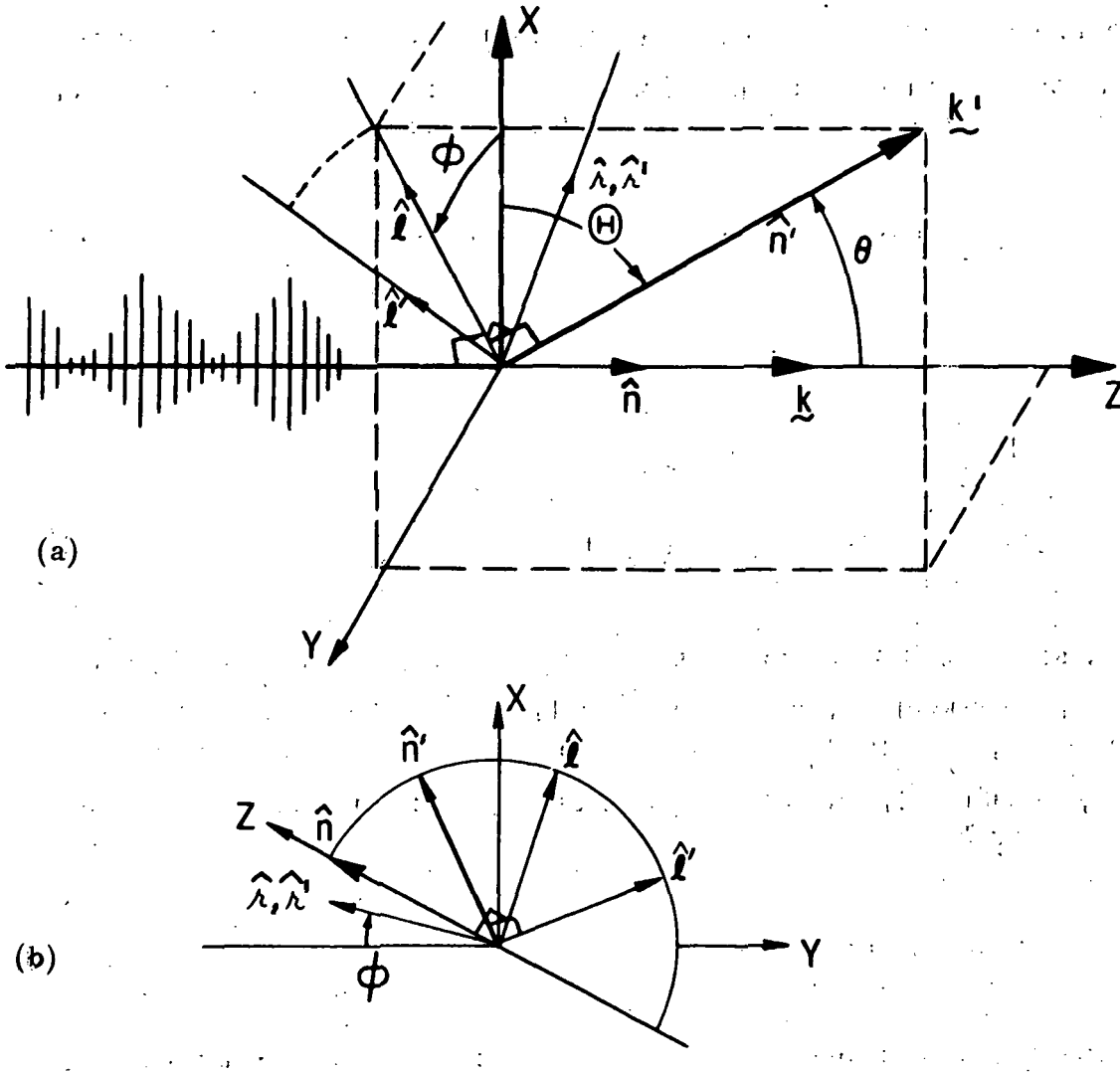

Figure 2. The geometry for incident and scattered radiation, and the scattering plane from a different perspective.

The X, Y, and Z axes are fixed to the scattering center and oriented such that the Z-axis is along the direction of the incident radiation. The unit vector $\hat{n}$ and the propagation vector $\underset{\sim}{k}$ are in the direction of the incident radiation. The unit vector $\hat{n}'$ and propagation vector $\underset{\sim}{k}'$ are defined similarly

for the scattered radiation. $\hat{n}$ and $\hat{n}'$ define the scattering plane and the scattering angle, θ, which is the angle between them $(0 \leq \theta \leq 180 \text{ deg})$. $\hat{r}$ and $\hat{r}'$ are the same and are perpendicular to the scattering plane which is inclined an angle, ϕ, to the X-axis. Since the amplitudes are transverse to $\underset{\sim}{k}$, the unit vectors $\hat{\ell}$ and $\hat{\ell}'$ are perpendicular to $\hat{r}$, $\hat{n}$ and $\hat{r}'$, $\hat{n}'$, respectively. The quantities E_{or} and $E_{o\ell}$ are the electric field components of the incident radiation $\hat{r}$ and $\hat{\ell}$. Likewise, E_r and E_ℓ are the electric field components of the scattered radiation along $\hat{r}'$ and $\hat{\ell}'$. The amplitudes of the incident and scattered waves are related by the scattering matrix $\underset{=}{S}$,

$$\underset{\sim}{E}_{sca} = A(\theta, \phi) \frac{e^{ikr}}{r} = \underset{=}{S}(\theta, \phi) \underset{\sim}{E}_0 \frac{e^{ikr}}{r} \tag{2}$$

or

$$\begin{pmatrix} E_\ell \\ E_r \end{pmatrix} = \begin{pmatrix} S_2 & S_3 \\ S_4 & S_1 \end{pmatrix} \begin{pmatrix} E_{o\ell} \\ E_{or} \end{pmatrix} \frac{e^{ikr}}{r} . \tag{3}$$

In general, scattering amplitude functions S_1, S_2, S_3, and S_4 are dependent on the particle properties, complex, and functions of θ and ϕ. The components (E_ℓ, E_r) and $(E_{o\ell}, E_{or})$ are referenced to coordinate systems $(\hat{\ell}', \hat{r}')$ and $(\hat{\ell}, \hat{r})$, respectively. Hence, the scattering matrix is a function of $\underset{\sim}{k}$ and $\underset{\sim}{k}'$,

$$\underset{=}{S}(\theta, \phi) = \underset{=}{S}(\underset{\sim}{k}, \underset{\sim}{k}')$$

where $\underset{=}{S}$ reduces to the unit matrix for no scattering. The S-matrix contains all the information one can obtain about the particle from a scattering analysis.

For a spherically symmetric particle, the scattered $\hat{\ell}'$ component is directly related to the incident $\hat{\ell}$ component only, and similarly for the $\hat{r}$ component. Hence, the S_3 and S_4 elements of the $\underset{=}{S}$ matrix are zero.

In the case of a spherical particle, the energy at a given wavelength which crosses a unit area in unit time at a distance r is given by

$$\xi_{\lambda}^{(\ell,\lambda)} = k^{-2}r^{-2}\,\xi_{o\lambda}^{(\ell,\lambda)} \left| S_{(1,2)}(\theta) \right|^2 \tag{4}$$

where $\xi^{(\ell,\lambda)}$ is the spectral radiant density and is related to E by

$$\xi_{\lambda} = \tfrac{1}{2}\sqrt{\frac{\epsilon}{\mu}}\ |\underset{\sim}{E}|^2 \quad .$$

ϵ is the electric permitivity and μ is the magnetic permeability.

The scattering intensity functions i_1 and i_2 are defined as the square of $|S_1|$ and $|S_2|$, respectively. i_1 and i_2 are calculated for spherical particles by the use of the Mie theory [23, 110]. As will be seen, i_1 and i_2 play an important role in modeling zodiacal light.

Particles which have no three-dimensional rotational symmetry have elliptical polarization; i.e., the incident $\hat{\ell}$ and $\hat{\lambda}$ component will be scattered such that each will have a $\hat{\ell}'$ and $\hat{\lambda}'$ component. Therefore, S_3 and S_4 do not vanish; hence the general form for i_1 and i_2 is

$$i_1 = |S_1(\theta,\phi) + S_4(\theta,\phi)|^2$$

and

$$i_2 = |S_2(\theta,\phi) + S_3(\theta,\phi)|^2 \quad .$$

C. Differential Scattering Cross Section

The angular distribution of the scattered radiation can be described by the differential cross section. The differential cross section $d\sigma/d\Omega$ is defined as the ratio of the flux scattered from an object in the direction θ and ϕ per unit solid angle to the flux per unit area incident on the object,

$$\boxed{\frac{d\sigma}{d\Omega} = \frac{\text{energy scattered/unit time/unit solid angle}}{\text{energy incident/unit time/unit area}}} \quad . \tag{5}$$

In terms of the Poynting vector $\underset{\sim}{S}$ for the incident and scattered fluxes

$$\frac{d\sigma}{d\Omega} = \left| \frac{\underset{\sim}{S}_{sca}}{\underset{\sim}{S}_{inc}} \right| r^2 \tag{6}$$

where r is the distance of the observation point from the scattering center. The differential cross section has the dimensions of area per steradian. In terms of the flux density $\frac{d\sigma}{d\Omega}$ is

$$\frac{d\sigma}{d\Omega} = \left(\frac{\xi_{scat}}{\xi_{inc}} \right) r^2 \quad .$$

Hence, in terms of the components i_1 and i_2, the differential cross-section components are

$$\left(\frac{d\sigma}{d\Omega}\right)_{r,\ell} = \frac{i_{1,2}}{k^2} \quad .$$

The scattered flux density for unpolarized incident light is given by

$$\xi = \frac{1}{2}(\xi^{\ell} + \xi^{r}) = \frac{1}{2r^2} \left[\left(\frac{d\sigma}{d\Omega}\right)_{r} + \left(\frac{d\sigma}{d\Omega}\right)_{\ell} \right] \xi_o \quad .$$

Differential scattering cross sections of some well-known scatterers are listed in Table 2 for reference. The notation is that of Van de Hulst [120] except that $C_{p\ell}$ is polarizability.

TABLE 2. DIFFERENTIAL SCATTERING CROSS SECTIONS FOR SINGLE SCATTERERS [121]

Scatterer	$\frac{d\sigma}{d\Omega}$
Isotropic Scatterer	$a^2/4$
Lambertian Sphere	$\frac{2a^2}{3\pi}(\sin\theta - \theta\cos\theta)$
Circular Diffraction	$\frac{k^2a^4}{4}\left\lvert\frac{2J_1(ka\theta)}{ka\theta}\right\rvert^2$
Rectangular Diffraction	$\frac{k^2a^4}{4}\left\lvert E(\frac{1}{2}kb\sin\theta\cos\phi)\,E(\frac{1}{2}kc\sin\theta\cos\phi)\right\rvert^2$
Rayleigh	$\frac{C_{p\ell}^2\,a^4}{8\pi\epsilon}(1+\cos^2\theta)$
Electrons	$\left(\frac{e^2}{mc^2}\right)^2\frac{1}{2}(1+\cos^2\theta)$
Rayleigh-Gans Spheres	$\left(\frac{9\pi}{2u^3}\right)^{\frac{1}{2}}\frac{C_{p\ell}^2\,k^4}{8\pi\epsilon}(1+\cos^2\theta)\,J_{3/2}(u)$
Rayleigh-Gans Cylinders	$\left(\frac{\pi}{2v}\right)^{\frac{1}{2}}\frac{C_{p\ell}k^4}{4\pi\epsilon u}(1+\cos^2\theta)\,J_1(u)\,J_{\frac{1}{2}}(v)$
Mie Spheres	$\frac{1}{2}k^2\left(\lvert S_1(\theta)\rvert^2+\lvert S_2(\theta)\rvert^2\right)$
Cylinders	$\frac{k^2}{2}\left(\left\lvert\frac{k\ell}{\pi}E\left(\frac{k\ell\phi}{2}\right).T_1(\theta)\right\rvert^2+\left\lvert\frac{k\ell}{\pi}E\left(\frac{k\ell\phi}{2}\right).T_2(\theta)\right\rvert^2\right)$

D. Size Distributions

Electromagnetic radiation traveling through a scattering medium can be scattered one or more times, depending on the distance between scattering centers. In many situations (e.g., zodiacal light, fogs, haze, some clouds), the scattering centers are widely separated and, hence, the radiation is scattered only once before striking a detector. It is this special case of singular scattering that is considered in this section. Another condition that is usually assumed in single scattering is that the scattering centers are randomly located with respect to each other. When both conditions are met, each scattering center can be considered separately and the effects of all the centers is just the sum of the effects of each.

The components of the differential cross section from an isotropic homogeneous cloud of particles is given

$$\overline{\left(\frac{d\sigma}{d\Omega}\right)}_j = \frac{1}{k^2} \sum_{\Delta a} i_j \, (m, \theta, ka) \; n(a) \, \Delta a \qquad j = 1, 2$$

where the sum is over the particle sizes. For an isotropic, heterogeneous cloud, the differential cross section is the sum of the cross sections of each particle,

$$\overline{\left(\frac{d\sigma}{d\Omega}\right)}_j = \frac{1}{k^2} \sum_{\ell} \sum_{\Delta a} i_j \, (m_\ell, \theta, ka) \; n(a) \, \Delta a$$

where each sum is taken only for a given refractive index (material) and all particles are assumed to follow the same size distribution law.

If the size distribution is continuous, the summation can be replaced by an integral

$$\overline{\left(\frac{d\sigma}{d\Omega}\right)}_j = \frac{1}{k^2} \int i_j \, (m, \theta, ka) \; n(a) \, da$$

where n (a) represents the size distribution. As can be seen, n (a) plays an important role in scattering. For this reason, several families of size distributions are discussed in this section.

There are many size distributions used in the study of light scattering; most are empirical formulae. Usually, two parameters are sufficient to describe the distribution, one parameter being associated with a particular particle size (mean, mode, median) and the other defining the spread or variance in the distribution.

Distributions may be unimodel, bimodel, etc. However, since the simple bimodel and higher model distributions can be represented as a sum of unimodel distributions, only two parameter unimodel distributions will be considered.

The formulae for the distributions discussed below are categorized according to form. The four categories used are listed in Table 3.

TABLE 3. SIZE DISTRIBUTION FORMULAE

Category I. Modified Gamma Distribution

$$n(a) = n_o a^{\gamma} \exp(-ba^p)$$

Category II. Exponential Distributions

$$n_2(a) = n_o \exp(ca^p)$$

Category III. Logarithmic Distributions

$$n_3^m(a) = n_{o_m} a^m \exp\left[-\left(\frac{\ell n(a/\bar{a})}{\sqrt{2}\,\sigma}\right)^2\right]$$

Category IV. Inverse Power Law

$$n_4(a) = n_o(a/a_o)^{-p}$$

Category I is a modified gamma distribution

$$n_1(a) = n_o a^{\gamma} \exp(-ba^p) \tag{8}$$

which has been used by Deirmendjian (1966) to describe haze and clouds. n_o, γ, b, and p are real positive numbers and γ is an integer. As used by Deirmendjian, n_o, γ, b, and p are not independent of each other and are related to quantities in the frequency distribution. n_o is related to the total number of particles per unit volume, and b is related to the mode radius, provided γ and p are fixed. If p = 1, $n_1(a)$ reduces to the gamma distribution.

Differentiating $n_1(a)$ with respect to ℓn a, one obtains

$$a \frac{d}{da} [\ell_n n(a)] = \gamma \left[1 - \left(\frac{a}{a_c}\right)^p\right] \tag{9}$$

where a_c is the model radius. This formula represents the slope of the curve of log n(a) versus log a. Figure 3 shows the size distributions for some particular examples of n_1 (a). Table 4 gives the parameters used for each distribution. The mode radius is the same in each one, and the parameters were chosen so that the slope of the curves is −4 at a radius of 1.6 microns. A particle density of 1.5×10^{-15} cm $^{-3}$ was used.

TABLE 4. PARAMETERS FOR THE MODIFIED GAMMA DISTRIBUTION OF FIGURE 3.

Distribution	γ	p	n_o	b
1	6.0	0.1705	$7.4247 \times 10^{+8}$	54.1778
2	3.0	0.2828	3.7400×10^{-7}	21.7002
3	1.0	0.5372	2.9998×10^{-13}	7.2442

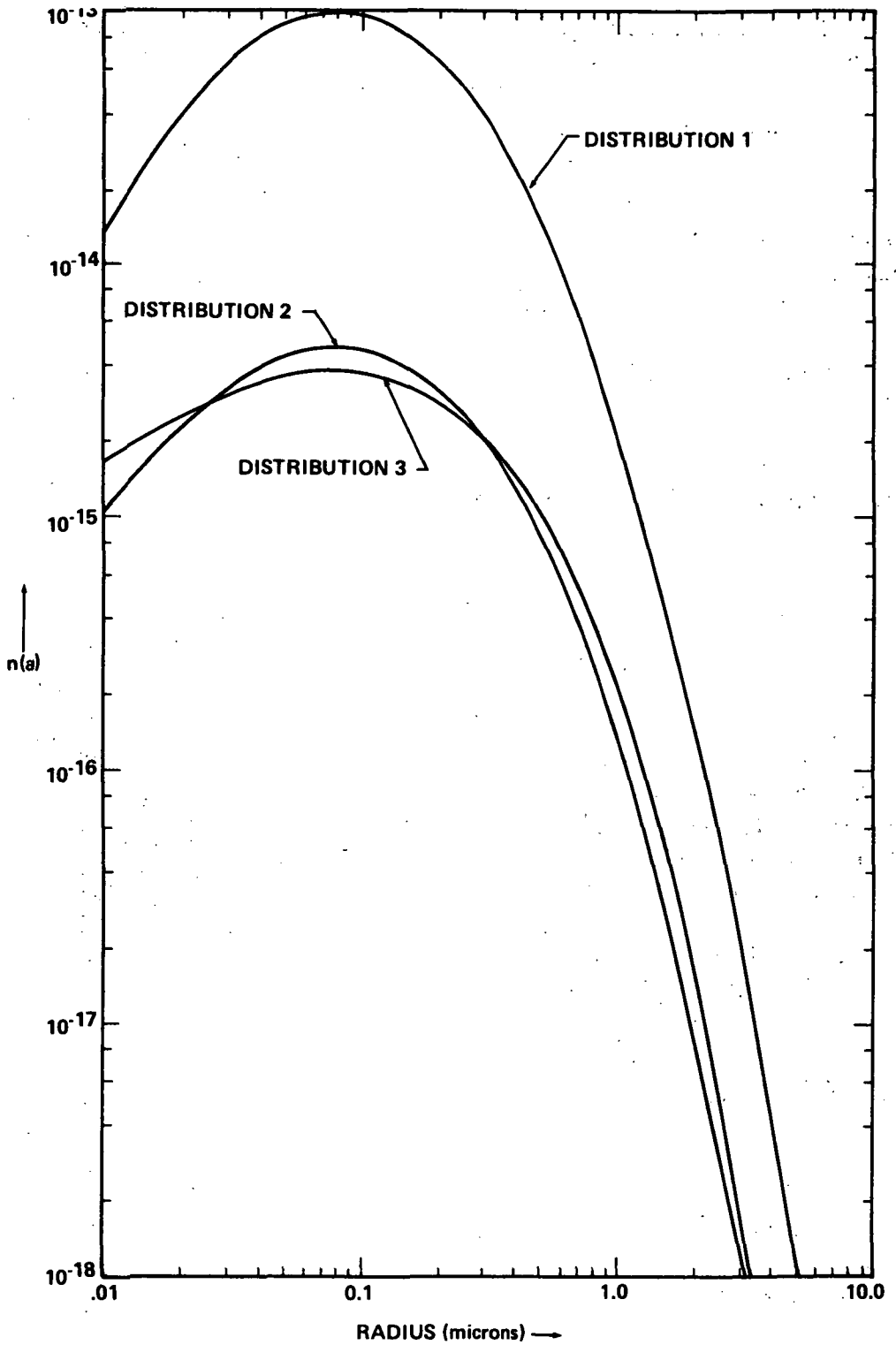

Figure 3. Category I distributions.
(All distributions have mode radius = 0.08.)

The family of distributions represented by

$$n_2(a) = n_o \exp(ca^p) \tag{10}$$

represents Category II distributions. It includes the normal or Gaussian distribution

$$n_2(a) = \frac{n_o}{\sqrt{2\pi}\sigma} \exp\left(-\frac{(a-\bar{a})^2}{2\sigma^2}\right) \tag{11}$$

where the parameters $\bar{a}$ and σ are the mean and standard deviation defined by

$$\bar{a} = \int_{-\infty}^{+\infty} a\, n_2(a)\, da$$

$$\sigma^2 = \int_{-\infty}^{+\infty} (a-\bar{a})^2\, n_2(a)\, da \quad .$$

This distribution has the disadvantage that it admits particles with "negative" radii. Figure 4 shows the Gaussian distribution for a mean radius of 1.0 and standard deviations of 1.0 and 3.0. Only the portion of the curve corresponding to positive radii is shown. Figure 5 shows the form of the Category II distribution for simple powers of exponent.

Category III distributions are those that are similar in form to the logarithmic distributions described by

$$n_3^m(a) = n_{om} a^m \exp\left[-\left(\frac{\ell n\,(a/\bar{a})}{\sqrt{2}\,\sigma}\right)^2\right] \tag{12}$$

where n_{om} is the normalizing factor for $n_3^m(a)$. m is a shape factor, $\bar{a}$ is one of the moments of the distribution (media, mean, mode, etc.), and σ is a measure of the width of the dispersion. Figure 6 shows a plot of equation (12) for several values of m. Note that this family of curves is skew symmetric.

A simple relation between the mode radius, $\bar{a}$, σ^2, and the shape factor m is found by differentiating n (a) with respect to a and setting it equal to zero. dn/da is zero at the model radius, hence, $m = \left(\frac{\ell n a_m - \ell n \bar{a}}{\sigma^2}\right)$.

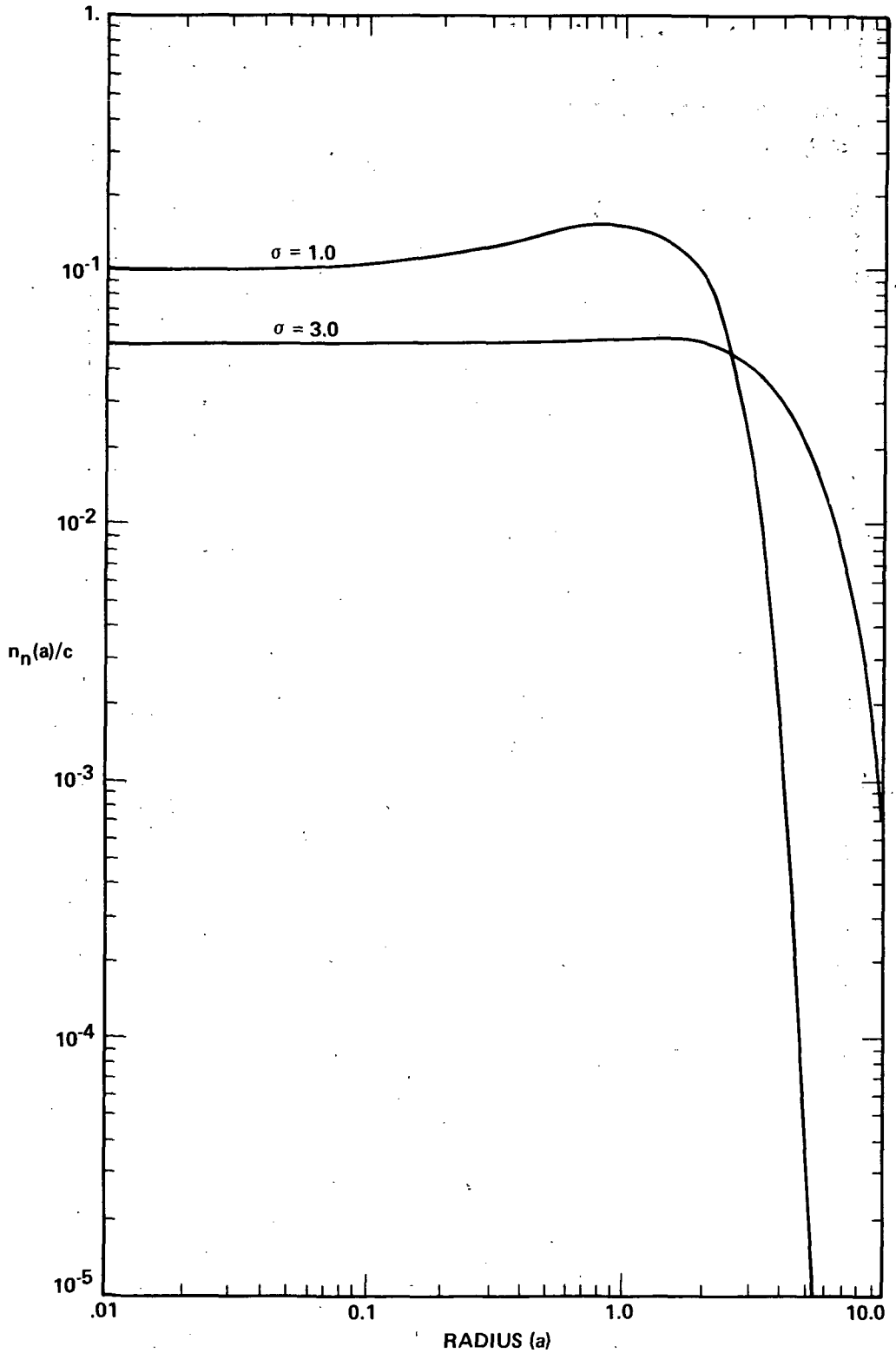

Figure 4. Gaussian particle size distribution for positive radii. (Mean radius = 1.0 and σ = 1.0 and 3.0.)

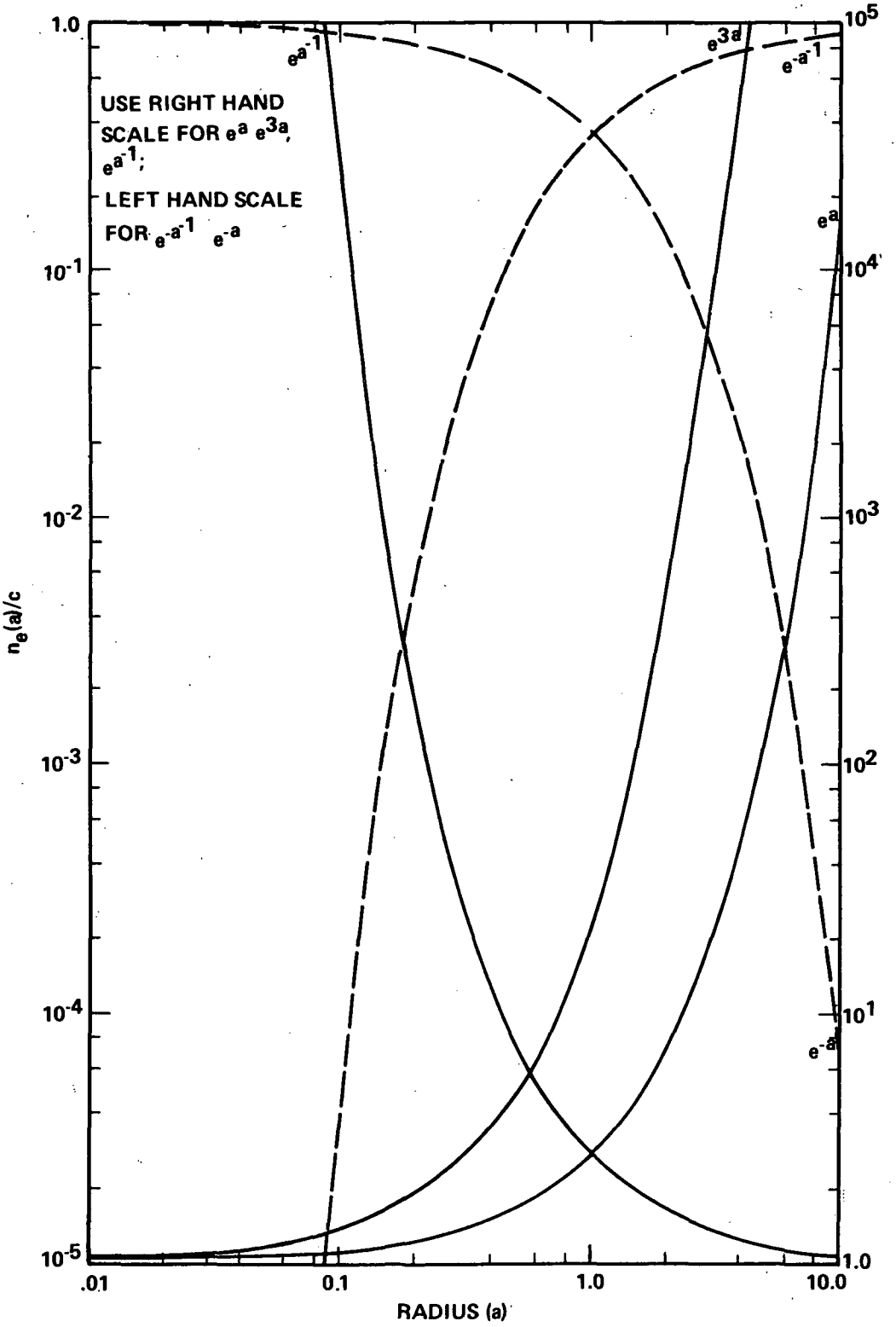

Figure 5. Category II distributions for some examples of simple powers of the exponential.

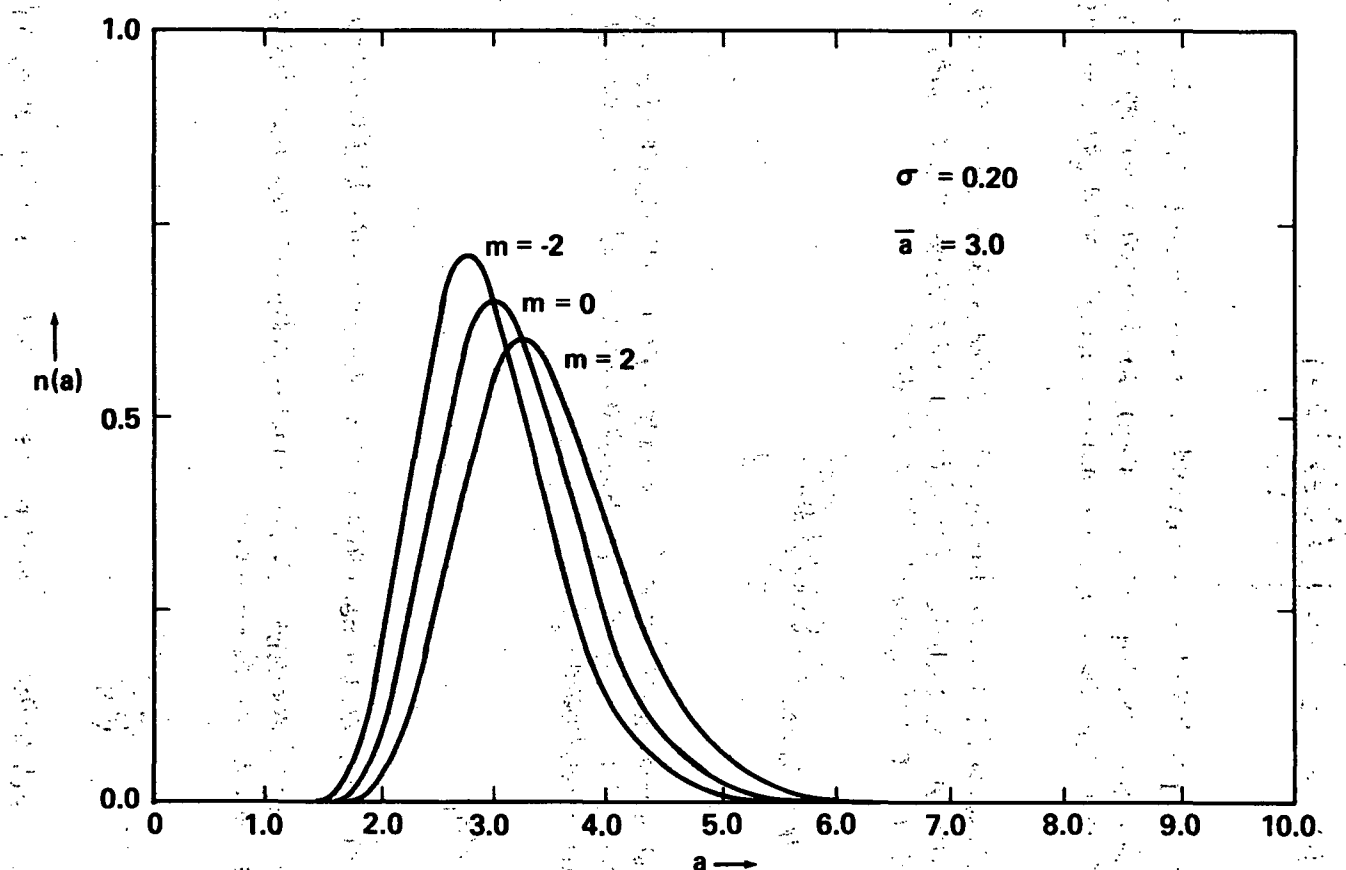

Figure 6. Effect of the shape factor m on the form of the logarithmic distribution.

If m = -1, the logarithmic distribution becomes the logarithmic normal distribution

$$n_3^{-1}(a) = n_{o-1} a^{-1} \exp\left[-\left(\frac{\ell n\,(a/\bar{a}_{-1})}{\sqrt{2}\,\sigma_g}\right)\right]. \tag{13}$$

In this case, $\bar{a}_{-1}$ is both the median and the mean value of a; σ_g is the standard deviation for ℓ na. The log normal distribution has the advantage that the median (which is also the geometric mean) remains invariant over all σ's (Fig. 7).

Espenschied [111] and Kerker [24] make extensive use of the zeroth order logarithmic distribution (ZOLD) in their work on aerosols. For this distribution, m = 0 and equation (12) reduces to

$$n_3^{o}(a) = n_o \exp\left[-\frac{(\ell na - \ell n\bar{a})^2}{2\sigma^2}\right] . \tag{14}$$

$\bar{a}$ is now the model value and remains invariant for all values of σ. If the distribution is narrow, i.e., if σ^2 is negligible compared to σ, then σ is related to the standard deviation σ_s by

$$\sigma = \bar{a}\,\sigma_s .$$

As σ gets smaller, ZOLD becomes symmetric as shown in Figure 8.

Category IV distributions are most popular for zodiacal light studies. The inverse power law distribution

$$n_4(a) = n_o \left(\frac{a}{a_o}\right)^{-p} \tag{15}$$

represents this distribution. For published zodiacal light models, k has usually been in the range of 2.5 to 4.0. As with the other distributions, the distribution can be modified; e.g., Aller et al. [22], in an attempt to obtain a

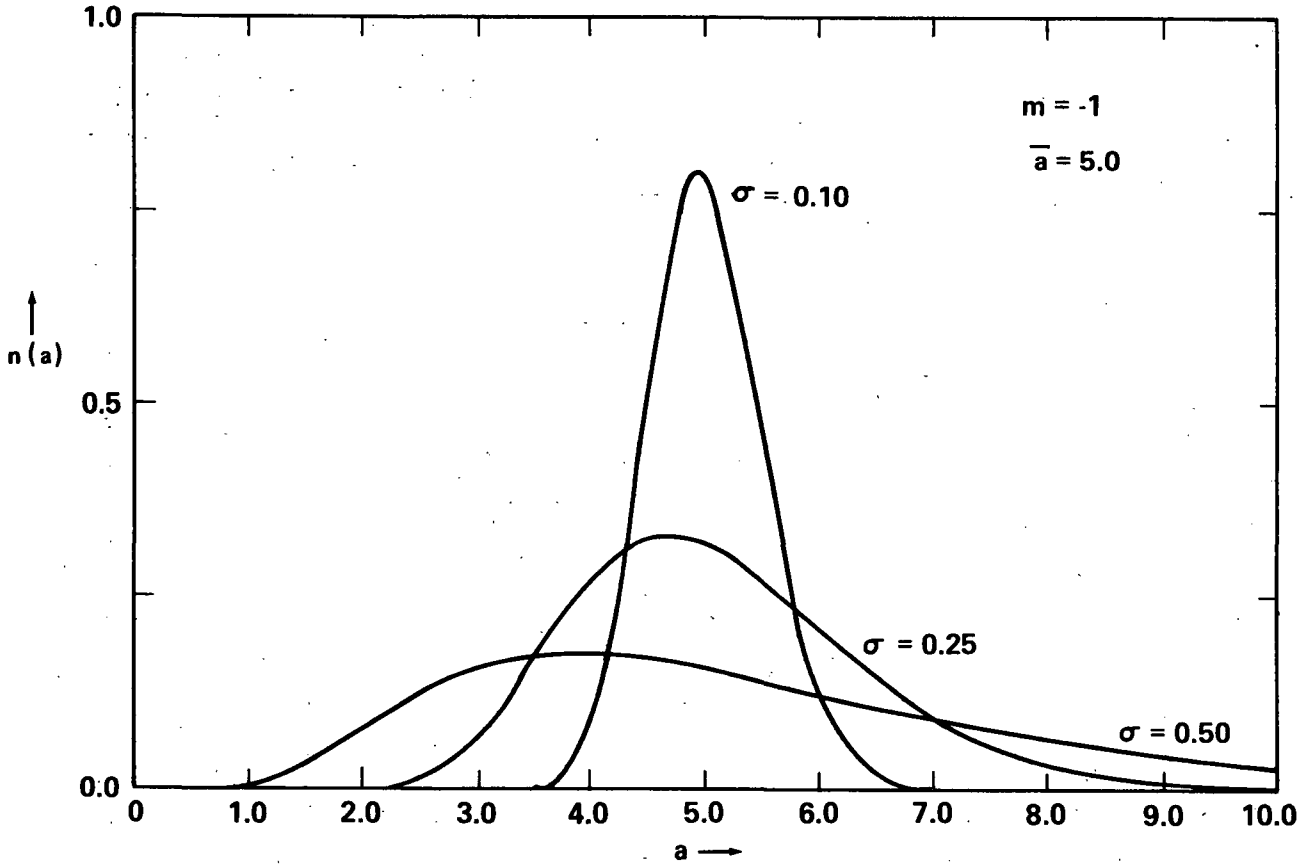

Figure 7. Logarithmic normal distribution curves for $\bar{a} = 5.0$ and $\sigma = 0.10$, 0.25, and 0.50.

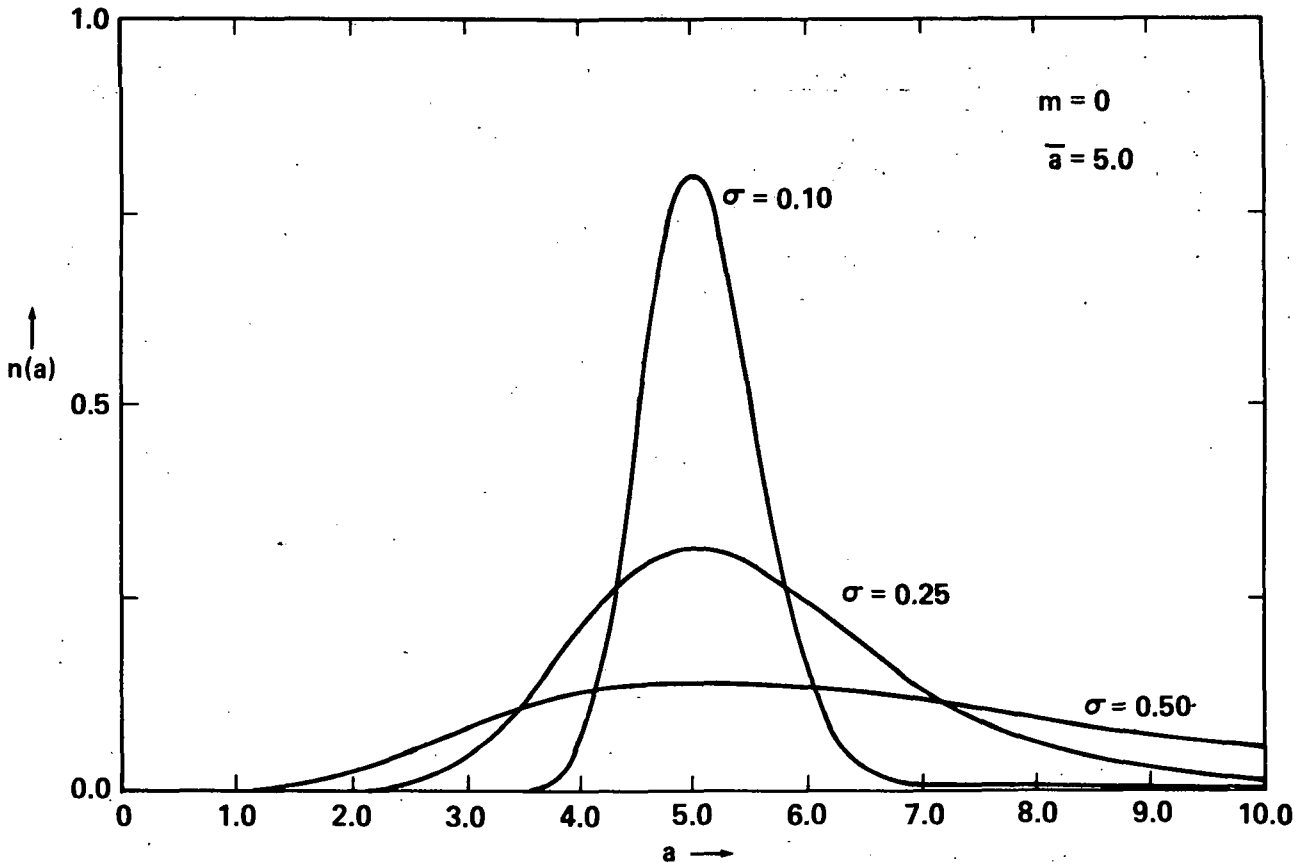

Figure 8. The zeroth-order logarithmic distribution (ZOLD) with $\bar{a} = 5.0$ and $\sigma = 0.10$, 0.25, and 0.50.

better model of the zodiacal light, allow k to vary for different ranges of a. This form of the Category IV distribution is the broken power law. Figure 9 shows the Category IV distribution for the values of k noted above. It is evident that the smaller particles dominate in this distribution.

The importance of the inverse power law comes from the fact that the cumulative mass distribution for meteors between 10 and 10^{-11} g (a radius between 1 cm and 1 micron) is relatively linear on a log-log plot [25]. This region covers the range from visual observations to dust-particle sensors on rockets and spacecraft. The number density increases with decreasing size, although there must be a physical limitation to this trend. If and when a lower particle size cut-off is determined, the other categories will be more important in the study of zodiacal light.

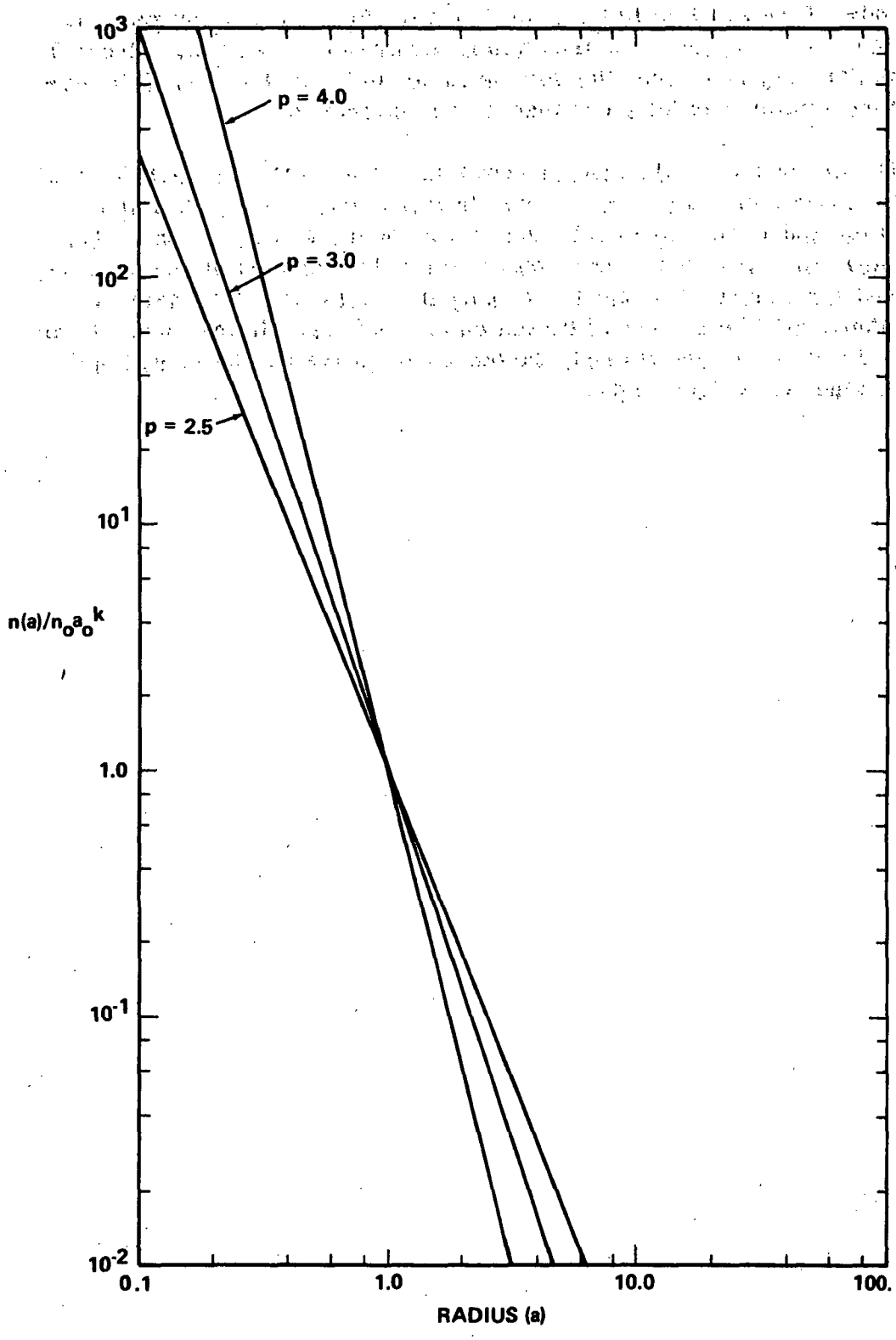

Figure 9. Category IV distributions for p = 2.5, 3.0, and 4.0.

SECTION III. MODEL CALCULATIONS

A. Introduction

The main objective in the study of zodiacal light is to deduce the nature, amount, and distribution of the particles responsible for this light. This knowledge is of fundamental importance in the theory of the origin and structure of the solar system. The zodiacal light can be interpreted on the basis of scattering of sunlight by a cloud of interplanetary particles. The properties of this cloud are to be determined without a priori knowledge of spatial extent, particle shape and size distribution, and concentration, and the variation of these parameters with radial distance from the sun. The mathematical formulation for the problem is relatively simple, though there are difficulties related to the observational uncertainties and the choice of models.

The basic scheme is to make as many models as feasible and to approach a solution by trial and error, checking for consistency, and agreement with other theoretical criteria. To date, the number of parameters for the models exceeds the number of observed integral quantities.

There are two important questions to be answered: (1) which forms of the mathematical functions permit the expression of the physical properties observed? (2) what are the values of the parameters of these functions which satisfy the observed quantities? It is by no means certain that there is a unique answer to each of these questions. The approach to the problem is through the integral equations which characterize the physical process of the scattering of the light. These equations for the radiance L are as follows:

$$L_\lambda^j(\epsilon) = \int\int\ldots\int \eta\,(a, \xi, m, x, y, z) \cdot i_\lambda^j\,(a, \xi, m, \phi, \Theta) \cdot da\, d\xi\, dm\, dx\, dy\, dz\, d\phi\, d\Theta \qquad j = 1, 2 \quad . \tag{16}$$

The number density η and the scattering intensity functions i_λ^j are to be determined. Generally, one postulates the form of these functions, evaluates the

integral equations, and compares the calculated values for the radiance components with observation. This approach manifests itself in the approximation of the functions η and i_λ^j with their dependence on the particle size a, refractive index m, position x, y, z, and other intrinsic variables ξ.

The calculation of the observable photometric radiance and polarization based on various models is presented in this section. The calculated values of these quantities are compared to the observed data in Section V. Radiometric quantities are used in the development. These quantities are defined in Table 5.

B. Cloud Radiance Integral

A basic assumption throughout the development is that of single scattering. For 1-micron particles with a density of 10^{-10} particles/m^3, the mean free path is on the order of 10^{11} AU. Single scattering appears to be an appropriate assumption. Hence, extinction of the solar radiation and multiple scattered radiation will be neglected.

Figure 10 shows the geometry for sunlight scattered by interplanetary particles in a cylindrical volume element of length $d\Delta$ and volume $dA_e\ d\Delta$ at a distance r from the sun and a distance Δ from the earth.

The particles in the volume element $dA_e\ d\Delta$ receive solar energy in the wavelength interval λ to $\lambda + \delta\lambda$ at the rate of

$$E_\lambda\ \delta\lambda\ [dA_e\ d\Delta\ \eta(a, r)\ da]\ G \tag{17}$$

where

G = the projected area normal to the incident sunlight (πa^2 for spheres of radius a) (m^2).

E_λ = the spectral radiant flux density at the surface of the volume element (w/m^2 - nm).

$\eta(a, r)$ = the number of particles per unit volume per unit increment of the size factor (radius) at a at a distance r from the sun (number/m^4).

From the definition of the differential cross section, the fraction of energy received that is scattered toward the earth is

TABLE 5. RADIOMETRIC QUANTITIES

Radiant Energy, Q, is the energy propagating in the form of electromagnetic waves (J).

Radiant Density, $W = dQ/dV$, is radiant energy per unit volume (J/m^3).

Radiant Flux, $\Phi = dQ/dt$, is the time rate of flow of radiant energy (w).

Spectral Radiant Flux, $\Phi_\lambda = d\Phi/d\lambda$, is the radiant flux per unit wavelength interval at wavelength λ (w/Nm).

Radiant Intensity, $I = d\Phi/d\omega$, of a source is the radiant flux proceeding from the source per unit solid angle in the direction considered (w/sr).

Spectral Radiant Intensity, $I_\lambda = dI/d_\lambda$, is the radiant intensity per unit wavelength interval at wavelength λ (w/sr-Nm).

Radiance, $L = d^2\Phi/d\omega(dA \cos\Phi)$, in a direction, at a point on the surface of a source, is the quotient of the radiant flux $d\Phi$ leaving and propagating in directions defined by an elementary cone containing the direction by the product of the projection of an element of the surface dA containing the point onto a plane perpendicular to the given direction and the solid angle $d\omega$ of the cone (w/sr-Nm).

Radiant Flux Density at a Surface (Irradiance), $E = d\Phi/dA$, is the quotient of radiant flux at that element of surface to the area of the element (w/m^2).

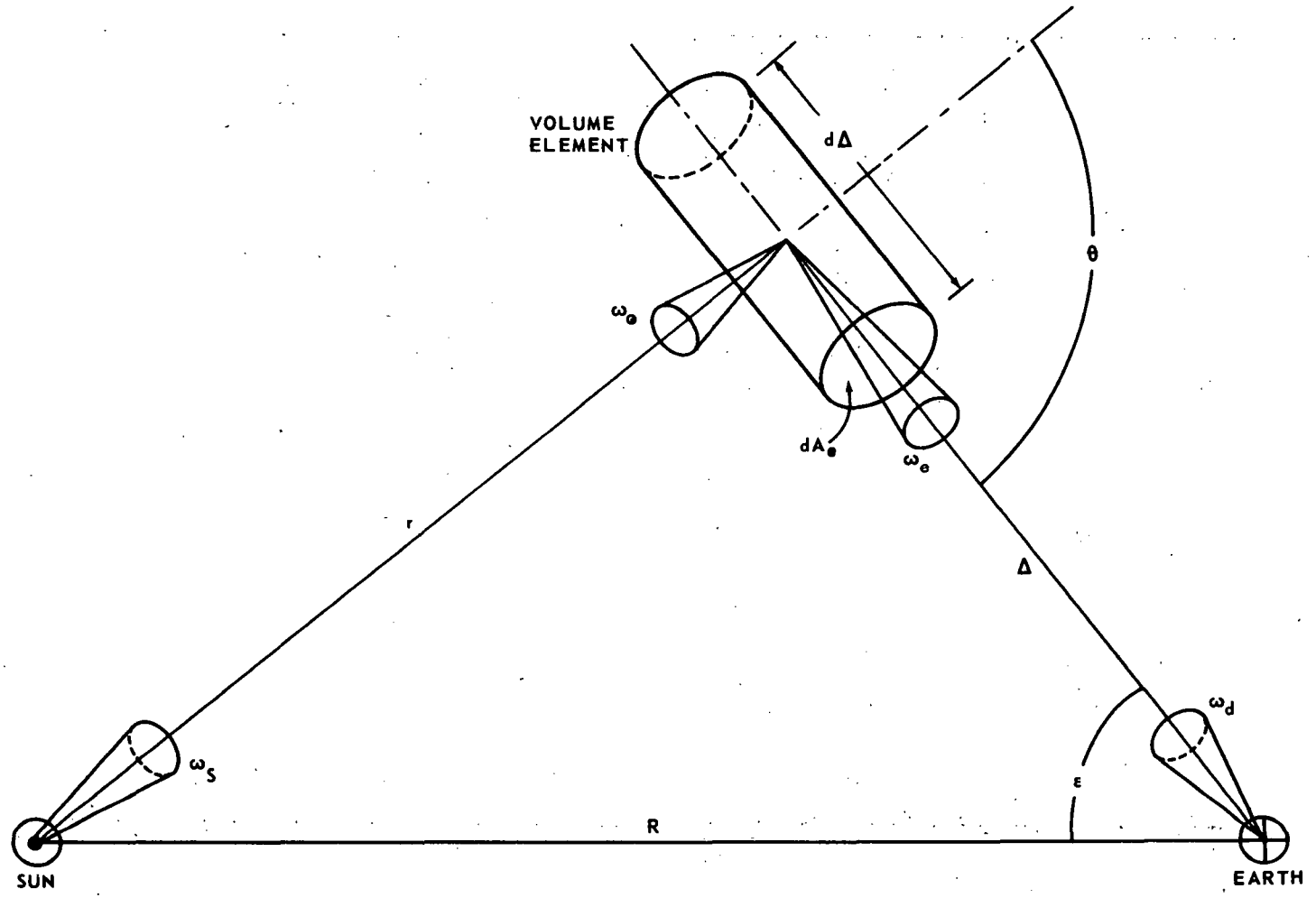

Figure 10. The geometry for light scattering from interplanetary medium.

$$\left(\frac{d\sigma}{d\Omega}\right) \quad \frac{\omega_e}{\pi a^2} \tag{18}$$

where ω_e is the solid angle the detector subtends at the volume element. For simplicity, spherical scatterers have been assumed.

To obtain the radiance, the flux coming from the particles is divided by the area element dA_e and by the solid angle through which it propagates from that area ω_e. The result is

$$dL_\lambda = E_\lambda \delta\lambda [dA_e \, d\Delta \eta(a, r) da] \pi a^2 \left(\frac{d\sigma}{d\Omega}\right) \frac{\omega_e}{\pi a^2} \cdot \frac{1}{\omega_e dA_e} \tag{19}$$

and

$$dL_\lambda = E_\lambda \, \delta\lambda \, d\Delta \, \eta(a, r) \, da \, \frac{d\sigma}{d\Omega} \quad . \tag{20}$$

In the literature, the term $\pi a^2 \bar{I}(\Theta)$ may appear in lieu of $d\sigma/d\Omega$. The scattering function of a sphere $\bar{I}(\Theta)$ is defined as the amount of radiation scattered per unit solid angle in a direction inclined at an angle Θ to the incident direction divided by the radiation that falls on the geometrical cross section of the particle;

$$\bar{I}(\Theta) = \frac{1}{\pi a^2} \frac{d\sigma}{d\Omega} \quad . \tag{21}$$

Since radiance L is the flux Φ per unit area of the emitting surface A_e per unit solid angle ω_e, then if a detector A_d at a distance Δ from the surface sees the surface through a solid angle ω_d, one has the relation:

$$L = \Phi/A_e\omega_e = \Phi/(A_e A_d/\Delta^2) = \Phi/A_d\omega_d \quad ; \tag{22}$$

a symmetry which causes derivations in the literature to differ in appearance.

The integrated radiance from all the volume elements along a given line of sight is from equations (6) and (16)

$$\bar{L}_\lambda = \int_0^\infty \int_{a_{min}}^{a_{max}} E_\lambda \, \delta\lambda \, \eta \, (a, r) \, \frac{d\sigma}{d\Omega} \, d\Delta \, da \tag{23}$$

where a_{min} and a_{max} are the minimum and maximum values of the particle size.

Equation (23) has been derived in various forms by numerous authors; e.g.; Searle [1], Schoenberg [2], Van de Hulst [13], Walter [15], Giese [26], Gillett [27], and Aller et al. [22].

C. Particle Size Distribution

Due to the mathematical difficulties involved in solving Maxwell's equation for a scatterer of arbitrary shape, the approaches to the scattering functions are limited to using the following:

1. Mie theory formulation for spherical particles.

2. Formulations for other basic shapes, e.g., cylinders and spheroids, from which the scattered radiation can be described in a closed form.

3. Perturbation methods and approximation.

4. Laboratory results.

Considerable analysis is based on the assumption that the interplanetary dust particles are spherical, even though in actuality, spherical particles in interplanetary space are thought to be rare. On the other hand, a large number of spheroids have been found in recent Apollo finds. These spheroids were formed by a process which may have produced spheroids in interplanetary space. However, one cannot, a priori, extend the properties of particles in the finds to particles in interplanetary space, even though the two may have had similar origins and histories.

In support of the assumption of spherical interplanetary dust particles, one must also note that distributions of large volume, irregularly-shaped particles can be approximated by equivalent distributions of spherical particles [28].

The distribution function η (a, r) can be separated into a particle-size distribution n(a) and a spatial distribution s(r). The size distribution function n is arbitrary, but in zodiacal light model calculations the assumption of an inverse power law is dominant because of meteor studies, physical considerations, photometric analysis, and simplicity.

The inverse power law particle-size distribution (Category IV)

$$n(a) = n_o \left(\frac{a}{a_o}\right)^{-p}$$

will be primarily used here. Section II.D lists other distributions which could be used. However, the particle sizes and materials have to be chosen so that the observed radiance and polarization curves are reproduced. It may be possible by using the dynamical forces (see appendix) and chemical and physical processes working on the interplanetary matter to derive a particular distribution, although this has not been done. The forces and processes are important in the selection of a distribution form.

D. Heliocentric Distributions of Scattering Particles

The spatial distribution function s(r) is primarily determined by the solar gravitation and radiation fields and, therefore, is assumed to be a heliocentric distribution and symmetric about the ecliptic. The various heliocentric spatial distribution models are divided into planar and ellipsoidal models. The planar models, due to Gillett, are the constant thickness plane model and the linearly increasing cone model. These models represent first approximations for calculations of the photometer functions out of the ecliptic. A somewhat more realistic model, the exponential model due to Aller et al. [22], has an exponential decay factor for the spatial density of the particles. The decay is in a direction perpendicular to the ecliptic.

The other models have ellipsoidal symmetry and are, at least partially, based on the orbital motions of meteors. The flatness of the ellipsoidal surface is characterized by one of the parameters.

Before studying these models, consider the photometric functions as observed in the ecliptic plane for heliocentric models.

Let the function η (a, r) have the form:

$$\eta(a, r) = n_o \left(\frac{a}{a_o}\right)^{-p} \left(\frac{R}{r}\right)^{m} \tag{24}$$

where $n_o (a/a_o)^{-p}$ is the particle size distribution and a_o, p, m, and n_o are parameters for the model.

The radiant flux surface density has an inverse square dependency on the solar distance due to the geometric attenuation. If we define the spectral radiant flux surface density at R = 1 AU to be E_λ^e, then the general spectral radiant flux surface density is

$$E_\lambda = E_\lambda^e \left(\frac{R}{r}\right)^2 \tag{25}$$

Equation (23) then becomes

$$\bar{L}_\lambda = \int_0^\infty \int_{a_{min}}^{a_{max}} E_\lambda^e \left(\frac{R}{r}\right)^2 \delta\lambda \; \eta(a, r) \; \frac{d\sigma}{d\Omega} \; d\Delta \; da \; . \tag{26}$$

From Figure 11 (Fig. 10 modified), it is seen that

$$\Delta = R \cos \epsilon - r \cos \Theta \; , \tag{27}$$

where ϵ is the elongation and Θ is the scattering angle. From the law of sines, we have

$$\frac{r}{R} = \frac{\sin \epsilon}{\sin \Theta} \; ; \tag{28}$$

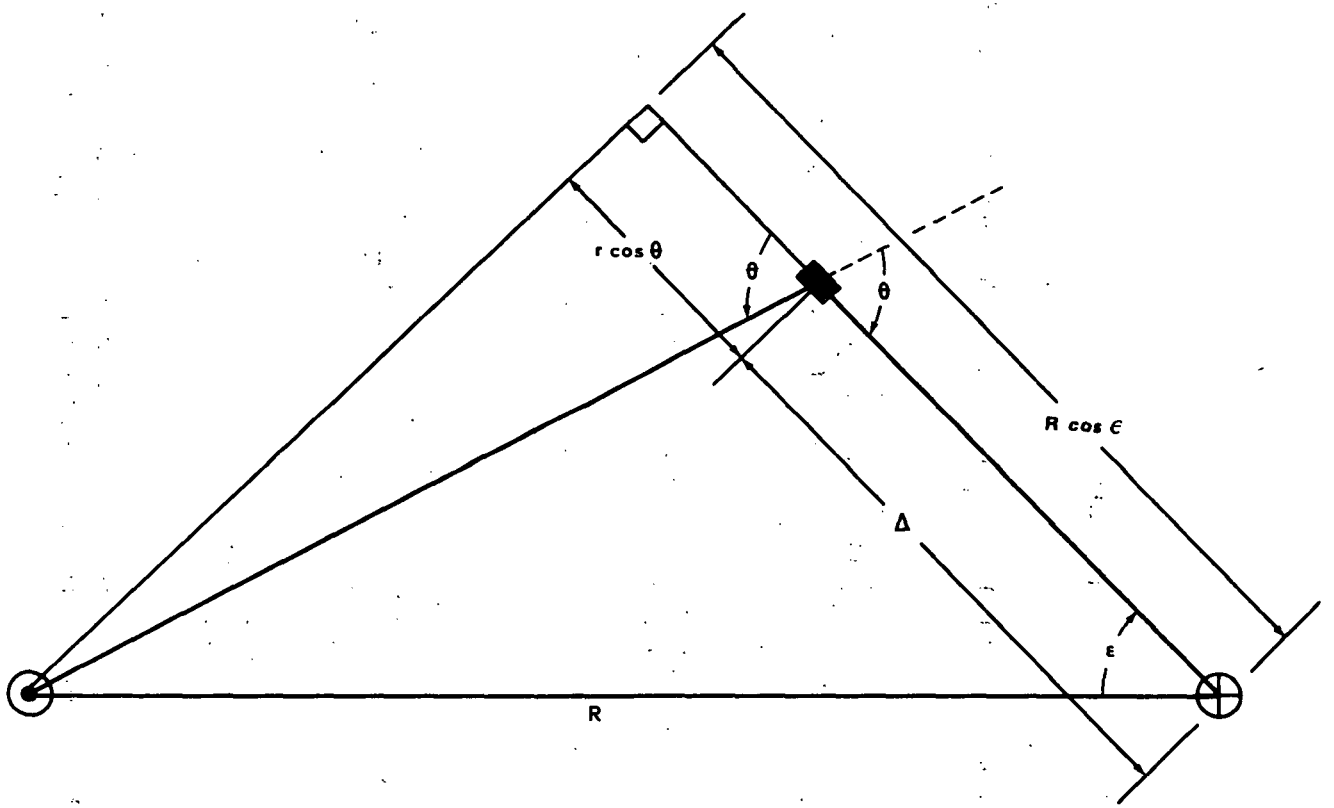

Figure 11. Modification of Figure 10.

hence,

$$\Delta = R \cos \epsilon - R \frac{\sin \epsilon}{\sin \Theta} \cos \Theta \quad . \tag{29}$$

Therefore,

$$d\Delta = R \sin \epsilon \, d\Theta / \sin^2 \Theta \quad . \tag{30}$$

Substitution of equations (24), (28), and (30) into expression (26) gives

$$\bar{L}_\lambda = \int_\epsilon^\pi \int_{a_{min}}^{a_{max}} E_\lambda^e \left(\frac{\sin \Theta}{\sin \epsilon}\right)^2 \delta\lambda \left(\frac{d\sigma}{d\Omega}\right) n_o \left(\frac{a}{a_o}\right)^{-p}$$

$$\times \left(\frac{\sin \Theta}{\sin \epsilon}\right)^m da \, \frac{R \sin \epsilon \, d\Theta}{\sin^2 \Theta} \quad , \tag{31}$$

or

$$\bar{L}_\lambda = \frac{R E_\lambda^e \, \delta\lambda}{\sin^{m+1} \epsilon} \int_{a_{min}}^{a_{max}} n_o \left(\frac{a}{a_o}\right)^{-p} da \int_\epsilon^\pi \sin^m \Theta$$

$$\times \left(\frac{d\sigma}{d\Omega}\right) d\Theta \quad . \tag{32}$$

Note that we now have an integration over Θ and that all scattering angles from ϵ to π contribute, as illustrated in Figure 12.

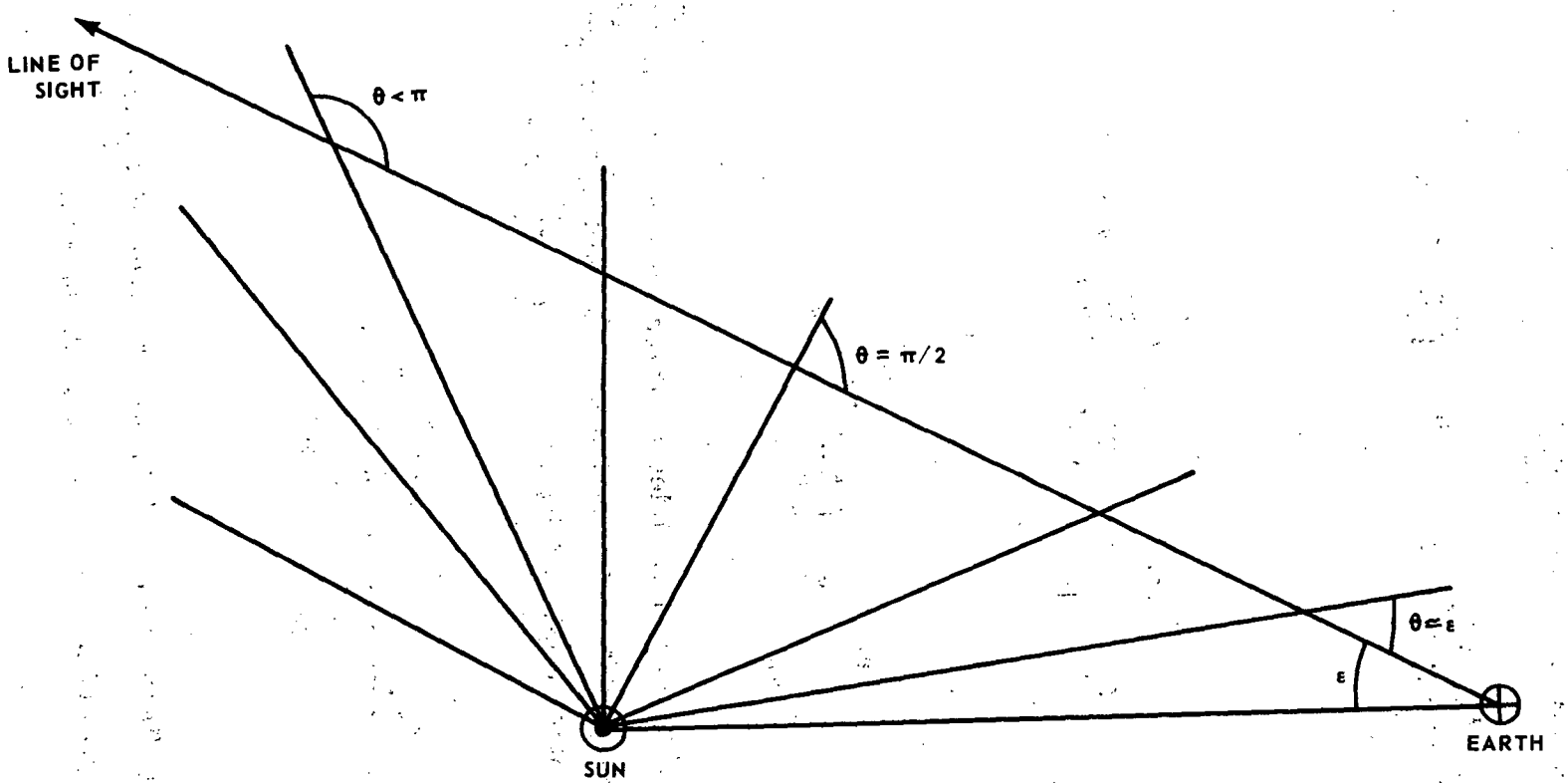

Figure 12. Scattering angle contributions from ϵ to 180 deg for an elongation of ϵ.

Equation (32) can be written as

$$\overline{L}_\lambda = \frac{RE_\lambda^e \, \delta\lambda \, N_o}{\sin^{m+1} \epsilon} \int_\epsilon^\pi \sin^m \Theta \, \overline{\left(\frac{d\sigma}{d\Omega}\right)} \, d\Theta \tag{33}$$

where

$$\overline{\left(\frac{d\sigma}{d\Omega}\right)} = \frac{1}{N_o} \int_{a_{min}}^{a_{max}} n_o \left(\frac{a}{a_o}\right)^{-p} \left(\frac{d\sigma}{d\Omega}\right) da \tag{34}$$

and

$$N_o = \int_{a_{min}}^{a_{max}} n_o \left(\frac{a}{a_o}\right)^{-p} da \tag{35}$$

N_o is the total number of particles per cubic meter at 1 AU and $\overline{\left(\frac{d\sigma}{d\Omega}\right)}$ is the average differential cross section over the distribution of particles. A change of the integration variable from a to $\alpha = \frac{2\pi a}{\lambda}$ yields

$$\overline{\left(\frac{d\sigma}{d\Omega}\right)} = \frac{\int_{\alpha_1}^{\alpha_2} \alpha^{-p} \left(\frac{d\sigma}{d\Omega}\right) d\alpha}{\int_{\alpha_1}^{\alpha_2} \alpha^{-p} \, d\alpha} \tag{36}$$

To investigate equation (33) for the simple behavior of L_λ, assume that $\overline{\frac{d\sigma}{d\Omega}}$ is independent of Θ. Hence, consider the integral,

$$I_m(\epsilon) = \frac{1}{\sin^{m+1}(\epsilon)} \int_{\epsilon}^{\pi} \sin^m(\Theta)\, d\Theta \quad .$$

For m = 0,

$$I_{m=0} = \frac{\pi - \epsilon}{\sin \epsilon} \quad ;$$

for m = 1,

$$I_{m=1} = \frac{1 + \cos \epsilon}{\sin^2 \epsilon} \quad ;$$

and for m = 2,

$$I_{m=2} = \frac{\frac{1}{2}(\pi - \epsilon + \sin \epsilon \cos \epsilon)}{\sin^3 \epsilon} \quad .$$

For m = 0, there is no radial dependence, $(R/r)^0 = 1$, except for geometric attenuation of solar radiation. These results are illustrated in Figure 13. Notice that for ϵ = 45 deg, I_m is approximately independent of m . Also, I_m has the form of the observed radiance data which indicates in the ecliptic that the dependence of $\overline{L}$ on $\overline{\frac{d\sigma}{d\Omega}}$ is limited.

As ϵ approaches π ,

$$\frac{1}{\sin^{m+1}\epsilon} \int_{\epsilon}^{\pi} \sin^m\Theta\, d\Theta \xrightarrow[\epsilon \to \pi]{} \frac{1}{y^{m+1}} \int_0^y x^m\, dx = \frac{1}{m+1} \quad ;$$

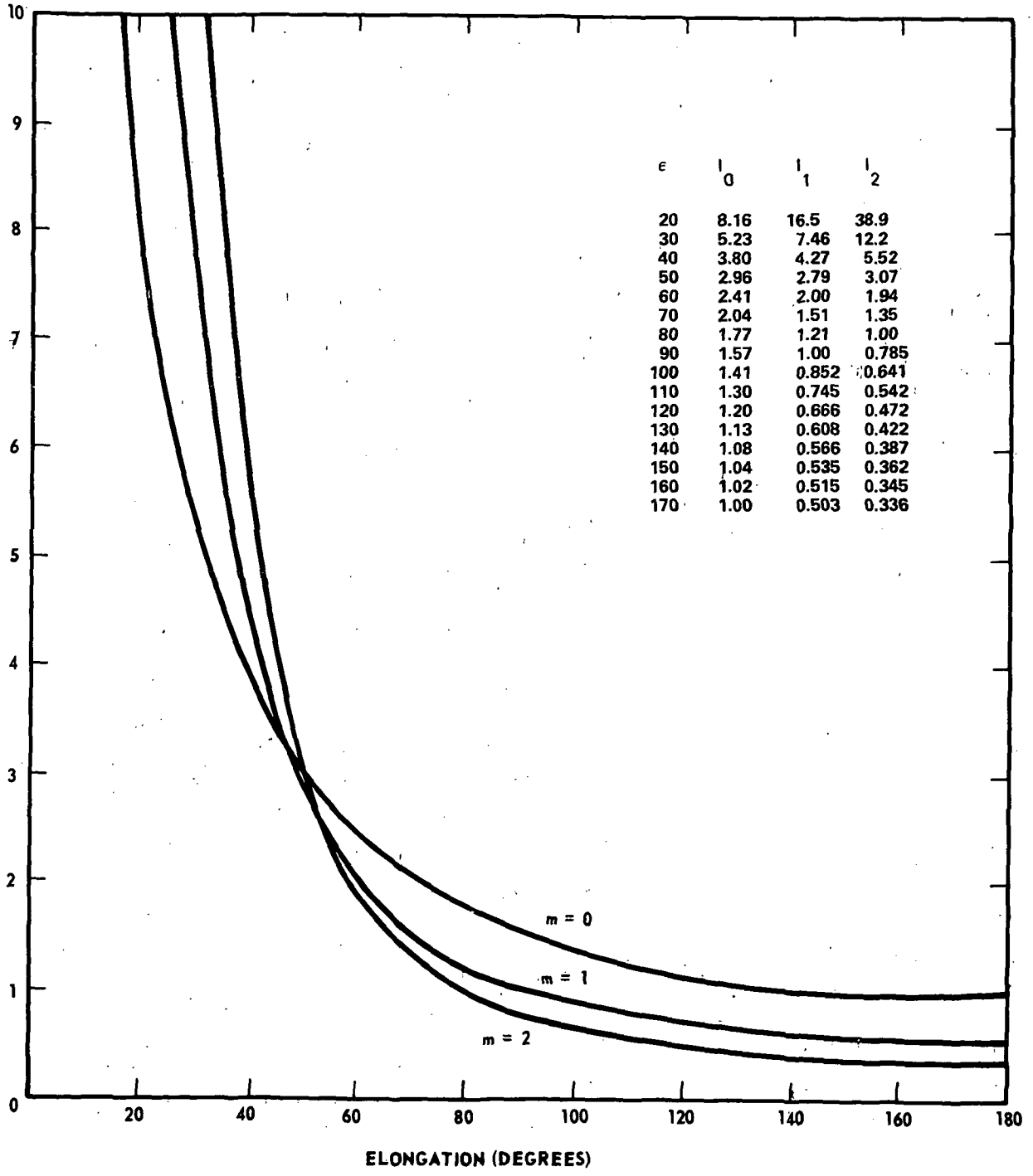

ϵ	I_0	I_1	I_2
20	8.16	16.5	38.9
30	5.23	7.46	12.2
40	3.80	4.27	5.52
50	2.96	2.79	3.07
60	2.41	2.00	1.94
70	2.04	1.51	1.35
80	1.77	1.21	1.00
90	1.57	1.00	0.785
100	1.41	0.852	0.641
110	1.30	0.745	0.542
120	1.20	0.666	0.472
130	1.13	0.608	0.422
140	1.08	0.566	0.387
150	1.04	0.535	0.362
160	1.02	0.515	0.345
170	1.00	0.503	0.336

Figure 13. I_m dependence on ϵ for $m = 0, 1,$ and 2.

hence, $I_m(\epsilon = \pi) = \frac{1}{m+1}$. This result can give an estimate for the value of the gegenschein, assuming that $\overline{\left(\frac{d\sigma(\Theta = 180 \text{ deg})}{d\Omega}\right)}$ is known and is behaving smoothly in this region.

E. Gillett Models

The two models now considered which are not limited to the ecliptic plane are due to Gillett [27]:

1. Model I - Constant thickness model (Fig. 14). The particles are distributed in space-like $s(r) = (R/r)^m$ up to a perpendicular distance W/2 from the ecliptic plane. For perpendicular distances greater than W/2, $s(r) = 0$.

2. Model II - Linear thickness model (Fig. 15). The particles have a spatial distribution of $(R/r)^m$ up to a perpendicular distance from the ecliptic equal to $r \sin \omega_o$, and $s(r) = 0$ for distances greater than $r \sin \omega_o$.

Since the physical density would not have the discontinuity from $s = (R/r)^m$ to $s = 0$ at the boundaries of Models I and II, it would be desirable to use a combination of layers of width W_1, W_2, W_3, etc., for Model I and various cone angles ω_{o1}, ω_{o2}, etc., for Model II. In addition, the components would not all have the same weighing factors, so that $\bar{L}_\lambda(\epsilon, i)$ would have the form:

$$\bar{\bar{L}}_\lambda(\epsilon, i) = \sum_{\ell=1}^{N} k_\ell \, \bar{L}_\lambda^\ell(\epsilon, i) \quad , \tag{37}$$

with the sum over the various layers. The angle i is the inclination of the scattering plane from the ecliptic.

Figure 16 shows the parameters of Model I. At point P, where the line of sight is at a perpendicular distance W/2 above the plane of the ecliptic, the scattering angle $\Theta = \Theta_{max}$. The length d, the distance from P to the earth-sun line, is given by $d = W/[2 \sin(i)]$. Θ_{max}, ψ, ϵ, and d are all in the scattering plane defined by the lines of sight to the point P from the earth and

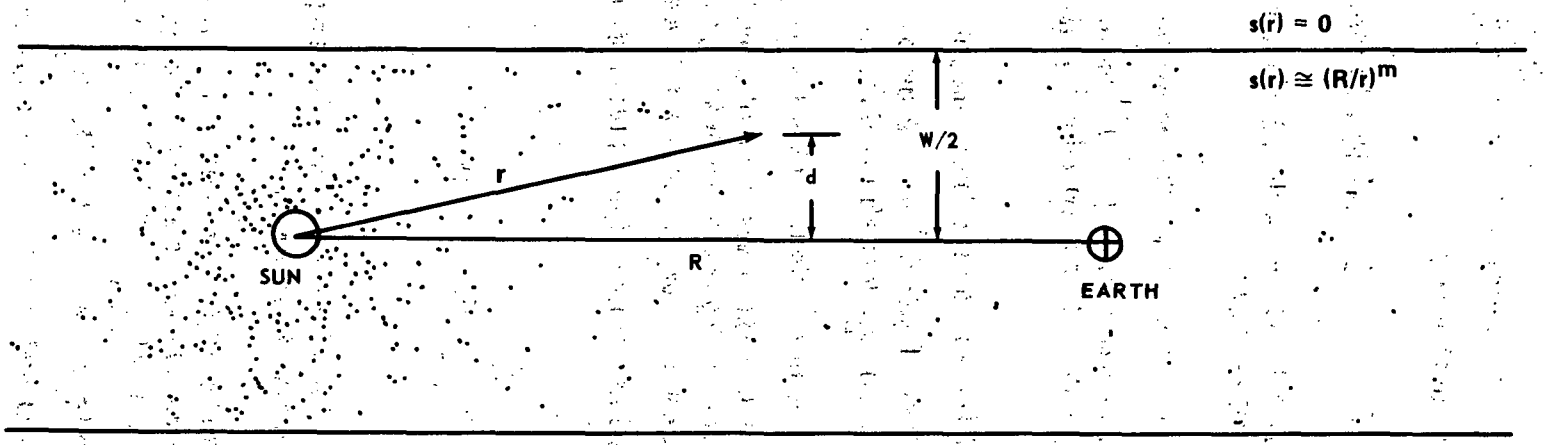

Figure 14. Constant thickness model.

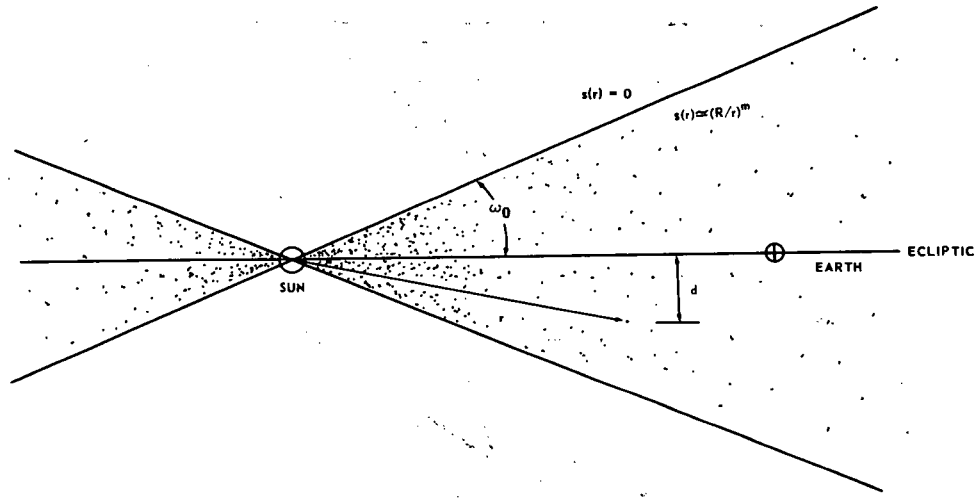

Figure 15. Linear thickness model.

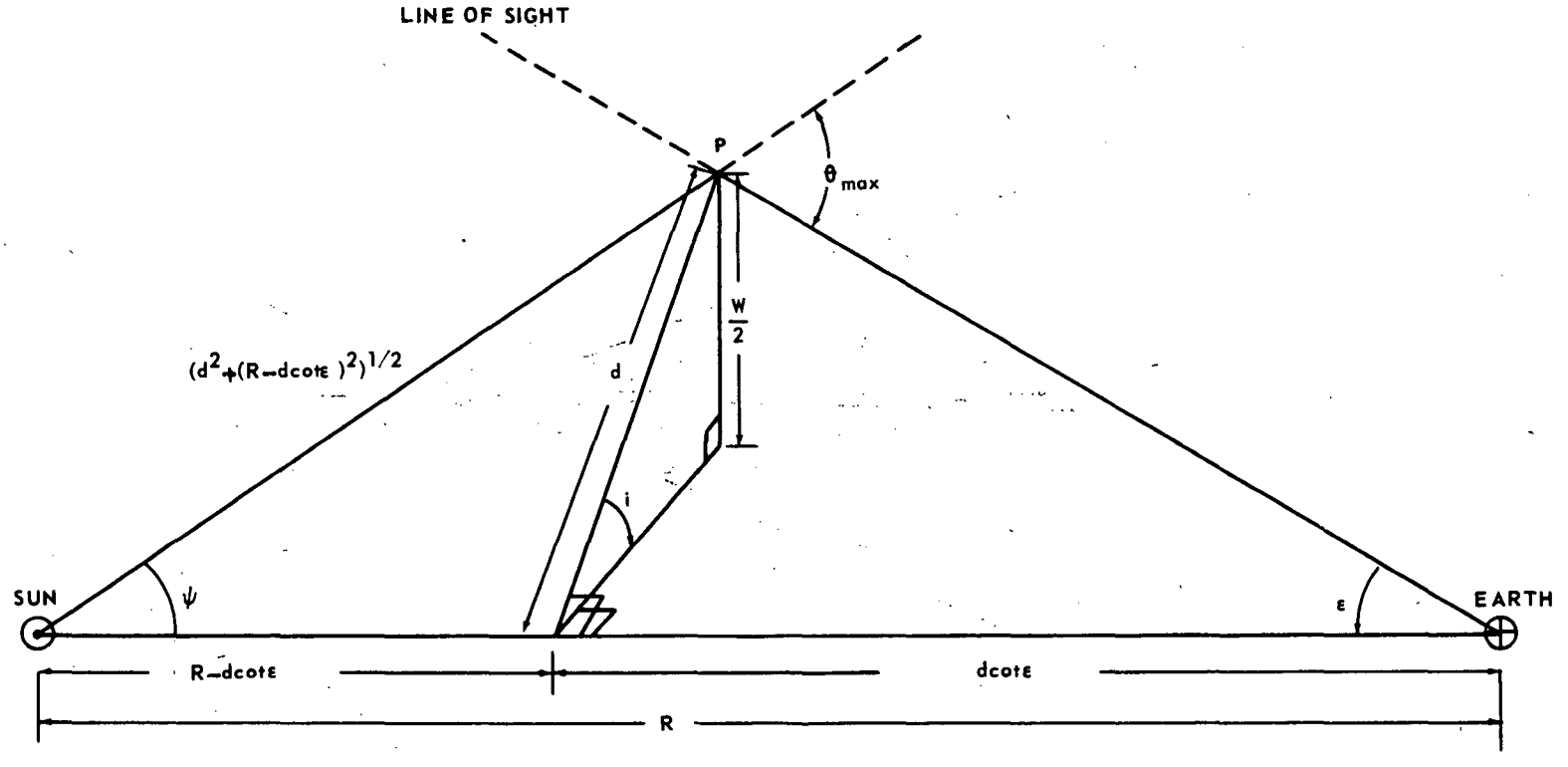

Figure 16. Geometry for constant thickness model.

the sun. The scattering plane is inclined an angle i to the ecliptic. In the scattering plane

$$\Theta_{max} = \psi + \epsilon \tag{38}$$

and

$$\sin \psi = d/\sqrt{d^2 + (R - d \cot \epsilon)^2} \quad ; \tag{39}$$

hence, for Model I,

$$\Theta_{max}(\epsilon, i, W) = \epsilon + \sin^{-1}\left(1\Big/\sqrt{1 + \left(\frac{2R}{W} \sin i - \cot \epsilon\right)^2}\right). \tag{40}$$

For Model II (Fig. 17), P is the point which is a distance $r \sin \omega_o$ from the ecliptic plane. The scattering angle for this point is $\Theta_{max}(\epsilon, i, \omega_o)$. The distance d of P from the earth-sun line is

$$d = r \sin \omega_o / \sin i \quad . \tag{41}$$

In the plane defined by the line of sight and the earth-sun line

$$\Theta_{max} = \epsilon + \omega \tag{42}$$

and

$$\sin \omega = \frac{d}{r} = \sin \omega_o / \sin i \quad ; \tag{43}$$

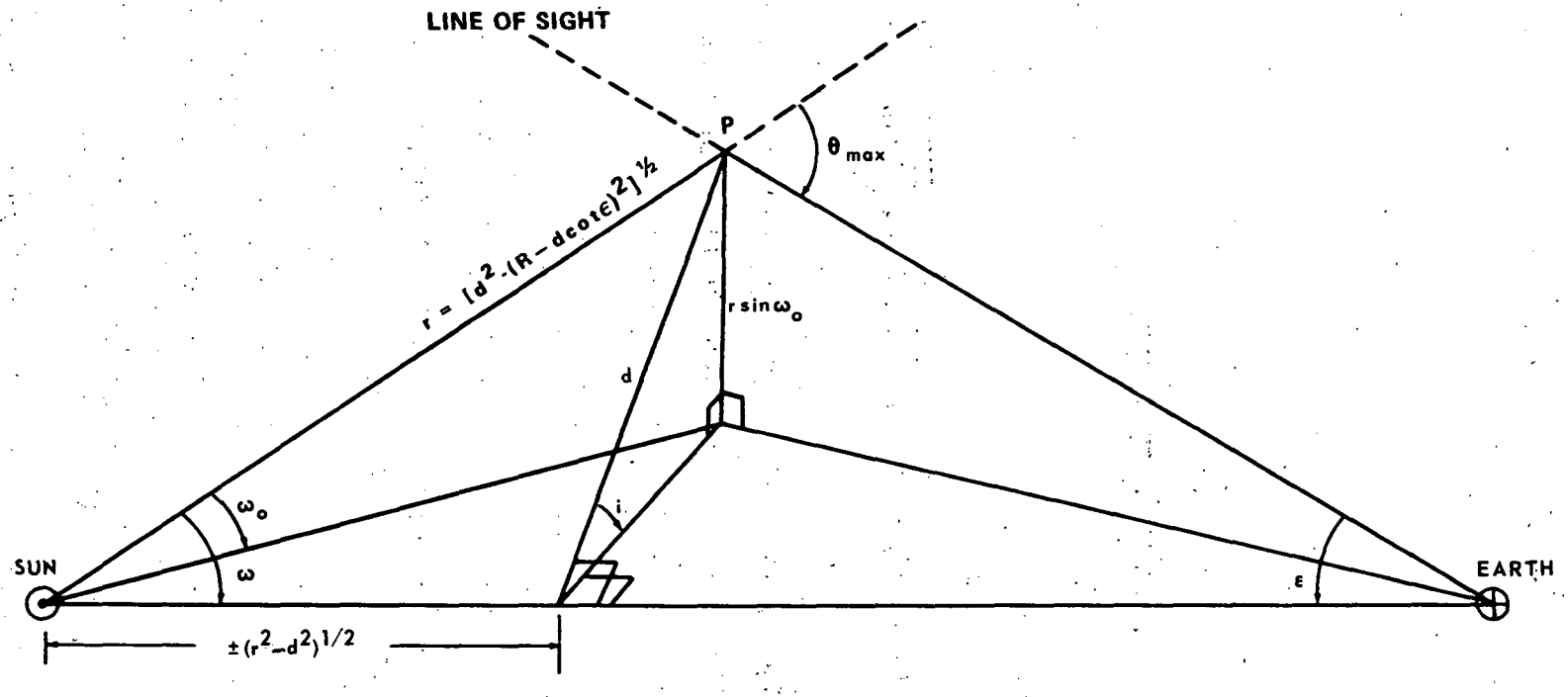

Figure 17. Geometry for linear thickness model.

therefore,

$$\Theta_{max}(\epsilon, i, \omega_o) = \epsilon + \sin^{-1}(\sin\omega_o/\sin i) \quad . \tag{44}$$

From this equation it is seen that for $i < \omega_o$, the line of sight never passes out of the dust envelope and no $\Theta_{max} < \pi$ exists. For these values of i, Θ_{max} is taken as $\Theta_{max} = \pi$. The line of sight can be such that Θ_{max} is doubly defined as shown in Figure 18 or as seen from the multivalueness of the $\sin^{-1}$ in equation (44). In this case, the integration limits are (ϵ, Θ_{max}) and (Θ'_{max}, π). The formula can be transformed to

$$\Theta_{max}(\epsilon, i, \omega_o) = \epsilon + \tan^{-1}\left(\sin\omega_o/\sqrt{\sin^2 i - \sin^2\omega_o}\right)$$

for $\sin^2\omega_o/\sin^2 i << 1$. The double cross relation is

$$\Theta'_{max}(\epsilon, i, \omega_o) = \epsilon - \tan^{-1}\left[\frac{\sin\omega_o}{\sqrt{\sin^2 i - \sin^2\omega_o}}\right] + \pi \tag{45}$$

for $\epsilon < \Theta'_{max} < \pi$. For $i \leq \omega_o$, then $\Theta'_{max} = \pi$.

The distribution of dust away from the plane of the ecliptic and up to a scattering angle, Θ_{max}, has the same form as in-the-ecliptic plane for Models I and II. Θ_{max} is determined by the elongation ϵ and inclination i.

The expression for the spectral radiance out of the ecliptic can be written as [27]

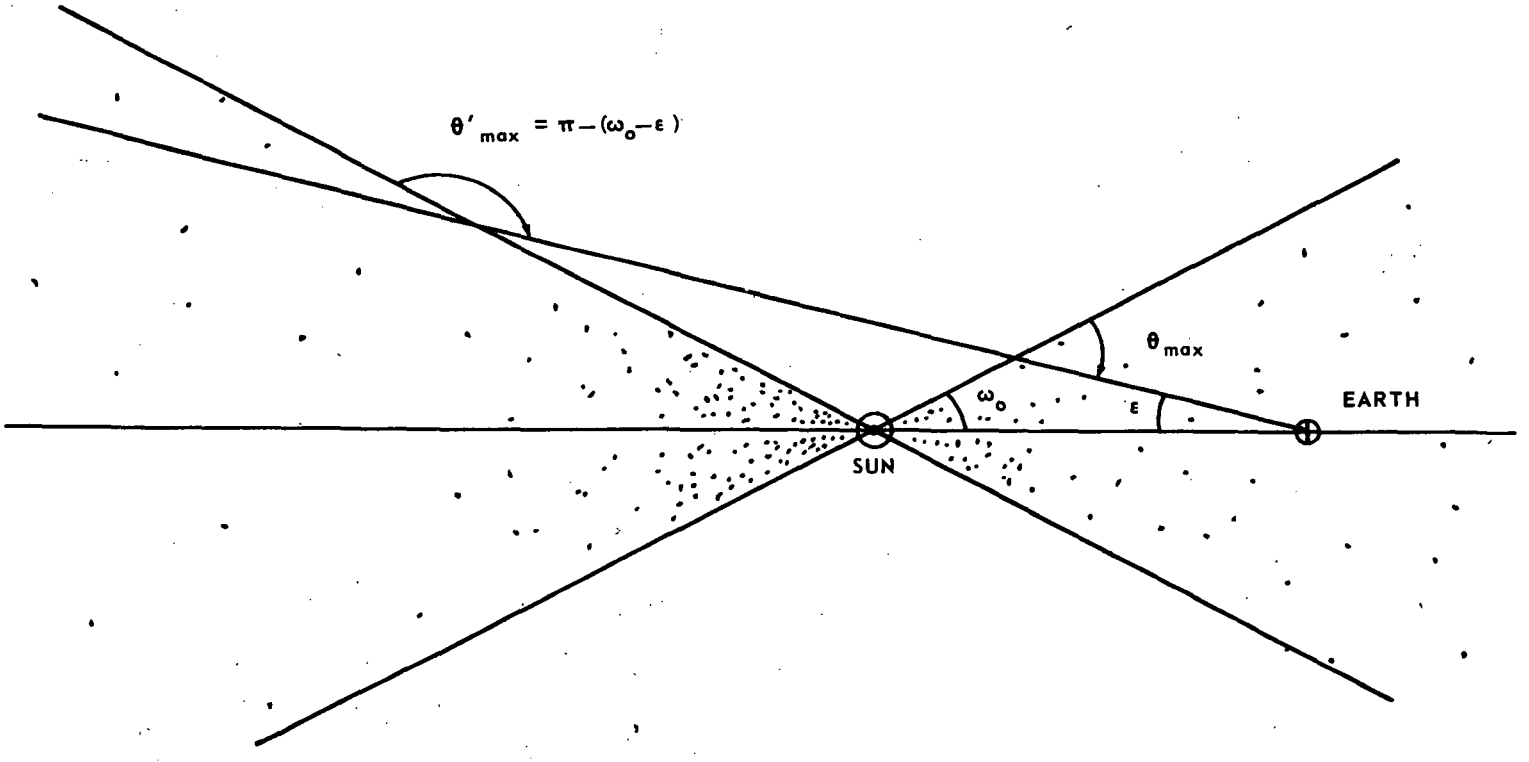

Figure 18. The double cross of the linear thickness model showing, for a plane perpendicular to the earth-sun line, the contribution from each region of ϵ to θ_{max} and θ'_{max} to π.

$$\bar{L}_\lambda(\epsilon, i) = \frac{RE_\lambda^e \, \delta\lambda \, N_o}{\sin^{m+1}\epsilon} \int_\epsilon^{\Theta_{max}(\epsilon, i)} \sin^m\Theta \left(\overline{\frac{d\sigma}{d\Omega}}\right) d\Theta \tag{46}$$

$$= \frac{RE_\lambda^e \, \delta\lambda \, N_o}{\sin^{m+1}\epsilon} \left[\int_\epsilon^\pi \sin^m\Theta \left(\overline{\frac{d\sigma}{d\Omega}}\right) d\Theta \right.$$

$$\left. - \int_{\Theta_{max}}^\pi \sin^m\Theta \left(\overline{\frac{d\sigma}{d\Omega}}\right) d\Theta \right] . \tag{47}$$

Define

$$\bar{L}_\lambda(\mathfrak{M}, o) \equiv \frac{RE_\lambda^e \, \delta\lambda \, N_o}{\sin^{m+1}\mathfrak{M}} \int_{\mathfrak{M}}^\pi \sin^m\Theta \left(\overline{\frac{d\sigma}{d\Omega}}\right) d\Theta \quad . \tag{48}$$

Now, equation (47) can be written in the form of in-the-ecliptic integrals:

$$\bar{L}_\lambda(\epsilon, i) = \bar{L}_\lambda(\epsilon, o) - \left(\frac{\sin\Theta_{max}}{\sin\epsilon}\right)^{m+1} \bar{L}_\lambda(\Theta_{max}, o) \quad . \tag{49}$$

Consider the spectral radiance equation for the ecliptic plane ($i = 0$):

$$\bar{L}_\lambda(\epsilon) = \bar{L}_\lambda(\epsilon, o) = \frac{C}{\sin^{m+1}\epsilon} \int_\epsilon^\pi \sin^m\Theta \left(\overline{\frac{d\sigma}{d\Omega}}\right) d\Theta \tag{50}$$

where $C = RE_\lambda^e \, \delta\lambda \, N_o$. Then, because

$o \leq \epsilon \leq \pi$,

$\epsilon \leq \Theta \leq \pi$,

$$o \leq \sin\Theta \leq 1,$$

and

$$\left(\overline{\frac{d\sigma}{d\Omega}}\right) \geq 0$$

for any value of $m \geq 0$, a smooth $\left(\overline{\frac{d\sigma}{d\Omega}}\right)$ which reproduces $\overline{L}_\lambda(\epsilon)$ can be found as long as $\overline{L}_\lambda(\epsilon)\sin^{m+1}\epsilon$ generally decreases with increasing ϵ. The integrand is positive and, as $\epsilon \to \pi$, the area under the curve decreases as ϵ increases toward its upper limit. Thus, there is a wide range possible for m and $\overline{d\sigma/d\Omega}$ which will reproduce $\overline{L}_\lambda(\epsilon)$. If, however, it is required that $\overline{d\sigma/d\Omega}$ reproduce $\overline{L}_\lambda(\epsilon, i)$ for points off the ecliptic, then another set of parameters, $\Theta_{max}(\epsilon, i)$, which describes the variation of the density of particles away from the ecliptic is introduced and the possibility exists of further limiting the range of acceptable values for m and $\overline{d\sigma/d\Omega}$:

$$\overline{L}_\lambda(\epsilon, i) = \frac{C}{\sin^{m+1}\epsilon} \cdot \int_\epsilon^{\Theta_{max}(\epsilon, i)} \sin^m\Theta \left(\overline{\frac{d\sigma}{d\Omega}}\right) d\Theta \quad . \qquad (51)$$

For the same value of m, an average polarization function $\overline{g}(\Theta)$ where $\overline{g}(\Theta) = \overline{i_1(\Theta)} - \overline{i_2(\Theta)}$ can be found which will reproduce the integrated polarization in the ecliptic

$$\overline{P}_\lambda(\epsilon) = \frac{C}{2\,\overline{L}_\lambda \sin^{m+1}\epsilon} \int_\epsilon^\pi \sin^m\Theta \; \overline{g(\Theta)} \; d\Theta \quad . \qquad (52)$$

This can be done because $\overline{g(\Theta)}$ can assume negative as well as positive values. This $\overline{g(\Theta)}$ together with $\Theta_{max}(\epsilon, i)$ must predict values of $\overline{P}_\lambda(\epsilon, i)$:

$$\bar{P}_\lambda(\epsilon, i) = \frac{C}{2\,\bar{L}_\lambda(\epsilon, i)\,\sin^{m+1}\epsilon} \int_\epsilon^{\Theta_{max}} \sin^m\Theta\,\overline{g(\Theta)}\,d\Theta \quad , \tag{53}$$

which are in accord with the observed values.

The model calculations were outlined by Gillett [27] in the following fashion:

1. For a given set of m's and using

$$\bar{L}_\lambda(\epsilon, o) = \frac{C}{\sin^{m+1}\epsilon} \int_\epsilon^{\pi} \sin^m\Theta\left(\overline{\frac{d\sigma}{d\Omega}}\right) d\Theta \quad , \tag{54}$$

$\overline{(d\sigma/d\Omega)}$ is found which reproduces the observed values of $\bar{L}_\lambda(\epsilon, o)$.

2. Using the $\overline{(d\sigma/d\Omega)}$ determined above, the values of $\Theta_{max}(\epsilon, i)$ are determined by fixing

$$\frac{\bar{L}_\lambda(\epsilon_o, i)}{\bar{L}_\lambda(\epsilon_o, o)} = \int_{\epsilon_o}^{\Theta_{max}(\epsilon_o, i)} \sin^m\Theta\left(\overline{\frac{d\sigma}{d\Omega}}\right) \times d\Theta \Big/ \int_{\epsilon_o}^{\pi} \sin^m\Theta\left(\overline{\frac{d\sigma}{d\Omega}}\right) d\Theta \quad , \tag{55}$$

where the experimental values appear on the left side of the equation and ϵ_o is a specific value.

3. The values of m, $\overline{(d\sigma/d\Omega)}$ and $\Theta_{max}(\epsilon_o, i)$ are tested by determining whether they can reproduce the values of the $\bar{P}_\lambda(\epsilon, o)$ and $\bar{P}_\lambda(\epsilon, i)$. Gillett has used the difference

$$\bar{L}_\lambda (\epsilon, i) - \bar{L}_\lambda (90, 90) \tag{56}$$

to compare observations of the zodiacal light. This allows observational values used to be less dependent on the total observed radiance and instrument calibrations obtained from various observers.

F. Exponential Model [22]

To avoid the discontinuities in Gillett's models, the spatial distribution can be written as a smooth function. The exponential model assumes the form:

$$s(\Sigma, Z) = N_o \left(\frac{R}{\Sigma}\right)^{\nu} \exp(-KZ/R)$$

where N_o is the particle density at the earth, ν and $1/K$ are density distribution parameters, and Σ is the length of the position vector projected onto the ecliptic plane.

Since the geometry is the same as the ellipsoidal model which is to be discussed, Figure 19 can be used to define,

$$r = R \sin \epsilon / \sin \Theta ,$$

$$\Delta = R \sin(\Theta - \epsilon)/\sin \Theta ,$$

$$d\Delta = \frac{R \sin \epsilon}{\sin^2 \Theta} d\Theta$$

$$Z = \Delta \sin \delta ,$$

and $\cos \epsilon = \cos \delta \cos \ell$. δ and ℓ are the ecliptic coordinates of the line of sight. If γ is defined by

$$Z = r \sin \gamma$$

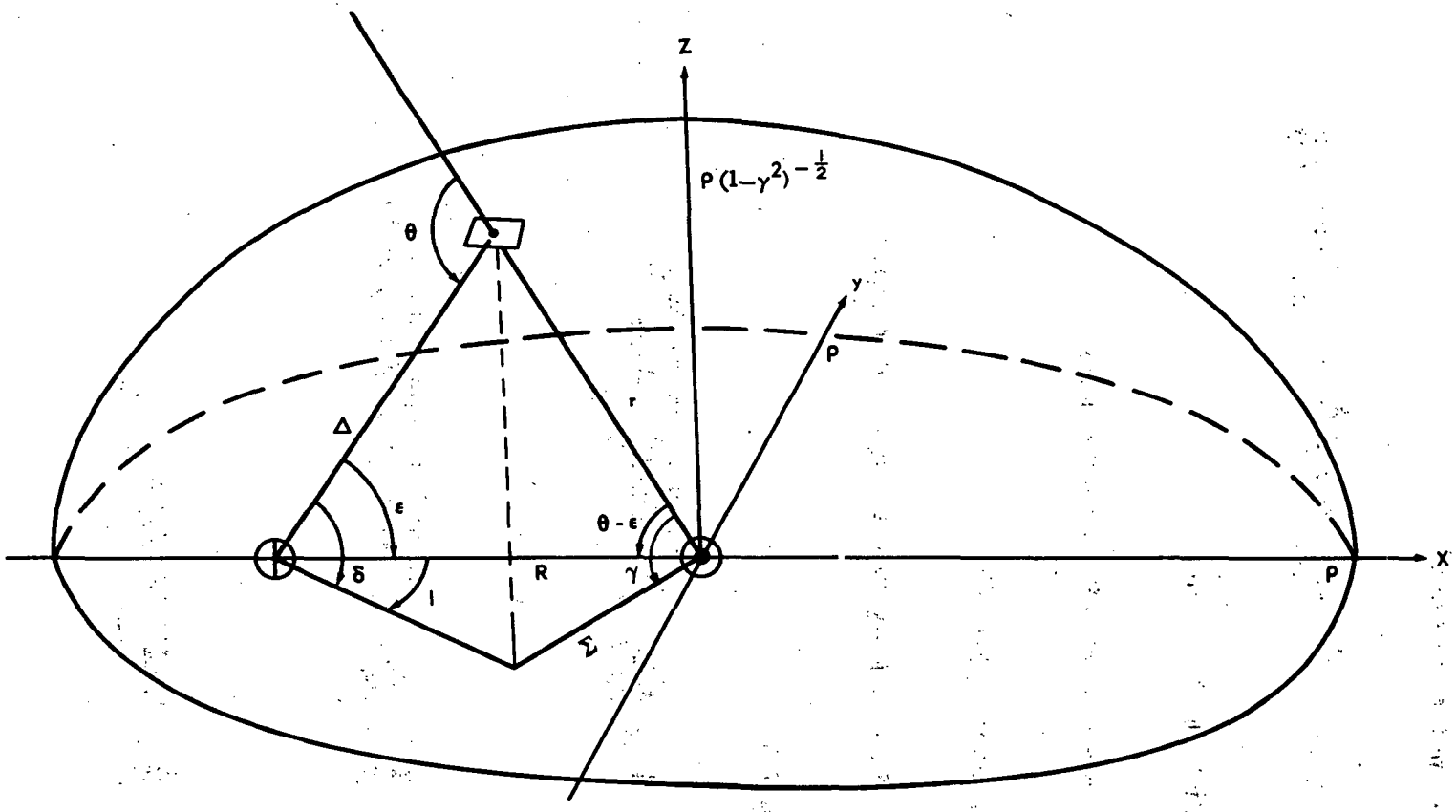

Figure 19. Geometry for the ellipsoid symmetry model.

then, from the equations above,

$$\sin\gamma = \frac{R \sin(\Theta - \epsilon) \sin\delta}{\sin\Theta} \cdot \frac{1}{R \sin\epsilon/\sin\Theta}$$

and Z/r takes the form

$$\sin\gamma = \sin(\Theta - \epsilon) \sin\delta/\sin\epsilon \quad .$$

Again, from Figure 19,

$$\Sigma/r = r\cos\gamma/R = \sin\epsilon \cos\gamma/\sin\Theta \quad .$$

Therefore,

$$\frac{\Sigma}{R} = \frac{\sin\epsilon}{\sin\Theta} \sqrt{1 - \frac{\sin^2(\Theta - \epsilon) \sin^2\delta}{\sin^2\epsilon}}$$

or

$$\frac{\Sigma}{R} = \frac{1}{\sin\Theta} \sqrt{\sin^2\epsilon - \sin^2(\Theta - \epsilon) \sin^2\delta}$$

and

$$\frac{Z}{R} = \frac{\sin(\Theta - \epsilon) \sin\delta}{\sin\Theta} \quad .$$

With these expressions, the equation for s (Σ, Z) becomes

$$s(\Sigma, Z) = s(\epsilon, \Theta, \delta)$$

$$= N_o \left[\frac{\sin^2 \Theta}{\sin^2 \epsilon - \sin^2 (\Theta - \epsilon) \sin^2 \delta} \right]^{\frac{1}{2}} \exp \left[\frac{-K \sin (\Theta - \epsilon) \sin \delta}{\sin \Theta} \right] \tag{57}$$

G. Belt Model [8, 30]

In this model, interplanetary space (in the ecliptic) is separated into a system of belts such that the boundary of each belt coincides with the orbit of a planet. The kth belt is populated with particles having a given size distribution and any refractive index In each belt one must take into account the dispersion forces which act or have acted on the particles. Behr and Siedentopf [8] used the belts to determine electron densities versus distance from the sun.

From equation (28) and Figure 21, we have

$$\Theta_j = \sin^{-1} \left[\frac{R \sin \epsilon}{r_j} \right] , \tag{58}$$

so that the belt model components of the spectral radiance from equation (32) become:

$$\bar{L}_\lambda^K (\epsilon, i) = \frac{R E_\lambda^e \, \delta\lambda}{\sin^{m+1} \epsilon} \sum_{j=1}^{N} \int_{a_{min}}^{q_{max}} n_o^{(j)}$$

$$\times \left(\frac{a}{a_o^{(j)}} \right)^{p(j)} \int_{\Theta_j}^{\Theta_{j+1}} \sin^m \Theta \left(\frac{d\sigma}{d\Omega} \right)_K d\Theta \tag{59}$$

where $\Theta_{j=1} = \epsilon$. Figure 20 indicates that equation (58) must be used with care

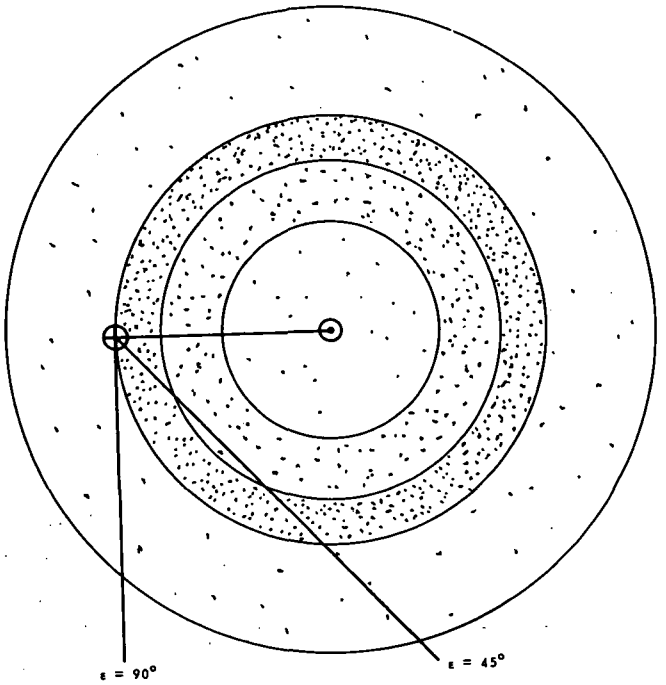

Figure 20. Belt model.

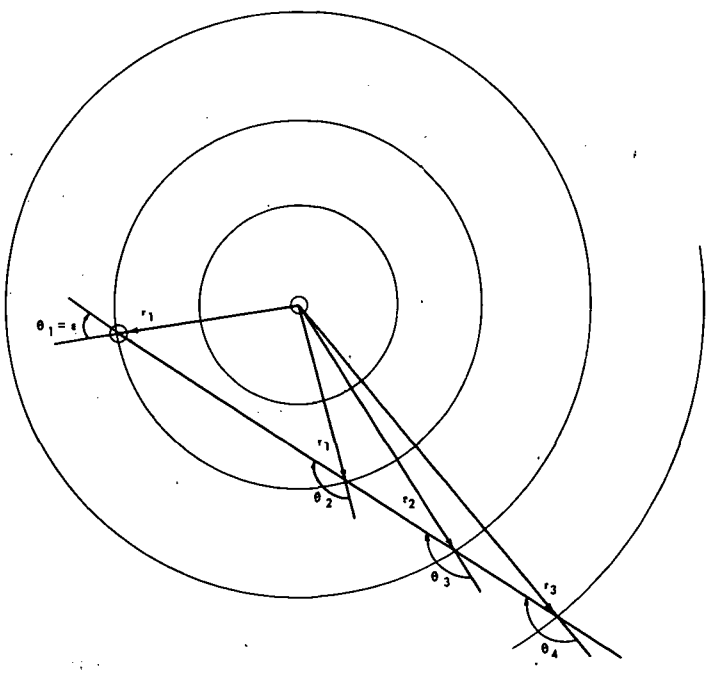

Figure 21. Geometry for the belt model.

since a single r_j can define two Θ_j's. This model has the property that the spatial density can be increased at specified distances, such as at the asteroid belt [31].

H. Ellipsoidal Symmetry Model [32, 33]

In the ellipsoidal symmetry model, the particle number spatial density distribution is assumed to have equal values at ellipsoid surfaces. These ellipsoids are in a Cartesian coordinate system centered on the sun with x- and y-axes in the ecliptic plane and the +z-axis pointing into the Northern Hemisphere (Fig. 22).

For this model, the spatial number density s (x, y, z) of each particle component is assumed to decrease with the distance from the sun according to

$$s\,(x,y,z) = n_o \left(\frac{R}{\rho}\right)^{\beta} , \tag{60}$$

where in the ecliptic $x^2 + y^2 = \rho^2$, R is set equal to 1 AU and n_o is the number density of the particles at 1 AU. Outside the ecliptic, the particles are assumed to have an equal number of densities along the surfaces of the ellipsoids defined by

$$\frac{x^2}{\rho^2} + \frac{y^2}{\rho^2} + \frac{z^2}{\left(\rho/\sqrt{\gamma^2+1}\right)^2} = 1 . \tag{61}$$

Out of the ecliptic plane, γ is a parameter characterizing the flatness of the ellipsoidal surface corresponding to the number density, $n_o\,(R/\rho)^{\beta}$ [33]. In the ecliptic plane only, ρ represents the distance of the corresponding equidensity surface from the sun.

A spherical distribution of the particle number density would correspond to $\gamma = 0$, while values of $\gamma >> 1$ correspond to a strong concentration of interplanetary dust toward the ecliptic plane (a disc).

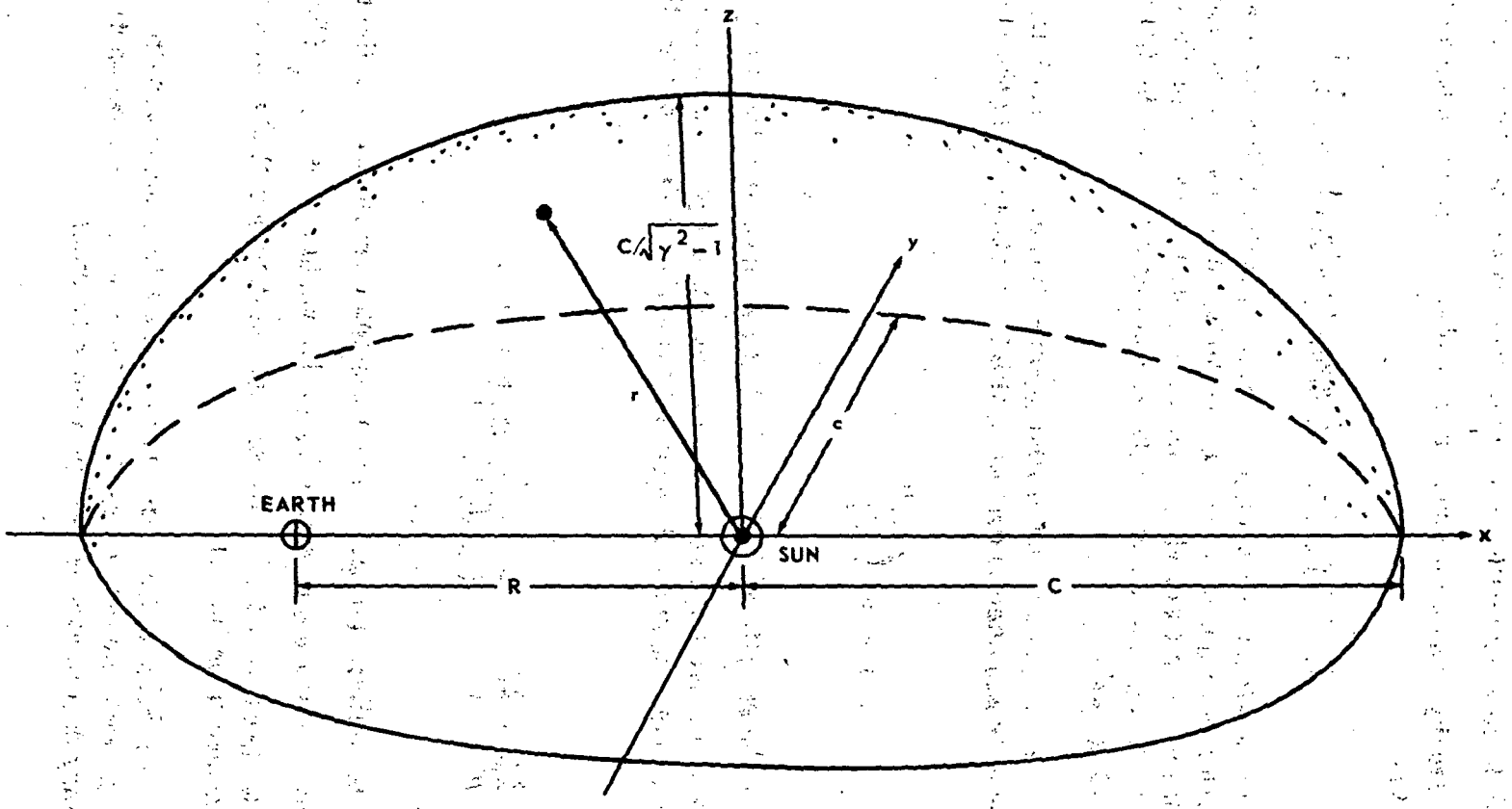

Figure 22. Ellipsoid symmetry model.

Using Figure 19 and equation (61), we have

$$x^2 + y^2 + z^2 (\gamma^2 + 1) = \rho^2 \tag{62}$$

or

$$\rho = r \left[1 + \left(\frac{z\gamma}{r} \right)^2 \right]^{\frac{1}{2}} ,$$

where

$$r^2 = x^2 + y^2 + z^2 .$$

Therefore,

$$s = n_o \Big/ \left(\frac{r}{R} \right)^{\beta} \left[1 + \left(\frac{z\gamma}{r} \right)^2 \right]^{\beta/2} . \tag{63}$$

From the law of sines, we have

$$r = R \sin \epsilon / \sin \Theta \tag{64}$$

and

$$\Delta = R \sin (\Theta - \epsilon) / \sin \Theta ,$$

and the element of distance $d\Delta$ is given by

$$d\Delta = R \sin \epsilon \, d\Theta / \sin^2 \Theta . \tag{65}$$

From Figure 19,

$$z = \Delta \sin \delta \tag{66}$$

and

$$\cos \epsilon = \cos \delta \cos \ell \quad . \tag{67}$$

Since we have a continuous distribution, no Θ_{max} exists; hence, the formulation of the spectral radiance equation becomes

$$\bar{L}_\lambda = \frac{RE_\lambda^e \delta \lambda N_o}{\sin^{\beta+1} \epsilon} \int_\epsilon^\pi \frac{\sin^\beta \Theta \overline{\left(\frac{d\sigma}{d\Omega}\right)} d\Theta}{\left[1 + \left(\frac{\gamma \sin \delta \sin (\Theta - \epsilon)}{\sin \epsilon}\right)^2\right]^{\beta/2}} , \tag{68}$$

which is evaluated by numerical integration.

As reported by Schoenberg [2], Van Rhijn [3] used spheroids as constant density surfaces. He assumed the density distribution

$$s(x, y) = n_o (R^2 - a(x^2 + y^2) - bz^2)$$

with the condition

$$R^2 - a(x^2 + y^2) - bz^2 = 0$$

at the upper boundary of the radiance integral. x, y, and z are the orthogonal heliocentric coordinates (i.e., centered at the sun with the x-y plane in the ecliptic). The integral cut-off condition can be written as

$$\sin^2 \Theta_{max} - a \sin^2 \epsilon \, (b - a) \sin^2 \delta \, \sin^2 (\Theta_{max} - \epsilon) = 0 \quad ,$$

where δ is the geocentric latitude of the line of sight. The last condition used

$$x^2 + y^2 = R^2 \left[\frac{\sin^2 \epsilon - \sin^2 \delta \, \sin^2 (\Theta - \epsilon)}{\sin^2 \Theta} \right] \quad ,$$

and z as is in equation (66).

To determine the polarization at the celestial poles, Fesenkov [34] assumed surfaces of constant density that were ellipsoids of revolution

$$\frac{x^2 + y^2}{a^2} + \frac{z^2}{g^2 a^2} = 1 \quad .$$

Assuming that the size and spatial distribution are separable,

$$\eta \, (\alpha \, , \, r) = n_o \, n \, (\alpha) \, s \, (r) \, .$$

and using the relations

$$r^2 = R^2 + z^2 = R^2 \, (1 + g^2 q^2 - g^2)$$

$$\Delta = g \sqrt{a^2 - R^2} = g \, R \sqrt{q^2 - 1} \quad ,$$

where g is a constant, $q = a/R$, and Δ has been assumed to be equal to z (i.e., along the line of sight), equation (26) becomes

$$\bar{L}_\lambda^j = \frac{E_\lambda^e \, \lambda^2 \, \delta \lambda \, R^2 \, N_o}{4\pi^2} \int_o^\infty \frac{s(r) \, \bar{i}_j \, d\Delta_o}{r^2} \qquad j = 1, \, 2 \quad .$$

As before,

$$N_o = \frac{\lambda}{2\pi} \int_{\alpha_{min}}^{\alpha_{max}} n_o \, n(\alpha) \, d\alpha$$

$$\bar{i}_j = \int_{\alpha_{min}}^{\alpha_{max}} n(\alpha) \, i_j(\Theta, \alpha) \, d\alpha \Bigg/ \int_{\alpha_{min}}^{\alpha_{max}} n(\alpha) \, d\alpha \quad .$$

In terms of q, $\bar{L}_\lambda^j$ becomes

$$\bar{L}_\lambda^j = \frac{\lambda^2 E_\lambda \, \delta\lambda \, R^2 N_o}{4\pi^2} \int_1^\infty \frac{s(r) \, \bar{i}_j(\Theta) \, g \, Rq \, dq}{R^2 (1 - g + q^2 g^2)(q^2 - 1)^{1/2}} \quad .$$

If s(r) varies as 1/a, then

$$\bar{L}_\lambda^j = gC' \, N_o \int_1^\infty \frac{\bar{i}_j(\Theta) \, dq}{(1 + g^2 q^2 - g^2)(q^2 - 1)^{1/2}}$$

where $C' = E_\lambda \lambda^2 \, \delta\lambda \, R/4\pi^2$. Assuming $q = \sec\phi'$, then

$$\bar{L}_\lambda^j = \frac{g \, C' \, N_o}{R} \int_0^{\pi/2} \frac{\bar{i}_j(\phi) \, d\phi'}{\cos\phi' \, (1 + g^2 \tan^2\phi')} \quad , \qquad (69)$$

where

$$\Theta = \cos^{-1} \left(\frac{-g \tan\phi'}{\sqrt{1 + g^2 \tan^2\phi'}} \right) \quad .$$

For any point in the sky, Fesenkov gives the general expression for the variables a, r, and Θ as:

$$a^2 = R^2 + \Delta^2 \cos^2\delta - 2R\Delta \cos\delta \cos\ell + \Delta^2/g^2 \sin^2\delta ,$$

$$r^2 = \Delta^2 + R^2 - 2R\Delta \cos\epsilon ,$$

$$\sin(\theta - \epsilon) = \Delta/r \sin\epsilon,$$

and

$$\cos\epsilon = \cos\delta \cos\ell ,$$

where δ and ℓ are the ecliptic coordinates for the line of sight.

I. Meteor Model [35]

As a logical starting point, observations of asteroids, meteors, and comets have been used to develop zodiacal light models. Most of the early work used large interplanetary matter as a source of the scattering functions or the equivalent phase function (e.g., see Ref. 1). In the meteor model to be described, the distribution of the orbital elements is used.

In the meteor model, the concentration of dust material in interplanetary space is calculated as a function of the distance from the sun and the heliocentric latitude Φ on the basis of a bivariate distribution f(j, a) of meteor orbits with respect to inclination j from the ecliptic and semimajor axis a.

The number N(j, a) of orbits with parameters j and a within the intervals (j, j + dj) and (a, a + da) is

$$N(j, a) = f(j, a)\, dj\, da .$$

If the orbits are circular, then within a segment $d\ell$ of the orbit (Fig. 24), confined to the interval (Φ, $\Phi + d\Phi$) in heliocentric latitude, a particle will make

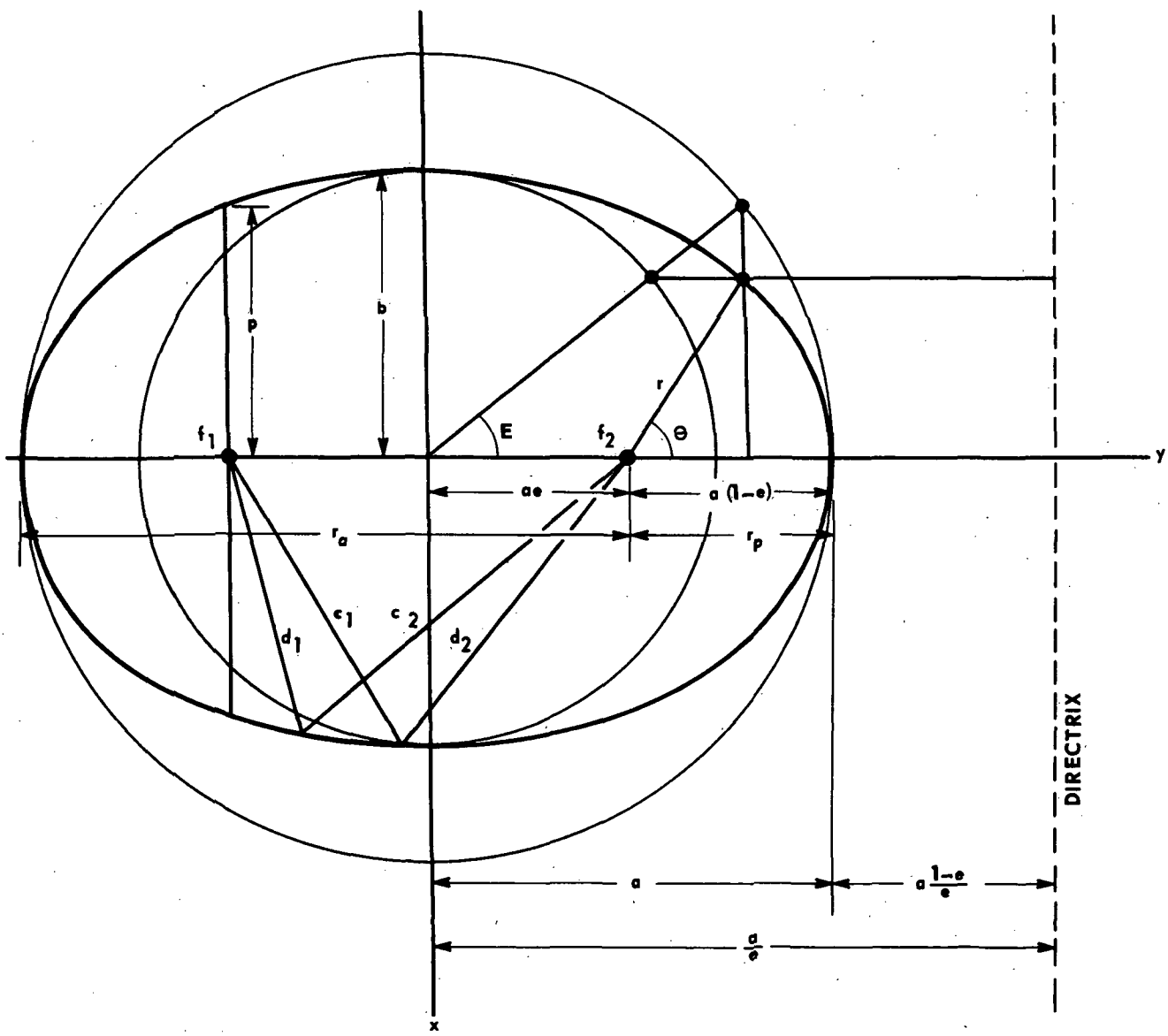

Figure 23. Parameters of an elliptical orbit.

TABLE 6. ELLIPTICAL ORBITS

1. Standard Equation in Polar Coordinates:

$$r = p/(1 + e \cos \Theta)$$

where

$$r_p = \frac{p}{1+e} \qquad r_a = \frac{p}{1-e}$$

$$e = 1 - r_{p/a} \qquad a = \frac{r_a + r_p}{z}$$

2. Standard Equation in Rectangular Coordinates:

$$\frac{x^2}{a^2} + \frac{y^2}{b^2} = 1$$

where

$$b = a(1 - e^2)^{1/2} \qquad p = a(1 - e^2)$$

$$d_1 + d_2 = c_1 + c_2 = a$$

3. Parametric Equations

$$x = a \cos E$$

$$y = b \sin E$$

$$\cos E = \frac{e + \cos \Theta}{1 + \cos \Theta}$$

where E = eccentric anomaly
$M = E - e \sin E$ = mean anomaly

4. Kinematics

$$\text{Total Energy} = U + \tfrac{1}{2}mV^2 - \frac{GmM}{r^2}$$

$$\text{Eccentricity} = e = \sqrt{1 + 2\frac{h^2 U}{m\mu^2}}$$

$$\text{Semimajor axis} = a = \frac{m\mu}{2U}$$

$$\text{Period} = \sqrt{a^3/\mu}$$

where

$$h = 1/m = r^2\dot{\Theta}$$
$$\mu = GM.$$

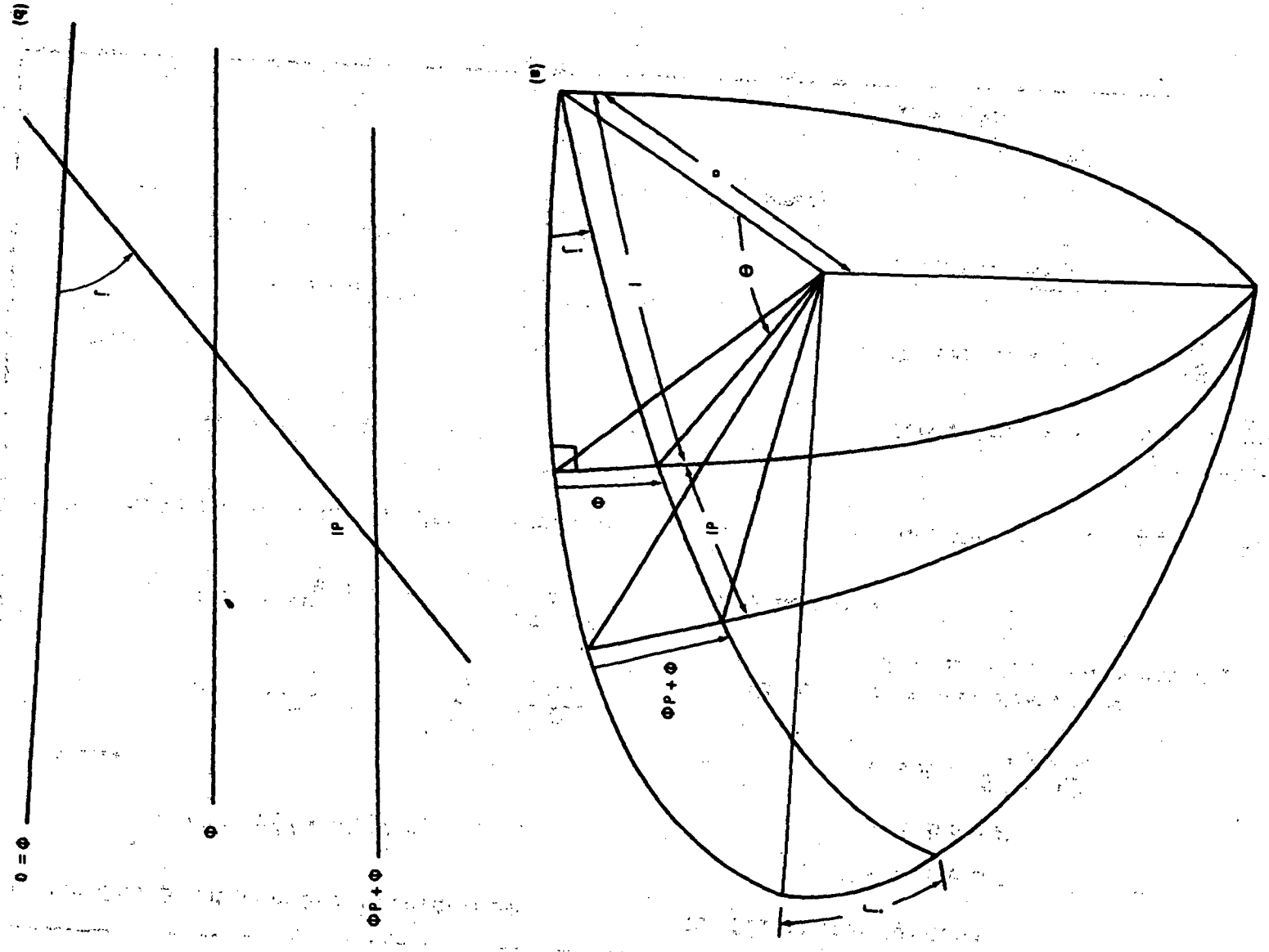

Figure 24. The meteor model.

a contribution to the number of particles in $d\ell$ which is proportional to the ratio of the time dt it is within this interval to the total period T. This contribution is equal to the ratio of the element $d\ell$ to the circumference $2\pi a$; i e., $d\ell/2\pi a = dt/T$. The element $d\ell$ can be found in terms of j using (Fig. 24):

$$\frac{\sin j}{\sin \Phi} = \frac{\sin (\pi/2)}{\sin (\ell/a)}$$

and

$$\Theta = \ell/a \ ;$$

hence,

$$\sin \Phi = \sin j \cdot \sin (\ell/a) \ . \tag{70}$$

Differentiating both sides with respect to ℓ, we have

$$\frac{d \sin \Phi}{d\Phi} \quad \frac{d\Phi}{d\ell} = \sin j \ \frac{d \sin \ell/a}{d\ell}$$

$$\cos \Phi \ \frac{d\Phi}{d\ell} = \sin j \left(\cos \frac{\ell}{a}\right) \frac{d\ell}{a} \ .$$

By using equation (70), we have

$$\cos \Phi \ \frac{d\Phi}{d\ell} = \sin j \sqrt{1 - \frac{\sin^2 \Phi}{\sin^2 j}} \ \frac{d\ell}{a}$$

or

$$\frac{d\ell}{a} = \frac{\cos\Phi \, d\Phi}{\sqrt{\sin^2 j - \sin^2\Phi}} \quad . \tag{71}$$

Assuming that the number of particles is proportional to the number of orbits and that the longitudes of the ascending nodes are distributed uniformly, then the number of particles located in the segment $d\ell$ and having orbits with parameters j and a is proportional to the quantity

$$\frac{f(j, a)}{2\pi a} \, dj \, da \, d\ell = \frac{f(j, a) \cos\Phi \, dj \, da \, d\Phi}{2\pi \sqrt{\sin^2 j - \sin^2\Phi}}$$

where all these particles refer to a volume of $dv = 2\pi r^2 \cos\Phi \, dr \, d\Phi$. The volume element dv is determined by the surfaces between Φ, $\Phi + d\Phi$, r, and $r + dr$. A unit volume at a point having the coordinates (r, Φ) will contain a number of particles proportional to the quantity

$$\frac{\cos\Phi \, f(j, r) \, dj \, dr \, d\Phi}{2\pi \sqrt{\sin^2 j - \sin^2\Phi}} \quad \frac{1}{2\pi r^2 \cos\Phi \, d\Phi \, dr}$$

$$= \frac{f(j, r) \, dj}{4\pi^2 r^2 \sqrt{\sin^2 j - \sin^2\Phi}} \quad . \tag{72}$$

Integrating with respect to j, we obtain the dependence $F(\Phi, r)$ of the particle concentration on the heliocentric latitude Φ and the radius $(r = a)$ of the circular orbit:

$$F(\Phi, r) = \frac{C}{4\pi^2 r^2} \int_{\Phi}^{\pi - \Phi} \frac{f(j, r)}{\sqrt{\sin^2 j - \sin^2\Phi}} \, dj \, , \tag{73}$$

where C is the normalization constant. Recalling equation (44),

$$\Theta = \epsilon + \sin^{-1} \frac{\sin \Phi}{\sin i} ,$$

one finds that

$$\Phi(\Theta, \epsilon, i) = \sin^{-1} [\sin(\Theta - \epsilon) \sin i] .$$

From equations (28) and (30), the integrated radiance [equation (26)] becomes

$$\bar{L}_\lambda(\epsilon, i) = \frac{CE_\lambda^e \, \delta\lambda}{4\pi^2 R \sin^3 \epsilon} \int_\epsilon^\pi \int_{a_{min}}^{a_{max}} \int_{\sin^{-1}[\sin(\Theta - \epsilon) \sin i]}^{\pi - \sin^{-1}[\sin(\Theta - \epsilon) \sin i]} n(a) \sin^2\Theta \frac{d\sigma}{d\Omega} \frac{f(j, R \sin\epsilon/\sin\Theta)\, dj\, da\, d\Theta}{\sqrt{\sin^2 j - \sin^2(\Theta - \epsilon) \sin^2 i}} \quad (74)$$

where

$$n(a, r) = n(a, j, r) ,$$

and n(a, j, r) is assumed separable into a particle size and a spatial distribution; i.e.,

$$n(a, j, r) = n(a)\, n(j, r) .$$

This method can be generalized [21] by writing the distribution f (j, r) as a function of the following parameters:

a = semimajor axis

e = eccentricity

j = inclination

s = radius of dust particle

B = shape parameter

δ = physical density

and time. Then

$$f\,(q,\ e,\ j,\ s_j\ B_j\ \delta_j\ t) = d^6\,\eta\,(t)/da\ de\ dj\ ds\ dB\ d\delta \quad ,$$

where η refers to the total number of particles in interplanetary space. For the spatial and size dependency, it could be assumed that f is separable into a product of functions of each independent variable:

$$f\,(a,\ e,\ j,\ s) = f_1\,(a)\ f_2\,(e)\ f_3\,(j)\ f_4\,(s)$$

Assuming $f_4 = s^{-p}$, then the number density as a function of r and Θ is

$$n(r,\Theta) = \frac{1}{r}\int_{r/2}^{\infty}\int_{|r/a-1|}^{1}\int_{\pi/2-\Theta}^{\pi/2}\frac{a^{-2}\,f(a,e,j)\ da\ de\ dj}{\left\{\left[e^2-\left(\frac{r}{a}-1\right)^2\right]\cdot\left(\sin^2 j-\cos^2\Theta\right)\right\}^{1/2}} \quad . \tag{75}$$

J. Generalized Method For Meteor Models [36]

The particle number density can be generalized and formulated in terms of the distribution of orbital elements semimajor axis, a, eccentricity, e, inclination, j, node, Ω, and argument of perihelion, ω. The number density of particles having orbital elements between $(a,\ e,\ j,\ \Omega,\ \omega)$ and $(a + da,\ e + de,\ j + dj,\ \Omega + d\Omega,\ \omega + d\omega)$ with period P and velocity V is equal to

$$d^3N = \frac{f\,(a,\ e,\ i,\ \Omega,\ \omega)\ da\ de\ dj\ d\Omega\ d\omega}{r^2\,dr\ \sin\Theta\ d\Theta\ d\phi}\ \frac{dL}{VP} \quad . \tag{76}$$

The time spent by a particle in the volume is equal to dL/V where dL is the pathlength of the stream in the volume element at r, V is the stream velocity, and P is the normalization factor.

The differential area $d\Omega\ d\omega$ is related to the differential area $d\Theta\ d\phi$ by the Jacobian:

$$\frac{d\Omega\ d\omega}{d\Theta\ d\phi} = J(\Omega, \omega, \Theta, \phi) = \begin{vmatrix} \left(\frac{\partial\Omega}{\partial\Theta}\right)_\phi & \left(\frac{\partial\omega}{\partial\Theta}\right)_\phi \\ \left(\frac{\partial\Omega}{\partial\phi}\right)_\Theta & \left(\frac{\partial\omega}{\partial\phi}\right)_\Theta \end{vmatrix} . \tag{77}$$

To deduce the Jacobian, refer to Figures 23 and 25 where the geometry of an elliptical orbit is defined and to Table 6 which gives the properties of an elliptical orbit. The elliptical orbit is defined by

$$r = \frac{a(1 - e^2)}{1 + e \cos \zeta} \tag{78}$$

where angles referenced in Figure 25 are

ζ = true anomaly

Ω = longitude of the ascending node

ω = argument of perihelion

r, Θ, ϕ = spherical coordinates

i = angle of inclination

$\Phi = \omega + \zeta$ = argument of latitude

$\tilde{\omega} = \omega + \Omega$ = longitude (amplitude) of perihelion

$\Omega + \omega + \zeta$ = free longitude.

Using the following basic equations of spherical geometry (Fig. 26),

$$\cos a = \cos b \cos c + \sin b \sin c \cos A$$

$$\frac{\sin A}{\sin a} = \frac{\sin B}{\sin b} = \frac{\sin C}{\sin c}$$

$$\sin a \cos B = \cos b \sin c - \sin b \cos c \cos A \quad ,$$

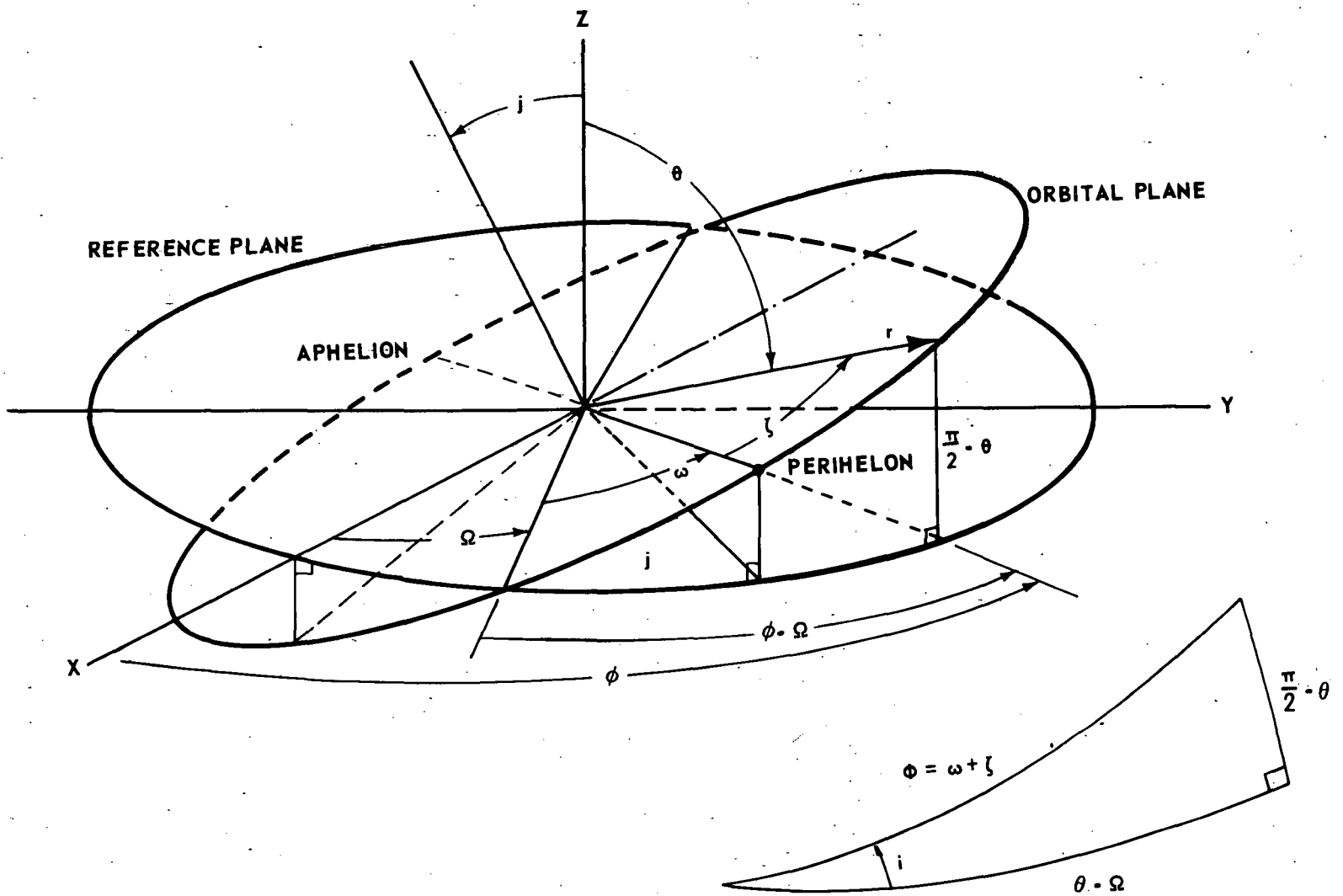

Figure 25. Generalized meteor model geometry.

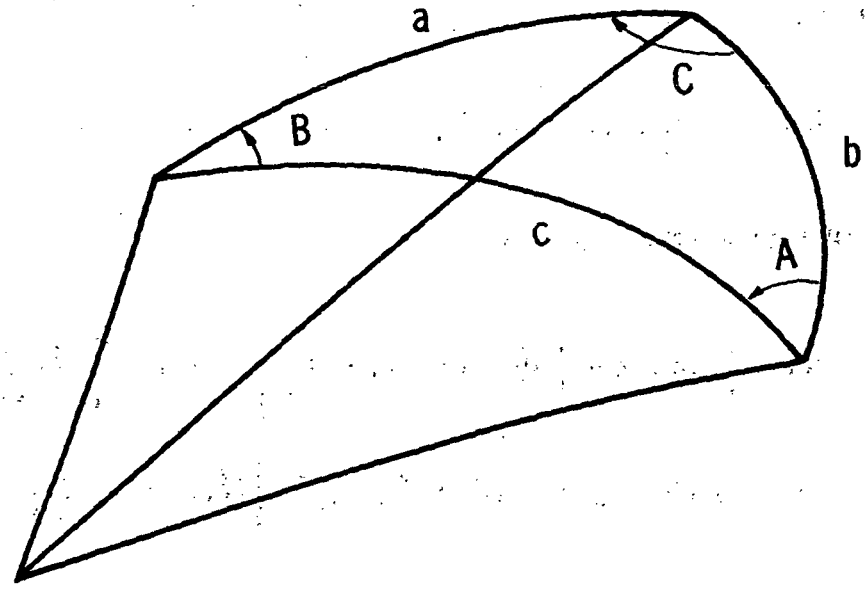

Figure 26. Definition of the spherical angles a, b, c and A, B, C.

we have the following relations:

$$\cos(\omega + \zeta) = \sin\Theta \cos(\phi - \Omega) \tag{79}$$

$$\cos\Theta = \sin j \sin(\omega + \zeta) \tag{80}$$

$$\sin(\omega + \zeta) \cos j = \sin\Theta \sin(\phi - \Omega) \tag{81}$$

and equation (81) divided by equation (80) yields

$$\cot j = \tan\Theta \sin(\phi - \Omega) \quad . \tag{82}$$

From equations (78) and (79),

$$\omega = \cos^{-1}[\sin\Theta \cos(\phi - \Omega)] - \cos^{-1}\left[\frac{a(1 - e^2)}{re} - \frac{1}{e}\right] ,$$

but equation (82) yields

$$\Omega = -\sin^{-1}(\cot j \cot \Theta) + \phi \quad ;$$

thus, the expression for ω becomes

$$\omega = \cos^{-1}\left\{\sin\Theta \cos\left[\sin^{-1}(\cot j \cot \Theta)\right]\right\} - \cos^{-1}\left[\frac{a(1-e^2)}{re} - \frac{1}{e}\right]$$

$$\omega = \cos^{-1}(\sin^2\Theta - \cot^2 j \cos^2\Theta)^{1/2} - \cos^{-1}\left[\frac{a(1-e^2)}{re} - \frac{1}{e}\right] \quad ; \quad (83)$$

hence

$$\left.\begin{aligned} \left.\frac{\partial\omega}{\partial\phi}\right)_\Theta &= 0 \\ \left.\frac{\partial\Omega}{\partial\phi}\right)_\Theta &= 1 \end{aligned}\right\}$$

$$\left.\frac{\partial\Omega}{\partial\Theta}\right)_\phi = \frac{\cot j/\sin^2\Theta}{(1 - \cot^2 j \cot^2\Theta)^{1/2}}$$

$$\left.\frac{\partial\omega}{\partial\Theta}\right)_\phi = \frac{-\frac{1}{2}(\sin^2\Theta - \cot^2 j \cos^2\Theta)^{1/2}(2\sin\Theta\cos\Theta + 2\cot^2 j \cos\Theta \sin\Theta)}{[1 - (\sin^2\Theta - \cot^2 j \cos^2\Theta)]^{1/2}}$$

$$= -\sin\Theta/\sqrt{\sin^2 j - \cos^2\Theta} \quad .$$

This dependence is seen directly from Figure 25. Therefore,

$$J(\Omega, \omega, \Theta, \phi) = \sin\Theta / \sqrt{\sin^2 j - \cos^2\Theta} \quad . \tag{84}$$

The relations

$$\frac{d}{du} \cos^{-1} u = -1/(1 - u^2)^{1/2}$$

$$\text{arc} \sin x = \pm \text{arc} \cos (1 - x^2)^{1/2}$$

with a, e, j, and r assumed constant were used in the derivation.

Note that $dL/dt = V_r$, hence, upon dividing the numerator and denominator of equation (76) by dt, one obtains:

$$d^3N = \frac{f(a, e, j, \Omega, \omega)\, da\, de\, dj}{r^2 V_r P(a) (\sin^2 j - \cos^2\Theta)^{1/2}} \quad .$$

From the dynamics of two particle orbits

$$\underline{P} = 2\pi a^{3/2}/(G M_o)^{1/2}$$

and

$$V_r = G M_o \left[\frac{e^2 a^2 - (r - a)^2}{r^2 a} \right] \quad .$$

Therefore,

$$N = \frac{1}{2\pi r} \int_{r/2}^{\infty} \int_{|r/a-1|}^{1} \int_{\pi/2-\Theta}^{\pi/2} \frac{f(a, e, j)\, da\, de\, dj}{a^2 \left\{ \left[e^2 - \left(\frac{r}{a} - 1 \right)^2 \right] (\sin^2 j - \cos^2 \Theta) \right\}^{1/2}} \quad . \tag{85}$$

The argument of perihelion and the node is assumed to be uniformly distributed over $(0, 2\pi)$. Azimuthal symmetry exists in $dN(r)$, since ϕ does not appear in the equation.

If only gravity and radiation drag are important, the inclination of the orbit does not change with time and one can assume that

$$f(a, e, j) = \zeta(a, e)\, \zeta(j) \quad .$$

The integration over the inclination can be performed and will yield a quantity $M(\Theta)$, depending only on Θ:

$$M(\Theta) = \int_{\pi/2-\Theta}^{\pi/2} \frac{\zeta(j)\, dj}{(\sin^2 j - \cos^2 \Theta)^{1/2}} \quad . \tag{86}$$

If $\zeta(a, e) = g(a)\, h(e)$, where $h(e)$ is continuous between 0 and 1, and if $g(a)$ is given by a power law [If $\zeta(a, e) = ea^2$ for small e, then dN is independent of r].

$$g(a) \simeq a^{\gamma} \quad ; \tag{87}$$

then, upon making the change of variables $x = r/a$,

$$dN \simeq \frac{M(\Theta)}{r^{2-\gamma}} \int_0^2 x^{-\gamma}\, dx \int_{|x-1|}^{1} \frac{h(e)\, de}{\left[e^2 - (x-1)^2 \right]^{1/2}}$$

$$\simeq M(\Theta)/r^{2-\gamma} \simeq r^{-\beta} M(\Theta) \quad ,$$

thus yielding a power law in r.

For the particle radius s, assume

$$\frac{d N_s(r)}{ds} = C_{\zeta, h}(\beta)\, s^{-p}\, r^{-\beta} \int_{\pi/2-\Theta}^{\pi/2} \frac{\zeta(j)\, dj}{(\sin^2 j - \cos^2 \Theta)^{1/2}} \qquad (88)$$

where

$$f_s(a, e, j) = \text{const.}\ s^{-p}\, a^{\gamma}\, h(e)\, \zeta(j) \quad , \qquad (89)$$

$$\beta \equiv 2 - \gamma$$

and $C_{\zeta,h}(\beta)$ is a constant depending on ζ and h.

ζ (j) represents the distribution of inclinations on a sphere, but it has already been assumed that there is no ϕ dependence. Hence, a uniform distribution of inclinations would not give a uniform dust population on the celestial sphere. If the intersection of the pole of the orbit with the sphere is represented by a point, then the density of points is given by

$$\frac{\#\ \text{points}}{dA} = \frac{\#\ \text{points}}{\sin j\ dj\ d\phi} \quad .$$

But, since there is no ϕ dependence, ζ (j) must be proportional to sin j to have a uniform distribution of dust.

Distributions of the forms $\zeta(j) \simeq \exp(-bj) \sin j$

$$\zeta(j) \simeq (\cos j)^k \sin j$$

(k = integer) are suggested from meteor studies [36].

SECTION IV. INVERSE FUNCTION ANALYSIS

A. Integral Inversion

The analysis of the observations of radiance $\overline{L}_\lambda$ and polarization $\overline{P}_\lambda$ of zodiacal light would be simplified if it could be reduced to a consideration of the average scattering intensity functions, where the average is over the particle size distribution. Several methods for doing this are considered in this section.

Assuming (a) the particle size distribution to be independent of the spatial distribution, (b) one refractive index for all the particles, and (c) the spatial distribution to vary as $(R/r)^m$, then the components of radiance in the ecliptic plane are given by

$$\overline{L}_\lambda^1 = \frac{C}{\sin^{m+1}\epsilon} \int_\epsilon^\pi \sin^m\theta \; \overline{i_1(\theta)} \; d\theta$$

$$\overline{L}_\lambda^2 = \frac{C}{\sin^{m+1}\epsilon} \int_\epsilon^\pi \sin^m\theta \; \overline{i_2(\theta)} \; d\theta$$

where $\overline{i_j(\Theta)}$ are the average scattering intensity functions and C is a constant.

The radiance and polarization values are given by

$$\overline{L}_\lambda = \frac{\overline{L}_\lambda^1 + \overline{L}_\lambda^2}{2}$$

$$\overline{P}_\lambda = \frac{\overline{L}_\lambda^1 - \overline{L}_\lambda^2}{\overline{L}_\lambda^1 + \overline{L}_\lambda^2} ,$$

from which the relations between the calculated values $(\overline{L}_\lambda^1, \overline{L}_\lambda^2)$ and the observed values $[F_1'(\epsilon), F_2'(\epsilon)]$ can be found:

$$\overline{L}_\lambda^1 = \overline{L}_\lambda (1 + P_\lambda) \equiv F_1'(\epsilon) \tag{90}$$

$$\overline{L}_\lambda^2 = \overline{L}_\lambda (1 - P_\lambda) \equiv F_2'(\epsilon) \quad . \tag{91}$$

F_1' and F_2' are the values obtained from observations and are related to $\overline{i_{1,2}(\theta)}$ by

$$F'_{1,2} = \frac{C}{\sin^{m+1}\epsilon} \int_\epsilon^\pi \sin^m \theta \, \overline{i_{1,2}(\theta)} \, d\theta \quad . \tag{92}$$

For later convenience, define $F_{1,2}(\epsilon)$ such that

$$F_{1,2}(\epsilon) = \frac{F'_{1,2}(\epsilon) \sin^{m+1}\epsilon}{C} = \int_\epsilon^\pi \sin^m \theta \, \overline{i_{1,2}(\theta)} \, d\theta \quad . \tag{93}$$

Given $F_{1,2}(\epsilon)$ from observations, the problem is to find $\overline{i_{1,2}(\theta)}$. Equations (92) and (93) are of the form

$$F(x) = \int_a^x K(\xi, x) f(\xi) \, d\xi \tag{94}$$

which are known as Volterra equations of the first kind, where $K(\xi, x)$ is the kernel, ξ is the auxiliary variable, and x is the current variable. Numerical methods for the solution of this type integral equations are given by Hildebrand [37]. Several such methods are presented below.

B. Numerical Approximation Methods [37]

A general method for obtaining solutions of integral equations consists of reducing the integral to a finite set of algebraic equations. The solution of equation (94)

$$F(x) = \int_a^b K(x,\xi)\, y(\xi)\, d\xi \tag{95}$$

may be approximated by a linear combination of n suitably chosen functions $\phi_1, \phi_2, \ldots, \phi_n$ of the form

$$Y(x) \simeq \sum_{k=1}^{n} A_k \phi_k(x) \tag{96}$$

The n constants of combination are determined to satisfy equation (95) as nearly as possible over the interval (a, b). If y(a) and y(b) are known, it is convenient to assume the approximation in the form

$$Y(x) \simeq \phi_o(x) + \sum_{k=1}^{n} A_k \phi_k(x)$$

where ϕ_o is chosen so that it satisfies the end conditions,

$$\phi_o(a) = y(a)$$

$$\phi_o(b) = y(b)$$

and the remaining ϕ's are made to vanish at the corresponding ends of the interval. In some cases, ϕ_o may be chosen so that it approximates y(x) closely. The remaining terms, the summation, can then be considered to constitute a perturbation expansion.

C. The Method of Collocation [37]

For the particular problem, equation (93), assume that

$$\overline{i_{1,2}(\theta)} \simeq \sum_{k}^{n} C_k\, i_{1,2}(\alpha_k, \theta) \tag{97}$$

where the α_k's are preselected particle size parameters and the C_k's are constants whose values are to be determined. Then

$$F_{1,2}(\epsilon) = \int_\epsilon^\pi \sin^m(\theta) \sum_{k}^{n} C_k\, i_{1,2}(\alpha_k, \theta)\, d\theta$$

becomes

$$F_{1,2}(\epsilon) = \sum_{k}^{n} C_k \int_{\epsilon}^{\pi} \sin^m(\theta)\ i_{1,2}(\alpha_k, \theta)\ d\theta \tag{98}$$

$$= \sum_{k}^{n} C_k\, g_k^{1,2}(\epsilon) \quad . \tag{99}$$

A set of n equations for the determination of the C_k's can be obtained by requiring that equation (99) be an equality at n distinct points in the interval (ϵ, π). If we denote these points by ϵ_i, the resultant equations are then of the form:

$$\sum_{k=1}^{n} C_k g_k^{1,2}(\epsilon_i) = F_{1,2}(\epsilon_i) = F_{1,2}(\epsilon_i) \quad i = 1, 2, 3, \ldots, n$$

or in matrix form

$$\underline{C}\ \underline{\underline{G}} = \underline{F} \ .$$

D. The Methods of Least Squares [37]

The method of least squares requires that the integral of the difference between two functions over an interval be as small as possible. In the present case we wish to determine the best fit of

$$\int_{\epsilon}^{\pi} \sin^m(\theta) \left[\sum_{k=1}^{n} C_k\, g_k(\theta)\right] d\theta \tag{100}$$

to the observed values $F(\epsilon)$ by varying the C_k's for a chosen set of known functions $g_k(\theta)$. Hence the method of least squares requires

$$\int_0^{\pi} \left[\sum_{k=1}^{n} C_k \int_{\epsilon}^{\pi} \sin^m(\theta)\, g_k(\theta)\, d\theta - F(\epsilon) \right]^2 d\epsilon \tag{101}$$

be a minimum. For notational simplicity, define

$$\phi_k(\epsilon) \equiv \int_{\epsilon}^{\pi} \sin^m(\theta)\, g_k(\theta)\, d\theta \quad . \tag{102}$$

In order that equation (101) be a minimum, its derivatives with respect to each parameter C_k must vanish; thus,

$$\int_0^{\pi} \phi_i \left[\sum_{k=1}^{n} C_k \phi_k(\epsilon) - F(\epsilon) \right] d\epsilon = 0 \qquad i = \ , 2, \ldots, n \tag{103}$$

or

$$\sum_{k=1}^{n} C_k \int_0^{\pi} \phi_i(\epsilon)\, \phi_k(\epsilon)\, d\epsilon = \int_0^{\pi} \phi_i(\epsilon)\, F(\epsilon)\, d\epsilon \quad . \tag{104}$$

Since $F(\epsilon)$ are observed values, this is not a functional form, and a numerical approximation method must be used to solve equation (104). The integrals are approximated by a weighted sum of the relevant ordinates of N conveniently chosen points resulting in

$$\sum_{k=1}^{n} C_k \sum_{r=1}^{N} D_r\, \phi_i(\epsilon_r)\, \phi_k(\epsilon_r) = \sum_{r=1}^{N} D_r\, \phi_i(\epsilon_r)\, F(\epsilon_r)$$

$$i = 1, 2, \ldots, n \tag{105}$$

where D_r (r=1, 2..N) are the appropriate weighting functions associated with points $\epsilon_1, \epsilon_2, \ldots, \epsilon_N$ involved in the numerical integration method. By suitably choosing $g_k(\theta)$, the integrals of equation (102) can be carried out in closed form.

Several integration procedures applicable to equation (104) exist; e.g., a Gauss-Legendre quadrature, the trapezoidal quadrature, Simpson's rule, etc. For the examples given here, Simpson's rule was used. Simpson's rule is based on the area under a parabola and is,

$$\int_a^b y\,(x)\,dx = \frac{h}{3}\left(y_0 + 4y, + 2y_2 + \ldots + 2y_{n-2} + 4y_{n-1} + y_n\right)$$

where

$$\begin{aligned} y_0 &= y\,(a) \\ y_1 &= y\,(a+h) \\ &\vdots \\ y_n &= y\,(a+nh) = y\,(b) \end{aligned}$$

and $h = (b-a)/(n-1)$ for $n>2$ and n odd. But, since equation (105) is homogeneous in the D's, the coefficients can be taken as $\frac{1}{2}$, 2, 1, ..., 1, 2, $\frac{1}{2}$. In matrix notation, equation (105) becomes

$$\underline{\underline{\alpha}}\ \underline{C} = \underline{\beta} \tag{106}$$

where

$$\alpha_{ij} = \sum_{r=1}^{N} \phi_{ri}\, D_r\, \phi_{rj} \qquad i,\ j = 1,\ 2,\ \ldots,\ n, \tag{107}$$

$$\beta_i = \sum_{r=1}^{N} \phi_{ri}\, D_r\, F_r\,, \tag{108}$$

$$\phi_{ri} = \phi_i\,(\epsilon_r)\,, \tag{109}$$

and

$$D_r = D_i\,\delta_{ir} \quad . \tag{110}$$

Equations (107) and (108) can be written as

$$\underline{\alpha} = \underline{\phi}^T \underline{\underline{D}}\ \underline{\phi} \tag{111}$$

$$\underline{\beta} = \underline{\phi}^T \underline{\underline{D}}\ \underline{F} \tag{112}$$

where, since $\underset{\sim}{D}$ is diagonal,

$$\underline{\phi}^T \underline{D} = (\underline{D}\underline{\phi})^T \quad .$$

T signifies that a matrix has been transposed, [e.g., $(\phi_{ij})^T = \phi_{ji}$]. Hence, equation (106) using equations (111) and (112) is the matrix equation that has to be solved to find the C_k's.

When N = n, the number of chosen points ϵ_r is equal to the number of C_k's to be determined. However, when N > n, one can choose a number of points greater than n and require that the integral equation be satisfied as nearly as possible at those points, thereby obtaining a best fit for all points. The errors committed by not satisfying the equation at the respective points ϵ_i are weighed in proportion to the influence of the ordinate in the integration of the squared error over $(0, \pi)$ by the coeffecients D_i. The comparison of

$$F(\epsilon_r)$$

and

$$\int_{\epsilon_r}^{\pi} \sin^m(\theta) \sum_{k=1}^{n} C_k\, g_k(\theta)\, d\theta$$

at the N chosen points gives an indication of the accuracy of the solution.

The result gives $\overline{i_{1,2}(\theta)}$ with the assumption of the spatial variation and number density; hence, uniqueness is dependent on these two parameters. For further analysis of $\overline{i(\theta)} = \sum_k C_k\, g_k(\theta)$, one can use the least-squares method a second time so that

$$\int_{o}^{\pi} \left[\overline{i\ (\theta)} - \int_{\alpha_{min}}^{\alpha_{max}} \sum_{k=1}^{n} a_k\ \alpha^{-k}\ i\ (\theta, \alpha)\ d\alpha \right]^2 d\theta = \min$$

where

$$\sum_{n=1}^{n} a_k\ \alpha^{-k}$$

is an assumed form for the particle size distribution. Possible candidates for the values of various parameters such as refractive index, α_{max}, α_{min}, and n can be found by this process.

The methods of collocation and least squares were used for the intensity functions

Model A: $\overline{i_{1,2}(\theta)} = a_o^{1,2} + a_1^{1,2} e^{-\theta}$

Model B: $\overline{i_{1,2}(\theta)} = b_o^{1,2} + b_1^{1,2} e^{-\theta} + b_2^{1,2} \sin\theta$

assuming a particle density of $N_o = 10^{-12}\ cm^{-3}$. The results are given in Table 7. m in equation (98) is set to zero. In the collocation method, equalities were required at $\epsilon = 40$ and 120 deg for Model A and $\epsilon = 40$, 120, and 160 deg for Model B. Weinberg's [17, 18] data were used as the experimental data. The intensity from Model B is the better fit to the data in both collocation and least squares than that from Model A. Both the collocation and least squares fit tend to be inaccurate for angles larger than 140 deg. This would indicate that data for these angles are not weighted enough in either method.

Neither method gives satisfactory polarization for the models used. This is the main problem in using average scattering functions; i.e., either the polarization or the intensity can be matched easily, but it is not as easy to find one function that will reproduce both. It is apparent that these functions are not unique.

TABLE 7. COLLOCATION AND LEAST SQUARES RESULTS FOR MODELS A AND B USING WEINBERG'S DATA

Measured					Model A						Model B					
					Collocation*			Least Squares			Collocation*			Least Squares		
ϵ (deg)	L_λ S_{10}(vis)	P_λ	F_1	F_2	F_1	F_2	P	F_1	F_2	P	F_1	F_2	P	F_1	F_2	P
40	1130	0.171	5.374	3.804	5.374	3.804	0.171	5.048	3.274	0.213	5.374	3.804	0.171	5.394	3.722	0.183
60	520	0.218	3.465	2.225	3.755	2.752	0.154	3.533	2.375	0.196	3.518	2.488	0.171	3.452	2.267	0.207
80	300	0.217	2.272	1.462	2.587	1.969	0.136	2.438	1.704	0.177	2.332	1.686	0.161	2.263	1.476	0.210
100	215	0.151	1.540	1.136	1.736	1.376	0.116	1.639	1.194	0.157	1.590	1.214	0.134	1.563	1.097	0.175
120	185	0.095	1.108	0.916	1.108	0.916	0.095	1.048	0.797	0.136	1.108	0.916	0.095	1.136	0.915	0.108
140	200	0.058	0.859	0.765	0.638	0.506	0.115	0.605	0.480	0.115	0.747	0.672	0.053	0.812	0.755	0.036
160	220	0.006	0.478	0.472	0.279	0.252	0.051	0.266	0.220	0.095	0.478	0.472	0.006	0.570	0.621	-0.043
180	220	0.000	0.000	0.000	0.000	0.000	0.000	0.000	0.000	0.000	0.000	0.000	0.000	0.000	0.000	0.000
Intensity Function Coefficients					* a_0^1	0.263		0.260			* b_0^1	0.695		0.911		
					a_0^2	0.400		0.359			b_0^2	0.879		1.219		
					a_1^1	10.414		9.712			b_1^1	13.555		14.669		
					a_1^2	6.223		5.278			b_1^2	9.715		11.732		
											b_2^1	-1.406		-1.979		
											b_2^2	-1.562		-2.597		

E. Liouville Solution [37]

Relaxing the assumption that the particle-size distribution is independent of the spatial distribution and allowing the particle-size distribution to be dependent on the spatial distribution, then another inverse method is available. By using

$$\frac{dF(x)}{dx} = \int_{A(x)}^{B(x)} \frac{\partial K(\xi, x)}{\partial x} f(\xi)\, d\xi + K(x, B) f(B) \frac{\partial B}{\partial x} - K(x, A) f(A) \frac{\partial A}{\partial x} ,$$

and if $\overline{i_{1,2}(\theta)} = \overline{i_{1,2}(\epsilon, \theta)}$, then

$$\frac{\partial F(\epsilon)}{\partial \epsilon} = -\sin^m \epsilon\, \overline{i(\epsilon = A, \epsilon)} + \int_{\epsilon}^{\pi} \sin^m \theta \frac{\overline{\partial i(\epsilon, \theta)}}{\partial \epsilon}\, d\theta .$$

This can be used only if $\overline{i_{1,2}}$ is dependent on ϵ, which will be the case if the particle-size distribution is spatially dependent; i.e.,

$$\overline{i_{1,2}(\epsilon, \theta)} = \int_{\alpha_{min}}^{\alpha_{max}} \eta(\epsilon, \alpha)\, i_{1,2}(\alpha, \theta)\, d\alpha .$$

Solving for $\overline{i(\epsilon, \epsilon)}$,

$$\overline{i(\epsilon, \epsilon)} = \frac{\frac{-\partial F(\epsilon)}{\partial \epsilon}}{\sin^m \epsilon} + \int_{\epsilon}^{\pi} \frac{\sin^m \theta}{\sin^m \epsilon} \frac{\overline{\partial i(\epsilon, \theta)}}{\partial \epsilon}\, d\theta$$

to which one can apply the method of successive substitutions; i.e., assume a value for i on the right side and solve for the left side, then iterate upon the solution.

F. Southworth Analysis [38]

Southworth [38] analyzed, by a least squares method, the data of Smith, Roach, and Owens for the phase function and particle size distribution. It is assumed that a unique average scattering function $\overline{i(\theta)}$ exists and the distribution is heliocentric of the form

$$\eta\,(r,\beta) = n(r)\;\; s(\beta),$$

and symmetric with respect to an axis through the sun and ecliptic poles. β is the heliocentric latitude and $n(r)$ is defined by

$$\log_{10}\; n\,(r) = C_1 \log_{10}\; r + C_2\; (\log_{10} r)^2 \quad . \tag{113}$$

The phase function and the function for the latitude distribution, S, are taken to be the linear combination of seven triangular functions.

$$s\;(\sin\beta) = \sum_j^7 s_j q_j\,(\sin\beta) \tag{114}$$

and

$$\overline{i\;(\theta)} = \sum_k^7 h_k\; t_k\;(\theta) \quad . \tag{115}$$

$t_k\;(\theta)$ is defined by $t_k\;(\theta<\theta_{k-1}) = 0$, $t_k\;(\theta>\theta_{k+1}) = 0$, and $t_k\;(\theta=\theta_k) = 1$. $t(\theta)$ between θ_{k-1} and θ_k and between θ_k and θ_{k+1} is represented by straight lines. $q_j(\sin\beta)$ is similarly defined. The radiance equation then becomes

$$L = \int_{\substack{\text{line of}\\ \text{sight}}} n\, s\, \bar{i}\; d\ell = \sum_j^7 s_j \sum_k^7 h_k \int_{\substack{\text{line of}\\ \text{sight}}} q_j\, t_k\, n\, d\ell \quad . \tag{116}$$

Southworth stopped the integration at $r = 5$ AU since contributions beyond this are negligible. A least squares successive approximation method was used to solve the equations for q_j and h_k. For Southworth's case with the least root mean square residual intensity,

$$\log_{10} n(r) = -1.8 \log_{10} r - 2.0(\log_{10} r)^2 \quad .$$

The phase function and latitude distribution at selected values of $\sin\beta$ and θ for the triangular functions are given in Table 8. For $\theta>54$ deg, Lambert's law roughly fits the phase functions. For $\theta<54$ deg, a diffraction peak appears.

TABLE 8. SELECTED VALUES OF $\overline{i(\theta)}$ AND $s(\sin\beta)$

θ deg	30.0	54.0	79.2	104.4	129.6	154.8	180.0
$\overline{i(\theta)}$	0.52	0.00	0.26	0.40	0.64	0.76	1.00
$\sin\beta$	0.0	0.1	0.3	0.5	0.7	0.9	1.0
$s(\sin\beta)$	1.00	0.84	0.51	0.38	0.25	0.20	0.23

G. Cumulative Function [39]

Powell and Circle [39] formulated a mathematical procedure to remove the integrals over the scattering angle and particle size which occur in analyzing observations of the zodiacal light. The resulting algebraic equations are expressed in terms of scattering functions with known and recognizable properties. Consequently, the uniqueness of deductions concerning the nature of the interplanetary dust is determined by studying the mathematical behavior of these functions. The development in this section is based on that given by Powell and Circle.

Consider a uniform size distribution of particles $N(X, R_o)$ per unit volume per increment $\delta\alpha$ in the range $0<\alpha<X$ at a radial distance R_o from the sun. X is called the termination parameter since it terminates the unit step function at

$$X = \frac{2\pi a_{max}}{\lambda} \tag{117}$$

where a_{max} is the radius of the largest particle in the uniform distribution. The scattering from the terminated unit step size distribution of particles with refractive index m* is given by the cumulative scattering ratio:

$$F_j(\theta, m^* X) = \int_o^X i_j(\theta, m^*, \alpha)\, d\alpha \quad , \qquad j = 1, 2 \quad . \tag{118}$$

The explicit functional dependence of m* will not be shown in the following equations.

An arbitrary, continuous size distribution of particles, $n(\alpha)$, can be expanded as a sum of terminated unit step functions with appropriate coefficents, $C(X_n)$:

$$n(\alpha) = \sum_n C(X_n)\, N(X_n) \quad , \tag{119}$$

where the radial dependence of $N(X, R_o)$ has been assumed and not shown explicitly. Some of the coefficients $C(X_n)$ may be negative, indicating a lack of particles in the range defined by X_n. However, the sum of the negative coefficients must be less than the sum of the positive coefficients since a negative number of particles in any region has no physical meaning. Using the step functions, the scattering from the actual size distribution of particles can be written as

$$\int_o^\infty n(\alpha)\, i_j(\theta, \alpha)\, d\alpha = \sum_n C(X_n)\, F_j(\theta, X_n) \quad . \tag{120}$$

The spectral radiant equation for a polarization component j:

$$\overline{L}_\lambda^j = \frac{RE_\lambda^e\, \delta\lambda\, \lambda^2}{8\pi^2 \sin^{m+1}\epsilon} \int_\epsilon^\pi \sin^m\theta\, d\theta \int_o^\infty n(\alpha)\, i_j(\theta, \alpha)\, d\alpha \tag{121}$$

becomes

$$\overline{L}_\lambda^j = \frac{RE_\lambda^e\, \delta\lambda\, \lambda^2}{8\pi^2 \sin^{m+1}\epsilon} \sum_n C(X_n) \int_\epsilon^\pi \sin^m\theta\, F_j(\theta, X_n)\, d\theta \quad . \tag{122}$$

The cumulative polarization function, $p(\theta, X_m)$ is defined as

$$p(\theta, X) = \frac{F_1(\theta, X) - F_2(\theta, X)}{F(\theta, X)} \tag{123}$$

where

$$F(\theta, X) = F_1(\theta, X) + F_2(\theta, X) \quad .$$

The measured polarization, $\overline{P}_\lambda$, due to all terminated step functions required to characterize an arbitrary continuous distribution, is given by

$$\overline{P}_\lambda = \frac{\sum_n C(X_n, R_o) \int_\epsilon^\pi \sin^m \theta \, \Delta(\theta, X_n) \, d\theta}{\sum_n C(X_n, R_o) \int_\epsilon^\pi \sin^m \theta \, F(\theta, X_n) \, d\theta} \tag{124}$$

where

$$\Delta(\theta, X_n) = F_1(\theta, X_n) - F_2(\theta, X_n) = p(\theta, X_n) \, F(\theta, X_n) \quad . \tag{125}$$

Hence, one has the following relation:

$$\overline{L}_\lambda \, \overline{P}_\lambda \left(\frac{\sin^{m+1} \epsilon}{RE^e_\lambda \, \delta\lambda} \right) \frac{8\pi^2}{\lambda^2} = \sum_n C(X_n) \int_\epsilon^\pi \sin^m \theta \, \Delta(\theta, X_n) \, d\theta \quad . \tag{126}$$

Now define two functions of the measured radiance and polarization:

$$M(m, \epsilon, \lambda) = \overline{L}_\lambda(\epsilon) \sin^{m+1} \epsilon \tag{127}$$

and

$$W(m, \epsilon, \lambda) = \overline{P}_\lambda(\epsilon) \, M(m, \epsilon, \lambda) \quad . \tag{128}$$

Then,

$$M(m, \epsilon, \lambda) = K(\lambda) \sum_n C(X_n) \int_\epsilon^\pi \sin^m \theta \, F(\theta, X_n) \, d\theta \tag{129}$$

and

$$W(m, \epsilon, \lambda) = K(\lambda) \sum_n C(X_n) \int_\epsilon^\pi \sin^m \theta \, \Delta(\theta, X_n) \, d\theta \tag{130}$$

where

$$K(\lambda) = \frac{E_\lambda^e R \delta \lambda \lambda^2}{8\pi^2} \quad . \tag{131}$$

Let

$$\int_\epsilon^\pi \sin^m \theta \, F(\theta) \, d\theta = q(\pi) - q(\epsilon) \tag{132}$$

and

$$\int_\epsilon^\pi \sin^m \theta \, \Delta(\theta) \, d\theta = Q(\pi) - Q(\epsilon) \quad . \tag{133}$$

Now, differentiating M and W with respect to ϵ , and noting that

$$\frac{\partial q(\pi)}{\partial \epsilon} = \frac{\partial Q(\pi)}{\partial \epsilon} = 0 \quad , \tag{134}$$

one obtains

$$\frac{\partial M}{\partial \epsilon} = -K(\lambda) \sum_n C(X_n) \frac{\partial q}{\partial \epsilon} \tag{135}$$

and

$$\frac{\partial W}{\partial \epsilon} = -K(\lambda) \sum_n C(X_n) \frac{\partial Q}{\partial \epsilon} \quad . \tag{136}$$

However,

$$\frac{\partial q}{\partial \epsilon} = \sin^m \epsilon \, F(\epsilon) \tag{137}$$

and

$$\frac{\partial Q}{\partial \epsilon} = \sin^m \epsilon \, \Delta(\epsilon) \quad , \tag{138}$$

so that

$$\frac{\partial M}{\partial \epsilon} = -K(\lambda) \sin^m \epsilon \sum_n C(X_n) F(\epsilon, X_n) \tag{139}$$

$$\frac{\partial W}{\partial \epsilon} = -K(\lambda) \sin^m \epsilon \sum_n C(X_n) \Delta(\epsilon, X_n) \tag{140}$$

From equations (125) and (126),

$$\frac{\partial M}{\partial \epsilon} = \frac{\partial \overline{L}_\lambda(\epsilon)}{\partial \epsilon} \sin^{m+1} \epsilon + (1+m) \overline{L}_\lambda(\epsilon) \sin^m \epsilon \cos \epsilon \tag{141}$$

and

$$\frac{\partial W}{\partial \epsilon} = \frac{\partial \overline{P}_\lambda(\epsilon)}{\partial \epsilon} \overline{L}_\lambda(\epsilon) \sin^{m+1} \epsilon + \overline{P}_\lambda \left[\frac{\partial \overline{L}_\lambda}{\partial \epsilon} \sin^{m+1} \epsilon + (1+m) \overline{L}_\lambda \sin^m \epsilon \cos \epsilon \right] . \tag{142}$$

Now define two new functions of the measured radiance and polarization:

$$S(\epsilon, \lambda, m) = \frac{-K^{-1}}{\sin^m \epsilon} \frac{\partial M}{\partial \epsilon} \tag{143}$$

$$T(\epsilon, \lambda, m) = \frac{-K^{-1}}{\sin^m \epsilon} \frac{\partial W}{\partial \epsilon} . \tag{144}$$

Combining equations (137) through (142), one obtains

$$S(\epsilon, C, X_n) = -\sum_n C(X_n) F(\epsilon, X_n) \tag{145}$$

and

$$T(\epsilon, C, X_n) = -\sum_n C(X_n)\, \Delta(\epsilon, X_n) \quad . \tag{146}$$

S and T are obtained from the measured radiance $\overline{L}_\lambda$ and polarization $\overline{P}_\lambda$ for various assumed values of m as follows:

$$S(\epsilon, \lambda, m) = \frac{-1}{K(\lambda)} \left[(1+m) \cos\epsilon\, \overline{L}_\lambda(\epsilon) + \frac{\partial \overline{L}_\lambda}{\partial \epsilon} \sin\epsilon \right] \tag{147}$$

$$T(\epsilon, \lambda, m) = \frac{-1}{K(\lambda)} \left[\overline{L}_\lambda(\epsilon) \left(\sin\epsilon \frac{\partial \overline{P}_\lambda}{\partial \epsilon} + (1+m)\, \overline{P}_\lambda \cos\epsilon \right) + \overline{P}_\lambda \frac{\partial \overline{L}_\lambda}{\partial \epsilon} \sin\epsilon \right] \quad . \tag{148}$$

Equations (145) through (148) represent the fundamental mathematical relationships between optically measurable quantities and the physical properties of the interplanetary dust. $S(\epsilon)$ and $T(\epsilon)$ can be obtained directly from the observed curves and plotted for various values of m. The resulting curves are smooth and continuous. However, the measured curves, $T(\epsilon)$ and $S(\epsilon)$, obtained by combining $\overline{L}_\lambda$, $\frac{\partial \overline{L}_\lambda}{\partial \epsilon}$, $\overline{P}_\lambda$, and $\frac{\partial \overline{P}_\lambda}{\partial \epsilon}$, according to equations (147) and (148) must be matched by a sum of the theoretical curves, $F(\epsilon, X_n)$ and $\Delta(\epsilon, X_n)$, as in equations (145) and (146), with appropriate coefficients, $C(X_n)$, to determine the unknown X_n, $C(X_n)$ and the refractive index which has been implicit in the equations. Powell and Circle accomplished this as follows:

1. Characterize the measured curves S and T.

2. Investigate the behavior of $F(\epsilon)$ and $\Delta(\epsilon)$ by varying the refractive index and X_n.

3. Choose a refractive index and X_n for which the curves of $F(\epsilon)$ and $\Delta(\epsilon)$ are similar to S and T.

4. Substitute $F(\epsilon)$ and $\Delta(\epsilon)$ into equations (145) and (146) and solve.

5. Find a set of curves, $\Delta(\epsilon, X_n)$, which when summed match the product $C(X_n)\,\Delta(\epsilon, X_n)$, corresponding to nonnegative coefficients.

This scheme is a systematic way to match scattering diagrams. Steps 2. and 3. involve a great amount of computation and study since, for a large spread in α, the curves are complex. Also, the fact still exists that this procedure does not give unique values for m* or X_n.

SECTION V. OBSERVATIONAL RESULTS

Although the radiance and polarization of the zodiacal light have been measured many times, there is considerable disparity among the values found by observers. Most observers have restricted their studies to the deduction of radiance of the zodiacal light in the ecliptic as a function of elongation from the sun. Observations at small elongation are necessarily close to the horizon and although this region is intrinsically the brightest, it is more subject to uncertain corrections for atmospheric extinction and scattering. Larger elongations can be observed at greater distances above the local horizon, but uncertain corrections for extraneous light then plague the reduction procedure. Most investigators regard it sufficient to assume that the zodiacal light is symmetric about the sun and the ecliptic plane and have reduced their measurements accordingly. According to Weinberg [40], the main factors contributing to the differences in the reported values are as follows:

1. The lack of dark-sky, low-latitude, high-altitude sites.

2. The lack of a proven method for separating zodiacal light from airglow and starlight, especially at high geographic latitudes and when using broad-band spectral systems.

3. Difficulties associated with absolute calibration.

4. Limited observational coverage, in time, over the sky.

5. The lack of a satisfactory formulation for the effects of tropospheric scattering, especially near the horizon.

6. Real changes in the zodiacal light, if any.

The most photometric observations measure (1) the total radiance (L_{obs}), which for ground-based studies is a sum of various sources, (2) the total degree of polarization (P_{tot}), which is dominated by the zodiacal light polarization, and (3) the orientation angle of the plane of polarization.

The measurement of the total radiance involves a number of terms from which the zodiacal light must be separated [17, 18]:

$$L_{obs} = \left[L_{\substack{\text{zodiacal}\\ \text{light}}} + L_{\substack{\text{galactic}\\ \text{light}}} + L_{\substack{\text{integrated}\\ \text{starlight}}} \right] e^{-\tau_1} M_1(z)$$

$$+ L_{\substack{\text{scattered}\\ \text{components}}} + \left[\sum L_{\substack{\text{airglow}\\ \text{emission lines}}} + L_{\substack{\text{airglow}\\ \text{continuum}}} \right] e^{-\tau_2} M_2(z) , \tag{149}$$

where τ_1, τ_2 are diffuse-source extinction coefficients for the astronomical and the atmospheric components, respectively;

$M_1(z)$ is the total air mass (equal to unity in the zenith at sea level);

$M_2(z)$ is the air mass to the level of the atmospheric components;

$L_{airglow}$ is the component arising from the line and continuum emission earth's atmosphere;

$L_{scattered\ components}$ is the component arising from scattering in the earth's atmosphere;

$L_{integrated\ starlight}$ is the diffuse component of radiance that comes from faint stars which are below the instrument threshold for resolution;

$L_{galactic\ light}$ is the scattered light from interstellar grains (which would be expected to have a polarization component);

$L_{zodiacal\ light}$ is the light from the interplanetary particles.

Various methods are invoked to determine the zodiacal light from the non-linear multivariable function L_{obs} [41]. These methods usually involve the symmetry characteristic of each source to its natural coordinate system (e.g., ecliptic, altazimuth, and galactic coordinates).

Figure 27 is a collection of representative results for the zodiacal light radiance in units of S_{10}(vis) between elongations of 25 and 110 degrees in the ecliptic. The data included are only in the visible spectral region.

The relative variation of the radiance of the zodiacal light as a function of elongation ϵ can be approximated sufficiently by a power function of the form

$$\epsilon^{-\kappa}$$

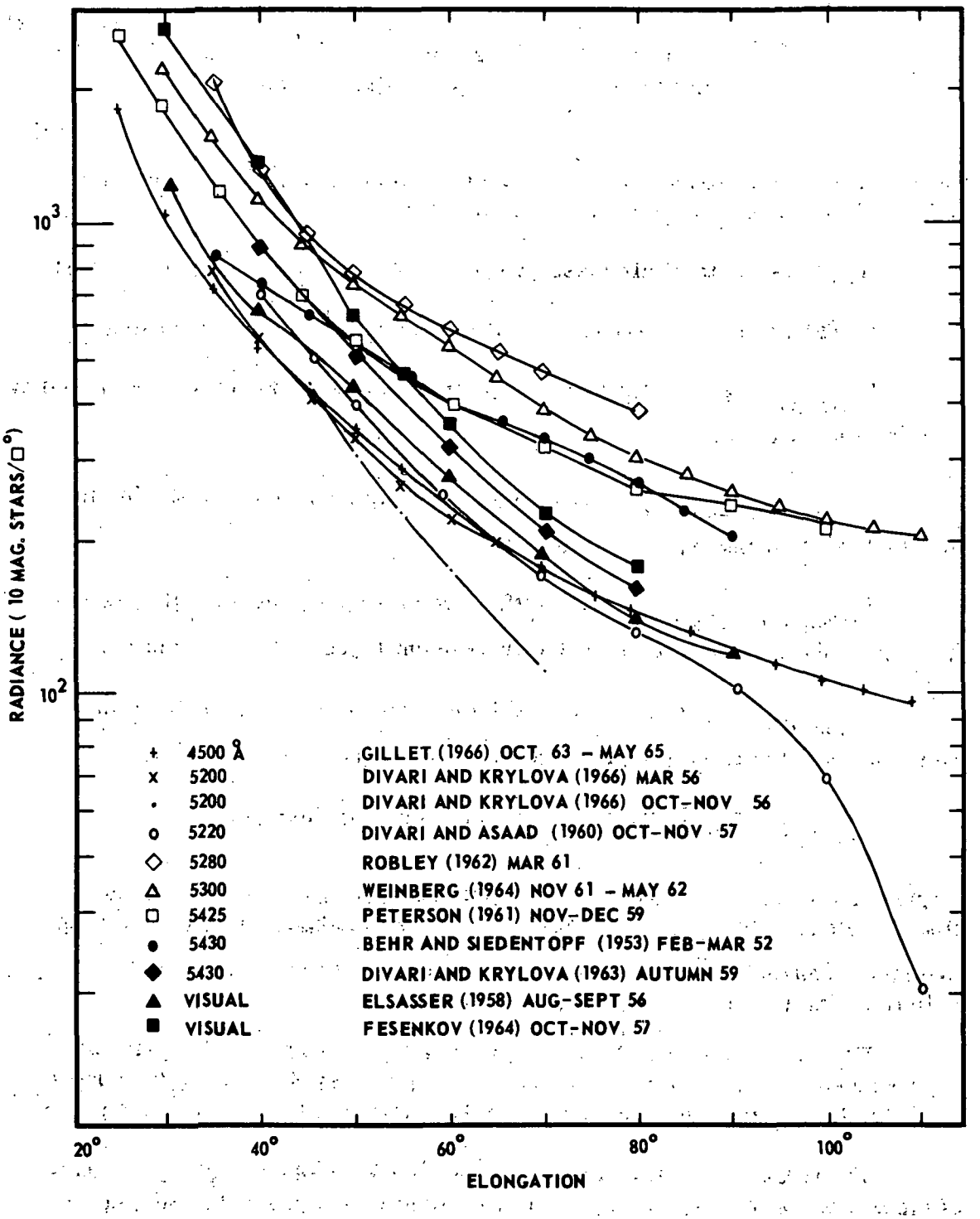

Figure 27. Collection of representative results between 25 and 110 deg for the radiance of the zodiacal light in the ecliptic [40, 27].

for $\epsilon \leq 80$ deg. Table 9 lists the values of the gradient exponent κ for the data of several observers.

Table 9 shows that considerable discrepancies exist in the relative variation of the radiance along the ecliptic (as obtained from different observations). The influence of the atmosphere on these data has yet to be determined.

TABLE 9. VALUES OF THE RADIANCE GRADIENT EXPONENT κ [42, 43]

Observer	Range (deg)	κ Value (λ, nm)
Divari/Krylova [44]	35 to 65	2.4 (520.0) 3.5 (520.0)
Blackwell/Ingham [9]	20 to 70	2.4 (620.0)
Elvey/Roach [5]	40 to 70	1.9 (450.0)
Robley [45]	35 to 65	2.3 (463.0) 2.3 (616.5)
Weinberg [46, 47, 48]	30 to 60	2.1 (530.0)
Peterson [49]	25 to 60	2.2 (435.5) 2.2 (542.5) 2.2 (638.0)
Behr/Siedentopf [8]	35 to 60	1.5 (543.0)
Divari/Krylova [50]	40 to 80	2.5 (540.0)
Elsasser [51]	30 to 60	1.5 (visual)
Fesenkov [34]	30 to 60	2.9 (-)
Gillett [27]	30 to 60	2.1 (350.0-500.0)
Smith/Roach/Owen [19]	30 to 60	2.2 (530.0)
Regener/Van de Noord [52]	25 to 35	3.0 (435.0) 3.0 (550.0)

Figure 28 presents the distribution of the degree of polarization in the plane of the ecliptic [40]. Considerable discrepancies also exist in the values of the degree of polarization. For an elongation of 60 deg, the values shown

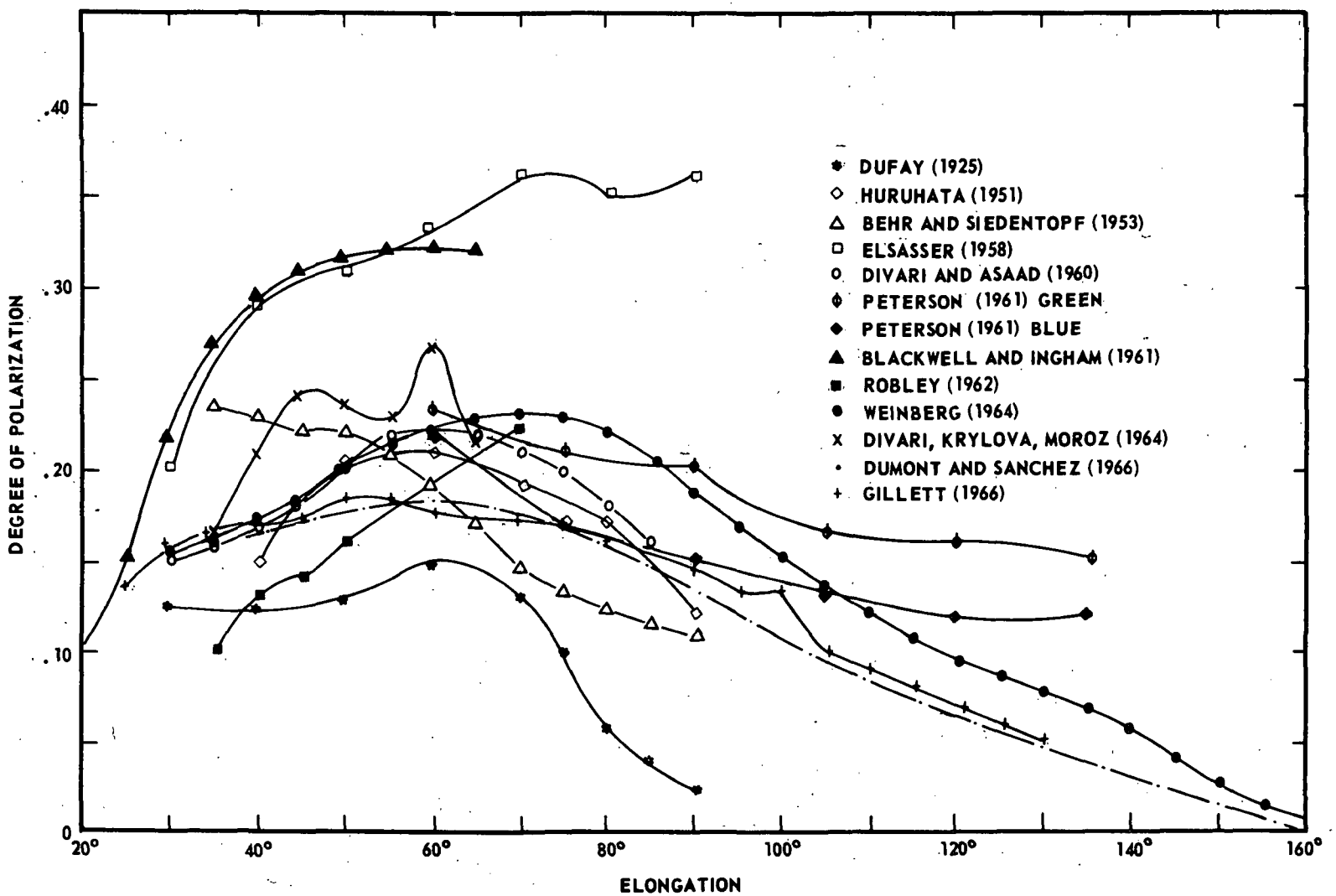

Figure 28. Collection of representative results between 20 and 160 deg for the polarization of the zodiacal light [40, 27].

vary from 0.15 to 0.33. Generally, however, the polarization seems to increase when the elongation increases from 30 to ≈ 65 deg. In the 50 to 70-deg region, the degree of polarization changes little about the inflexion point. At elongations larger than 60 deg, the degree of polarization decreases with increasing elongation. The polarization vector in the ecliptic is dominated by the vertical component; i.e., the component perpendicular to the ecliptic.

In Table 10, the radiance and polarization values obtained by Weinberg [47] in the ecliptic are given for reference since his data were chosen as the base which the models are compared. The zodiacal light was observed at 530 nm with a photoelectric polarimeter atop Mt. Haleakala, Hawaii (geographic latitude 20° 43' N, altitude 3052 m) between November 1961 and May 1962. Simultaneous observations of the 557.7 nm airglow emission line were used to separate the components of night-sky radiation. The field of view of polarimeter was 3.2 deg in diameter.

For radiance and polarization values within 30 deg of the sun, the data of Blackwell and Ingham [53] are given in Table 11.

The results of Smith, Roach, the Owen [19] for the variation of the radiance out of the ecliptic are given in Table 12. The data were obtained from Mt. Haleakala using a photoelectric photometer having a 4-deg field of view and 530 nm filter. The results are also presented in Figure 29 in an isophotal map where the circumference represents the plane of the ecliptic with values of differential longitude, $(\lambda - \lambda_0)$ increasing from 0 to 180 deg. The ecliptic latitude, θ, increases from 0 deg at the ecliptic to 90 deg in the center of the circle. The photometric perturbation at 65 deg from the sun at high ecliptic latitudes has not been confirmed by other observers [54, 55].

Dumont's [56] data for the average radiance out of the ecliptic are given in Figure 30 for comparison. The minimum in the radiance for these data is at 70 deg and not at the ecliptic pole (90 deg) as indicated by Smith, et al. The difference between the data of Smith, et al., and Dumont is a typical example of the discrepancy between different observers. The discrepancies between observers are again shown when a comparison of the radiance value of the zodiacal light at the ecliptic pole is made. Table 13 presents data for such a comparison. Few observers have reported the polarization values at the ecliptic poles. Beggs et al. [57, 58] and Weinberg [54] found the values of ≅ 20 and ≅ 10 percent, respectively (Table 13). Color measurements have yielded color indices both redder and bluer than sunlight (Table 14). Also, the color index has been found to increase [8],

TABLE 10. OBSERVATIONAL RESULTS FOR THE RADIANCE AND DEGREE OF POLARIZATION OF THE AVERAGE ZODIACAL LIGHT AT 530 nm [47].

ϵ	$B/\bar{B}_\odot$ ($\times 10^{-13}$)	S_{10} (vis)	P	ϵ	$B/\bar{B}_\odot$ ($\times 10^{-13}$)	S_{10} (vis)	P	ϵ	$B/\bar{B}_\odot$ ($\times 10^{-13}$)	S_{10} (vis)	P
30	10.0	2200	0.148	76	1.50	330	0.225	122	0.841	185	0.091
32	8.64	1900	0.152	78	1.41	310	0.222	124	0.841	185	0.087
34	7.54	1660	0.157	80	1.36	300	0.217	126	0.841	185	0.083
36	6.50	1430	0.162	82	1.30	285	0.213	128	0.864	190	0.080
38	5.77	1210	0.166	84	1.25	275	0.207	130	0.864	190	0.077
40	5.14	1130	0.171	86	1.20	265	0.200	132	0.864	190	0.074
42	4.68	1030	0.176	88	1.16	255	0.193	134	0.886	195	0.071
44	4.27	940	0.181	90	1.14	250	0.186	136	0.886	195	0.068
46	3.89	855	0.185	92	1.09	240	0.178	138	0.909	200	0.063
48	3.59	790	0.192	94	1.04	230	0.171	140	0.909	200	0.058
50	3.32	730	0.197	96	1.02	225	0.165	142	0.909	200	0.052
52	3.09	680	0.202	98	1.00	220	0.158	144	0.909	200	0.045
54	2.86	630	0.206	100	0.977	215	0.151	146	0.909	200	0.038
56	2.68	590	0.210	102	0.954	210	0.144	148	0.932	205	0.033
58	2.50	550	0.215	104	0.932	205	0.138	150	0.932	205	0.027
60	2.36	520	0.218	106	0.909	200	0.132	152	0.954	210	0.023
62	2.20	485	0.222	108	0.909	200	0.126	154	0.977	215	0.018
64	2.09	460	0.224	110	0.886	195	0.120	156	0.977	215	0.014
66	1.95	430	0.226	112	0.886	195	0.115	158	1.000	220	0.010
68	1.82	400	0.228	114	0.864	190	0.109	160	1.000	220	0.006
70	1.75	385	0.229	116	0.864	190	0.105	165	1.040	230	
72	1.64	360	0.228	118	0.864	190	0.100	170	1.090	240	
74	1.57	345	0.226	120	0.841	185	0.095	175	1.110	245	
								180	1.180	250	

TABLE 11. BLACKWELL AND INGHAM DATA [53]

ϵ	$B/B_{\odot}$ ($\times 10^{-12}$)	S_{10}(vis)	P
5	56.9	125 610	0.021
11	12.6	27 815	0.034
15	5.24	11 567	0.059
20	2.34	5 188	0.099
25	1.38	3 046	0.151
30	0.884	1 951	0.216
35	0.609	1 344	0.268
40	0.442	976	0.292

TABLE 12. ZODIACAL LIGHT IN ECLIPTIC COORDINATES [19]

λ − λ⊙ \ β	0	5	10	15	20	25	30	35	40	45	50	55	60	65	70	75	80	85	90
180	205	195	185	175	165	155	150	140	125	130	125	125	125	125	115	115	115		110
175	195	190	175	165	160	150	150	135	125	130	125	125	125	125	115	115	115		
170	185	175	170	160	155	150	145	135	125	130	120	125	125	125	115	115	115		
165	175	170	165	160	150	145	145	135	125	130	120	125	125	125	115	115	115		
160	175	170	160	155	145	145	145	135	125	130	125	120	125	125	115	115	115		
155	170	165	160	155	150	145	145	135	125	130	125	125	125	125	115	115	115		
150	170	165	160	155	150	150	145	140	125	130	125	125	125	125	115	115	110		
145	175	170	165	155	155	155	145	140	125	135	130	125	125	125	115	115	110		
140	175	170	165	160	155	155	145	145	130	135	130	120	125	125	115	115	115		
135	175	170	170	160	160	155	145	145	135	135	135	120	125	125	115	115	115		
130	175	175	170	165	160	155	145	145	135	135	135	125	125	125	115	115	115		
125	180	175	175	165	165	160	145	145	135	135	135	125	125	125	115	115	115		
120	185	180	180	170	165	160	145	150	135	135	135	125	125	125	120	115	115		
115	190	185	180	175	170	165	150	150	135	135	135	125	125	120	120	115	115		
110	200	190	185	175	170	165	150	150	140	135	135	125	125	120	120	115	115		
105	210	200	190	180	175	170	150	150	145	135	135	130	125	120	120	115	115		
100	220	205	195	185	175	170	155	150	145	135	135	130	125	120	120	115	115		
95	235	215	205	190	180	170	155	155	150	135	135	130	125	125	120	120	120		
90	250	235	215	200	185	175	155	160	150	135	135	130	125	125	125	125	125		
85	265	255	235	215	195	180	155	165	155	135	140	130	125	125	125	125	130		
80	290	275	255	230	210	190	165	170	155	135	140	130	125	125	125	125	130	110	
75	320	300	285	245	225	200	185	175	160	135	145	130	125	130	125	130	130	110	
70	(370)	335	310	265	240	210	205	185	175	145	145	130	135	135	130	135	130	115	
65	(425)	370	345	285	255	225	205	205	200	170	150	140	140	140	130	135	130	115	
60	(500)	425	380	305	270	240	215	205	205	195	165	145	145	145	135	135	130	115	
55	(600)	505	430	330	290	255	225	205	205	200	180	160	155	150	135	135	135	120	
50	(745)	610	485	370	315	285	230	205	205	195	205	170	160	150	140	140	135	120	
45	(945)	735	555	425	345	315	240	215	210	190	205	190	170	155	140	140	135	120	
40	(1185)	870	655	505	390	360	250	220	215	190	195	205	170	160	140	140	135	125	
35	(1595)	(1145)	845	690	450	410	270	225	215	190	185	200	175	165	145	145	140	125	
30	(2330)			905	545	465	300	230	220	195	180	195	185	170	145	150	145	125	
25						520		245	225	200	180	190	190	175	150	150	145	130	
20									230	205	180	185	190	180	150	150	145	135	
15									235	205	180	180	185	185	155	155	150		
10										210	180	175	185	185	155	155	150		
5												175		185	155	160			
0				(6150)	(1820)	(995)	(525)	(330)	(250)	(215)	(180)	(175)	(185)	(185)	155	160	(150)	(135)	

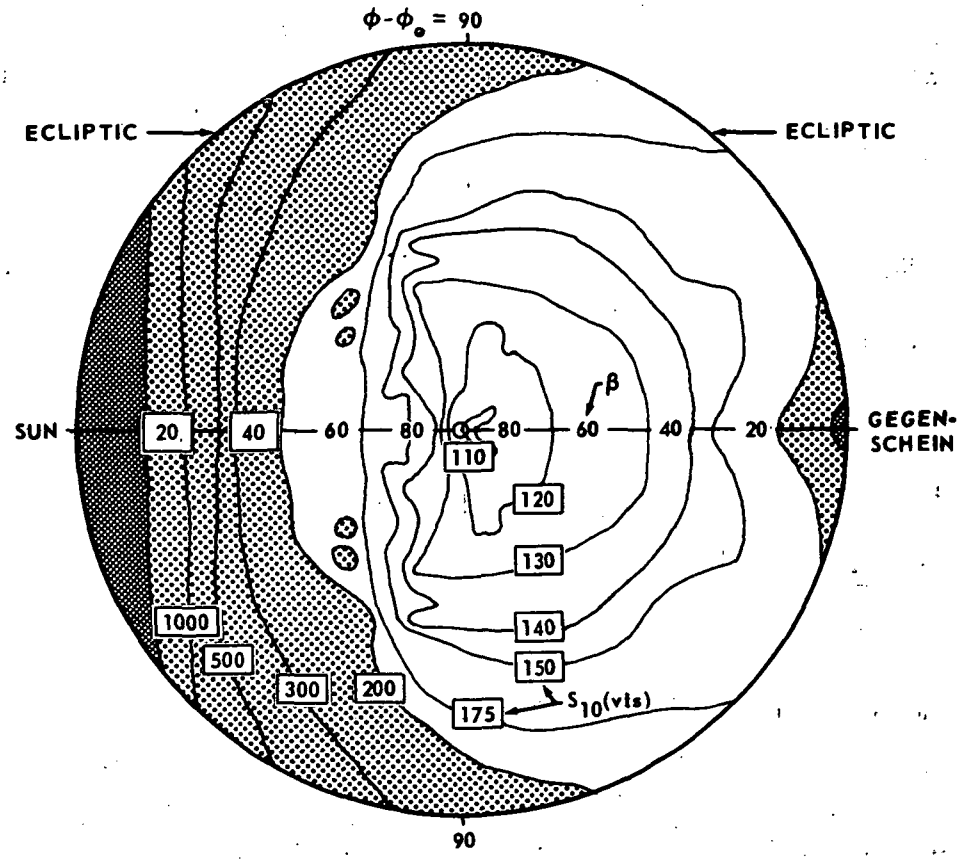

Figure 29. Isophotal map of Smith, Roach, and Owen [19] observations of the zodiacal light out-of-the-ecliptic. (The ecliptic plane lies on the circumference, and the center is the north ecliptic pole. The Sun is at the left.)

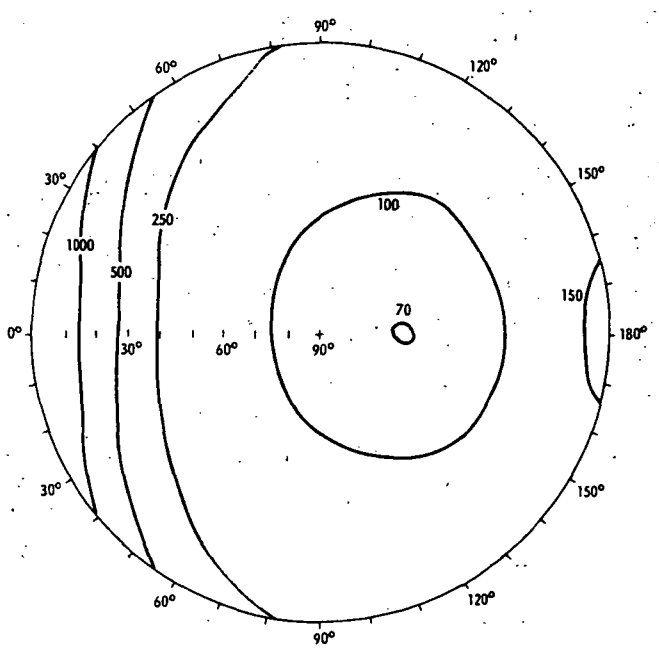

Figure 30. Dumont [56] results for out-of-the-ecliptic.

TABLE 13. RADIANCE AND POLARIZATION OF THE ZODIACAL LIGHT AT THE ECLIPTIC POLE [59, 60]

Observer	(1) Pole [S_{10} (vis)]	(2) ϵ = 45 on the Ecliptic [S_{10} (vis)]	Ratio $\frac{(2)}{(1)}$	Polarization at Pole
Elvey/Roach [5]	73	1323	18.1	
Beggs/et al. [57, 58]	177	661	3.73	0.20
Weinberg [54]	186	897	4.82	0.09
Smith/Roach/Owen [19]	110	945	8.60	
Dumont [61]	70	700	10.0	0.18
Wolstencroft/Rose [62]	143	840	5.87	0.19
Gillett [63]	48	416	8.67	0.21
Sparrow/Ney [60]	50	—	—	0.21

TABLE 14. VALUES OF THE COLOR INDEX (CI) OF THE ZODIACAL LIGHT [42]

Observer	CI (zl)	CI (sun)	Δ	λ_b/λ_g
Behr/Siedentopf [8]	0.63	0.43	+0.20	444/542
Divari/Asaad [64]	0.35	0.45	-0.10	414/541
Nikol'skii [cf 42]	0.56	—		414/540
Peterson [49]	0.48	0.45	+0.03	435/543
Divari/Krylora [50]	0.47	0.63	-0.16	406/543
Robley [45]	—	—	+0.16	463/528
Divari/Krylova/Moroz [112]	—	—	+0.14	460/520

to decrease [64], and to remain constant [49]. If, indeed, an elongation dependence of the zodiacal light color index exists, it must be very small. However, if such a dependence is found, it will yield information on the dust-particle sizes.

Figure 31 shows the relationship between the neutral-point position in elongation and the wavelength in the plane of the ecliptic [40]. For larger wavelengths, the neutral point tends to move closer to the sun. The data have a 25-deg error spread so the linear nature shown may not be real. These data are important because neutral points calculated by models are dependent on the model chosen, at least more so than the general shape of the radiance curve produced by the models.

The components of the zodiacal light caused by dust and electrons can be separated by the use of the spectrum of the zodiacal light. Blackwell and Ingham [9, 10, 11] determined that the electron density at 1 AU should be no greater than 120 electrons/cm^3. The photoelectric observations of Beggs et al. [57, 58] which determine the electron contribution to be 16 ± 20 electrons/cm^3 have been confirmed as to the order of magnitude from space vehicles [65]. Thus, it may be confidently stated that free electrons play a negligible role in the scattering of sunlight except in the corona.

Photometric observations and recent results on the gegenschein have been summarized by Roosen [31, 66, 67]. He concludes that the gegenschein lies at the antisolar point, with no net displacement in either latitude or longitude to within 0.03 deg. The relative brightness of the gegenschein as a function of the distance in declination is shown in Figure 32. Its relative brightness as a function of longitude from the antisolar point is shown in Figure 33. The general shape of the gegenschein is oval. The shape parameter, Q, is determined as a function of angular distance by the ratio of the brightness of the gegenschein and zodiacal light in a plane at right angles to the ecliptic to that in the plane of the ecliptic. Figure 34 presents the shape parameter as found by various observers. The discrepancy in the brightness of the gegenschein between various observers is given in Table 15. The ratio of the brightness of the gegenschein, B_G, to the brightness at the ecliptic pole, B_{pole}, is given to find more consistency, but, again, a large amount of scatter is evident since the maximum is 4.00, the minimum is 1.40, and the average is 2.10. The important result of Roosen is that to within 1 percent earth's shadow did not effect the brightness distribution of the gegenschein.

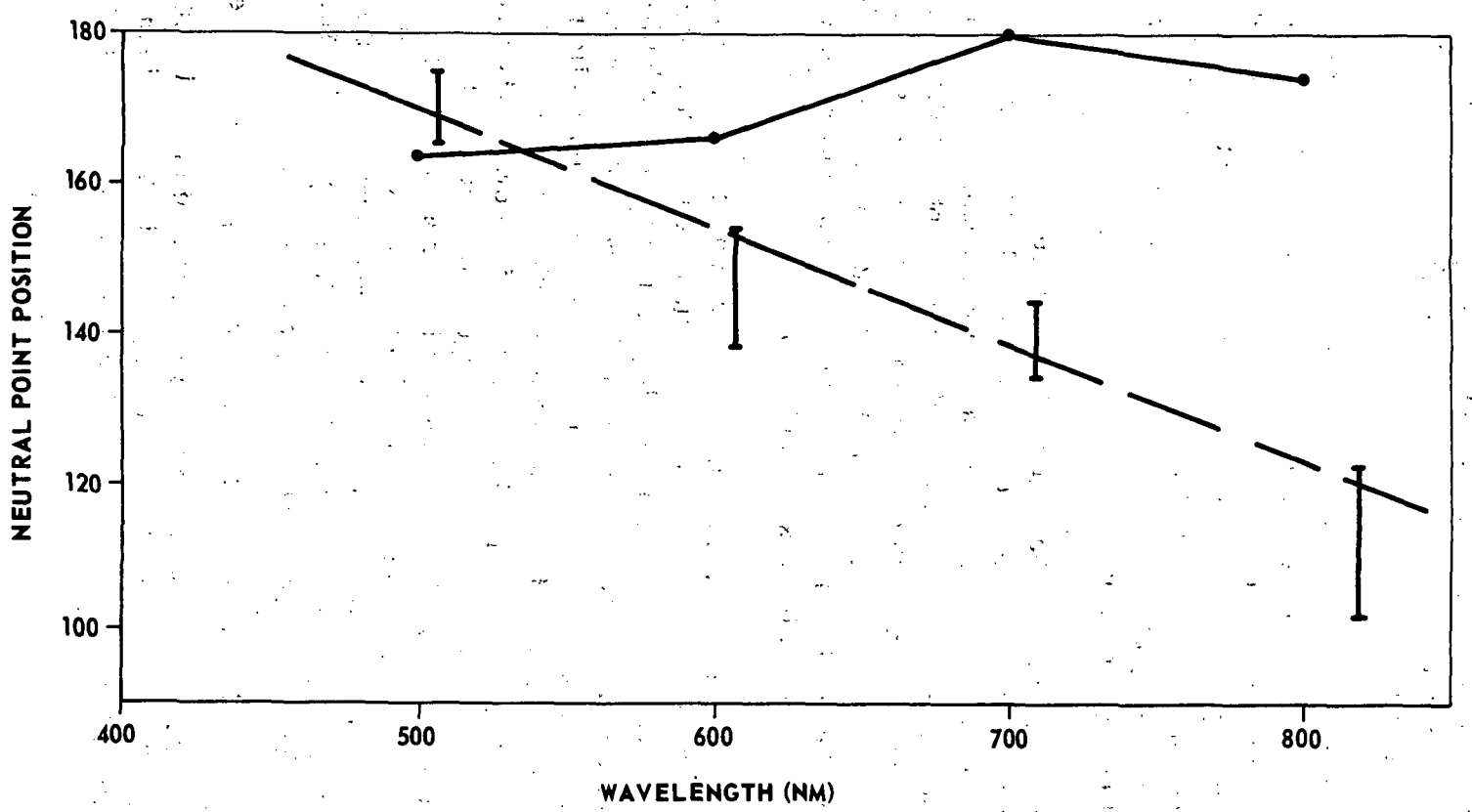

Figure 31. Relationship between the neutral-point position in elongation and the wavelength in the plane of the ecliptic. [The dashed line indicates the trend of Weinberg's data (error bars) for the dependence of the neutral point (zero polarization) in the ecliptic. The solid line represents result for the ice model P. 4]

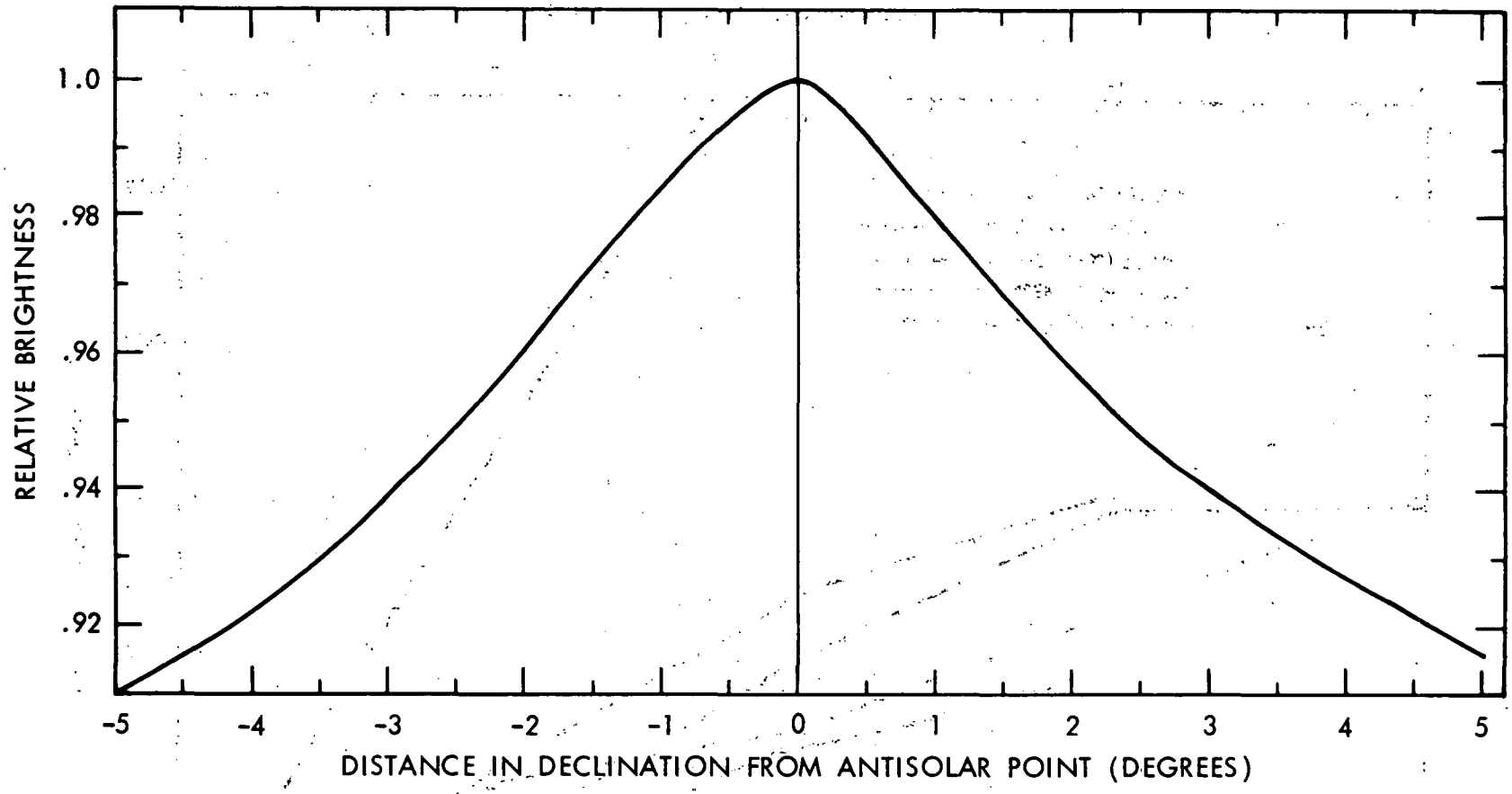

Figure 32. Normalized brightness of the gegenschein averaged from the 41 scans made March 12, 13, 18, and 19, 1969 [66, 67].

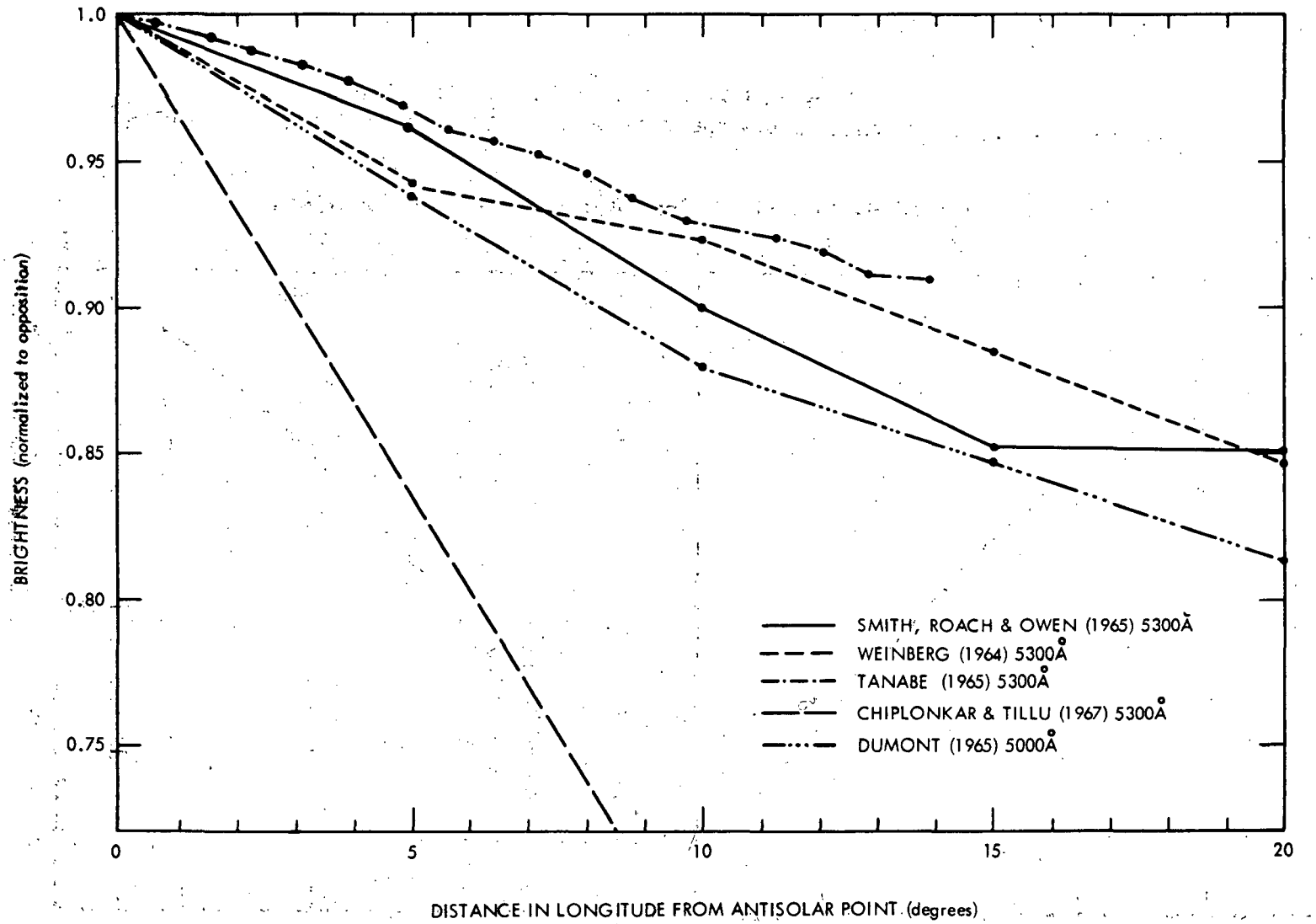

Figure 33. Brightness of the gegenschein in the ecliptic plane near 5300 Å, determined by various observers normalized to unity at opposition [66, 67].

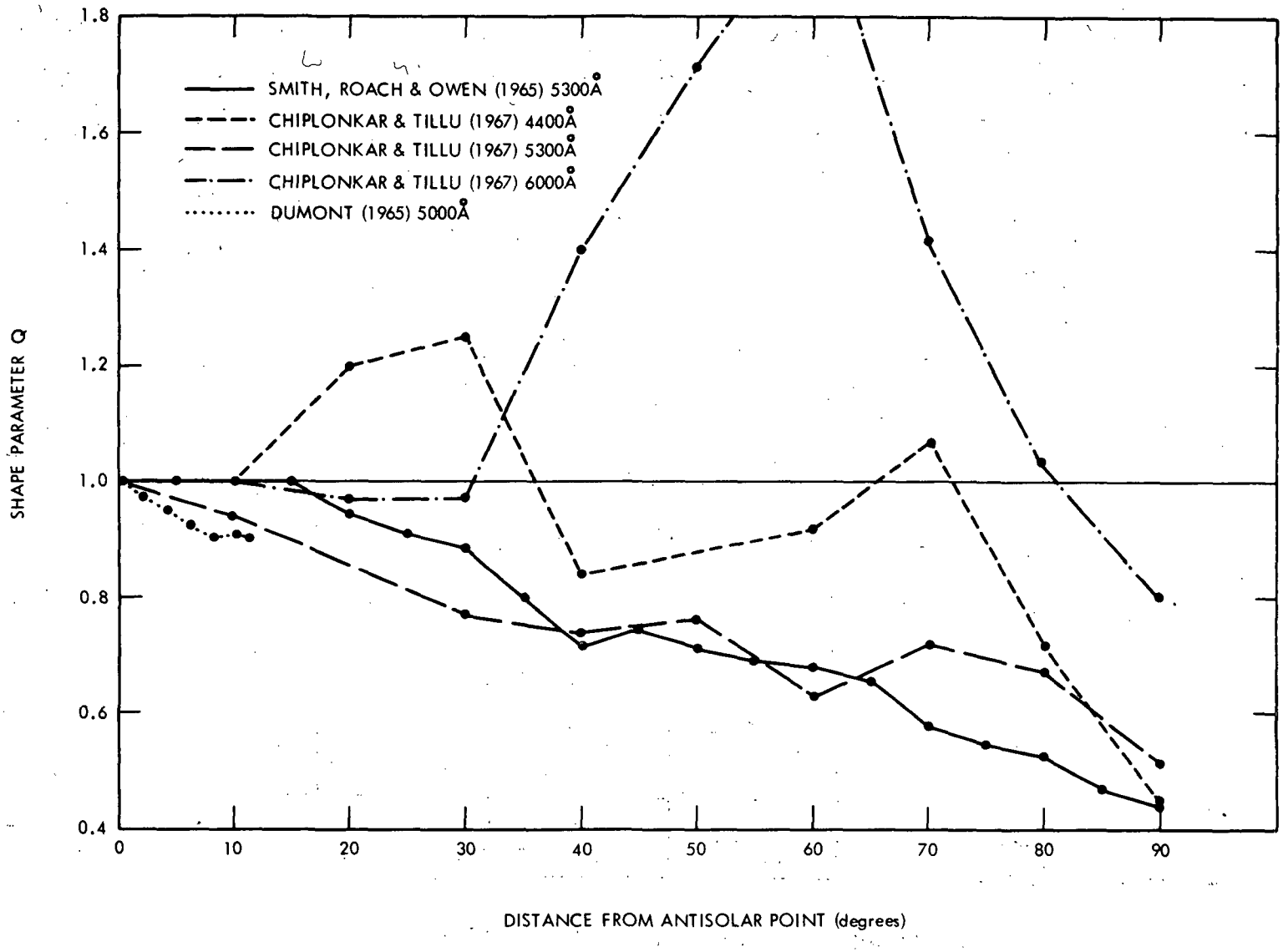

Figure 34. The shape parameter Q for various observers [66, 67].

TABLE 15. BRIGHTNESS OF THE GEGENSCHEIN, THE ECLIPTIC POLE, AND THEIR RATIO FOR VARIOUS OBSERVERS [66, 67]

Observer	Wavelength Range (Å) or System		Gegenschein		Ecliptic Pole		B_G/B_{pole}
			S_{10} system	S_{10} vis	S_{10} system	S_{10} vis	
van Rhijn	Visual (Harvard scale)			810		450	1.80
Elvey and Roach	Blue		160	285a	40	71a	4.00
Robley	4630	120Å half width		264.7		173.5	1.53
Robley	6165	170Å half width		272.7		180.3	1.51
Tanabe	5300	narrow band		156 ± 18		100	1.56
Weinberg	5300	narrow band		260		186 [62]	1.40
Dumont	5000			182 [122]		70	2.60
Robley	4550	120Å half width		166		85	1.95
Robley	5280	90Å half width		190		111	1.71
Robley	6080	220Å half width		249		160	1.56
Smith, Roach, and Owen	5300	narrow band		205		110 ± 22	1.86
Chiplonkar and Tillu	4400	198Å half width		125		45	2.78
Chiplonkar and Tillu	5300	75Å half width		195		79	2.47
Chiplonkar and Tillu	6000	196Å half width		90		56	1.61
Wolstencroft and Rose	Blue		166	295a	92	163a	1.80
Lillie	Blue		103	183a	30	53a	3.43

a. using V = 1.78 B (assuming solar color index)

SECTION VI. COMPARISON AND ANALYSIS OF MODEL CALCULATIONS

A. Model Comparison

From the preceding sections, one can see that to predict the observational quantities of the zodiacal light, the parameters of the models must be varied. Though the mathematical formulation for the problem is relatively simple, the observational uncertainties or lack of observational data has hindered the determination of definite values for the various parameters. In this section is presented an analytic approach to a method of variation of the parameters and a trial-and-error approach for matching the present data.

A comparison of model predictions with observational data will give information on the range of the following:

1. Particle spatial distribution.

2. Particle size and numerical distribution.

3. Particle shape and anisotropic effects.

4. Particle composition (refractive index).

The following procedure is adopted in this section:

1. Assuming $i(\theta)$ is independent of θ and assuming that no radial dependence ($m = 0$) exists, it is shown that the radiance dependence on elongation ϵ is approximately that which is observed. Also, assuming that the size distribution $n(\alpha)$ is a constant between α_{min} and α_{max} and otherwise zero, an indication of the number density parameter is given. As a further refinement to $i(\theta)$, simple models using diffraction scattering theory are investigated.

2. An indication of the material and a range on the particle size is found by comparing the radiance and polarization of the zodiacal light with that of single particles.

3. Further analysis in comparing polarization and radiance is accomplished by the use of scattering-intensity functions for a distribution over the particle size. This gives a further indication of particle size and materials. It is noted that a backscatter peak (gegenschein) in radiance is produced only by dielectric particles.

4. Zodiacal light models are investigated for ecliptic variation of radiance and polarization. This follows the work by Giese [26]. First, a variation of materials is investigated, and then a variation of the parameters is investigated. Specific parameters considered are as follows:

a. Spatial parameter (m).

b. Number density variation parameter (p).

c. Number density constant (n_o).

d. Minimum and maximum size parameter (α_{min} and α_{max}).

e. Material (refractive index m*).

f. Wavelength (λ).

g. Ecliptic thickness parameter (R/W).

An analysis of the integration procedure and the influence of the maximum size cutoff is cursorily investigated. Finally, the various models are compared.

5. Out-of-the-ecliptic calculations using the linear thickness model are presented. Thickness and distribution effects are investigated.

6. Cylindrical and other shapes are considered as to their influence on the variations of the zodiacal light.

Several conclusions have been made using restricted models for the zodiacal dust in the ecliptic. By comparing observations with models using spherical particles, it has been concluded that [54, 55]:

1. Only dielectric-component models produce a radiance enhancement corresponding to the gegenschein.

2. Dielectric-component models produce an irregular decrease of the degree of polarization such as that observed at large elongations ($\simeq$ 160 deg).

3. Dielectric-component models can give a maximum polarization at 70 deg.

4. Metallic-component models cannot account for observed radiance and polarization.

5. To include more than some tens of electrons per cm^{-3} at 1 AU, one must postulate the existence of a hypothetical nonpolarizing dust component.

6. A simple power law for particle-size distribution and spatial distribution seem partially correct.

7. The interplanetary matter has a low index of refraction ($m = 1.3 - 1.8$).

B. Basic Heliocentric Model

Results from the basic heliocentric model are presented to provide an understanding of the basic variation of radiance and polarization with particle number density and with elongation because of geometric considerations. The radiance equation for the heliocentric model is given by equation (33):

$$\overline{L}_\lambda = \frac{R\, E_\lambda^e\, \delta\lambda N_o}{\sin^{m+1}\epsilon} \int_\epsilon^\pi \sin^m\theta \left(\overline{\frac{d\sigma}{d\Omega}}\right) d\theta$$

where

$$\left(\overline{\frac{d\sigma}{d\Omega}}\right) = \frac{1}{N_o} \int_{a_{min}}^{a_{max}} n_o \left(\frac{a}{a_o}\right)^{-p} \left(\frac{d\sigma}{d\Omega}\right) da$$

and

$$N_o = \int_{a_{min}}^{a_{max}} n_o \left(\frac{a}{a_o} \right)^{-p} da \quad .$$

An investigation was carried out in Section III. D with emphasis on the product

$$I_m(\epsilon) = \frac{1}{\sin^{m+1} \epsilon} \int_{\epsilon}^{\pi} \sin^m \Theta \, d\Theta$$

specifically, for m = 0, 1, and 2. Employing

$$I_{m=0}(\epsilon) = \frac{\pi - \epsilon}{\sin \epsilon}$$

and

$$I_{m=0}(\epsilon = \pi) = 1,$$

one now uses that analysis assuming isotropic scattering (i.e., $\frac{d\sigma}{d\Omega} = C =$ constant) and a distribution independent on the solar radial distant. Let

$$\overline{\frac{i_1(\Theta) + i_2(\Theta)}{2}} = \frac{4\pi^2}{\lambda N_o} \int_{a_{min}}^{a_{max}} n_o \left(\frac{d\sigma}{d\Omega} \right) da \quad ,$$

then

$$\overline{L}_\lambda = \frac{\lambda^2 R E^e \delta \lambda N_o}{4\pi^2} \left(\frac{\pi - \epsilon}{\sin \epsilon} \right) \overline{\left(\frac{i_1 + i_2}{2} \right)} \quad . \tag{150}$$

To use units of the number of 10th magnitude bolometric stars, one uses [69]

$$\frac{\text{solar constant} = E^e}{(m_{bol} = 10)_{star}} = \frac{1.39 \times 10^3 \text{ w/m}^2}{2.52 \times 10^{-12} \text{ w/m}^2} = 0.551 \times 10^{15}$$

to obtain the value of

$$\frac{\lambda^2 R E^e}{4\pi^2} = 158.28 \times 10^{-12} \quad \frac{10 \text{ mag. stars. cm}^3}{\square \text{ deg}} \tag{151}$$

where $\lambda = 500$ nm. Using for $\overline{\frac{1}{2}(i_1 + i_2)}$ the value of 10 which is the average value for ice with an α on the order of 10 and $\Theta > 40$ deg (i.e., a $\simeq 1\mu$ at 500 nm) then at $\epsilon = 40$,

$$I_{m=0} = \frac{\pi - \epsilon}{\sin \epsilon} = 3.8;$$

hence, to match Weinberg's data for $\epsilon = 40$ deg, the radiance equation (150) becomes

$$1.13 \times 10^3 = 1.58 \times 10^{14} \; N_o (3.8) \; (10) \; ,$$

which gives

$$N_o \; (\epsilon = 40) = 1.88 \times 10^{-13} \; \frac{\text{particles}}{\text{cm}^3} \; .$$

For $\epsilon = 80$ deg, one has

$$N_o(80) = 1.07 \times 10^{-13} \; \frac{\text{particles}}{\text{cm}^3}$$

and, for $\epsilon = 140$ deg,

$$N_o \; (140) = 1.17 \times 10^{-13} \; \frac{\text{particles}}{\text{cm}^3} \; .$$

The values for the radiance, using the various values of N_o compared with Weinberg's data are presented in Table 16 and Figure 35. The last column (Δ) is the difference between the third and sixth column which gives an indication of the average total intensity as a function of Θ, although the radial dependence is also contained in this difference.

The 30 to 60 deg exponential gradient for these models is $\kappa = 1.2$, compared to 2.1 from Weinberg's data. Hence, in the basic model, the radiance rises slower in the solar direction than measured data. The wavelength or spectral dependence is the same as the sun (i.e., a GO-type star).

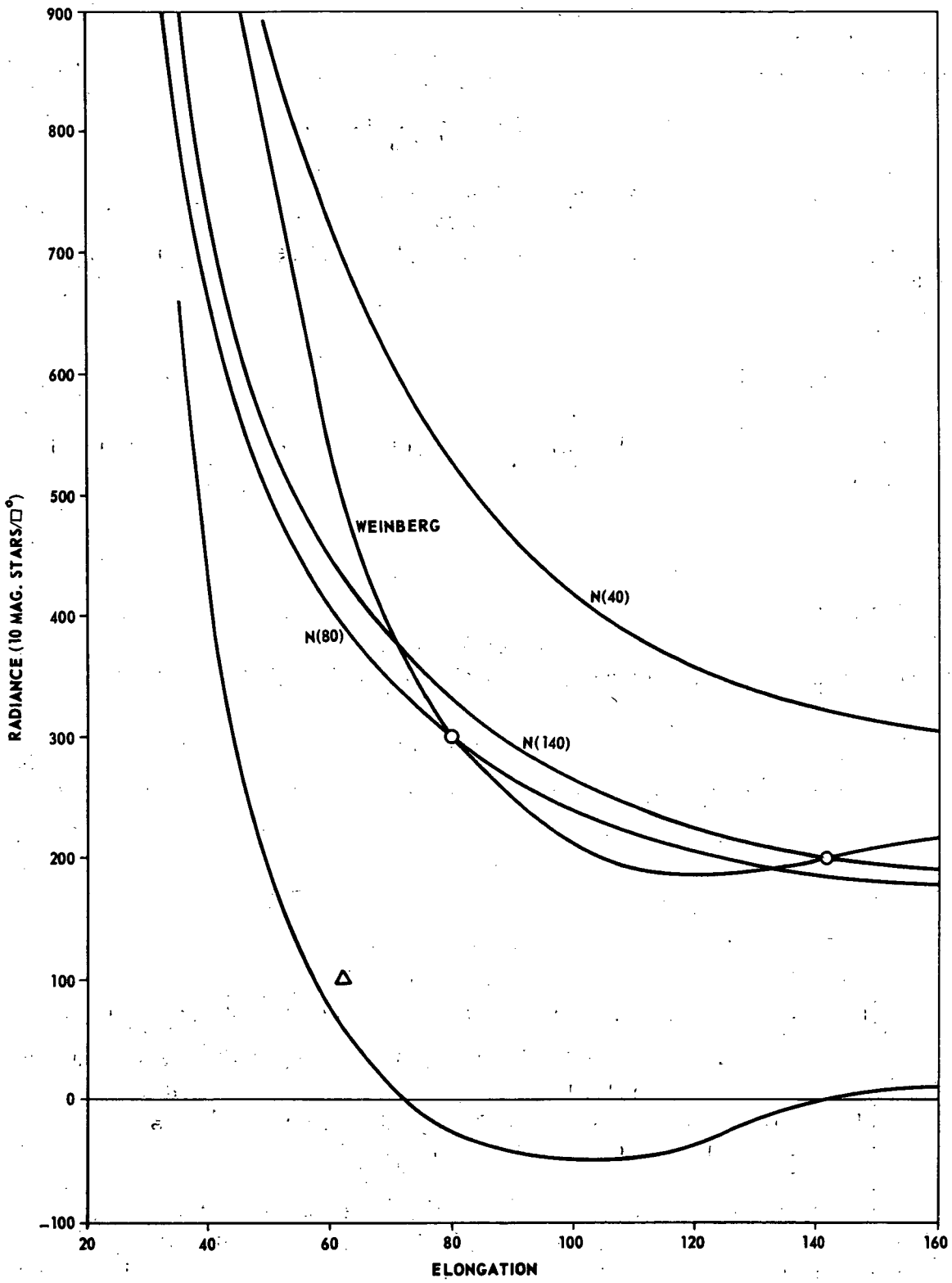

Figure 35. Comparison of the basic heliocentric model with Weinberg's data.

TABLE 16. COMPARISON OF THE BASIC HELIOCENTRIC MODEL WITH WEINBERG'S DATA

ϵ	$I_{m=o}$	Weinberg $S_{10}(v)$	Heliocentric Models			Δ
			$N_o(40)$	$N_o(80)$	$N_o(140)$	
30	5.23	2200	1555	886	967	1233
40	3.80	1130	1130	644	704	426
60	2.41	520	717	408	446	74
80	1.77	300	526	300	328	-28
100	1.41	215	419	239	261	-46
120	1.20	185	357	203	222	-37
140	1.08	200	321	183	200	0
160	1.02	220	303	173	189	+31

For a distribution of particle sizes of

$$n(a) = \begin{cases} 1 & a_{min} < a < a_{max} \\ 0 & \text{otherwise} \end{cases} ,$$

and for $a_{min} = 0.5\ \mu m$ and $a_{max} = 1.5\ \mu m$, then

$$N_o = n_o\ (a_{min} - a_{max})$$

or

$$n_o = \frac{N_o}{1\mu m}$$

Hence, for $N_o(140)$, the parameter n_o has the value

$$n_o(140) = 1.17 \times 10^{-9}\ \frac{\text{particles}}{\text{cm}^4} .$$

In conclusion, the radiance dependence on $\frac{d\sigma}{d\Omega}$ is not very great, as was noted in earlier theories [13], although the lack of this dependence is quite noticeable.

C. Basic Heliocentric Model with Spatial Dependence

The radiance variation of the basic heliocentric model (HM) does not correspond to Weinberg's data. To improve the basic model, a spatial dependence for the number distribution of the form.

$$s(r) \simeq 1/r^m$$

is included in the model. From the analysis of I_m, it is evident that m = 1. Hence,

$$I_{m=1}(\epsilon) = \frac{1 + \cos \epsilon}{\sin^2 \epsilon} \tag{152}$$

will give ϵ^{-2} dependence for the radiance as $\epsilon \to 0$. This is comparable with observed data (Table 9). Although for $I_{m=2}$, we have a ϵ^{-3} dependence as $\epsilon \to 0$, ϵ^{-2} dependence can be obtained for a higher range of ϵ. The result of these radial dependence models, normalized to Weinberg's value at $\epsilon = 140$ deg, is shown in Table 17 and Figure 36. Comparison of the 30- to 60-deg exponential gradient gives $\kappa_{m=1} = 1.7$ and $\kappa_{m=2} = 2.6$.

TABLE 17. HELIOCENTRIC MODEL WITH SPATIAL DEPENDENCE

ϵ	$I_{m=1}$	$I_{m=2}$	$\bar{L}_{m=1}$ [a]	$\bar{L}_{m=2}$ [b]
30	7.46	12.2	2635	6310
40	4.27	5.52	1508	2855
60	2.00	1.94	706	1050
80	1.21	1.00	427	517
100	0.852	0.641	301	332
120	0.666	0.4(80)	235	248
140	0.566	0.387	200	200
160	0.515	0.345	182	178

a. $N_o = 3.53 \times 10^{-13}$

b. $N_o = 5.17 \times 10^{-13}$

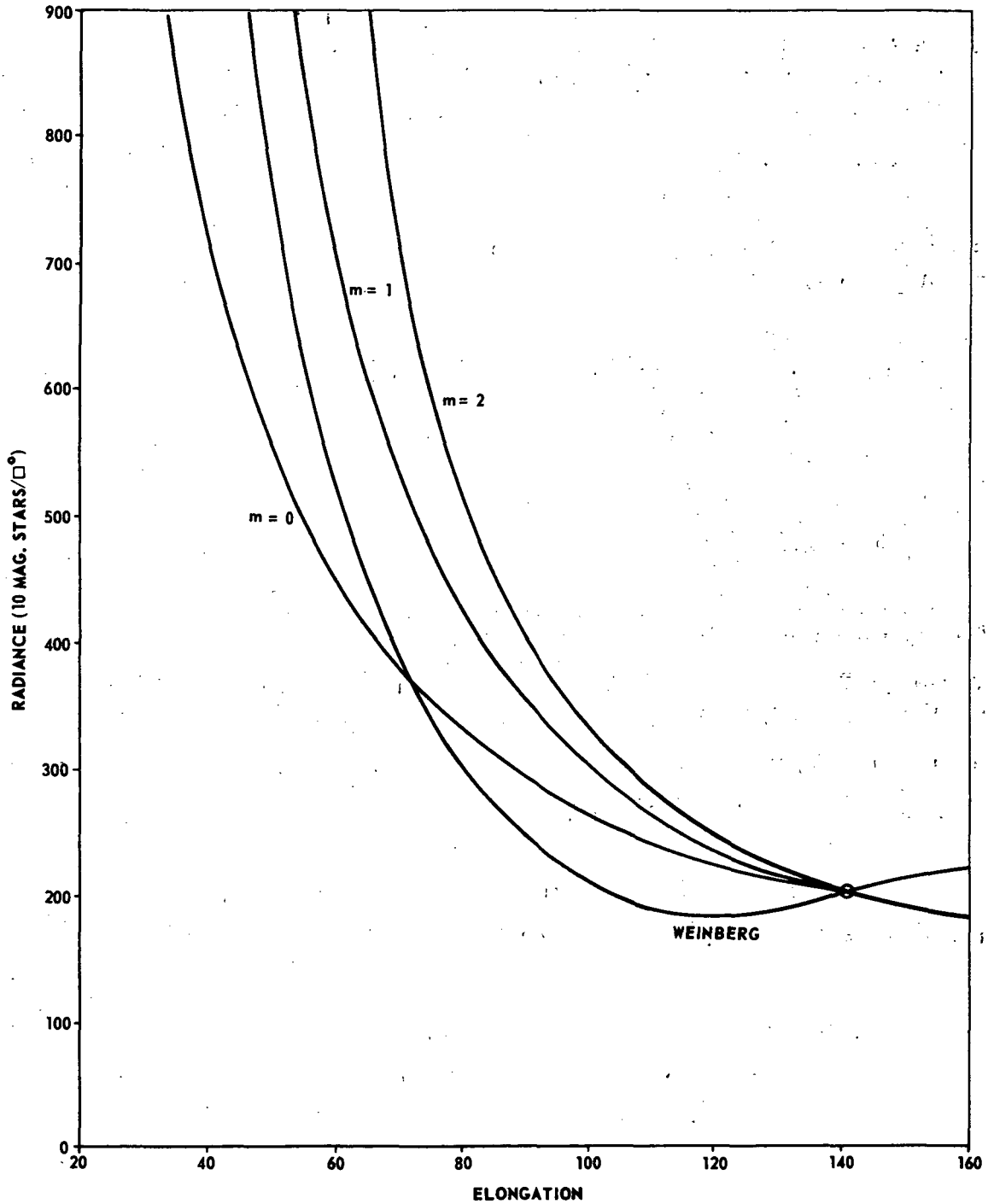

Figure 36. Comparison of a spatial dependent heliocentric model with Weinberg's data.

D. Belt Model for Isotropic Scattering

The variation of radiance with respect to elongation can be improved by the use of the belt model which is described in Section III. For simplicity, assume an isotropic scattering intensity functions; i.e.,

$$\frac{\overline{i_1(\Theta) + i_2(\Theta)}}{2} = \text{constant}$$

and $m = 0$. As before, the constant is chosen to be 10. In units of 10th magnitude stars per square degree, the radiance equation (59) becomes

$$\overline{L}(\epsilon) = \frac{158.28 \times 10^{12} \times 10}{\sin \epsilon} \sum_{j=1} N_j \int_{\Theta_j}^{\Theta_{j+1}} d\Theta ,$$

where

$$\Theta_j = \sin\left(\frac{R}{r_j} \sin \epsilon\right) .$$

The values $(R/r_j)^{-1}$ are chosen to be 0.723 and 1.00; i.e., the orbits of Venus and Earth. For sufficiently small elongations, the line of sight crosses the Venus-Earth belt twice. Note that N_j and/or Θ_j could be varied, but because of the dependence of Θ_j on the elongation, one determines, for ease of calculation, the Θ_j's by choosing the r_j's.

For N_j in units of 10^{-13} particles/cm^3 (using Weinberg's data), the following conditions exist: For $\epsilon = 40$ deg,

$$\begin{aligned} 1130 = \frac{158.28}{0.64279} [& N_3(1.09528 - 0.69813) \\ & + N_2 (2.04631 - 1.09528) \\ & + N_3 (2.44349 - 2.04631) \\ & + N_4 (3.14159 - 2.44349)]. \end{aligned}$$

For $\epsilon = 60$ deg:

$$520 = \frac{158.28}{0.86603} \left[N_3(2.09439 - 1.04720) + N_4(3.14159 - 2.09439) \right] .$$

For $\epsilon = 120$ deg:

$$185 = \frac{158.28}{0.86603} \left[N_4(3.14159 - 2.09440) \right] .$$

N_2 represents the density inside $r = 0.703$, N_3 represents the density between $r = 0.703$ and 1.00, and N_4 represents the density for $r > 1.00$. These equations yield

$$\left.\begin{aligned} N_2 &= 2.653 \times 10^{-13} \\ N_3 &= 1.747 \times 10^{-13} \\ N_4 &= 0.969 \times 10^{-13} \end{aligned}\right\} \quad \text{particles/cm}^3$$

where the factor 10^{-13} has been included. The comparison of the belt model and Weinberg's data is given in Table 18. Also, the comparison is made in Figure 37 which shows the basic heliocentric model for $m = 0$. The results are promising although more parameters are introduced relatively ad hoc. The 30- to 60-deg exponential gradient for the belt model is $\kappa = 1.8$.

The density calculated decreases with distance for the three separate concentric regions. Since $i(\Theta)$ is constant, the effect could represent either the actual spatial dependence or the diffraction peak, or both. The diffraction phenomena will be investigated in Section F.

In the belt model, when $r_j = 1.524$ and $\epsilon = 170$ deg, then only approximately the last 10 deg of the scattering intensity functions for particles outside Mars orbit contribute. Thus, particles with very large backscatter could be the main contributors to gegenschein. This effect could be a type of opposition effect for large particles (i.e., with a radius greater than 1 cm) outside the Martian orbit.

E. Approximation

In the calculation of scattered light, approximations can be used to represent the angular distribution of the scattered light. These approximations

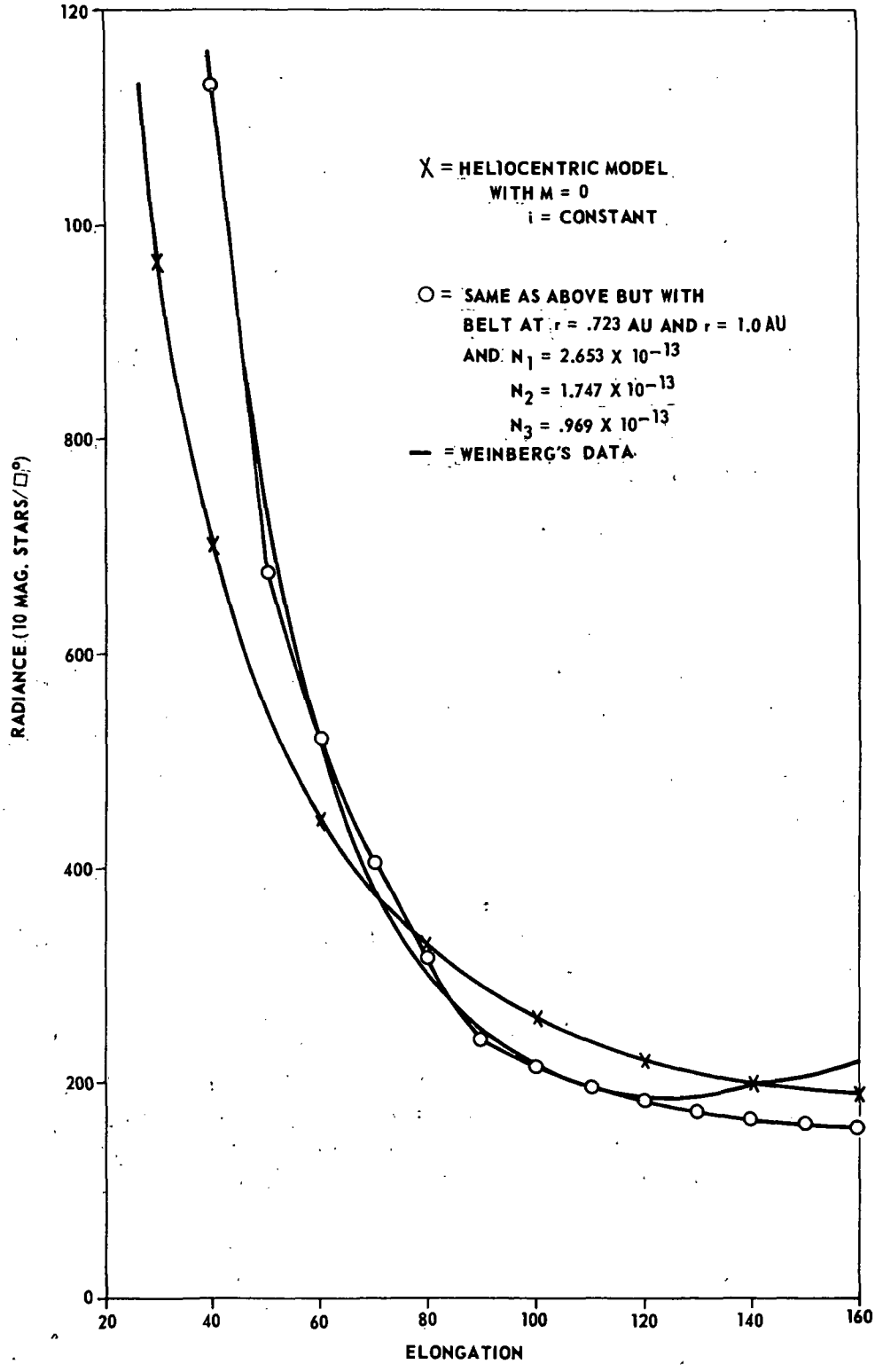

Figure 37. Comparison of a belt model with Weinberg's data.

TABLE 18. COMPARISON OF A BELT MODEL WITH WEINBERG'S DATA

ϵ	Weinberg	A Belt Model
30	2200	1782
40	1130	1130
50	730	678
60	520	520
70	385	404
80	300	315
90	250	240
100	215	217
110	195	199
120	185	185
130	190	174
140	200	166
150	205	160
160	220	156

were empirical and usually fit a particular scattering curve. The advantage of the approximations over exact expressions is easily seen when the labor needed to compute the exact scattering functions is compared to that needed for an approximation. Some of the earlier approximations to scattering functions of particles were those used to explain diffusely scattered light from a planet. As may be expected, no diffraction peaks were included. Figure 38 shows four such functions [2]:

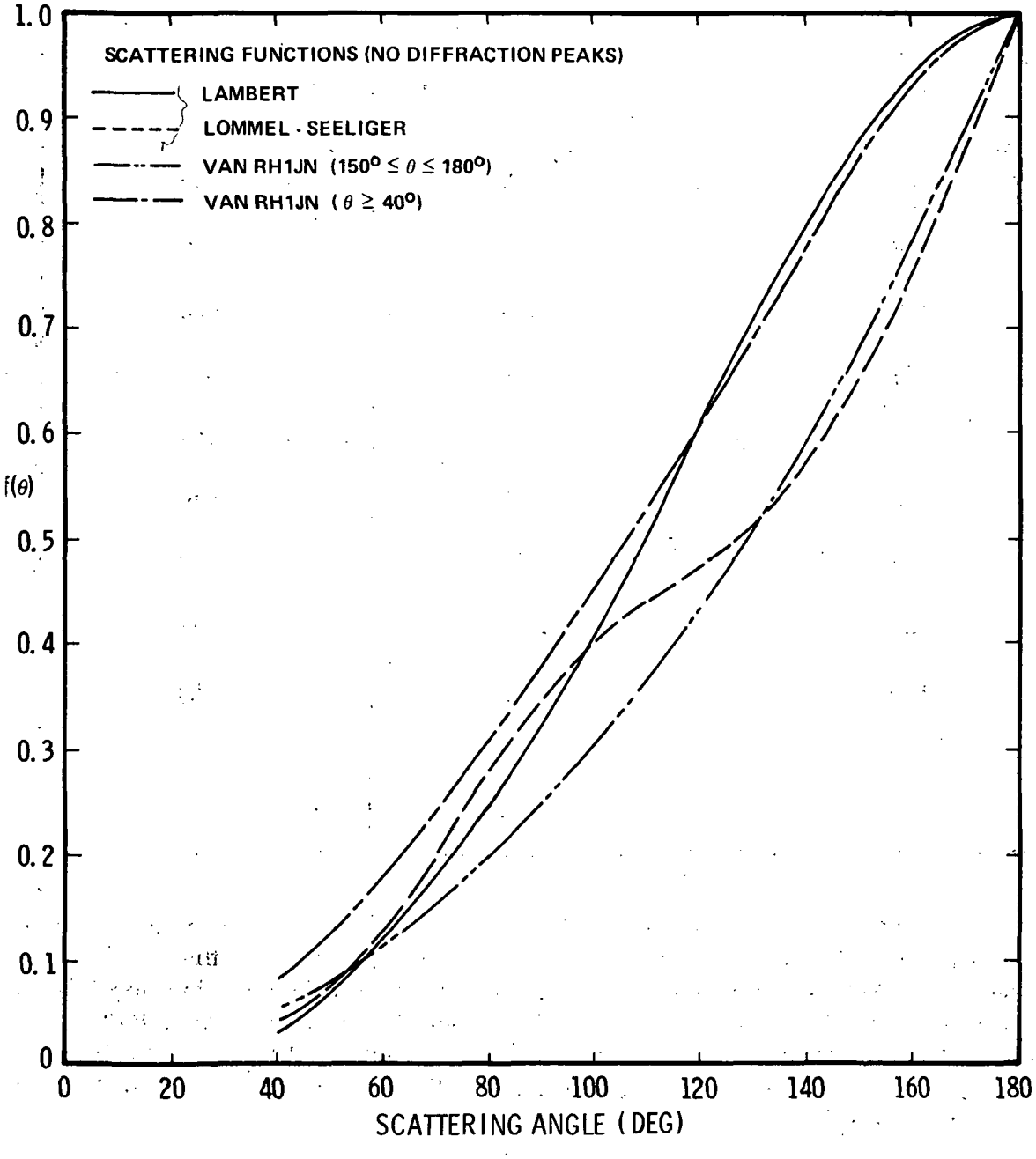

Figure 38. Approximate reflection scattering functions (no diffraction peak).

a. $\dfrac{\sin\Theta - \Theta\cos\Theta}{\pi}$ (Lambert)

b. $1 - \sin\left(\dfrac{\Theta - \pi}{2}\right)\tan\left(\dfrac{\Theta - \pi}{2}\right)\ell n \cot\left(\dfrac{\Theta - \pi}{4}\right)$
(Lommel-Seeliger)

c. $\left(\dfrac{\pi - \alpha}{\pi}\right)^2$ (Van Rhijn)
$150 \leq \Theta \leq 180$ deg

d. $0.655 - 0.711 \sin\Theta - 0.345 \cos\Theta + 0.406 \sin^3\Theta$ (Van Rhijn)
$40 \text{ deg} \leq \Theta$

Van Rhijn found his phase function from a best fit to observed radiance curves for zodiacal light. Lambert's law and the Lommel-Seeliger law have also been applied to such calculations [2].

To explain scattering from interplanetary media at small elongations from the sun, empirical scattering functions are needed which include a diffraction component and a reflection component. Allen [12] proposed that the F corona of the sun is due to diffraction on interplanetary material. He used an approximation to the diffraction function given as

$$\frac{C\,\alpha^2}{2 + \alpha^3 \sin^3\Theta} \tag{153}$$

It is plotted in Figure 39, although it was not intended to be used out to 180 deg. At almost the same time, Van de Hulst [13] also explaining the F corona separated the scattering function into a diffracted and reflected part, using Lambert's law for the reflection term. This separation procedure is valid for large particles. Van de Hulst's function is

$$\frac{J_1^2(\alpha \sin\Theta)}{\alpha^2 \sin^2\Theta} + \frac{\bar{\omega}}{4\pi}$$

where $\bar{\omega}$ is the albedo of the particles. Since the calculations of Van de Hulst represent a simple model of the zodiacal light which incorporates the diffraction effects, it will be considered further in Section F.

Schoenberg [2] used the general formula

$$1 - p\cos\Theta + q\cos^2\Theta \tag{154}$$

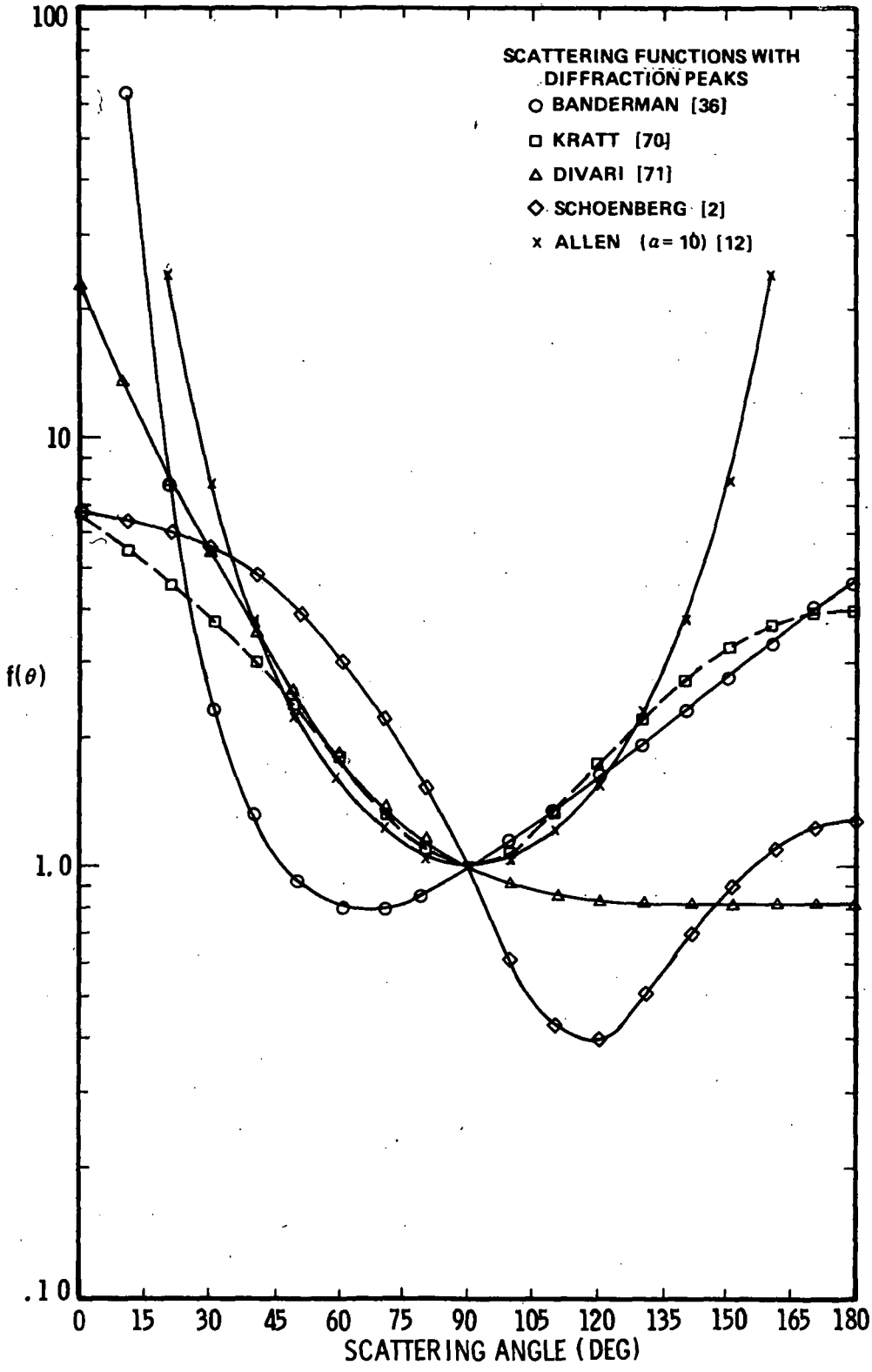

Figure 39a. Approximate scattering functions with a diffraction peak.

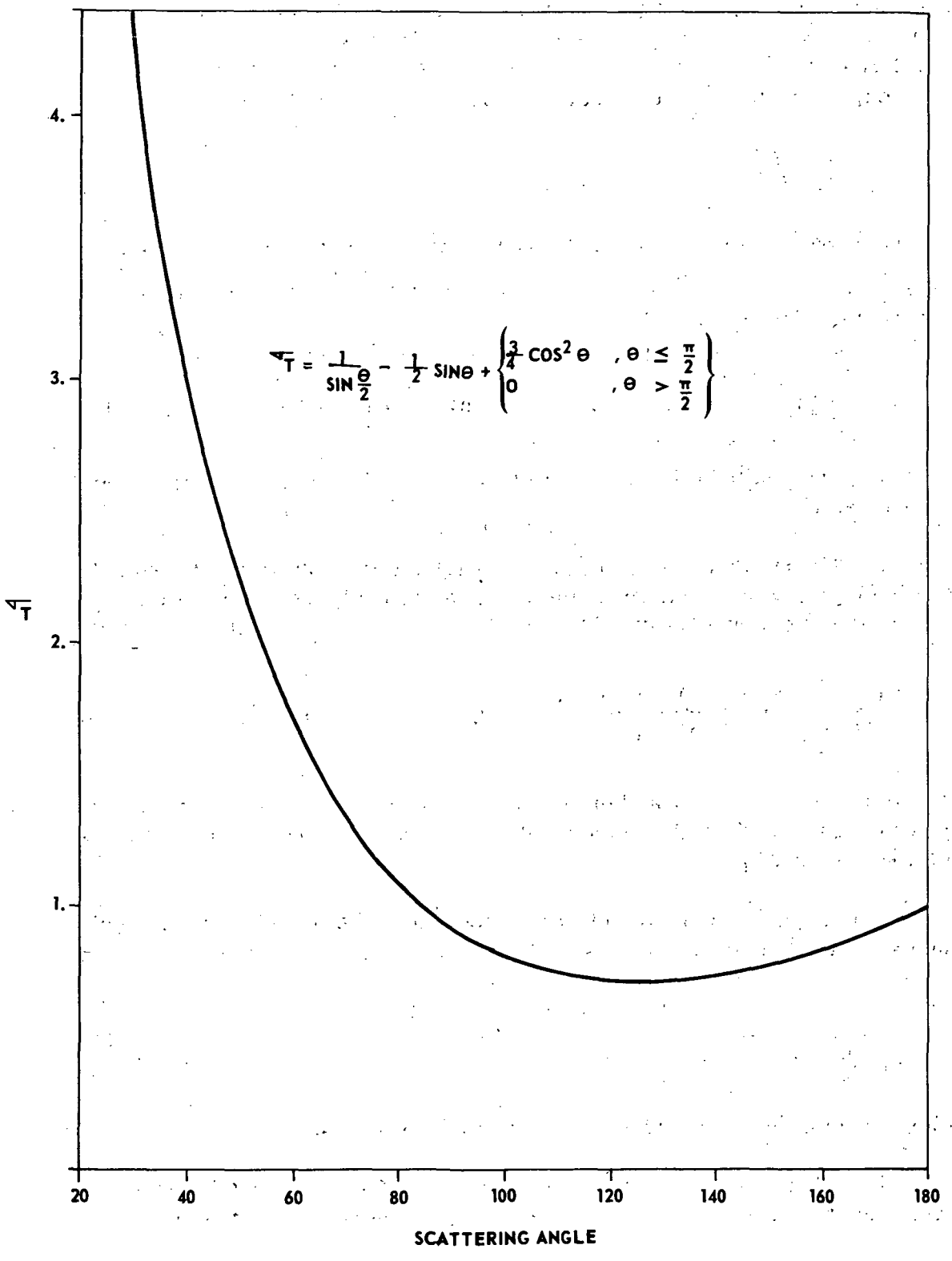

Figure 39b. The scattering functions of Gillett [27].

to characterize the properties of scattering in the atmosphere. He used $p = 2.7$ and $q = 3.0$. With $p = 0$ and $q = 1$, this formula reduces to that needed for a Rayleigh scatterer. To correct for the effects of relatively large particles, V. A. Kratt modified the Schoenberg formula to [70]

$$1 - p(e^{-3\Theta} - e^{-3\pi/2}) + q\cos^2\Theta \quad . \tag{155}$$

This has been further modified for corona, etc., by adding or subtracting terms $\left[\text{e.g., } 1 - p(e^{-3\Theta} - e^{-3\pi/2}) + q\cos^2\Theta + S\,e^{-36\Theta}\right]$ [113]. Divari [71] used the formula

$$\frac{1}{17.9}\left[1 + 22.3\,(e^{-3\Theta} - 0.009) + 0.02\cos^2\Theta\right] \tag{156}$$

to calculate the contribution of a dust cloud around the earth to the radiance of zodiacal light.

Banderman [36], by splitting the scattering function into a diffracted and a reflected component, found that, according to his meteor models, the zodiacal light radiance is given by

$$\frac{0.1}{2\pi}\left[\frac{1 + (1.056)^2}{1 + e^{1.056\pi}}\right] e^{1.056\Theta} + \frac{1}{2}\,(0.14)\,(\Theta\,\pi)^{-3} \quad . \tag{157}$$

The particle albedo is 0.1 and the ratio of the mean particle radius to the mean square of the particle radius is about 0.264. The wavelength used for the calculations was 0.53 μ.

Gillett [27], also attempting to model the zodiacal light for different models of the cloud of interplanetary medium, used as a best fit

$$\frac{1}{\sin\frac{\Theta}{2}} - \frac{1}{2}\sin\Theta + \begin{cases} 3/4\cos^2\Theta & \Theta \le \pi/2 \\ 0 & \Theta > \pi/2 \end{cases} \tag{158}$$

in his constant thickness models (Paragraph E of Section III).

Each function discussed above is plotted in Figure 39 and has been normalized to one at $\Theta = 90$ deg. Apparently, Bandermann's phase function

is the best approximation to the shape of the radiance curve for zodiacal light. Table 19 lists the functions and their authors.

TABLE 19. PHASE FUNCTION APPROXIMATIONS

Author	Function
F. Schoenberg [2]	$1 + p \cos \Theta + q \cos^2 \Theta$
V. A. Kratt [70]	$1 + p(e^{-3\Theta} - e^{-3\pi/2}) + q \cos^2 \Theta$
N. B. Divari [71]	$\frac{1}{17.9} [1 + 22.3 (e^{-3\Theta} - 0.009) + 0.02 \cos^2 \Theta]$
C. W. Allen [12]	$C \alpha^2/(2 + \alpha^3 \sin^3 \Theta)$
H. C. Van de Hulst [13]	$J_1^2 (\alpha \sin \Theta)/\alpha^2 \sin^2 \Theta + \bar{\omega}/4\pi$
L. W. Banderman [36]	$\frac{0.1}{2\pi} \left[\frac{1 + (1.056)^2}{1 + e^{1.056\pi}}\right] e^{1.056\,\Theta} + 0.07\,(\Theta\pi)^{-3}$
F. C. Gillett [27]	$\frac{1}{\sin\frac{\Theta}{2}} + \frac{1}{2} \sin \Theta + \begin{cases} 3/4 \cos^2 \Theta & \Theta \leq \pi/2 \\ 0 & \Theta \geq \pi/2 \end{cases}$
Van Rhijn [2]	$\begin{cases} 0.655 - 0.711 \sin \Theta - 0.345 \cos \Theta + 0.406 \sin^3\Theta \\ \left(\frac{\pi - \Theta}{\pi}\right)^2 \end{cases}$
Lommel-Seeliger [2]	$1 - \sin\left(\frac{\Theta - \pi}{2}\right) \tan\left(\frac{\Theta - \pi}{2}\right) \ln \cot\left(\frac{\Theta - \pi}{4}\right)$
Lambert [2]	$\sin \Theta/\pi - \Theta \cos \Theta/\pi$

Obviously, many approximate scattering functions exist which can be used. For zodiacal light, the most common are given as a sum of a reflected and a diffracted component. Chandrashekhar [114] points out that any phase function can be represented by a series of Legendre polynomials

$$h(\Theta) = \sum_n \omega_n P_n (\cos \Theta) \quad .$$

ω_n is a constant for a given particle size and material. In general, ω_n is a function of α and m. Hunt [72] uses a discrete least-squares method to find the phase function found from Mie theory calculations as a series of Legendre polynomials. Such representations of the phase function were found for both single scattering and scattering from a polydispersion of spherical particles, specifically the haze and cloud models of Diermendjian [115] were used. Hunt's method gives an overall relative error of 10^{-5} for single particles and 10^{-8} for the distributions. It should be noted that phase functions for polydispersed collections of particles are independent of the density of particles due to the normalization constant.

F. Diffraction - Reflection Models [12, 13]

Van de Hulst [37], in a study of zodiacal light in the solar corona, separated the differential cross section into a diffraction component and a reflection component

$$\frac{d\sigma}{d\Omega} = \left(\frac{d\sigma}{d\Omega}\right)_d + \left(\frac{d\sigma}{d\Omega}\right)_r \tag{159}$$

which is a first-order approximation that is valid for particles with a size parameter greater than 5. The first term is the differential scattering caused by forward diffraction of a sphere. It is dependent of the particle surface structure and refractive index. Fraunhofer diffraction gives

$$\left(\frac{d\sigma}{d\Omega}\right)_d = k^2 a^2 \left[\frac{J_1(ka \sin \Theta)}{ka \sin \Theta}\right]^2 \simeq a^2 \frac{J_1^2 (k a \Theta)}{\Theta^2} \quad . \tag{160}$$

The second term is for reflection of a diffusely reflecting sphere (Lambertian),

$$\left(\frac{d\sigma}{d\Omega}\right)_r = \frac{2 a^2 \gamma}{3\pi} (\sin \Theta - \Theta \cos \Theta) \tag{161}$$

which includes an albedo factor γ [13]. The reflection differential cross section is independent of the incident wavelength. These scattering functions are shown in Figure 40 for $\alpha = 10$ and $\gamma = 0.33$ [73].

From the photometric observation of Richter [74, 75], scattering from meteorites of 10^2 to 10^{-1} cm in diameter approximately agrees with Van de Hulst's equation (159). In the range of 10^{-2} cm, little variation of radiance exists with the scattering angle outside the forward diffraction zone. This gives rise to a simpler form for the reflection differential cross section. Assume the total cross section is the geometric cross section:

$$\sigma = \int \left(\frac{d\sigma}{d\Omega}\right) d\Omega = \int \frac{\frac{1}{2}(i_1 + i_2)}{k^2} \quad d\Omega = \pi a^2,$$

then for an isotropic scattering, i.e., $i_1 = i_2 =$ constant,

$$\frac{\frac{1}{2}(i_1 + i_2)}{k^2} \quad 4\pi = \pi a^2;$$

hence, for a sphere of radius a,

$$\frac{d\sigma}{d\Omega} = \frac{1}{2k^2} \quad (i_1 + i_2) = \frac{a^2}{4} \quad .$$

An albedo factor γ is added to give

$$\left(\frac{d\sigma}{d\Omega}\right)_r = \frac{\gamma a^2}{4} \quad , \tag{162}$$

for which Figure 41 displays the total differential cross section. The approximation is also good for metallic spheres [76]. Following Van de Hulst [13] and using equation (33), the radiance for fixed wavelength and particle size is given by

$$L_\lambda = \frac{R\, E_\lambda^e\, \delta\lambda\, N_o\, a^2}{4\epsilon} F(\epsilon)$$

where

$$F(\epsilon) = \frac{\epsilon}{\sin \epsilon} \int_\epsilon^\pi 4\pi \left[\frac{1}{\pi a^2} \frac{d\sigma(\Theta)}{d\Omega}\right] d\Theta = \frac{4\epsilon}{a^2 \sin \epsilon} \int_\epsilon^\pi \left(\frac{d\sigma}{d\Omega}\right) d\Theta \quad , \tag{163}$$

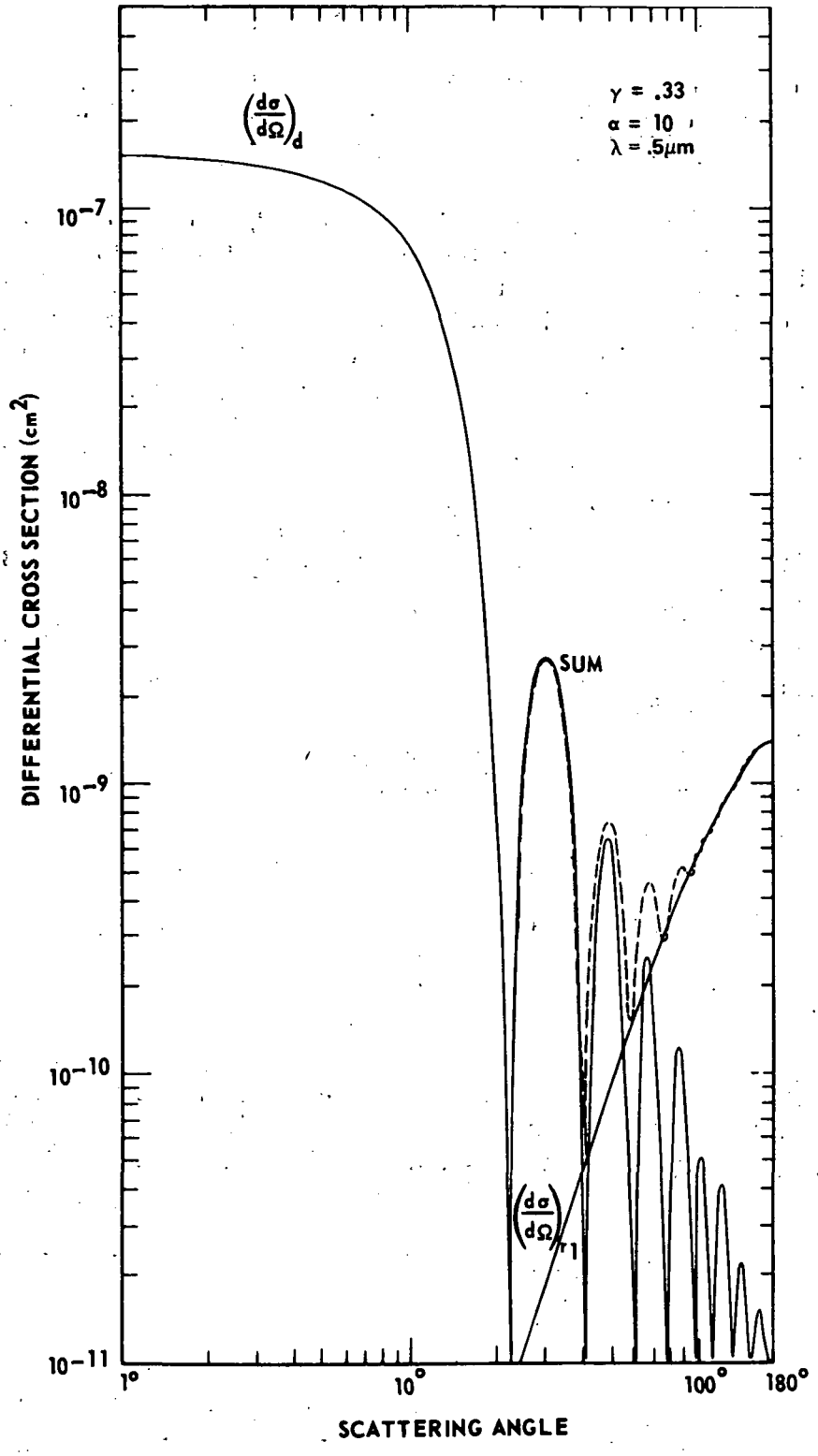

Figure 40. The differential cross section for a Lambertian sphere, the forward diffraction peak for a sphere, and the sum (α = 10, λ = 0.5 μm, γ = 0.33).

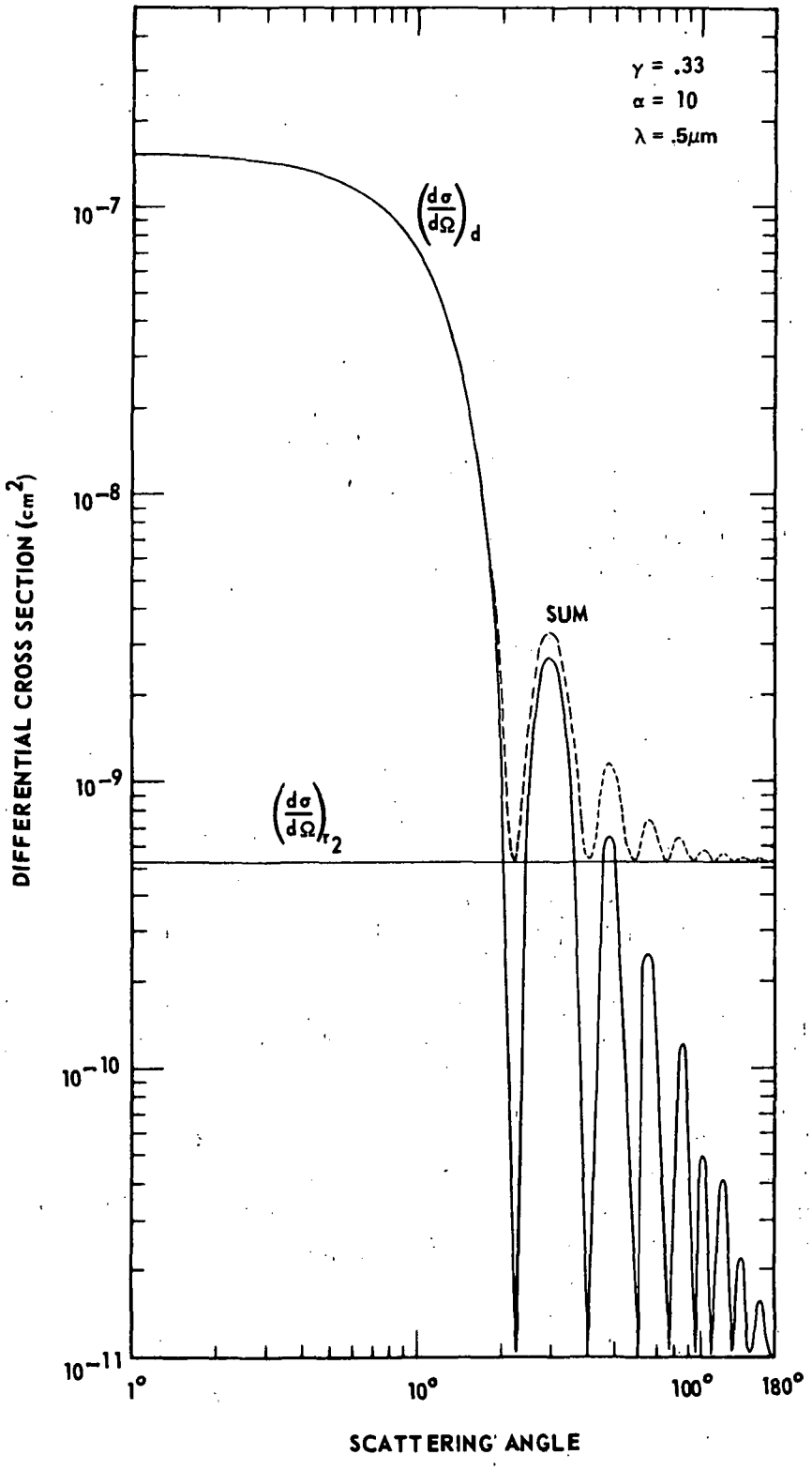

Figure 41. The differential cross section for an isotropic scatterer, the the forward diffraction peak for a sphere, and their sum ($\alpha = 10, \lambda = 0.5\ \mu m, \gamma = 0.33$).

and where the particle distribution has an r^{-1} radial dependence. For isotropic scatterers with $\gamma = 1$, the reflection part becomes

$$F_r(\epsilon) = \frac{\epsilon(\pi - \epsilon)}{\sin \epsilon} \quad , \tag{164}$$

which is approximately constant, varying from $\pi^2/4$ at $\epsilon = \pi/2$ to 0 at $\epsilon = 0$ or π. For the Lambertian function,

$$F_r(\epsilon) = \gamma \frac{\epsilon}{\sin \epsilon} \frac{8}{3\pi} (2 + 2 \cos \epsilon + \epsilon \sin \epsilon) \quad . \tag{165}$$

Both forms of the reflection functions remain relatively constant, giving radiance an ϵ^{-1} dependence.

For the diffraction component, Van de Hulst obtained

$$F_d(\epsilon) = ka\, \psi\, (ka\, \epsilon) \quad , \tag{166}$$

where

$$\psi(z) = \int_z^\infty \left(\frac{2\, J_1\, (z)}{z}\right)^2 dz \quad . \tag{167}$$

Since the diffraction term is only accurate for small values of Θ, the factor $\epsilon/\sin \epsilon$ has been omitted and the range of integration has been extended to ∞. The values of $\psi(z)$ are given in Table 20.

For large values of z, $\psi(z)$ fluctuates around $2/\pi z^2$ [77]. The radiance diffracted by large particles is therefore proportional to ϵ^{-3}. The values of $F_d(\epsilon)$ calculated by Van de Hulst [13] are shown in Figure 42. The radiance variation can be divided into three regions.

Region	Radiance Dependence		
I	ϵ^{-1}	F_d	
II	ϵ^{-3}	F_d	
III	ϵ^{-1}	F_r	(Lambertian)

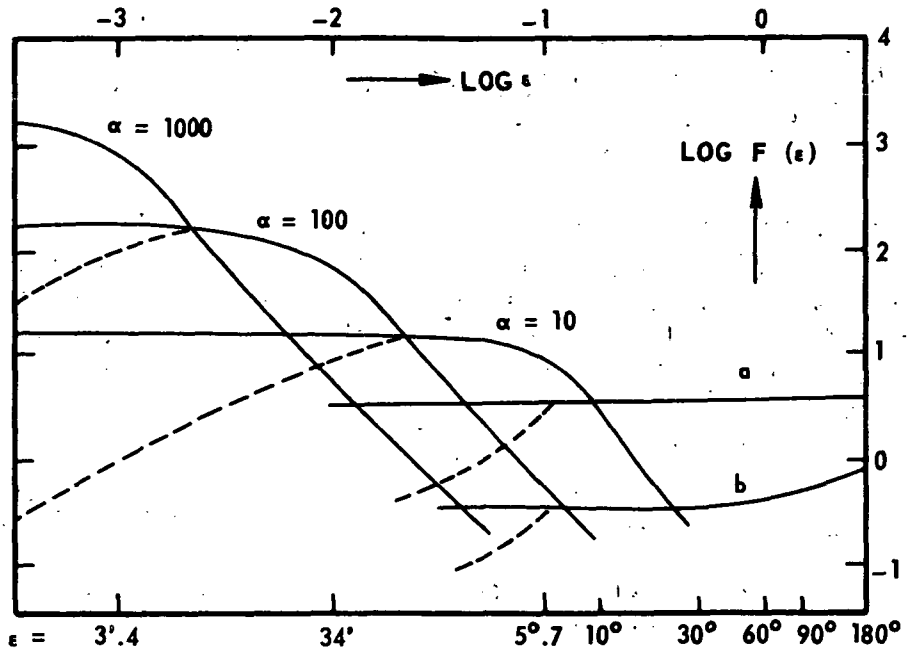

Figure 42. The scattering dependence $F_d(\epsilon)$ for diffraction of spherical particles for α = 10, 100, and 1000 {curves (a) and (b) are for a isotropic scatterer and a Lambertian sphere (γ = 0.1), respectively [13]}.

TABLE 20. $\psi(z)$ VALUES

z	$\psi(z)$	z	$\psi(z)$
0	1.698 = 16/3 π	6	0.0156
1	0.779	7	0.0127
2	0.225	8	0.0112
3	0.055	9	0.0074
4	0.040	10	0.0061
5	0.030		

Comparison with Weinberg's data is given in Table 21 and Figure 43 for N_o established at $\epsilon = 140$ deg and for $\alpha = 1$; 10, and 100. Although using $\alpha = 1$ for the diffraction peak is unrealistic, it gives the best fit and also gives an indication of the form of $d\sigma/d\Omega$.

As early as 1893, Searle, in modeling the zodiacal light by a dust cloud, used various simple scattering functions and a density distribution proportional to a constant or 1/r. It is interesting to compare his and Van de Hulst's results, although Searle's models do not include the diffraction contribution which originated with Van de Hulst's work.

Searle's models are:

Model	Scattering Function Form	Spatial Distribution Form
I	$\sin\Theta - \Theta\cos\Theta$ (Lambertian)	Constant
II	$1 - \cos\Theta$	Constant
III	$1 - \cos\Theta$	1/r
IV	Θ	Constant
V	Θ	1/r
VI	Θ^2	1/r

The scattering distributions reflect observations made of the asteroid scattering functions. Searle's [1] results of the normalized values are shown in Table 22. It is worthwhile to quote this early work:

> "A remark obviously suggested by the inspection of Table XXVII [Table 22 in this report] is that for small values of ϵ the hypothesis relating to the density of the meteoric matter is more important than that relating to the phases of the separate particles, while for large values of ϵ this last hypothesis chiefly determines the result. Compare, for example, the values derived from Formulas III and V, both of which assume the density to vary inversely to r. For small values of ϵ, these values are practically the same, although in the first case the projection of the illuminated surface, and in the second that surface itself, is assumed to represent the quantity of light reflected. Even when we employ the

TABLE 21. DIFFRACTION MODEL CALCULATIONS

ϵ	Weinberg	$F_r(\gamma = 0.1)$	$F_d(\alpha = 1.0)$	$F_d(\alpha = 10)$	$F_d(\alpha = 100)$	L(1)	L(10)	L(100)
10		0.34093	1.7382	3.2064	0.2216	8319	15 006	2394
20		0.34642	1.5668	0.4067	0.0505	3827	1 593	844
30	2200	0.35501	1.4005	0.2579	0.0228	2341	864	536
40	1130	0.36700	1.2417	0.1242	0.0124	1609	519	404
50	730	0.38235	0.7715	0.0771	0.0077	923	389	332
60	520	0.40100	0.5160	0.0516	0.0052	611	319	287
70	385	0.42291	0.3620	0.0362	0.0036	449	277	259
80	300	0.44797	0.2620	0.0262	0.0026	355	251	240
90	250	0.47611	0.1935	0.0194	0.0019	297	233	226
100	215	0.50719	0.1445	0.0144	0.0014	261	221	216
110	195	0.54108	0.1082	0.0108	0.0011	236	212	210
120	185	0.57762	0.0806	0.0080	0.0008	219	206	205
130	190	0.61659	0.0592	0.0059	0.0006	208	202	202
140	200	0.65777	0.0421	0.0042	0.0004	200	200	200
150	205	0.70086	0.0284	0.0028	0.0003	194	198	199
160	220	0.74552	0.0171	0.0017	0.0002	191	198	198
170	240	0.79133	0.0078	0.0007	0.0001	188	197	198
180	260	0.83776	0.0000	0.0000	0.0000	186	197	198
$N_o = 1.764 \cdot 10^{-11}$			$1.866 \cdot 10^{-13}$		$1.876 \cdot 10^{-15}$			

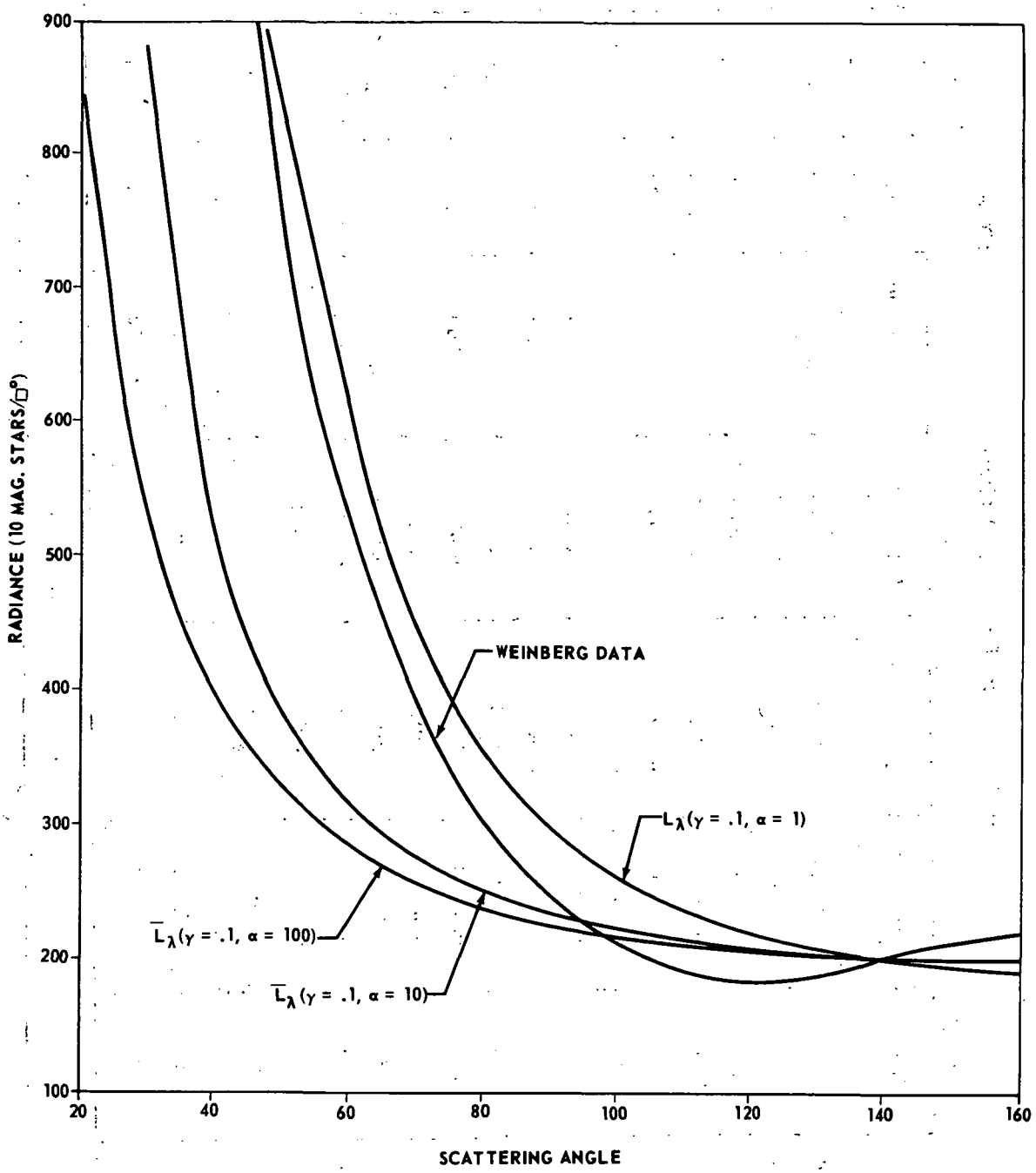

Figure 43. Comparision of diffraction model with Weinberg's data for albedo of $\gamma = 0.1$ and $\alpha = 1$, 10, and 100.

TABLE 22. COMPARISON OF HYPOTHESES [1]

ϵ (deg)	Formula I		Formula II		Formula III		Formula IV		Formula V		Formula VI	
	Light	Magn.	Light	Magn.	Light	Magn.	Light	Magn.	Light	Magn.	Light	Magn.
10	21.8	6.65	7.28	7.84	66.32	5.45	9.018	7.61	66.290	5.45	39.444	6.01
20	7.7	7.78	4.50	8.37	17.08	6.92	4.527	8.36	17.021	6.92	10.162	7.48
30	4.3	8.42	3.12	8.76	7.96	7.75	3.054	8.79	7.882	7.76	4.743	8.31
40	2.9	8.84	2.40	9.05	4.78	8.30	2.323	9.08	4.674	8.33	2.851	8.86
50	2.2	9.14	1.98	9.26	3.30	8.70	1.897	9.31	3.193	8.74	1.981	9.26
60	1.8	9.36	1.71	9.42	2.50	9.01	1.612	9.48	2.376	9.06	1.514	9.55
70	1.5	9.56	1.52	9.55	2.02	9.24	1.419	9.62	1.889	9.31	1.239	9.77
80	1.32	9.70	1.39	9.64	1.70	9.42	1.280	9.73	1.575	9.51	1.065	9.93
90	1.22	9.78	1.28	9.73	1.50	9.56	1.178	9.82	1.363	9.66	0.958	10.04
100	1.16	9.84	1.21	9.79	1.36	9.67	1.103	9.89	1.217	9.79	0.888	10.13
110	1.09	9.91	1.15	9.85	1.24	9.77	1.047	9.95	1.114	9.88	0.847	10.18
120	1.05	9.95	1.10	9.90	1.16	9.84	1.008	9.99	1.043	9.96	0.824	10.21
130	1.03	9.97	1.07	9.93	1.10	9.90	0.981	10.02	0.993	10.01	0.818	10.22
140	1.02	9.98	1.04	9.96	1.06	9.94	0.965	10.04	0.966	10.04	0.827	10.20
150	1.01	9.99	1.02	9.98	1.04	9.96	0.960	10.04	0.953	10.05	0.850	10.18
160	1.00	10.00	1.01	9.99	1.02	9.98	0.964	10.04	0.955	10.05	0.885	10.13
170	1.00	10.00	1.00	10.00	1.00	10.00	0.977	10.02	0.970	10.03	0.934	10.07
180	1.00	10.00	1.00	10.00	1.00	10.00	1.000	10.00	1.000	10.00	1.000	10.00

very forced hypothesis of Formula VI respecting the effect of small phases but retain the same hypothesis respecting density, we reduce the light only by half a magnitude. On the other hand, for the same small values of ϵ, Formulas II and IV, in which the hypothesis of uniform density is adopted, agree with each other and disagree with the remaining formulas. But for large values of ϵ, according to the respective hypotheses adopted for the phases of the particles, the first three formulas agree with each other and disagree with Formulas IV, V, and VI, in which the minimum of light occurs before opposition is reached, while the light at opposition becomes equal to that at an elongation of agout 85 deg to about 125 deg."

"All the formulas agree in representing fairly well the rapid diminution in brightness of the zodiacal light at small elongations and its much slighter subsequent changes, while the fourth and fifth formulas show that a representation of the phenomenon of gegenschein can be theoretically obtained even when the hypothesis respecting the phases requires very moderate assumptions, as will appear more clearly below. Upon the whole, the fifth formula best expresses the observed facts; the sixth unduly magnifies the relative amount of light at opposition, although so faint a gegenschein as that indicated by the fifth formula would possibly never be discovered."

This early work describes the important features of a model and shows how relatively simple models can depict the dominant effects on the zodiacal radiance.

Roosen [31, 66, 67] employs a reflection model for the scattering functions to predict the radiance of the gegenschein. Roosen was able to fit Weinberg's observations of the gegenschein by using a 0.023 mag/deg phase function and a spatial distribution corresponding to that for asteroids (Fig. 44a). He concludes from the observed lack of effect from the earth's shadow on illumination of the gegenschein that a spatial distribution of particles which follows an inverse power law cannot satisfactorily explain the gegenschein (Figs. 44b and 44c) and that there must be an increase in the spatial density outside the earth's orbit. He suggests the asteroid belt is the source for this material. The spatial distribution of asteroids gives support to this argument. Recent observations at 500 nm from OSO-6 [116] show, based on a preliminary calibration, a gradient for the gegenschein radiance which is in accord with Roosen's data (Fig. 44d).

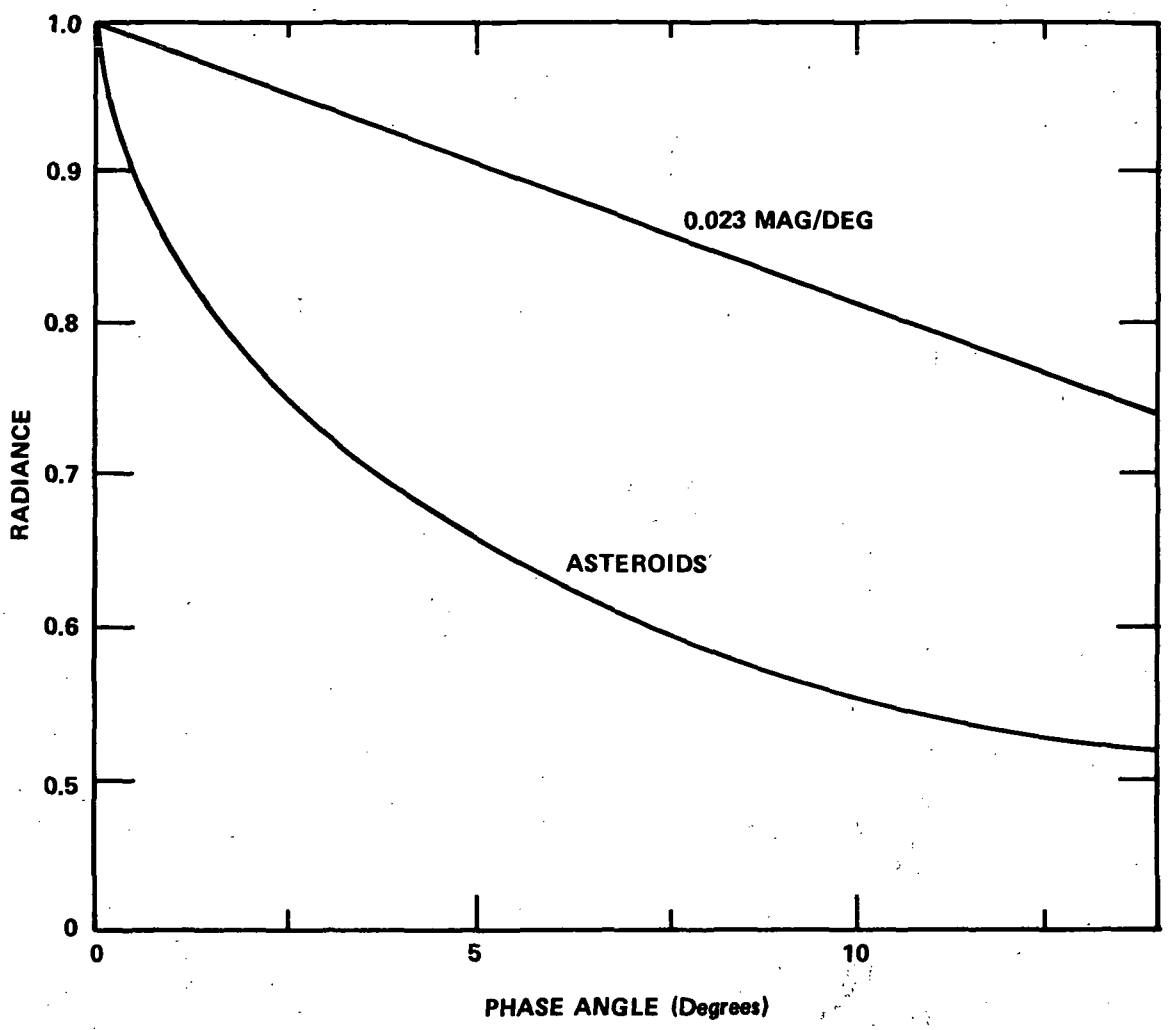

Figure 44a. The asteroidal phase function determined by Gehrels [78] showing the opposition effect. The phase function with the opposition effect removed [66, 67, 79].

G. Polarization - Empirical

The basic heliocentric models have been used with a simple scattering intensity function and therefore exhibited no polarization. In this section we consider the experimental investigations of Richter [14, 74, 75] on the polarization from single particle scattering and distributions of particles. An investigation on the polarization attributed to several particle sizes and materials will give an indication of the material and particle-size distribution of the interplanetary dust.

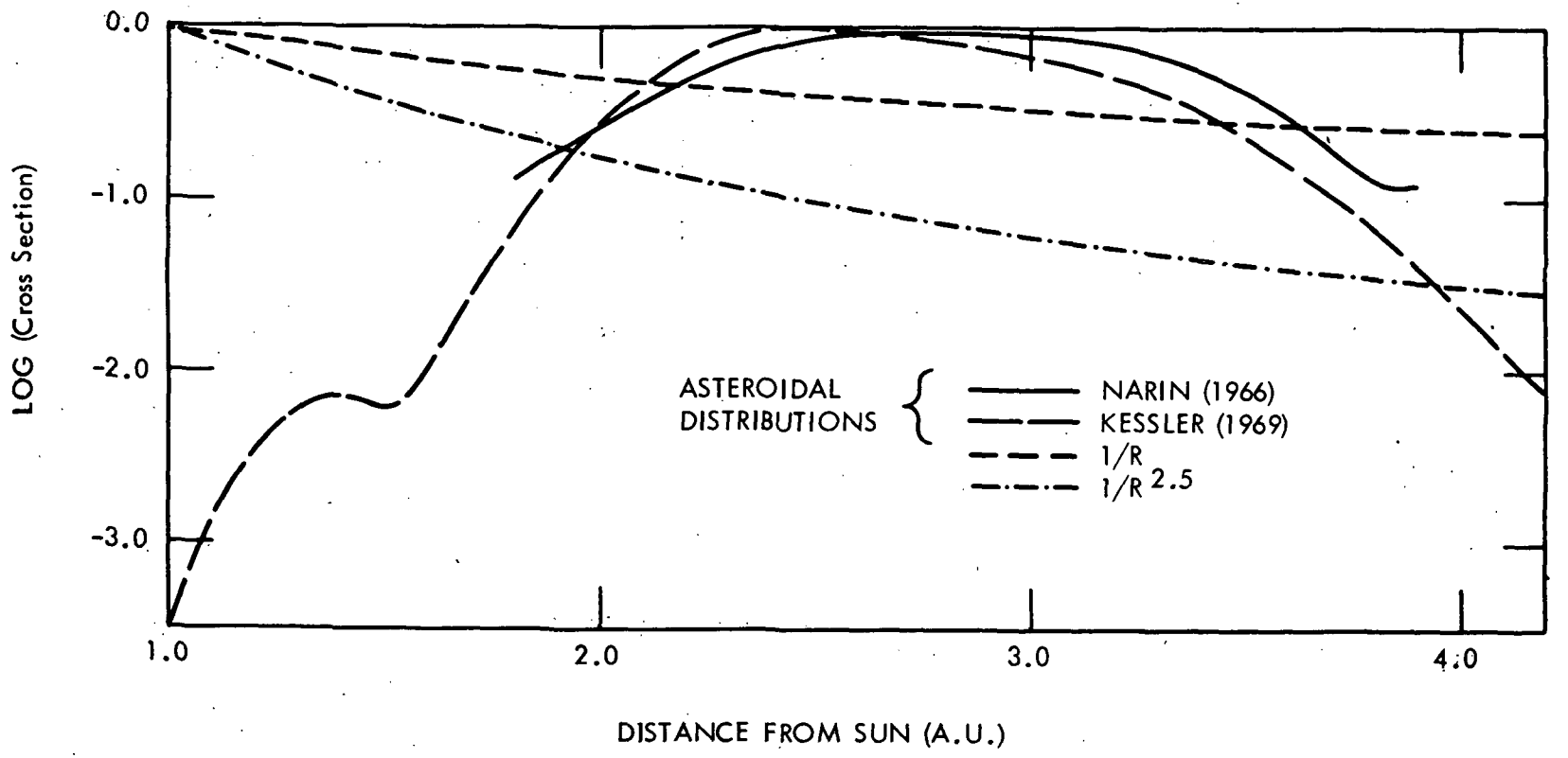

Figure 44b. Spatial distribution of numbered asteroids determined by Narin and corrected for selection effects by Kessler. (Also shown are curves for distributions following inverse power laws R^{-1} and $R^{-2.5}$.) [66]

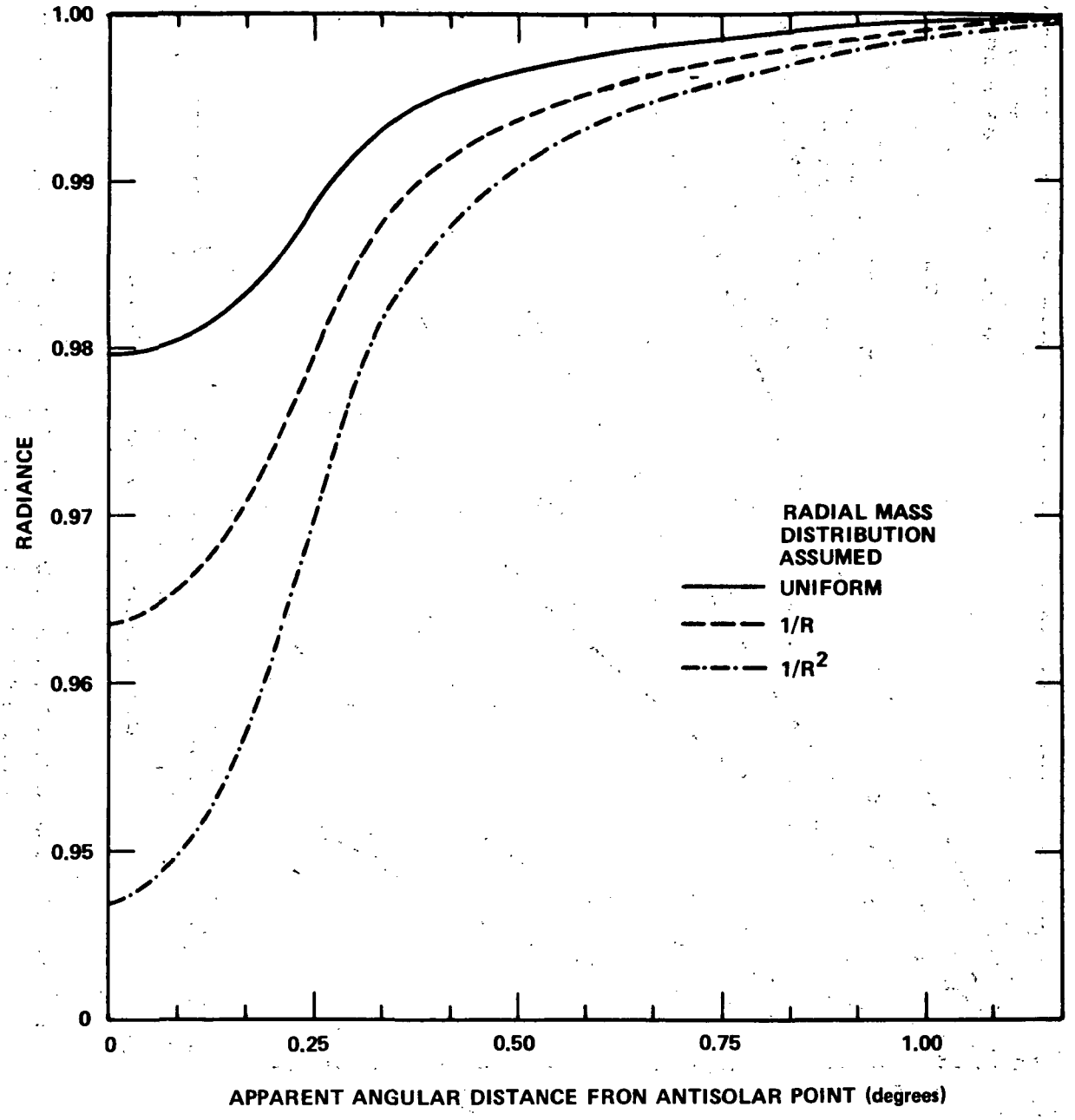

Figure 44c. Gegenschein brightnesses for models assuming the material is distributed according to an inverse power law R^{-m} (where R is the heliocentric distance) for an isotropic phase function [66, 67, 79].

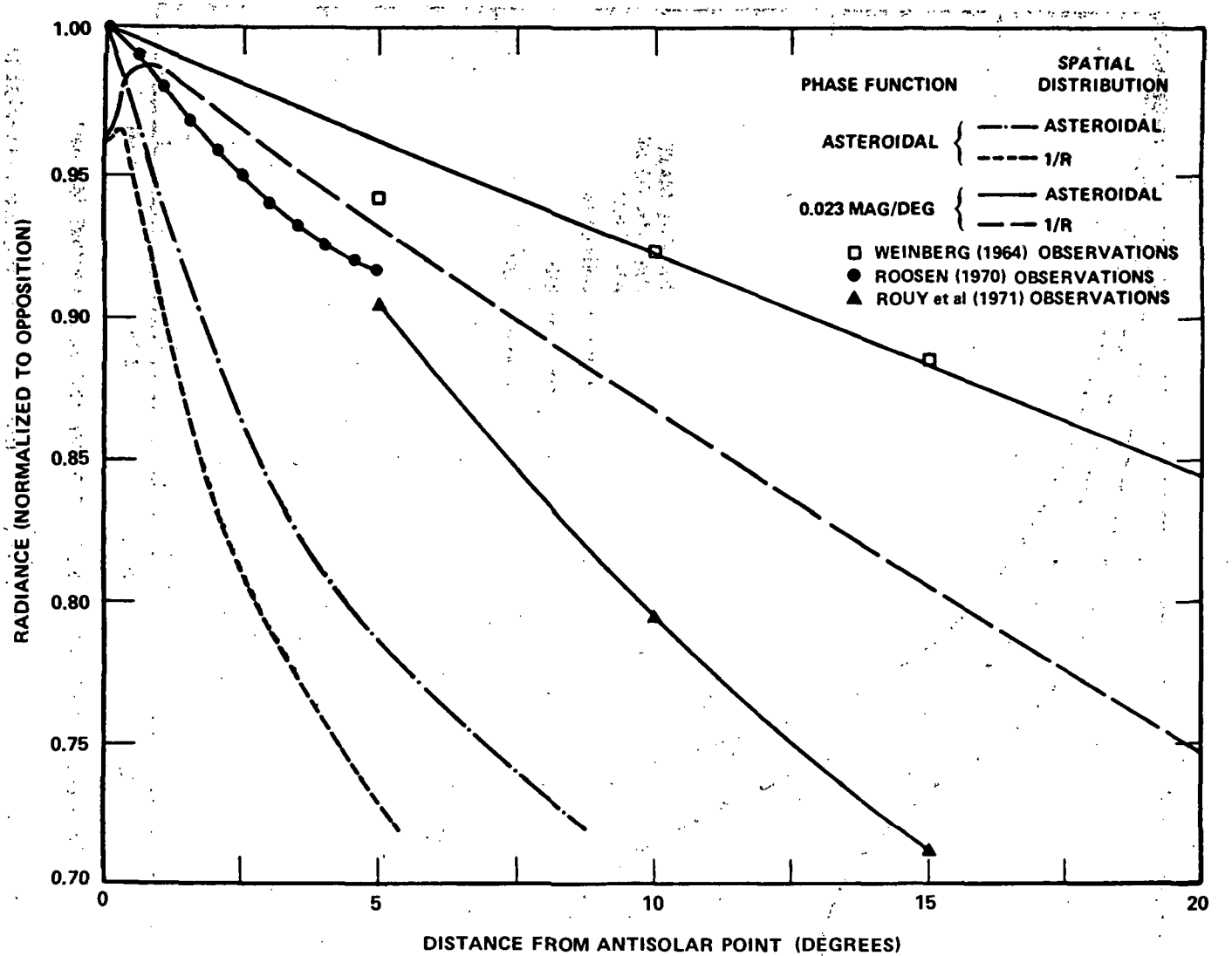

Figure 44d. Brightness of the gegenschein as calculated using different phase functions and as found by three observers [66, 116].

To introduce polarization in simple zodiacal light models, Ingham [53] used diffraction scattering and the empirical form

$$p(\Theta) = \frac{\sin^2\Theta}{q - \sin^2(\Theta)} \tag{168}$$

for the degree of polarization. q is a constant depending on the nature of the material. Figure 45 plots $p(\Theta)$ versus the scattering angle Θ for q = 3, 4, 5, 6, and 11. Note that $p(\Theta)$ given by equation (168) is symmetric around Θ = 90 deg and that the maximum value of polarization is given by

$$\max p(\Theta) = p(\Theta = 90 \text{ deg}) = \frac{1}{q-1} .$$

An inversion gives:

$$q = 1 + \frac{1}{p(\Theta = 90 \text{ deg})} .$$

The justification for assuming a form such as this results from the laboratory studies of Richter [74, 75, 80] and Kloverstrom and Rense [73] on photometric properties of meteorites.

Figures 46 and 47 show a portion of Richter's results. In Figure 46a, radiance dependence on scattering angle is shown for pulverized iron, graphite, and quartz dust in the $\simeq$ 1- to 10-μm size range. The size distributions were roughly Gaussian. The modes are indicated in Figures 47a, b, and c which show the variation of polarization with angle. According to Little [86], Richter's results show that dielectric and metallic powders differ from one another in the observed radiance (directly related to the scattering intensity function). The radiance of the dielectrics decreased more or less smoothly to Θ = 140 deg and then rose again slightly toward 180 deg; the metallic variation declined to about 100 deg, rose to a secondary maximum near 150 deg, and then declined toward 180 deg. The polarization curves of iron and quartz powder are similar in that both rise to a flat maximum not exceeding 20 percent near Θ = 90 deg (Fig. 47), giving experimental foundation for Ingham's polarization function. Quartz powder polarization differs from the iron powder since the maximum is shifted towards larger values of Θ (Fig. 47b). Graphite dust shows a difference in that the observed polarization attains a maximum of 30 percent near 55 deg.

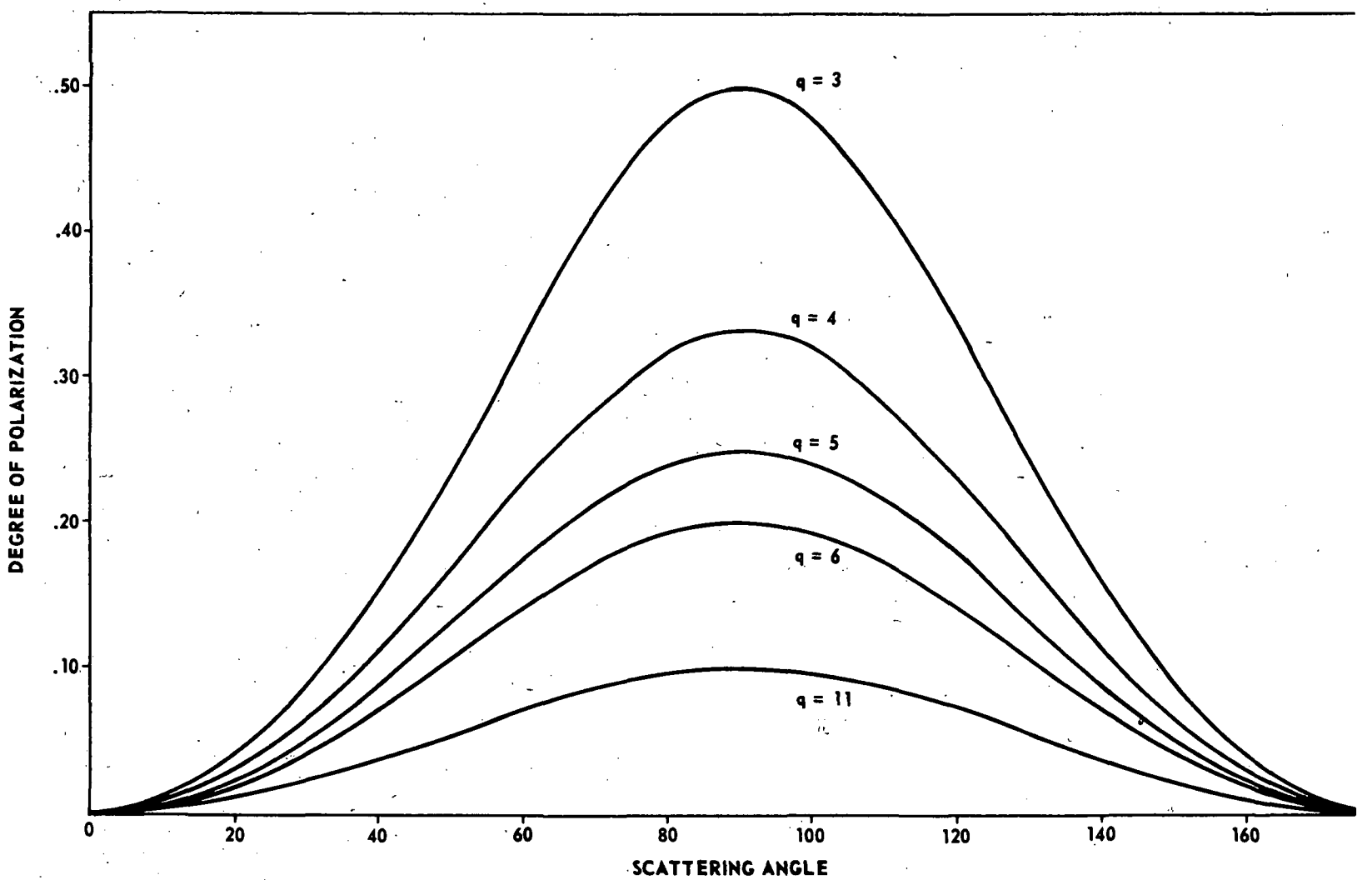

Figure 45. The degree of polarization predicted by Ingham's empirical form for q = 3, 4, 5, 6, and 11.

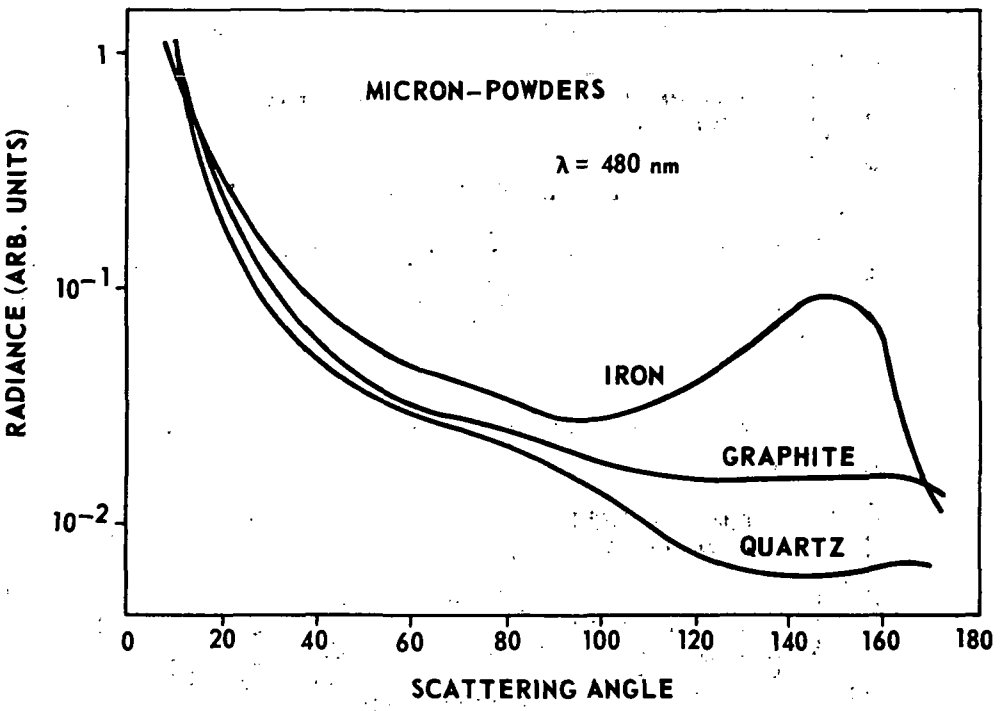

Figure 46a. Radiance of powders with micron-size particles for iron, graphite, and quartz [80].

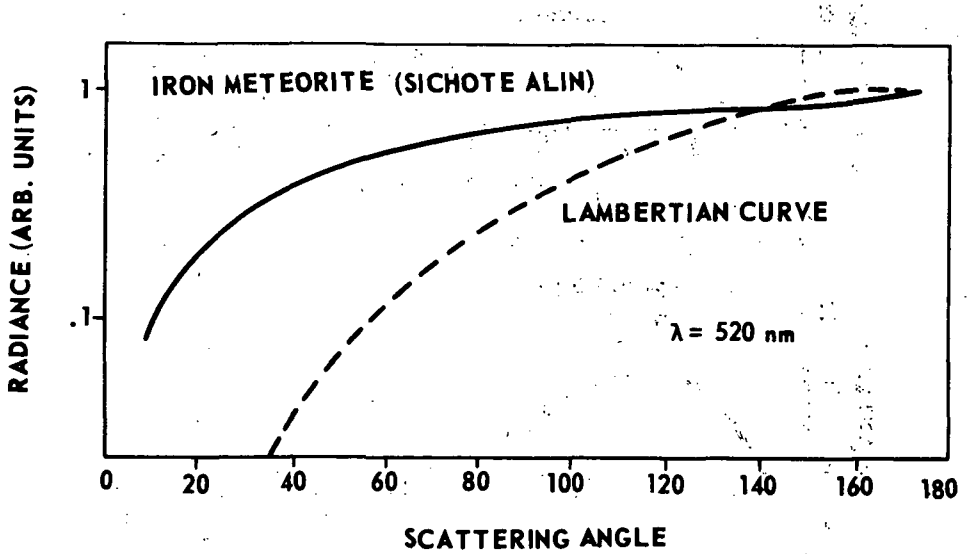

Figure 46b. Radiance of 6-cm iron meteorite compared with the Lambertian curve [75].

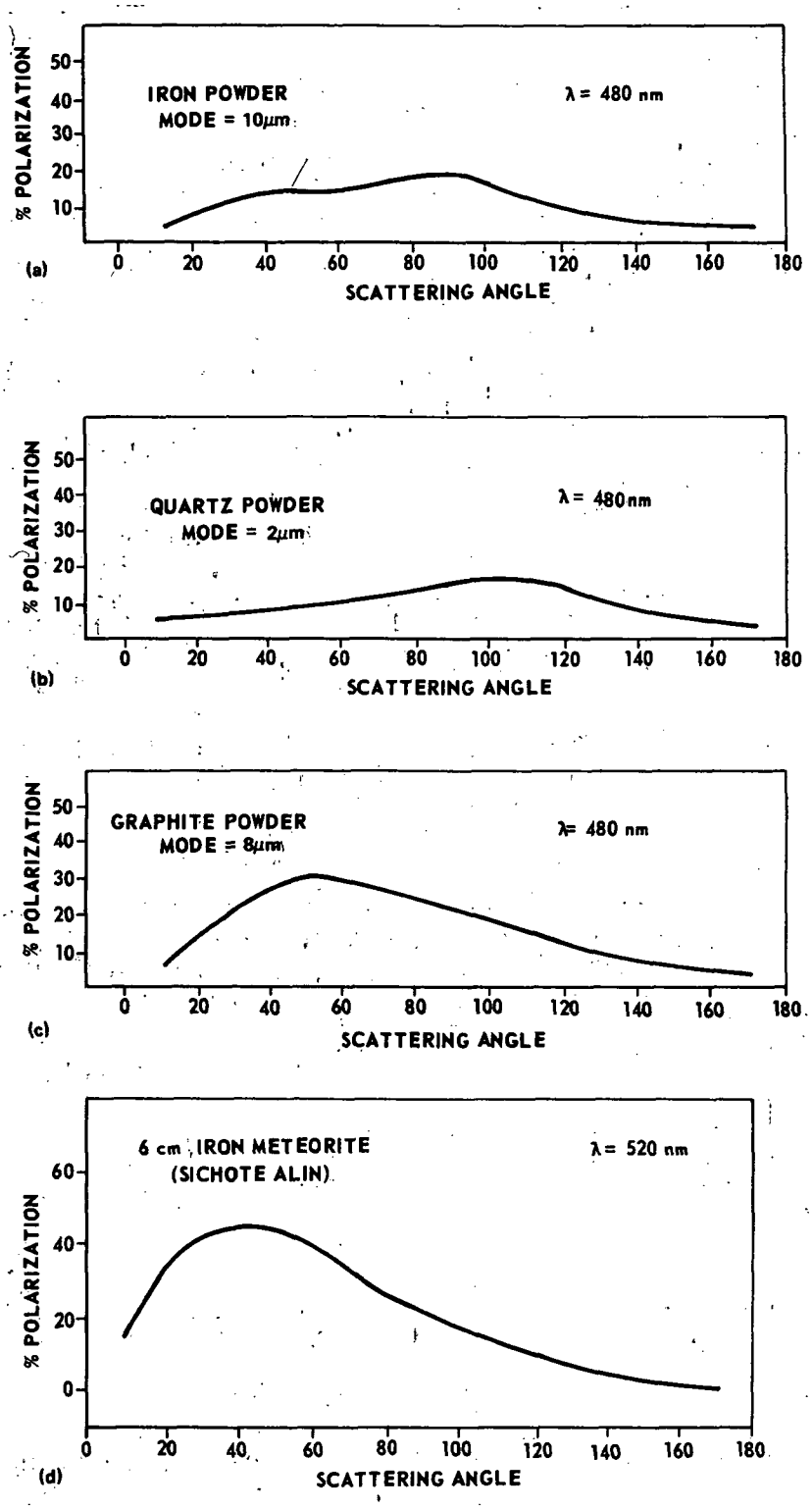

Figure 47. Percent polarization of powders and of a 6-cm iron meteorite for Figure 46 [75, 80].

Mie theory (spherical particles) can be used to match the radiance and polarization of the irregular bodies of the powder studied by Richter. The results [86] indicate that dielectrics with a small imaginary component in the refractive index in the Mie theory can represent Richter's data, although the radiance and polarization of the powder in Richter's data were not reproduced by Mie theory.

In Figures 46b and 47b, the observed radiance and polarization for a 6-cm iron meteorite is given for comparison with that from the micron powders. The radiance does not show the diffraction peak but only the reflection component. The 47-percent polarization maximum occurs near 40 deg. In general, the stony meteorites have a smaller radiance and polarization than metallic meteorites [74, 75]. For submicron particles, Rayleigh's theory can be applied.

Following Ingham [53], the heliocentric model is used with an isotropic scattering function:

$$\frac{i_1 + i_2}{2} = \frac{\gamma \alpha^2}{4}$$

and an empirical polarization function

$$p(\Theta) = \frac{i_1 - i_2}{i_1 + i_2} = \sin^2\Theta / (q - \sin^2\Theta) \quad .$$

Hence,

$$i_1 - i_2 = \frac{\gamma \alpha^2}{2} \left(\frac{\sin^2\Theta}{q - \sin^2\Theta} \right) \quad .$$

By equation (52), one has (in the ecliptic) the zodiacal light polarization as

$$\overline{P}_\lambda = \frac{c}{2 \overline{L}_\lambda \sin^{m+1} \epsilon} \int_\epsilon^\pi \sin^m \Theta \, \overline{g}(\Theta) \, d\Theta$$

where

$$\overline{g}(\Theta) = \int_{\alpha_{min}}^{\alpha_{max}} [i_1(\Theta, \alpha) - i_2(\Theta, \alpha)] \frac{n(\alpha)}{k^2} d\alpha$$

$$\overline{L}_\lambda(\epsilon) = \frac{C}{\sin^{m+1}\epsilon} \int_\epsilon^\pi \sin^m\Theta \overline{\frac{d\sigma}{d\Omega}} d\Theta$$

$$\overline{\frac{d\sigma}{d\Omega}} = \int_{\alpha_{min}}^{\alpha_{max}} (i_1(\Theta, \alpha) + i_2(\Theta, \alpha)) \frac{n(\alpha)}{2k^2} d\alpha \quad .$$

Now, assuming $n(\alpha) = \alpha^{-p}$, the polarization of the zodiacal light is expressed by

$$\overline{P}_\lambda(\epsilon) = \frac{\int_\epsilon^\pi \frac{\sin^{2+m}}{q - \sin^2\Theta} d\Theta}{\int_\epsilon^\pi \sin^m\Theta \, d\Theta} \tag{169}$$

with

$$\overline{L}_\lambda(\epsilon) = \frac{\gamma C \lambda^2}{16 \pi^2 \sin^{m+1}\epsilon} \int_\epsilon^\pi d\Theta \sin^m\Theta \int_{\alpha_{min}}^{\alpha_{max}} \alpha^{2-p} d\alpha \quad . \tag{170}$$

Ingham's results for m = 1 q = 3.2 and m = 3/2 q = 3.3 for $p(\Theta)$ and $\overline{p(\epsilon)}$ are given in Table 23. Figure 48 gives the degree of polarization versus elongation for q = 3, 4, and 5 for three values of m(0, 1, 2). Ingham's choice of q was arrived at by maintaining the electron density derived by Blackwell and Ingham [9, 10, 11] and Giese [26]. The q's give values of P(90 deg) which are higher than any $P(\Theta)$ measured by Richter for freely suspended particles. Dollfus [81], however, measures a maximum polarization greater than this at angles greater than 90 deg. However, the powders of Dollfus were spread on a surface and were not freely suspended.

TABLE 23. INGHAM'S POLARIZATION RESULTS FOR THE ISOTROPIC SCATTERS [53]

ϵ	$p(\Theta) = \frac{\sin^2\Theta}{q - \sin^2\Theta}$		$\overline{P(\epsilon)}$	$\overline{P(\epsilon)}$
	$q = 3.2$	$q = 3.3$	$m = 1,\ q = 3.2$	$m = 3/2,\ q = 3.3$
0	0.000	0.000	0.279	0.290
10	0.009	0.009	0.281	0.290
20	0.038	0.037	0.287	0.295
30	0.085	0.082	0.296	0.300
40	0.148	0.143	0.306	0.309
50	0.225	0.216	0.315	0.317
60	0.306	0.294	0.320	0.324
70	0.381	0.365	0.317	0.324
80	0.435	0.416	0.303	0.312
90	0.455	0.435	0.279	0.290
100	0.435	0.416	0.246	0.255
110	0.381	0.365	0.203	0.213
120	0.306	0.294	0.159	0.169
130	0.225	0.216	0.115	0.123
140	0.148	0.143	0.076	0.082
150	0.085	0.082	0.045	0.051
160	0.038	0.037	0.018	0.029
170	0.009	0.009	0.007	0.003
180	0.000	0.000	0.000	0.000

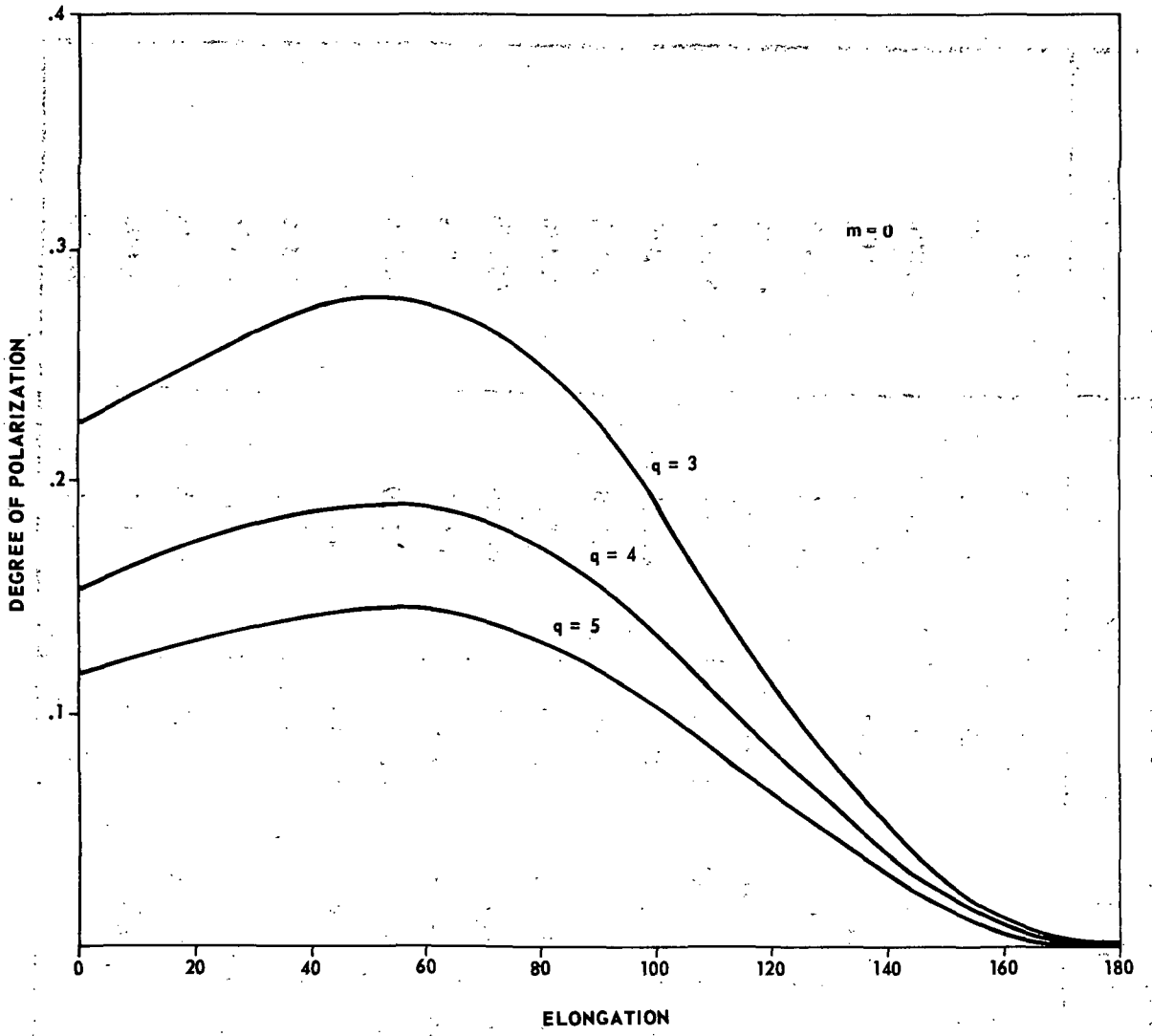

Figure 48. The degree of polarization for the zodiacal light for Ingham's empirical model for q = 3, 4, and 5 and m = 0, 1, and 2.

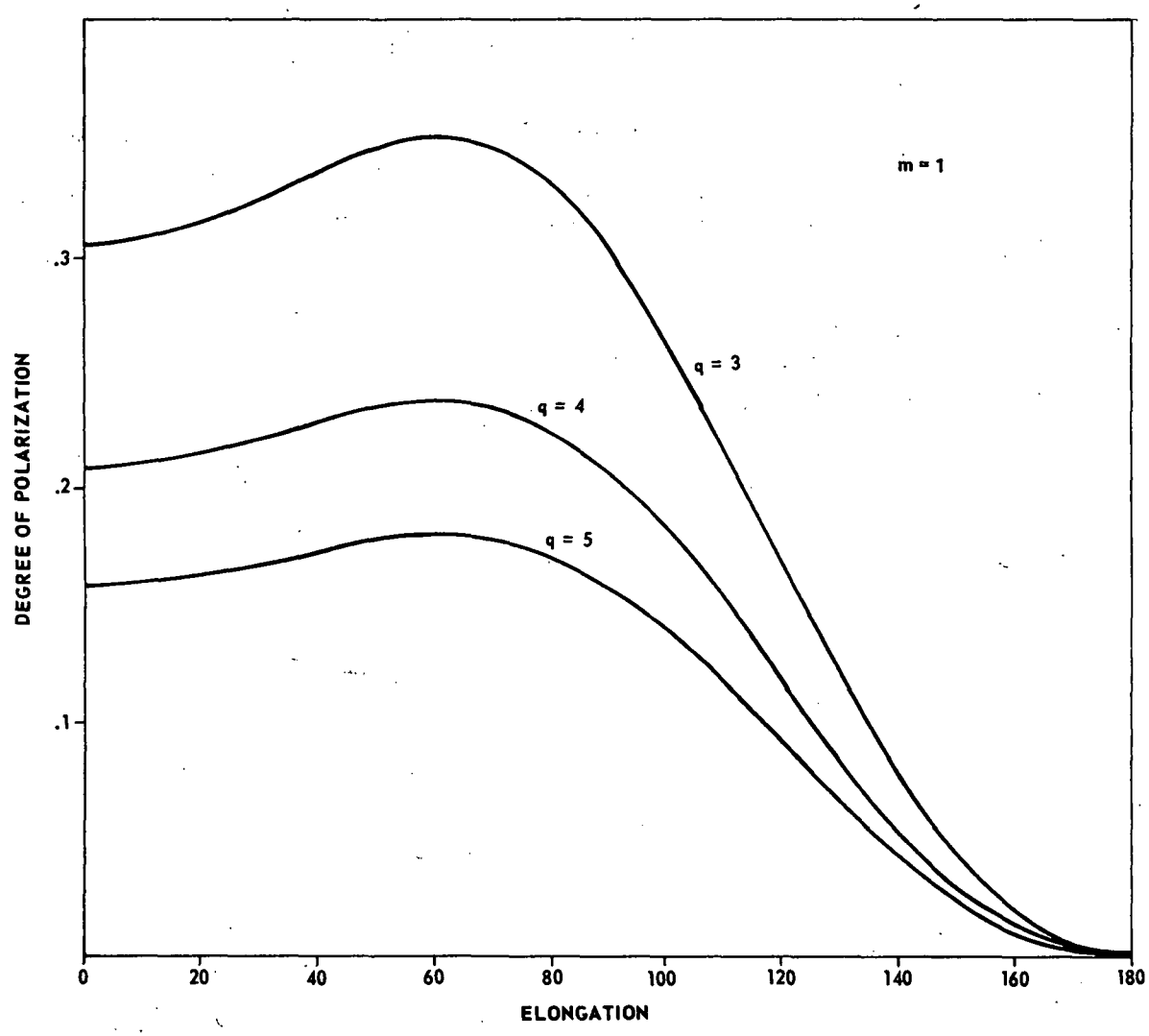

Figure 48. (Continued).

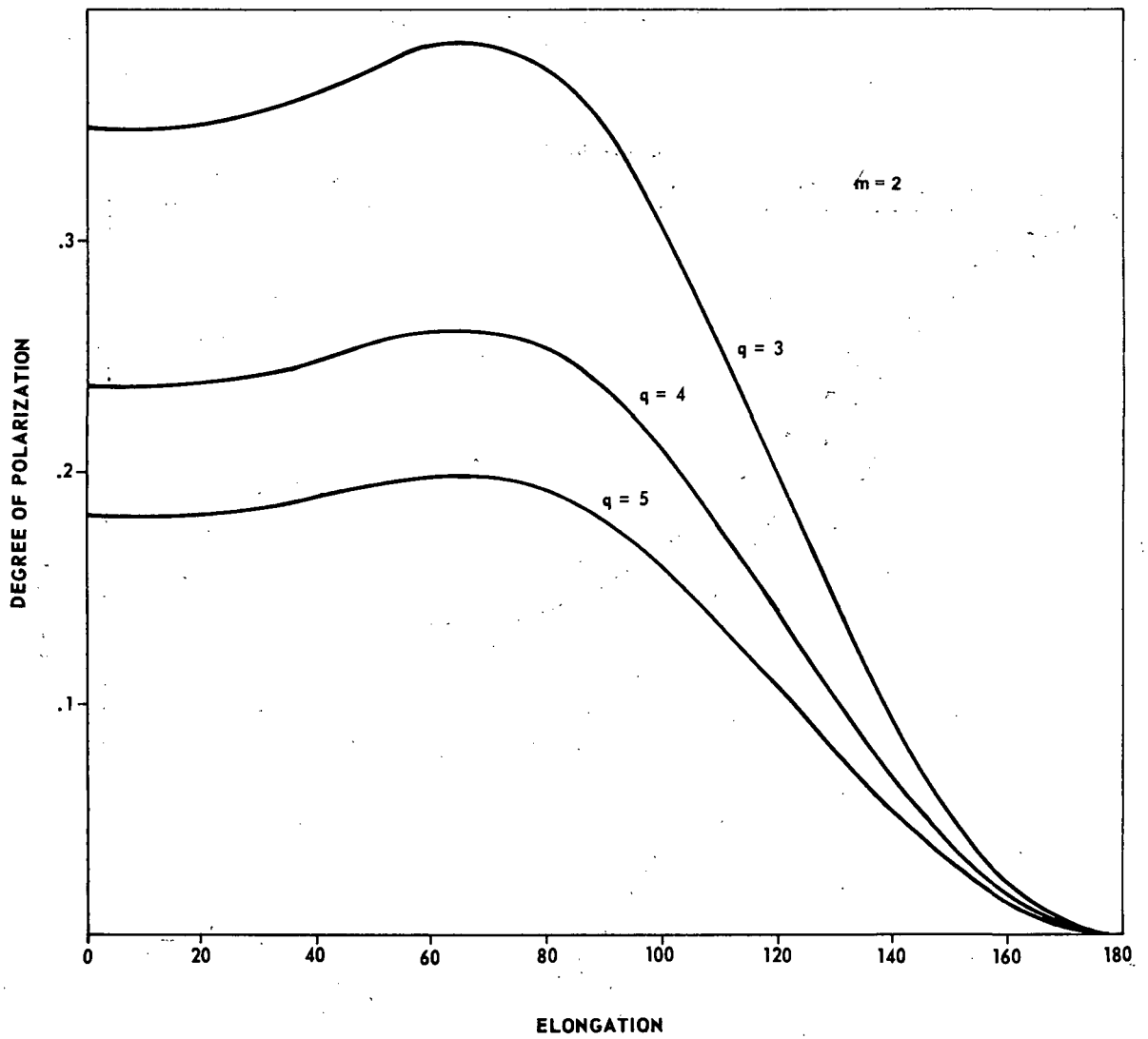

Figure 48. (Concluded).

H. Polarization-Single-Particle Scattering

To reproduce the variation of radiance with elongation, the empirical scattering function used by Ingham does as well as more sophisticated ones, but polarization depends markedly upon the nature of the material and physical dimension of the particle. Mie theory can be used to investigate the polarization and radiance dependence on particle size and material [24, 82, 83]. The results of such an investigation can be used to predict or isolate certain ranges of these variables for a given light-scattering situation. In this section the radiance and polarization from single particles is discussed. In Figures 49 and 50 the total scattering intensity functions versus the scattering angle for a single spherical particle with a refraction index of 1.33 (dielectric ice) is shown for various values of α ($=2\pi$ a/λ). The corresponding polarizations are shown in Figures 51 and 52. For small particles, the scattering follows the Rayleigh law with a symmetric polarization of about 90 deg. As α increases, the diffraction peak appears, the patterns become asymmetrical, and the number of maxima and minima in the scattering intensity functions increases. The polarization deviates from the Rayleigh case as α increases and oscillates about zero more with the higher α's. This can be seen in Figure 53 which shows the degree of polarization for a particle with $\alpha = 20$. Figure 54 shows the total intensity for this particle. The diffraction peak has become very narrow and an increase in backward scattering occurs.

Figures 55 and 56 show the dependence of the scattering intensity function and polarization upon the absorption term of the refractive index. In these figures, $m^* = 1.33 + ik$ ($k = 0.00, 0.05, 0.10, 0.50$) and $\alpha = 5.0$. The total scattering intensity function decreases by a factor of 2 in the forward direction, and 10 in the backward direction. The polarization for a small absorption term does not differ much from the pure dielectric, but for $k = 0.50$ the polarization is totally positive, showing a metallic nature. The behavior is further shown in Figures 57, 58, 59, and 60, where data for dielectric and metallic particles of size parameter $\alpha = 5$ are presented. The polarization from the dielectrics oscillates in sign while the metals give a predominantly positive polarization.

An analysis using single-site particles indicates that the positive polarization of the zodiacal light can be obtained from small particles ($\alpha \leq 1$) or metallic particles with α greater than 1. This must be considered a primitive result because of the integration over particle size and scattering angle that is necessary in a model of zodiacal light.

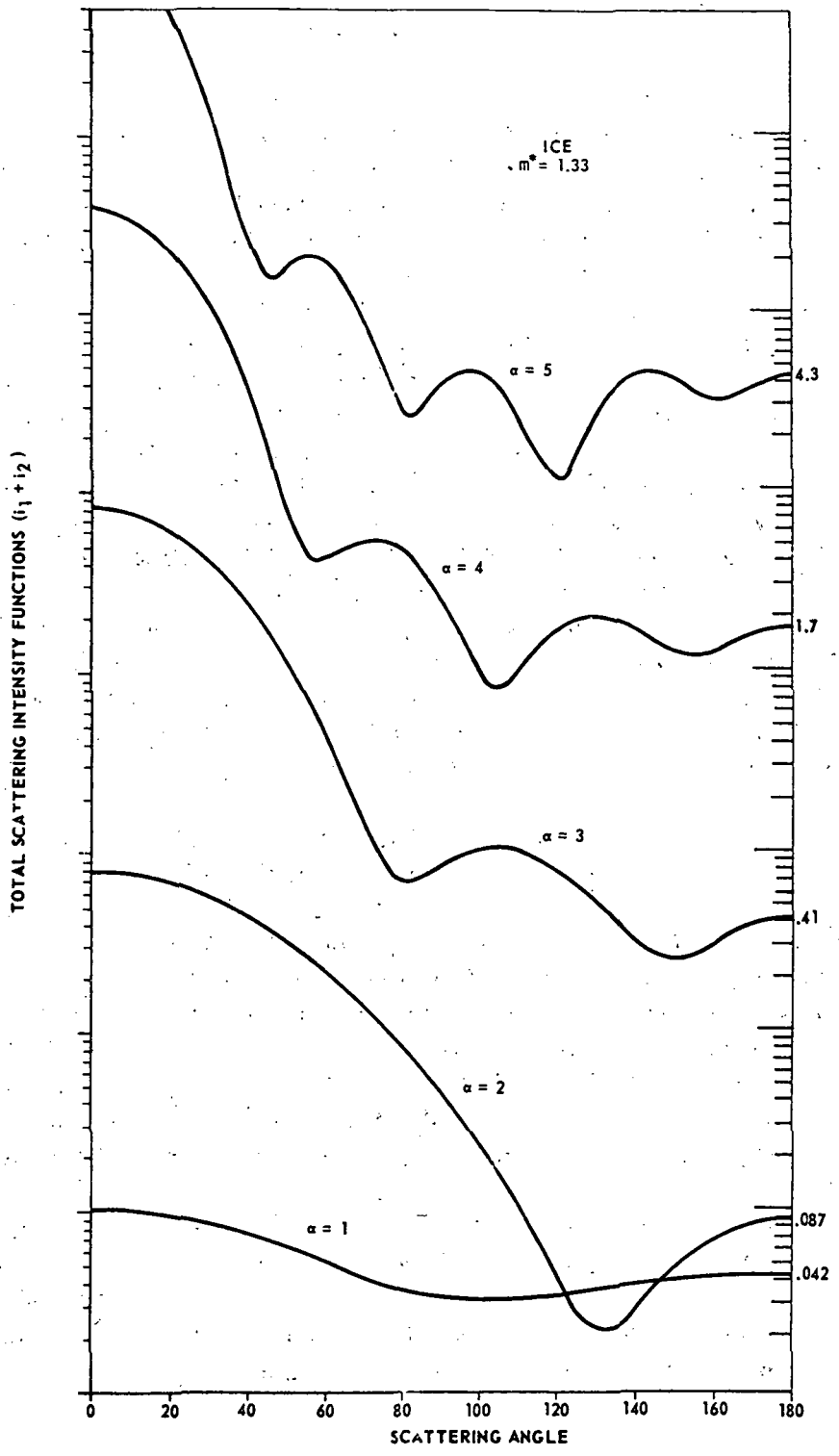

Figure 49. Total scattering intensity function for spherical ice particles ($m^* = 1.33$) for $\alpha = 1 - 5$.

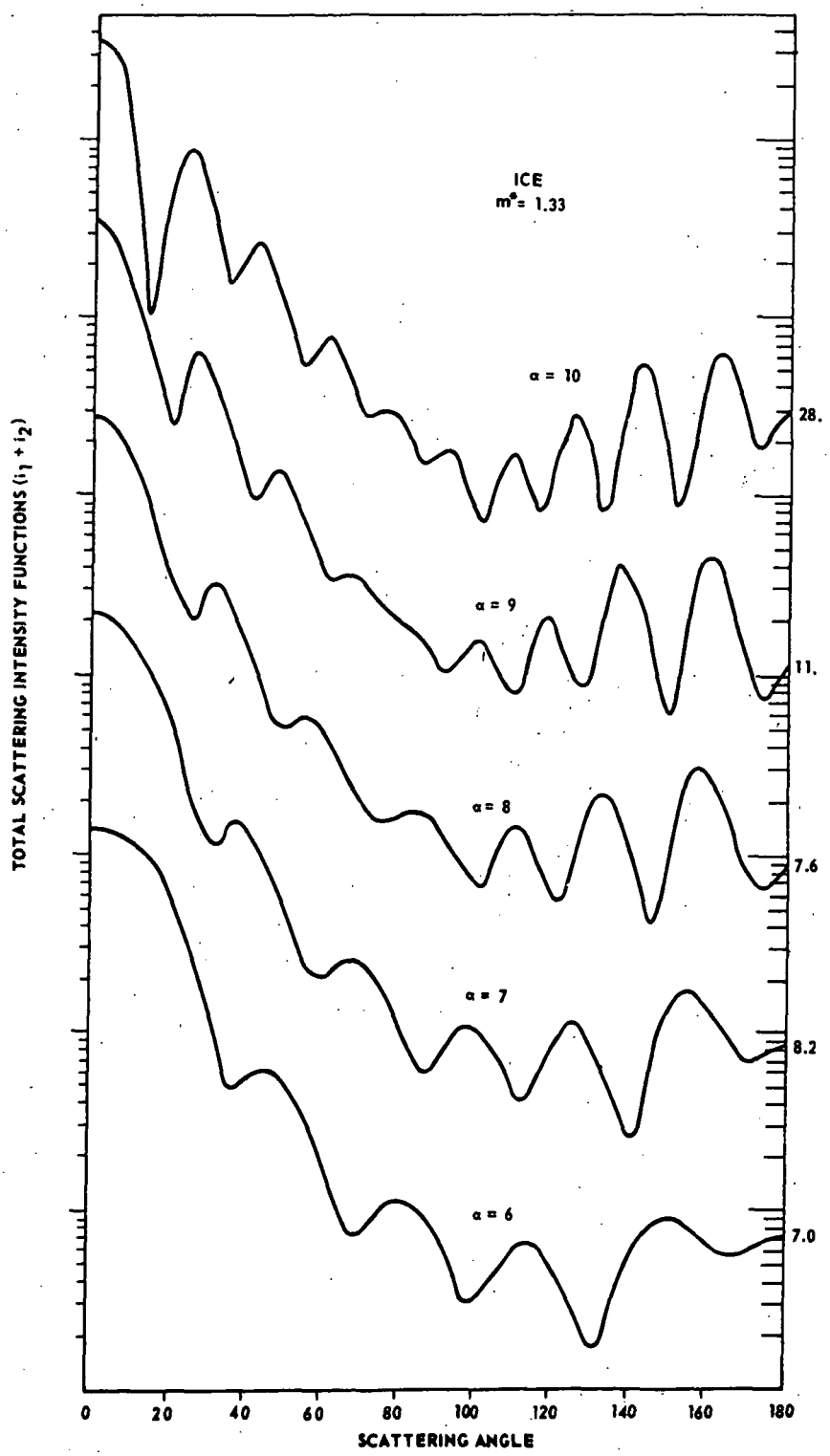

Figure 50. Total scattering intensity functions for spherical ice particles ($m^* = 1.33$) for $\alpha = 6 - 10$.

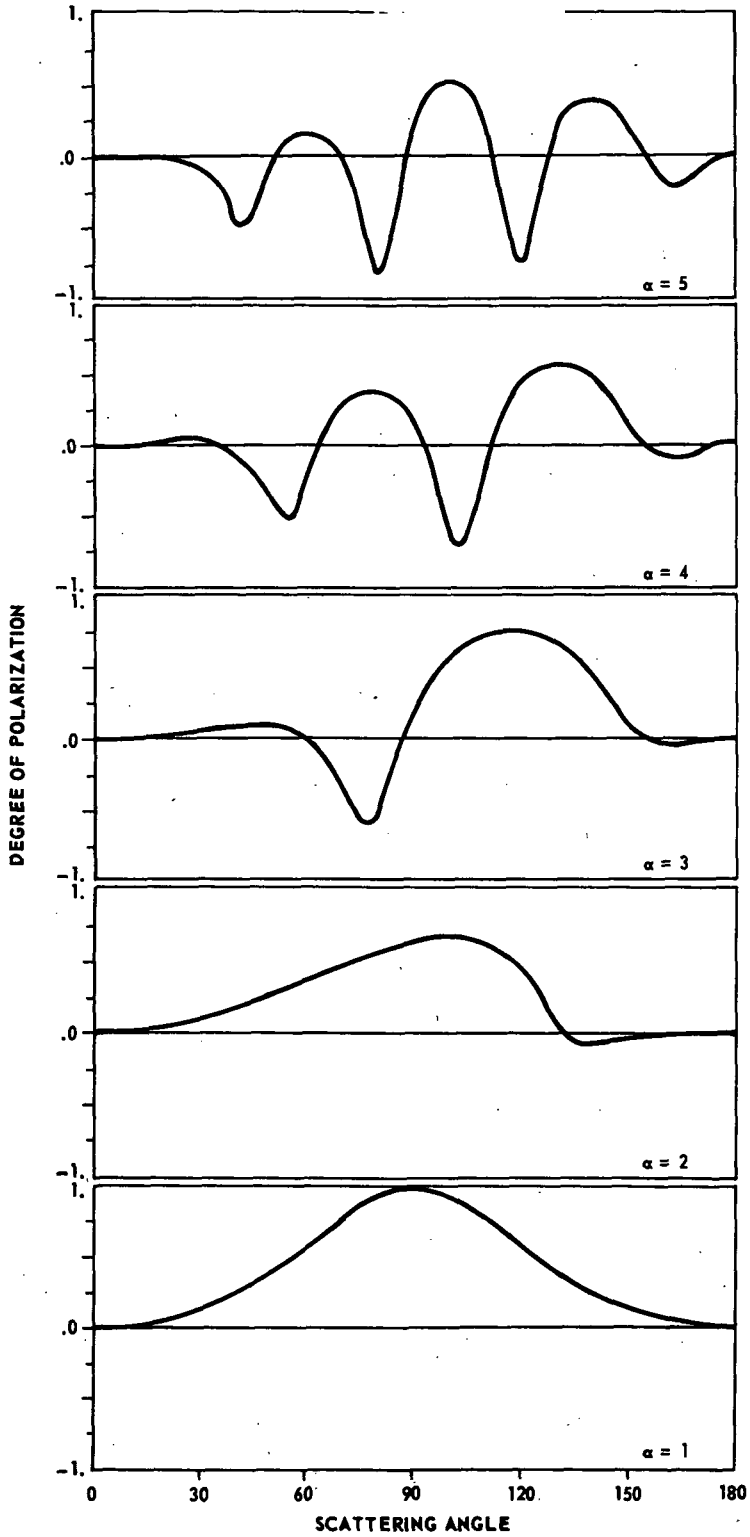

Figure 51. The degree of polarization for particles of Figure 49 (α = 1 - 5).

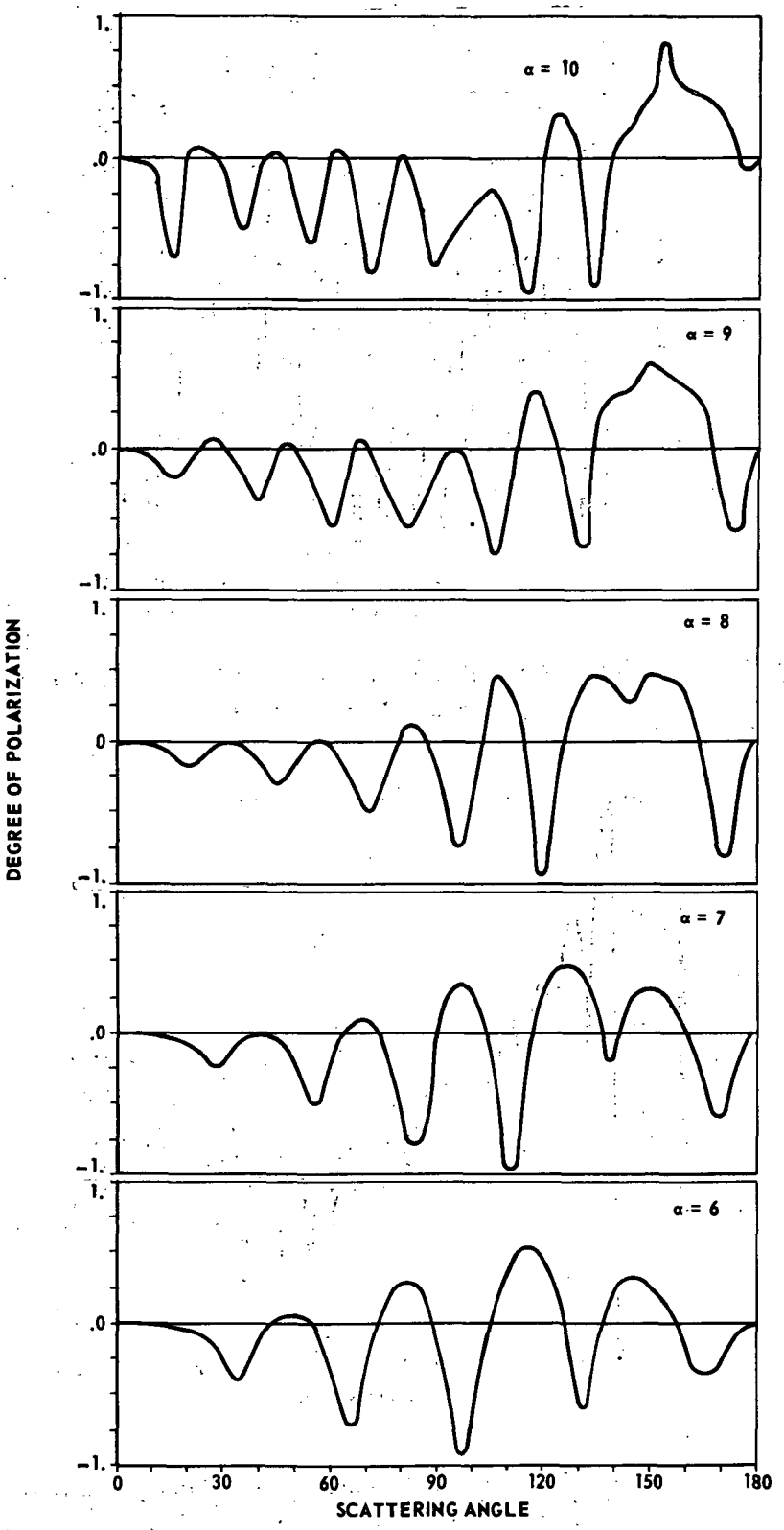

Figure 52. The degree of polarization for particles of Figure 50 (α = 6 - 10).

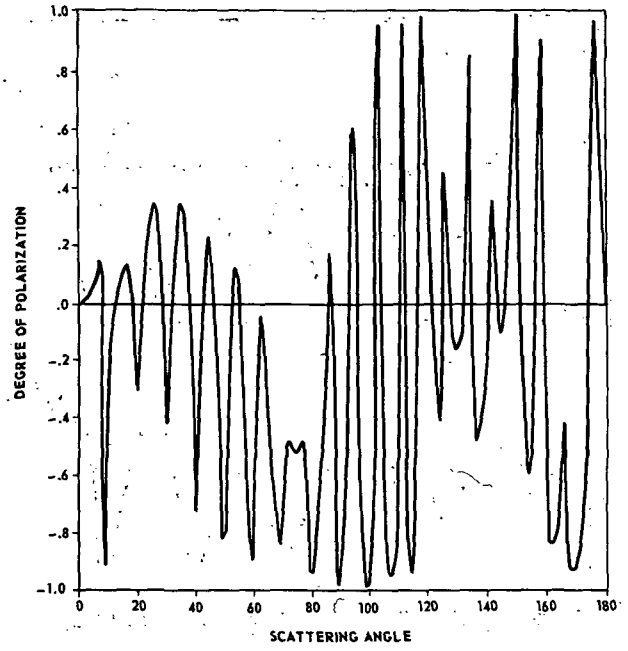

Figure 53. The degree of polarization for a spherical ice particle ($m^* = 1.33$) for $\alpha = 20$.

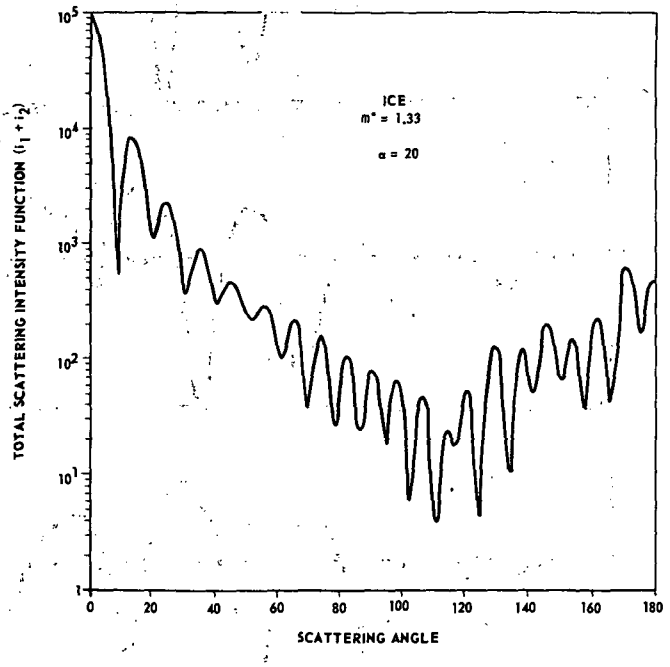

Figure 54. The total intensity scattering function for a spherical ice particle ($m^* = 1.33$) for $\alpha = 20$.

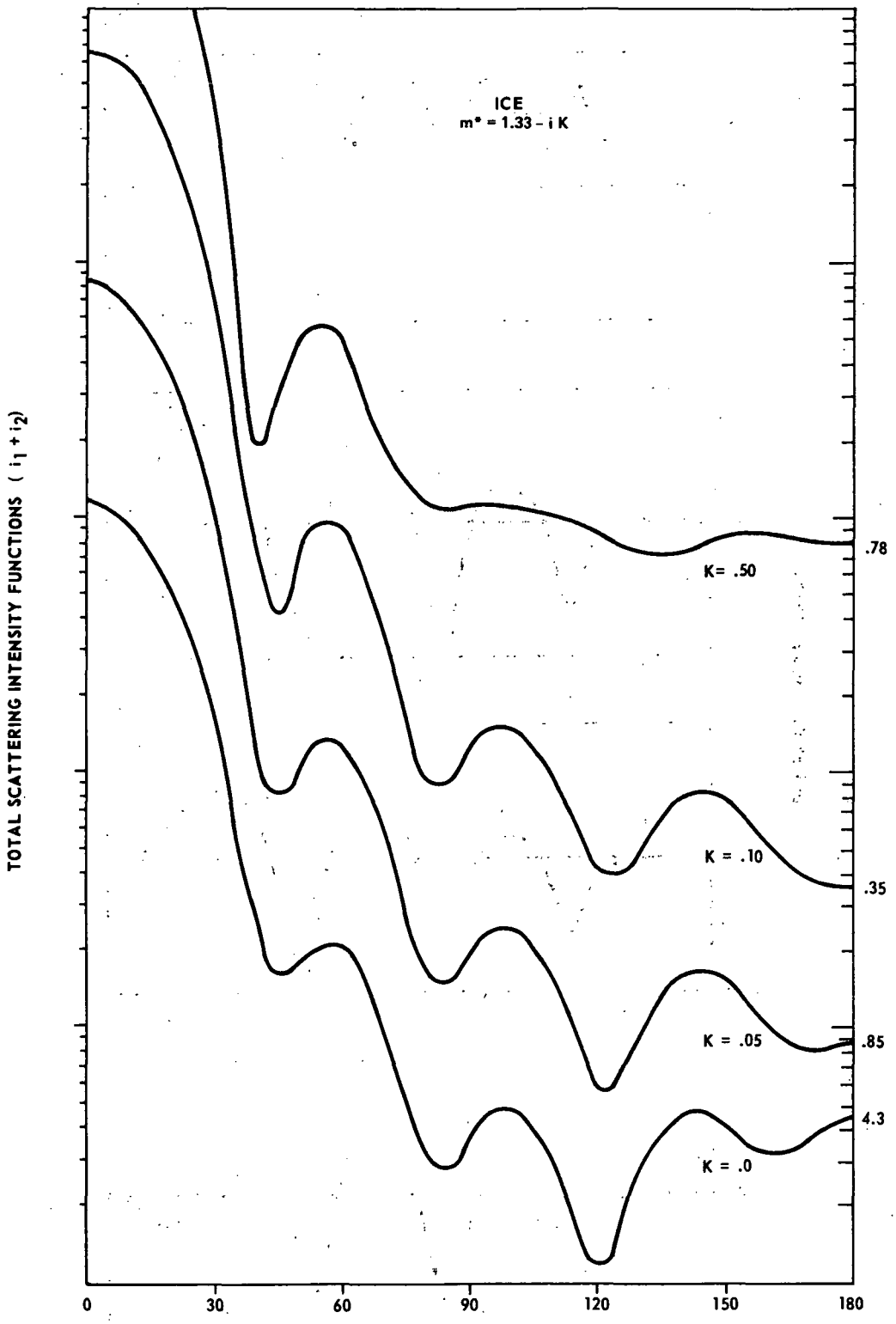

Figure 55. Total scattering intensity function for spherical particles with various values of the absorptive part of the refractive index ($m^* = 1.33 - iK$).

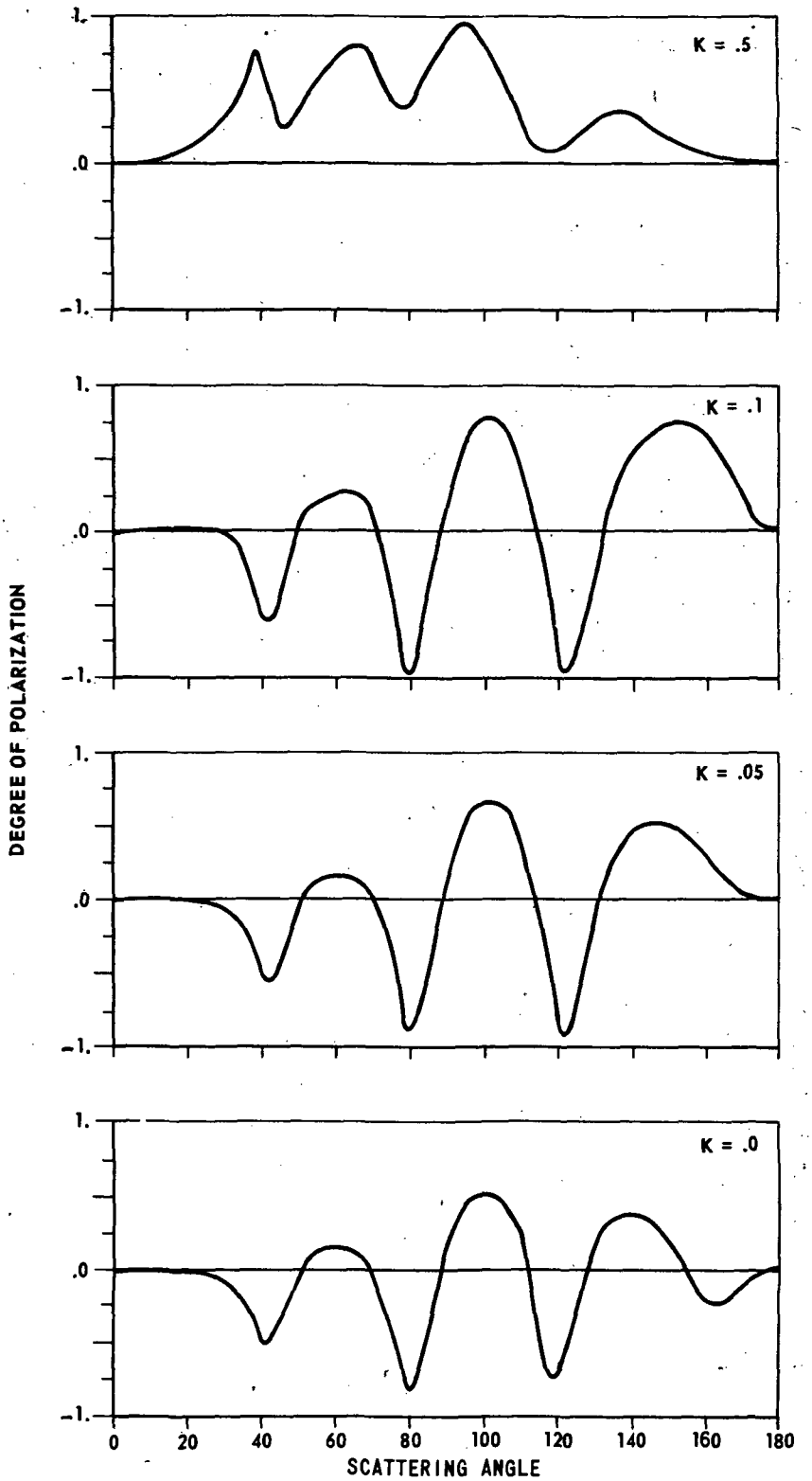

Figure 56. Degree of polarization for particles of Figure 55.

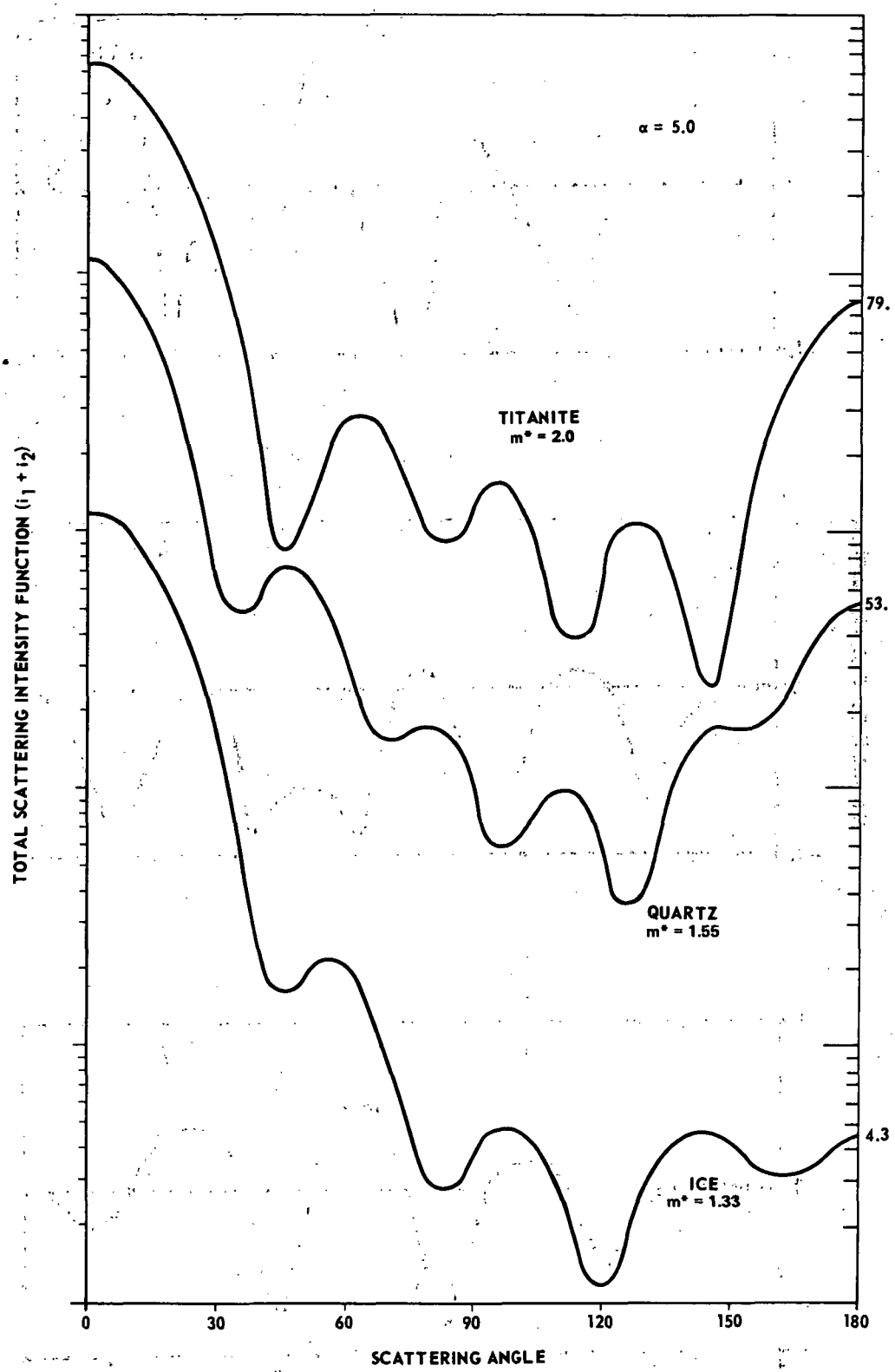

Figure 57. Total scattering intensity functions for various spherical dielectric particles with $\alpha = 5.0$.

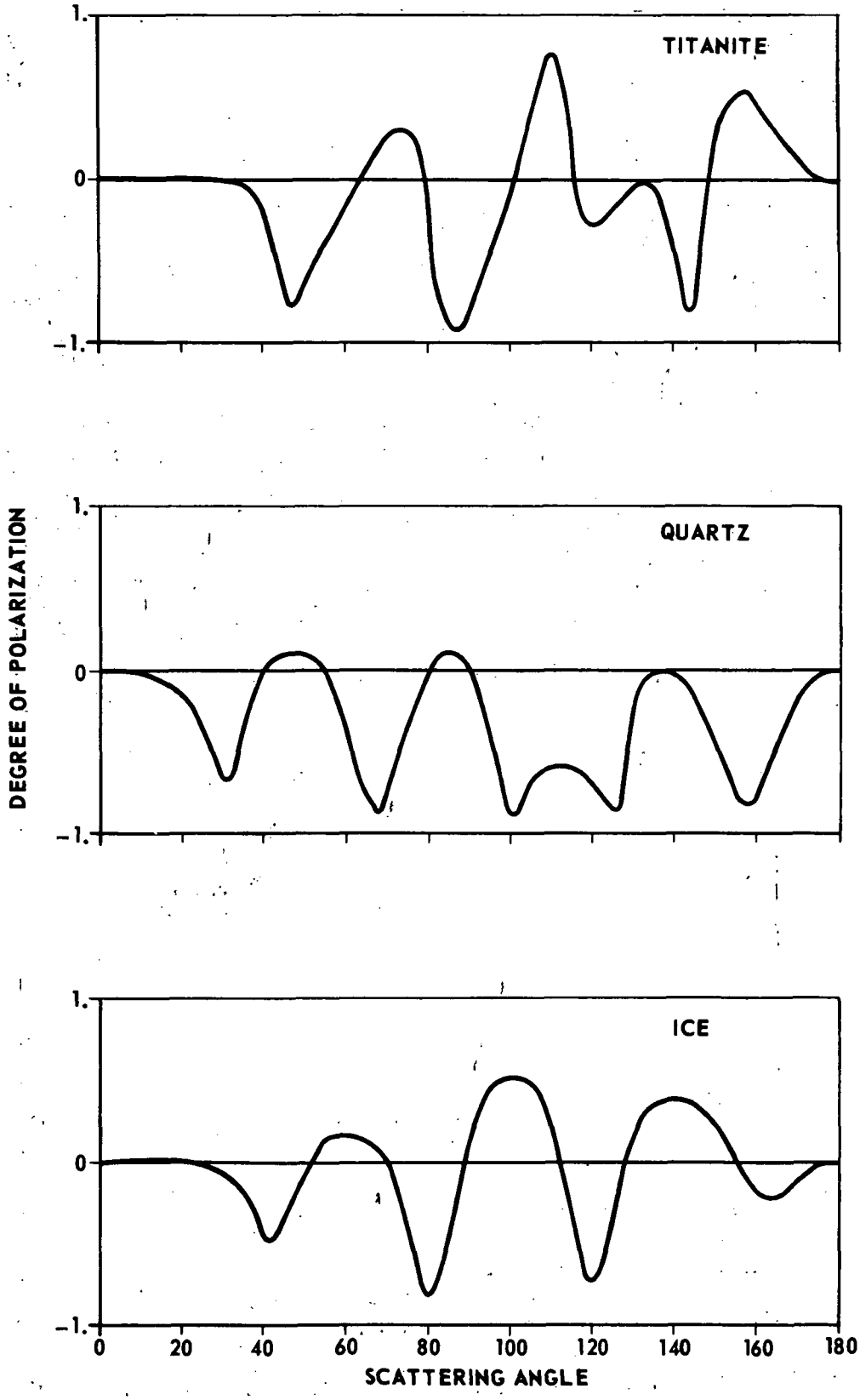

Figure 58. Degree of polarization for the dielectric particles of Figure 57.

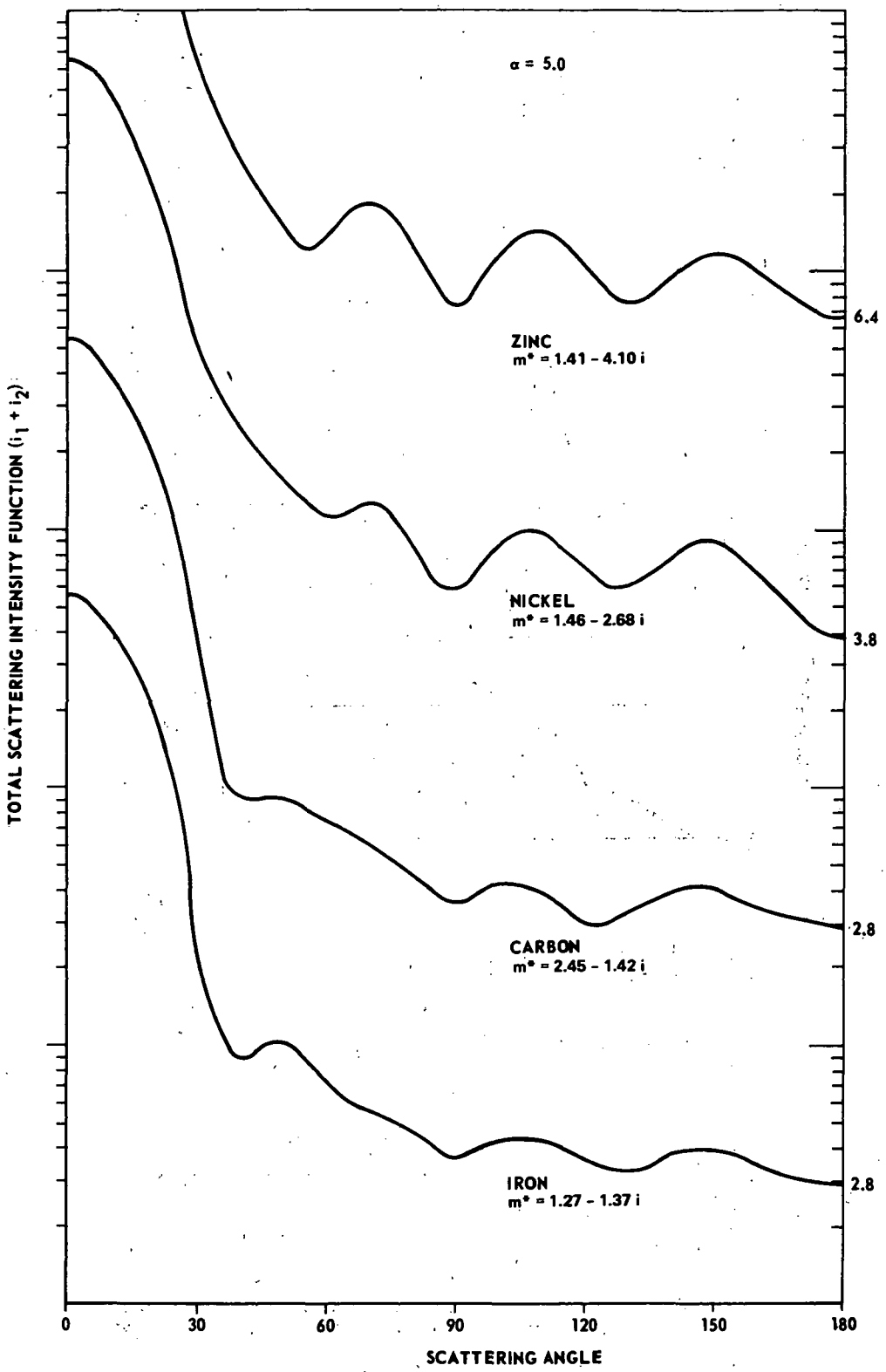

Figure 59. Total scattering intensity functions for various spherical metallic particles with $\alpha = 5.0$.

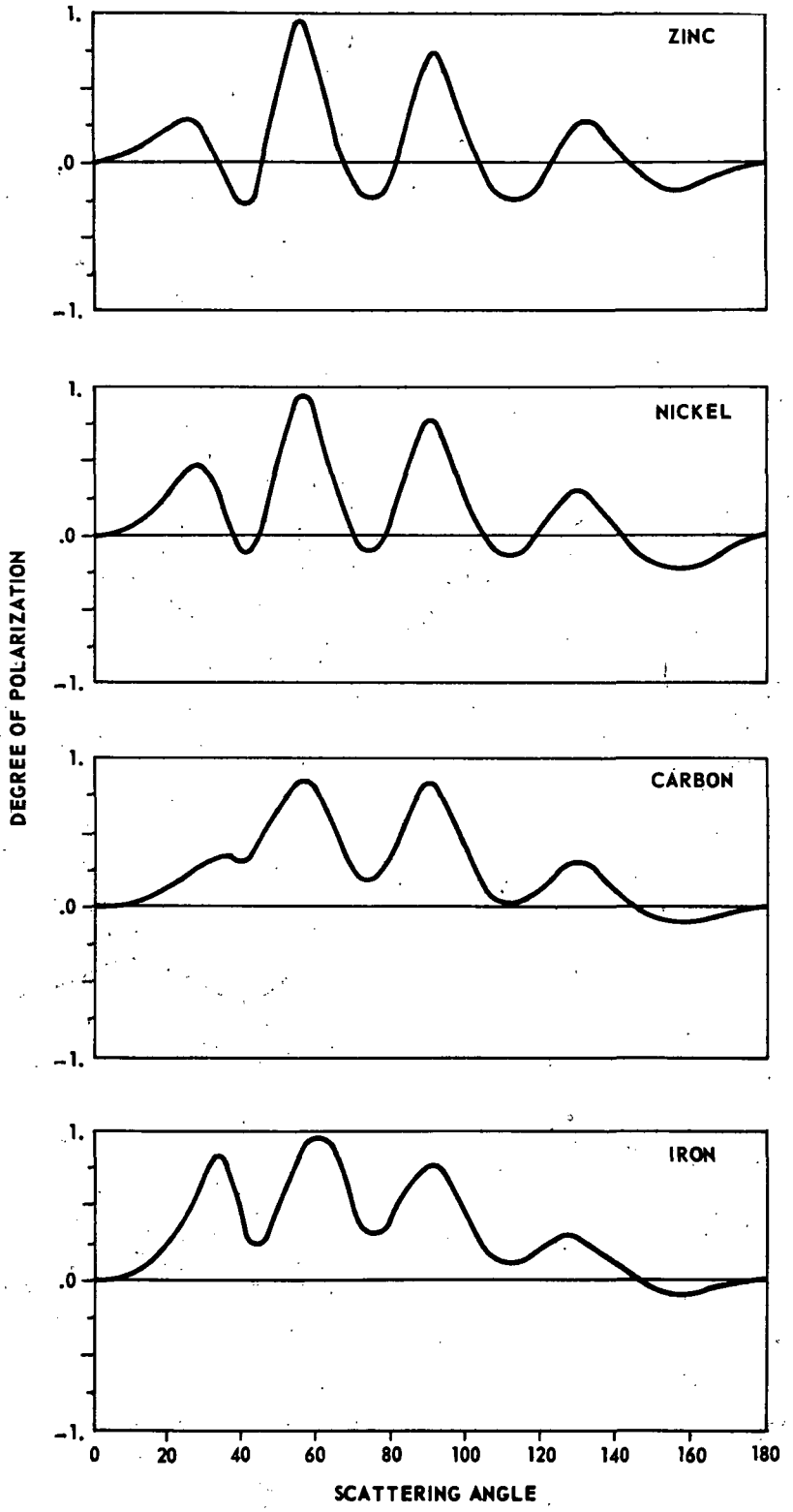

Figure 60. Degree of polarization for particles of Figure 59.

I. Scattering from Distributions

A distribution of particles will tend to average and smooth the oscillations of the radiance and polarizations curves of single particles. The results using examples of each of the four categories of distributions are compared and discussed in this section. Particle sizes between $\alpha = 1$ and $\alpha = 20$ and $\alpha = 0.1$ and $\alpha = 20$ were used, since this represents a possible size range of particles of zodiacal dust and does not require excessively long computer times.

Power Law Distribution. Since this distribution is used extensively in zodiacal light calculations, it has been the most frequently used in the present studies of light scattering from a distribution of spherical particles, particularly with $p = -4$. The materials considered were water (ice), quartz, titanite, carbon, iron, zinc, and nickel. The scattering intensity functions were calculated from

$$\bar{i}_j = \frac{\int_{\alpha_{min}}^{\alpha_{max}} i_j(\theta, m^*, \alpha)\, n(\alpha)\, d\alpha}{\int_{\alpha_{min}}^{\alpha_{max}} n(\alpha)\, d\alpha} \qquad j = 1, 2, \quad (171)$$

where α_{min} is the minimum particle size in the distribution and α_{max} is the maximum particle size. $i_j(\Theta, m^*, \alpha)$ was calculated from the Mie theory. Figures 61a and 61b show the intensity versus scattering angle for the materials. (Each curve is displaced a cycle upward for clarity.) The backscatter peak is visible for the dielectrics, this being one of the well-known distinguishing characteristics between metals and dielectrics. Another distinguishing characteristic is the degree of polarization, being positive for metals in which the absorption term k is at least a fourth of the real part of the index of refraction [39]. Dielectrics produce negative polarizations at some scattering angles. For the materials used, these properties are clearly visible in Figures 62 and 63. With ice, the radiance and polarization for distributions with $\alpha_{max} > 20$ does not vary much from that found with particles with $\alpha_{max} = 20$, as seen from Figures 64 and 65. For iron particles, the polarization is changed very little by particles with $\alpha > 5$ as seen from Figures 66 and 67.

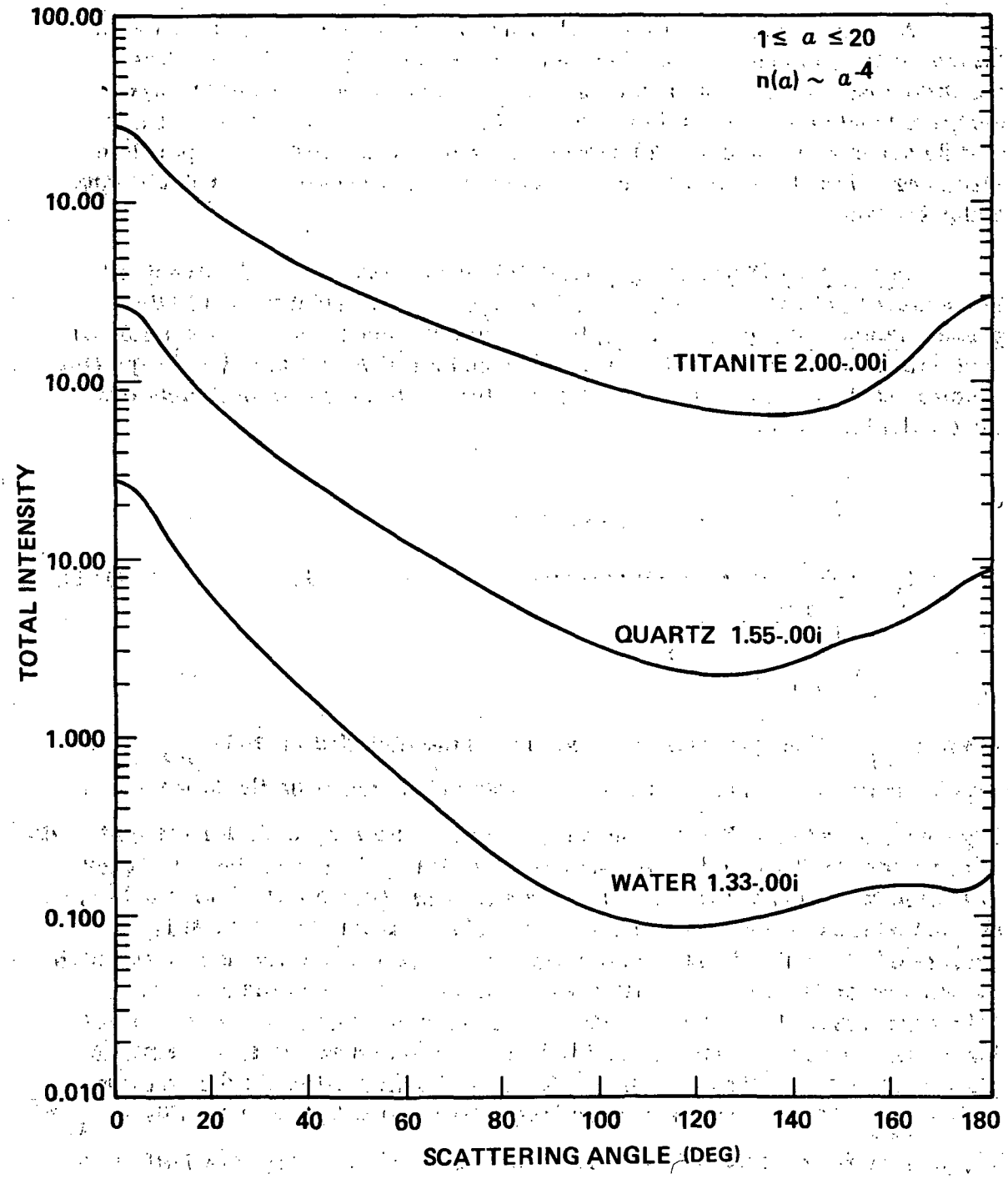

Figure 61a. Radiance versus scattering angle for dielectrics.

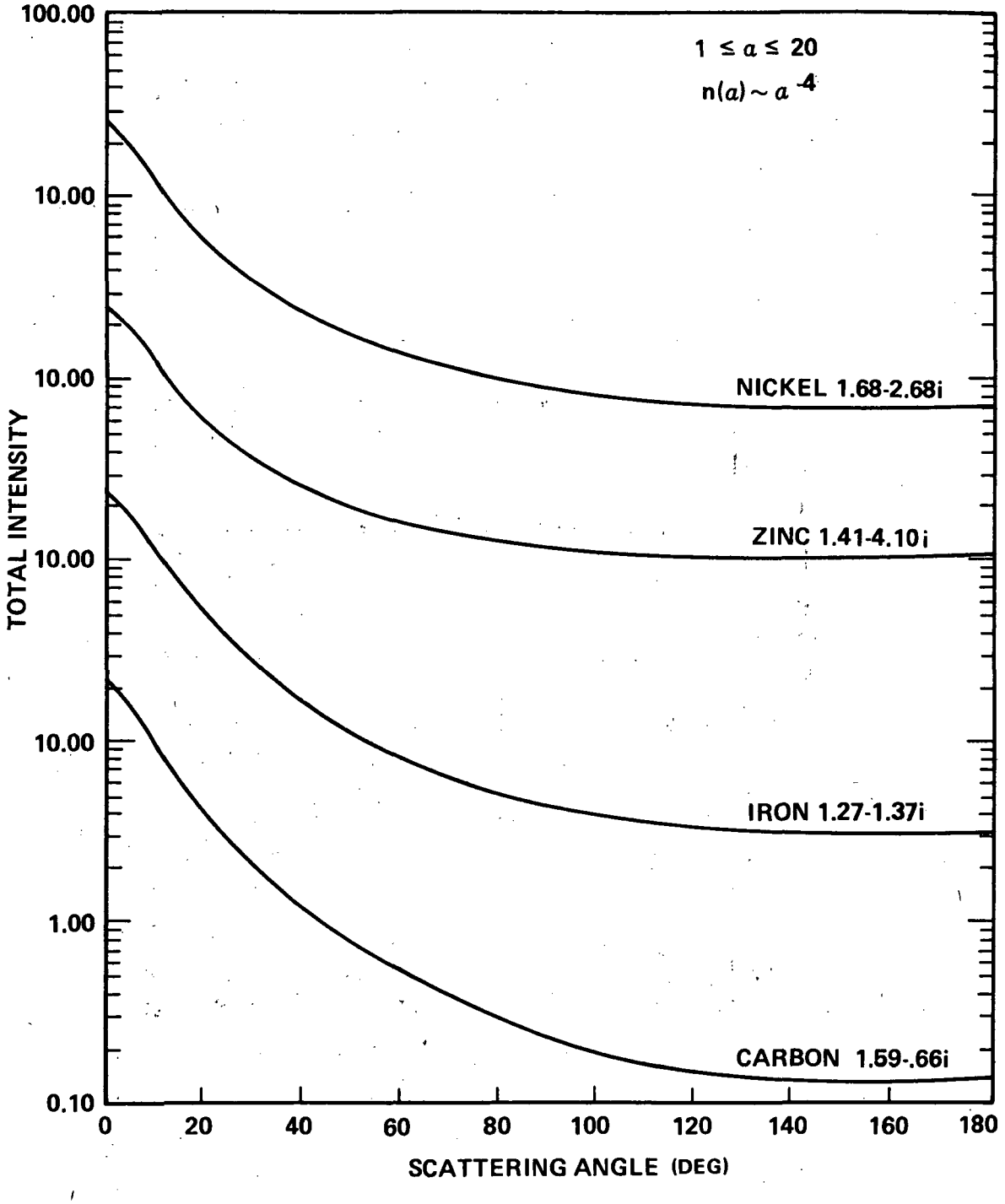

Figure 61b. Radiance versus scattering angle for metals. [Curves are displaced a cycle, $n(\alpha) \sim \alpha^{-4}$.]

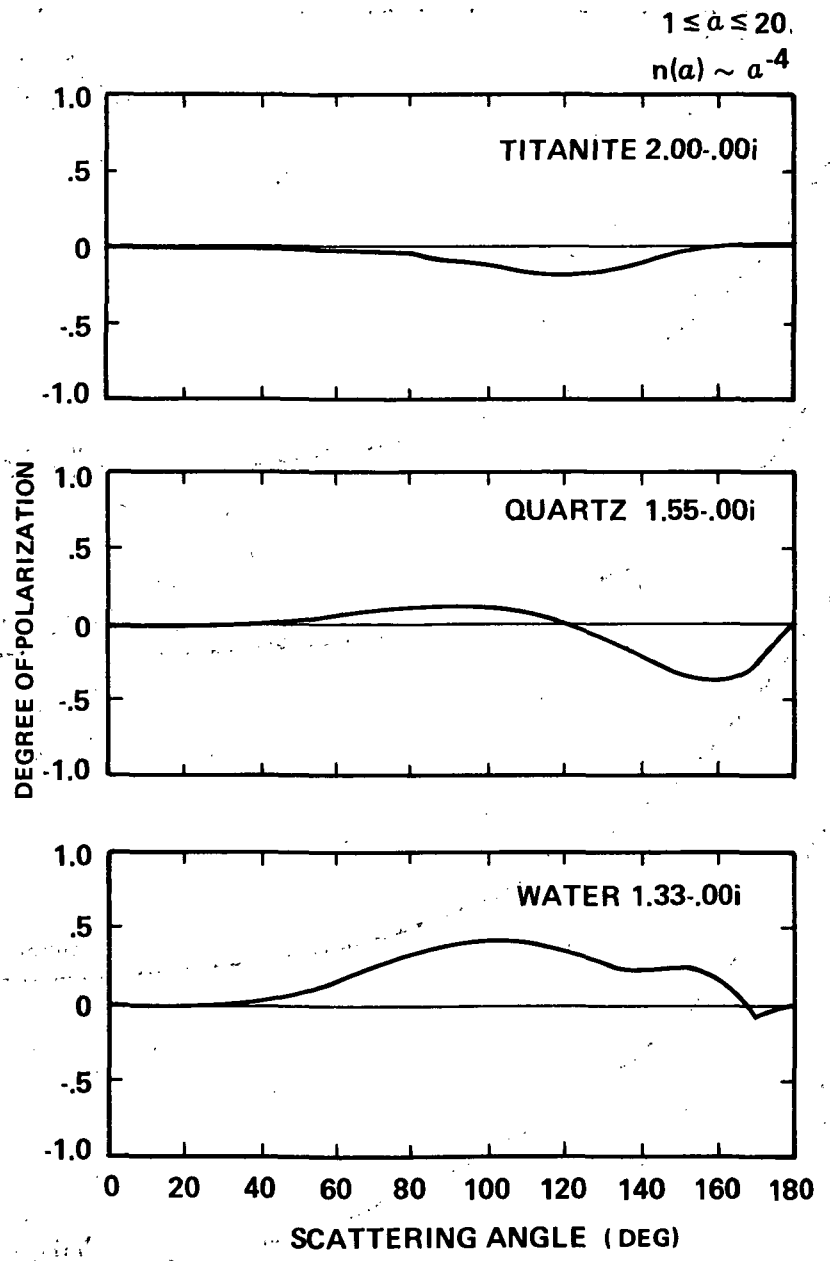

Figure 62. Polarization versus scattering angle for dielectrics of Figure 61a.

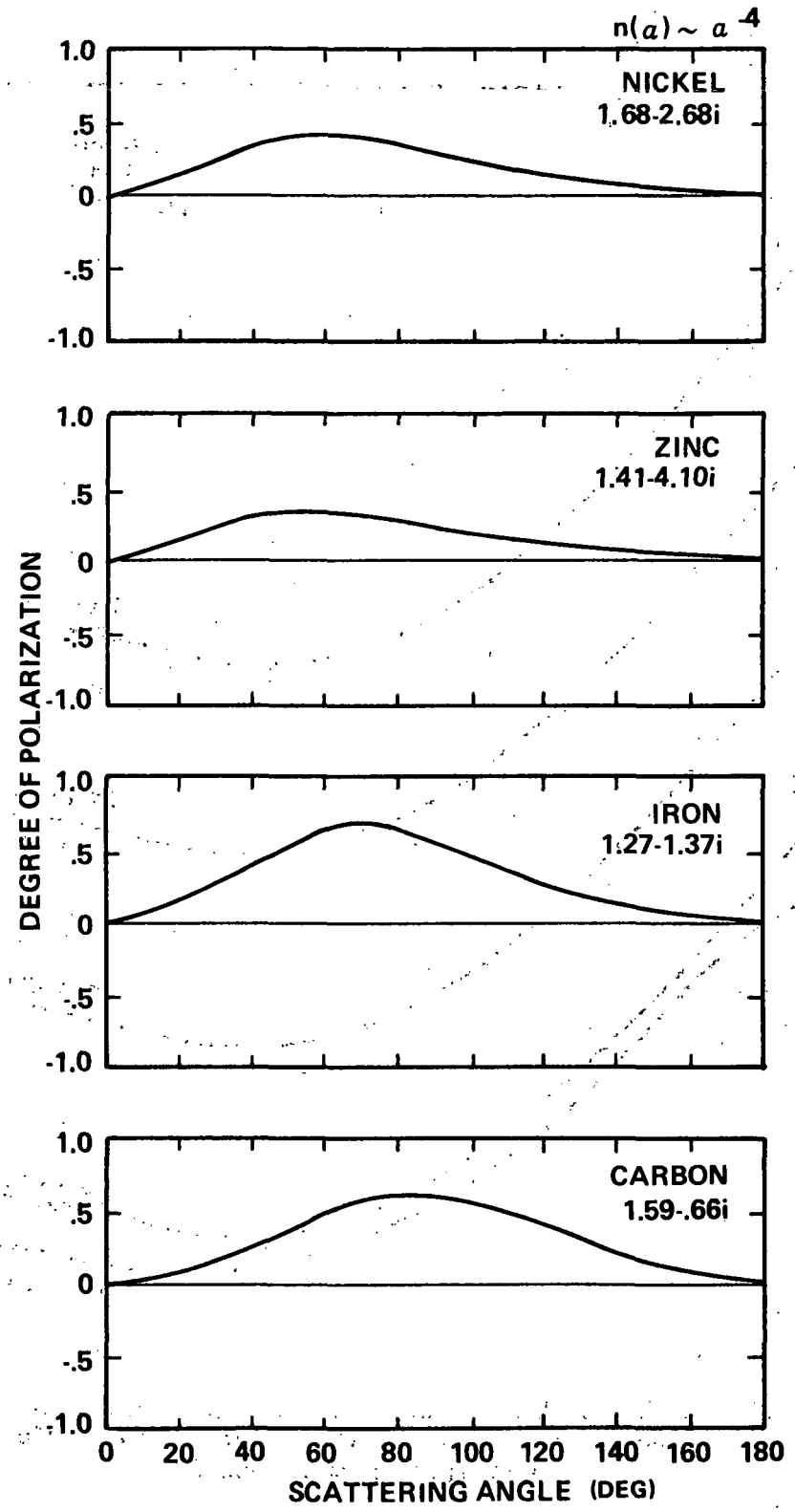

Figure 63. Polarization versus scattering angle for metals of Figure 61b.

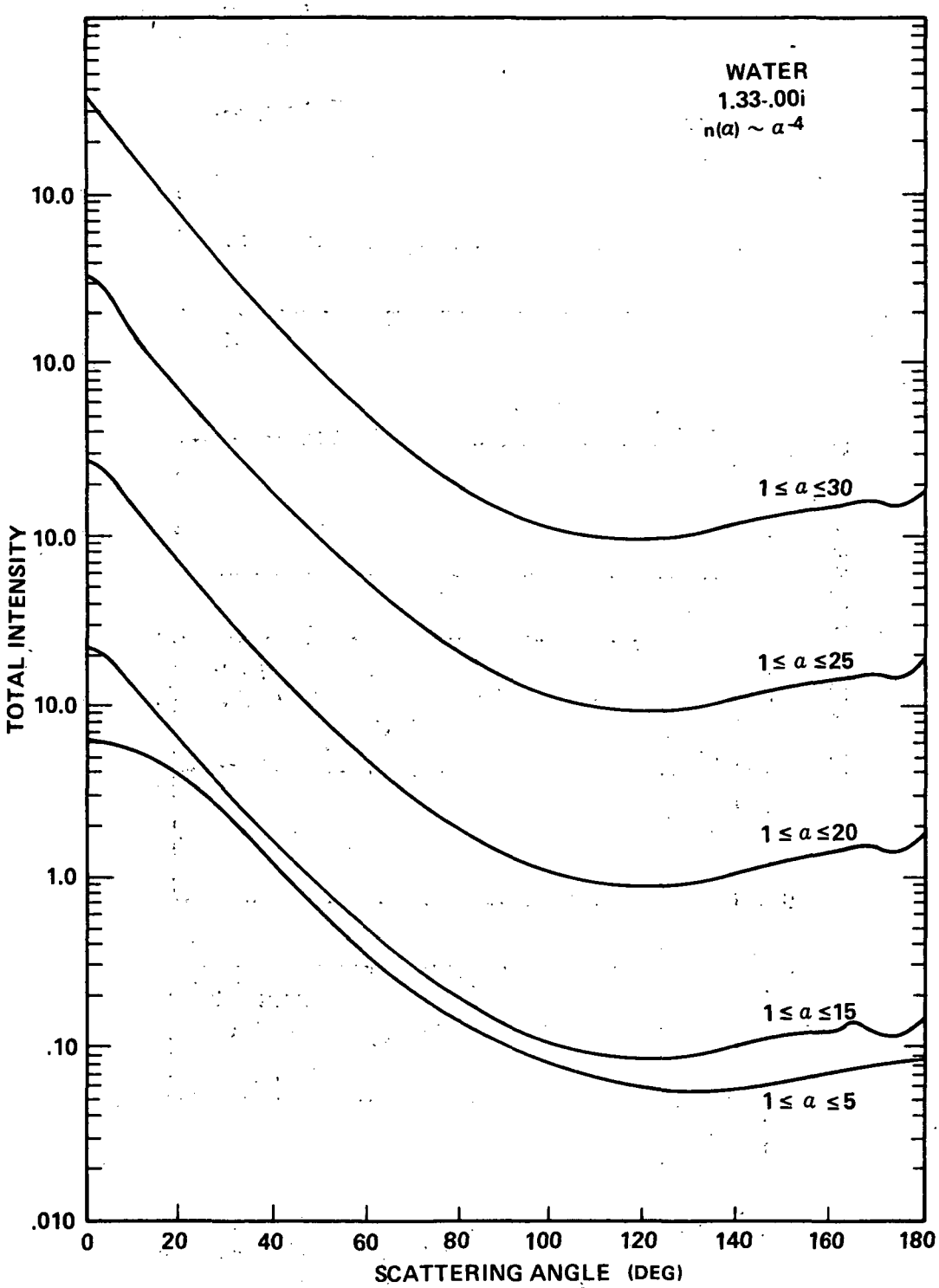

Figure 64. Radiance versus scattering angle for ice with distributions of particles for which α_{max} = 5, 15, 20, 25, and 30.

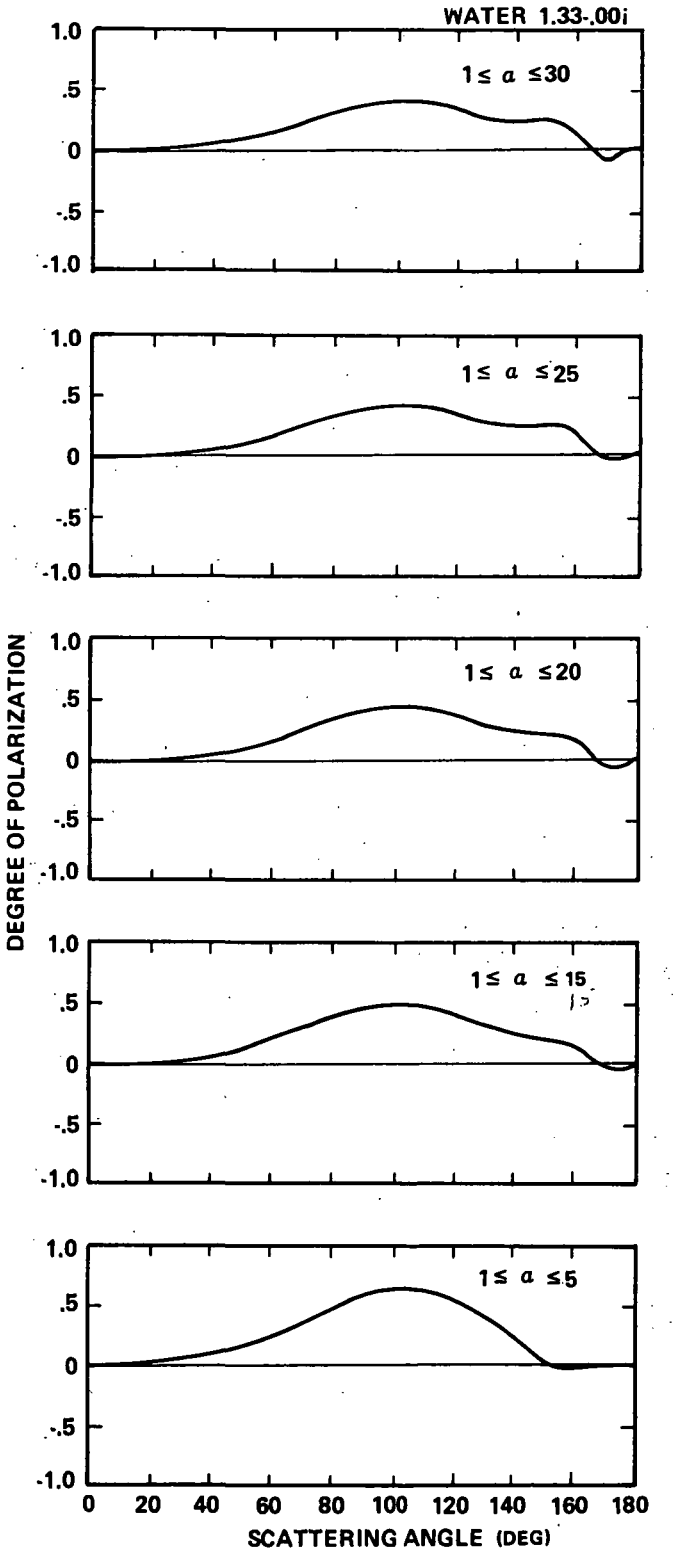

Figure 65. Polarization versus scattering angle for distributions of Figure 64.

The radiance does increase slightly in both cases as α_{max} increases (Figs. 64 and 67). Due to the distribution, very few particles exist with $\alpha > 15$. Their contribution to the total scattered radiance or polarization is small. The effect of cutting off the small particles for ice is seen in Figures 68 and 69. The effect is especially noticeable in the polarization diagrams. If Figure 65 is compared to Figure 69, it may be seen that the particles with $\alpha < 2$ produce a strong positive polarization in the range $40 < \Theta < 100$ deg. This is caused by Rayleigh scattering from these particles. The dip at approximately 170 deg is due mainly to particles with size $\alpha \geq 5$.

Many cases occur for which a cloud of particles is not homogeneous. Results of radiance and polarization calculations for a half-and-half mixture of ice and quartz are given in Figures 70 and 71. As before, the backscatter peak of dielectric particles tends to indicate that these particles are necessary for the zodiacal light. The positive polarizations of water in Figures 62 and 65 indicate that dielectrics as well as metals could be candidates for the interplanetary material.

The normalized scattered intensities and polarizations obtained from Categories I through III distributions are shown in 72. A size range of 0.1 to 20 was used so that in the cases of Categories I and III both sides of the peak would be covered. Figures 72a through 72d show the radiance and polarization from the modified gamma distribution (specifically distribution 1, Table 4);

$$n(\alpha) = (1.49 \times 10^5)\, \alpha^6 \exp(-35.18\, \alpha^{0.1705}) \quad .$$

This distribution was tailored to peak at $\alpha = 1.0$ and to have a slope of -4 at $\alpha = 20$. The large particle contributions are evident in the large diffraction peak and also in the degree of polarization for ice.

Figures 72e through 72h show the radiance and degree of polarization of ice and iron as obtained from an exponential size distribution,

$$n(\alpha) = (1.0 \times 10^{-14})\, e^{1/\alpha} \quad .$$

The relative number of particles with size parameter α near 10 is larger for this distribution than for the particular Categories I and III distributions considered. Curves for the degree of polarization have structure which indicates the effects of the large particles. The logarithmic distribution used is

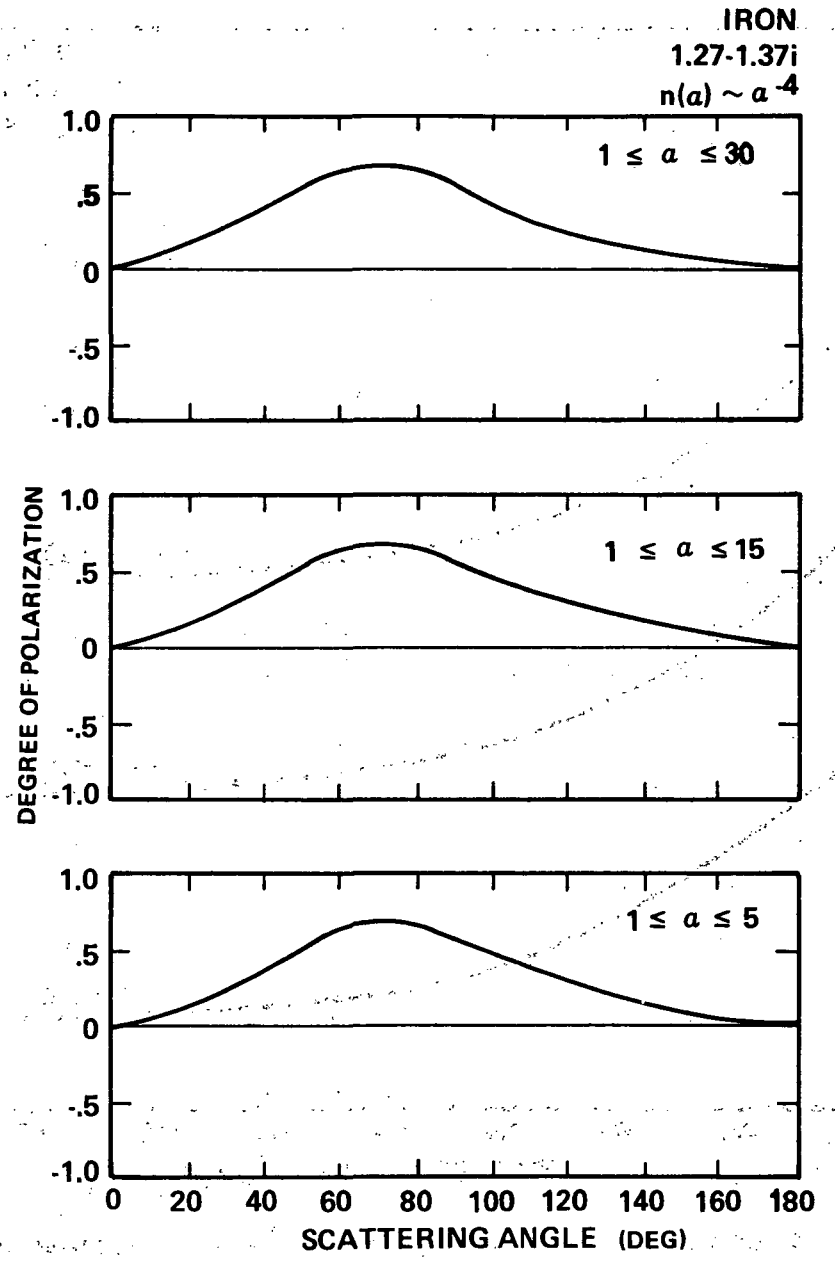

Figure 66. Polarization versus scattering angle for iron with distributions for which α_{max} = 5, 15, and 30.

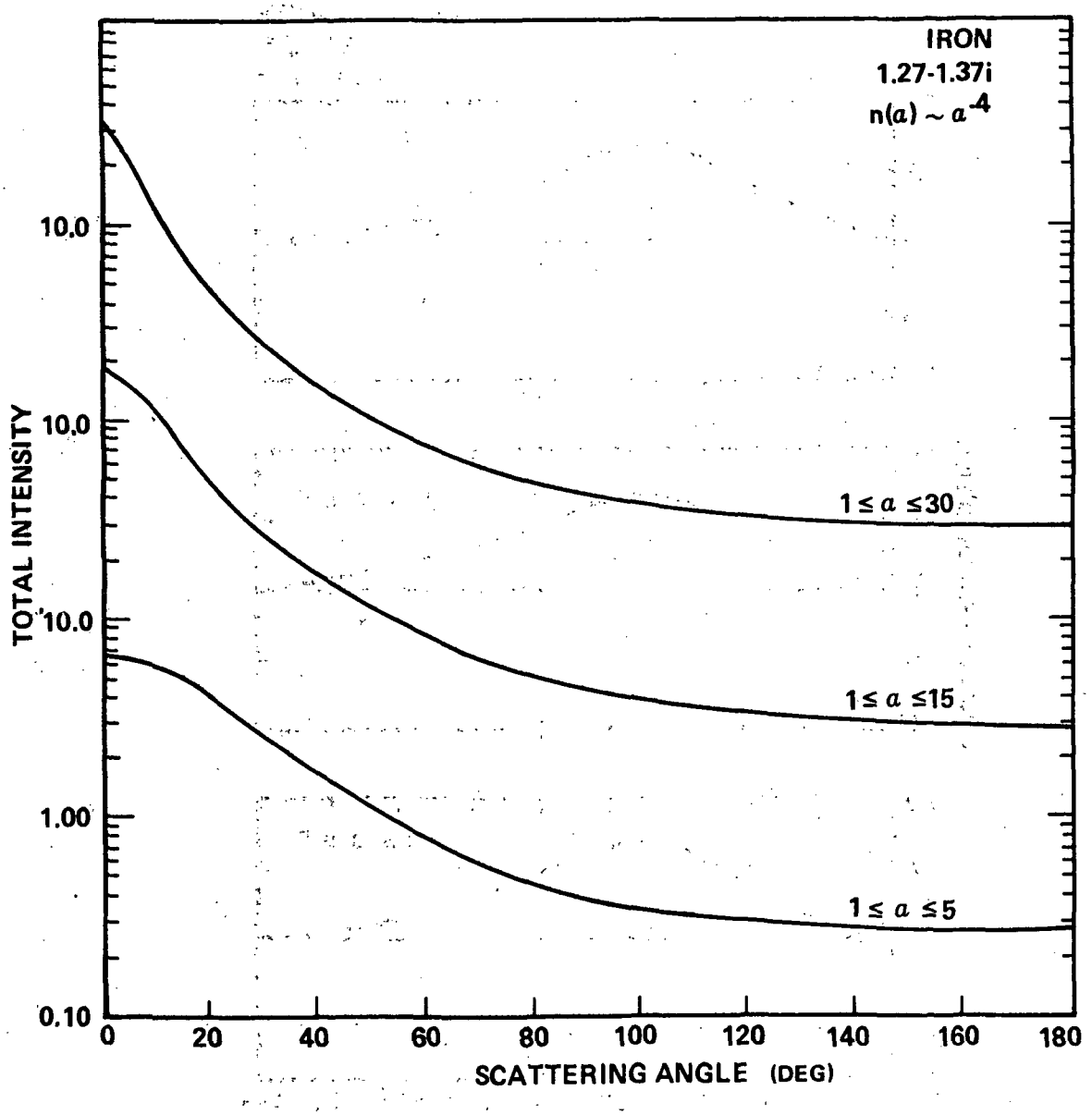

Figure 67. Radiance versus scattering angle for iron in distributions for which $n(\alpha) \sim \alpha^{-4}$ and α_{max} = 5, 15, and 30.

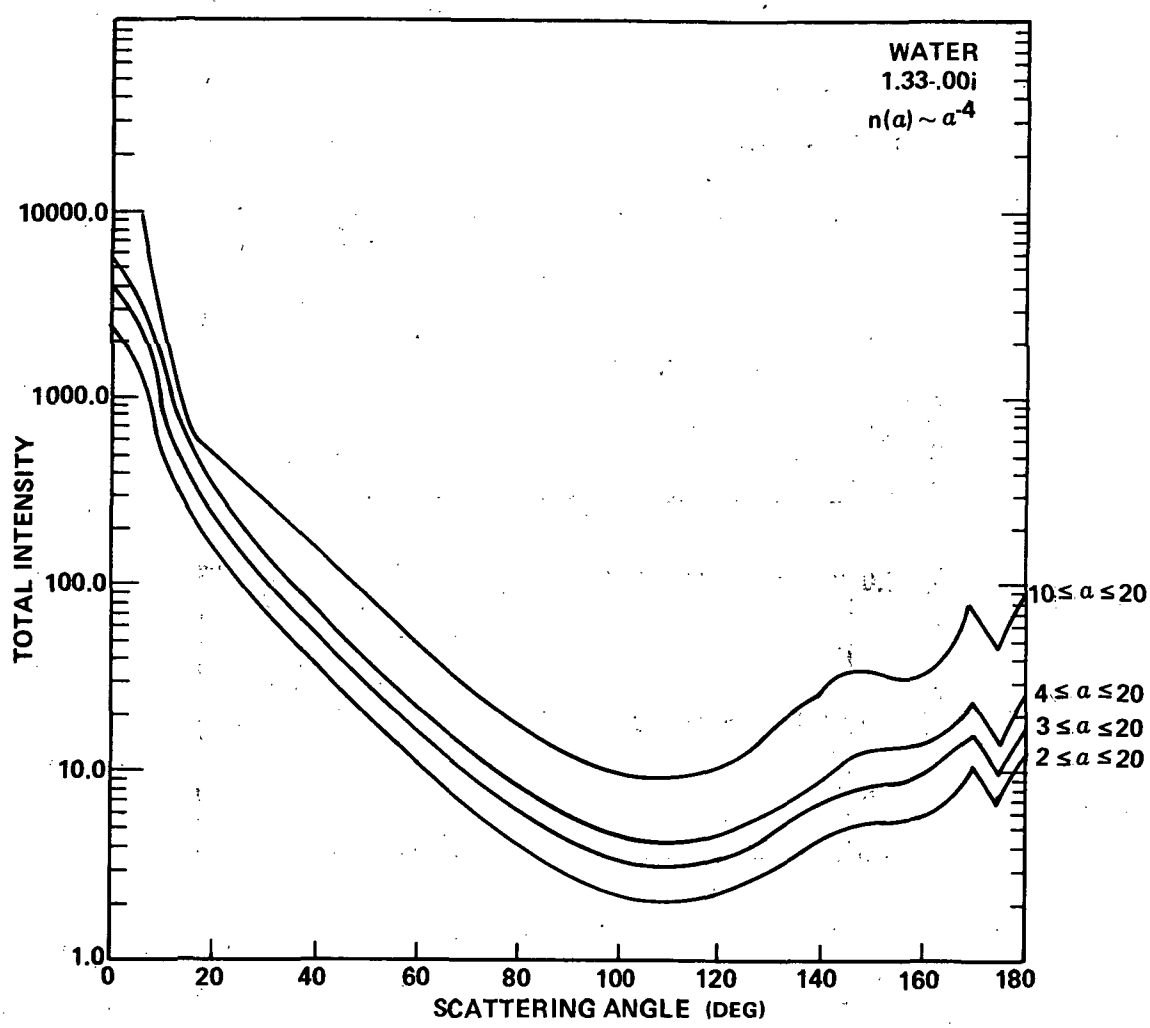

Figure 68. Radiance of water in distributions for which α_{min} = 2, 3, 4, and 10.

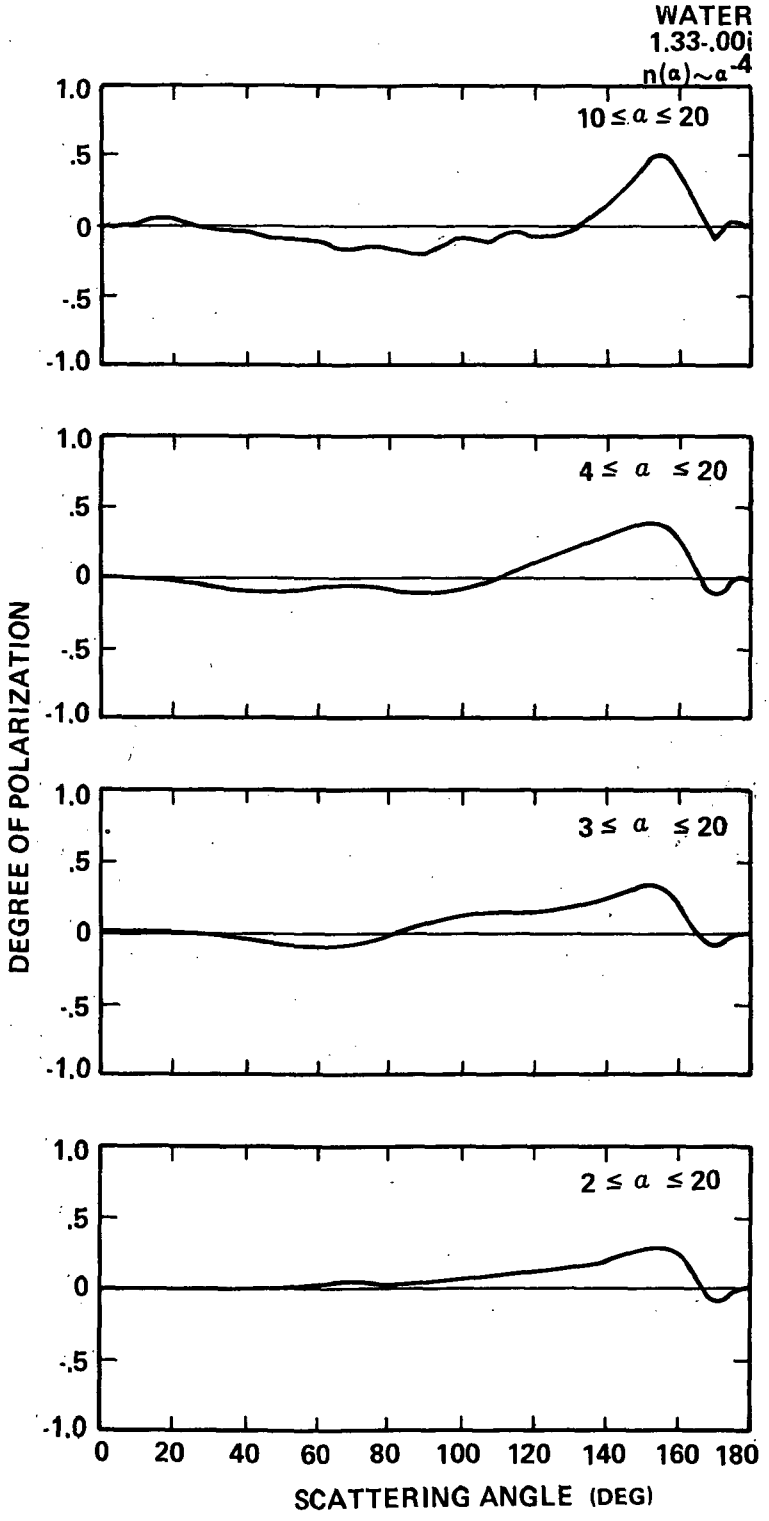

Figure 69. Polarization for water in distributions in which α_{min} = 2, 3, 4, and 10.

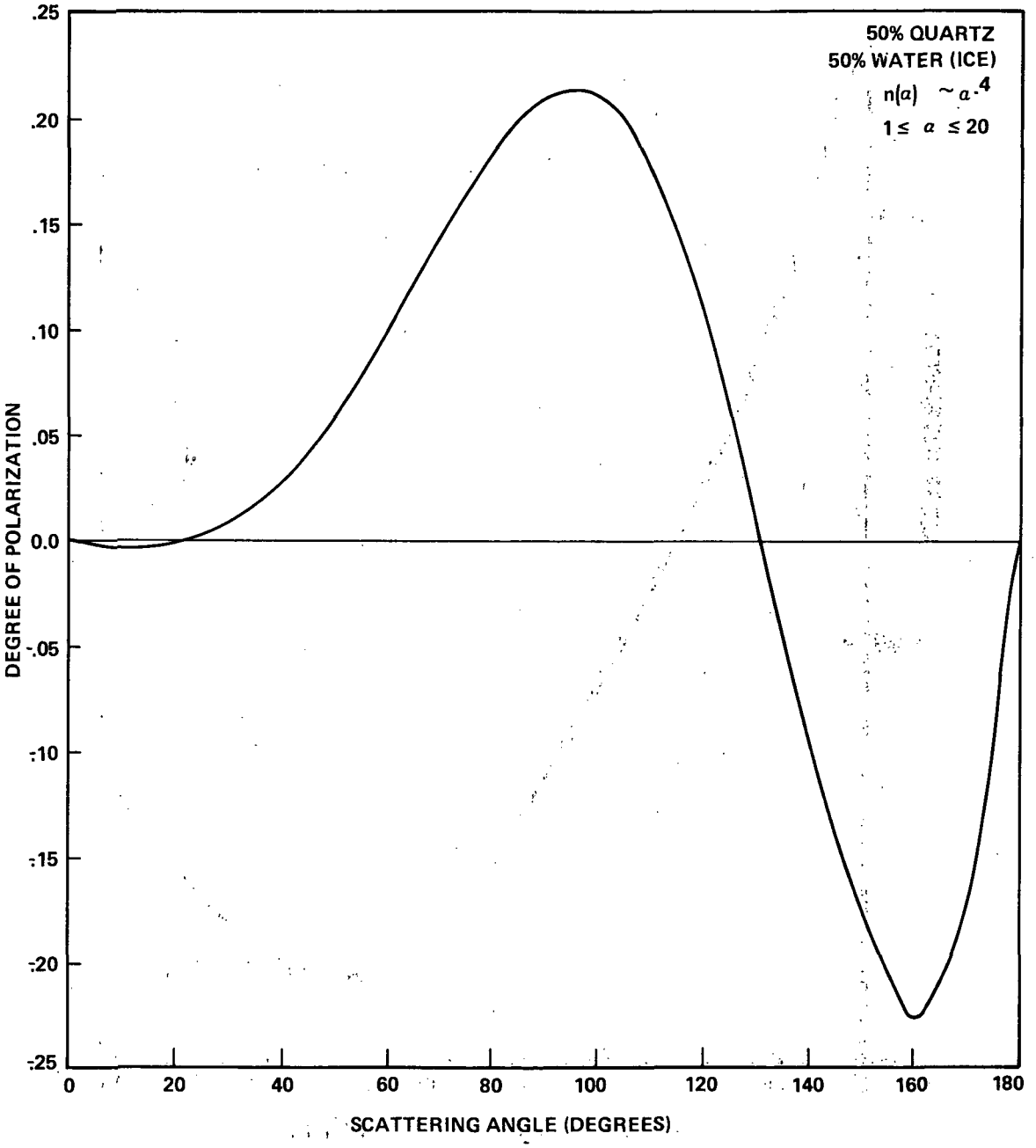

Figure 70. Polarization of 50-50 mixture of water and quartz.

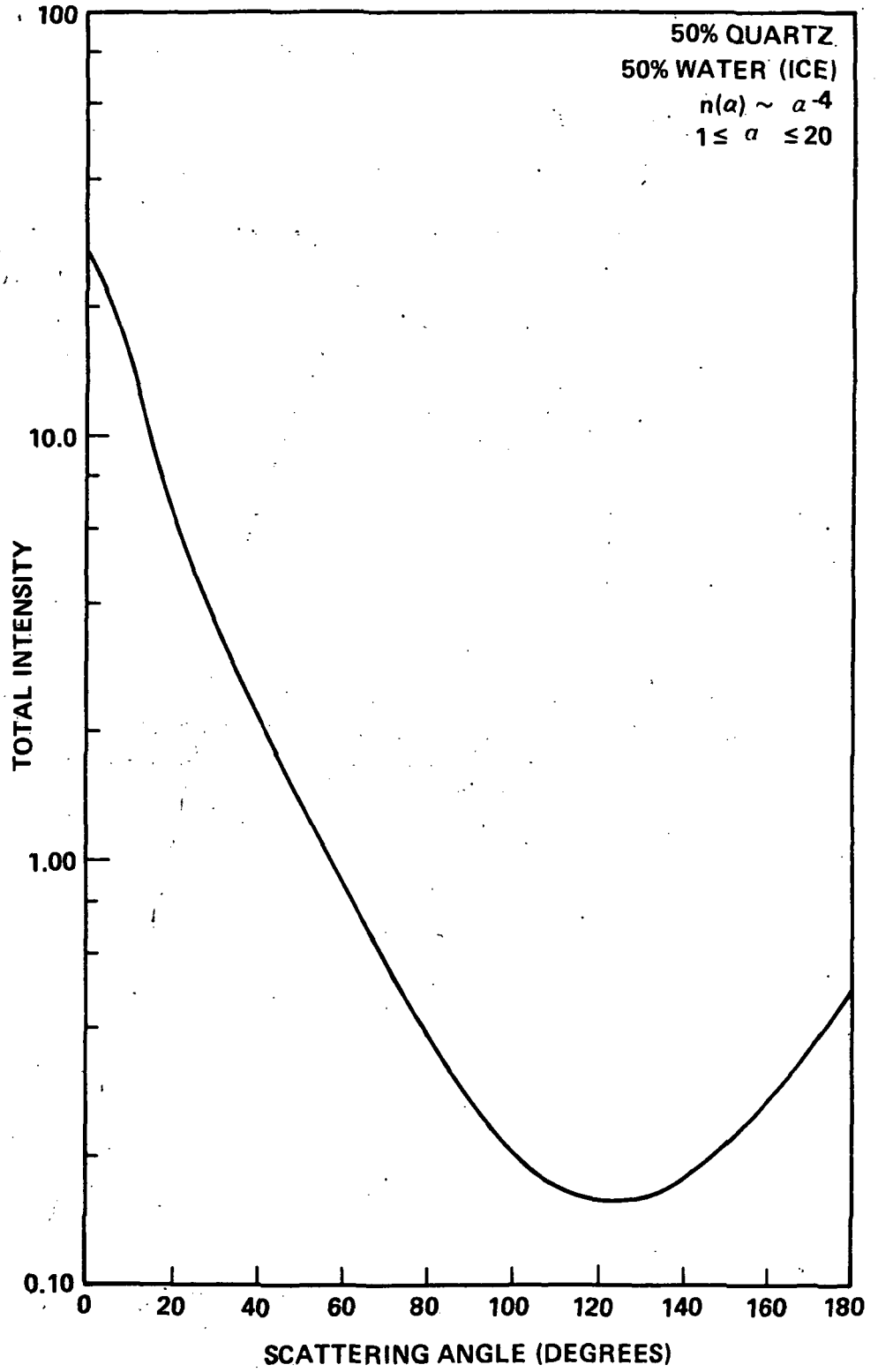

Figure 71. Radiance of 50-50 mixture of water and quartz.

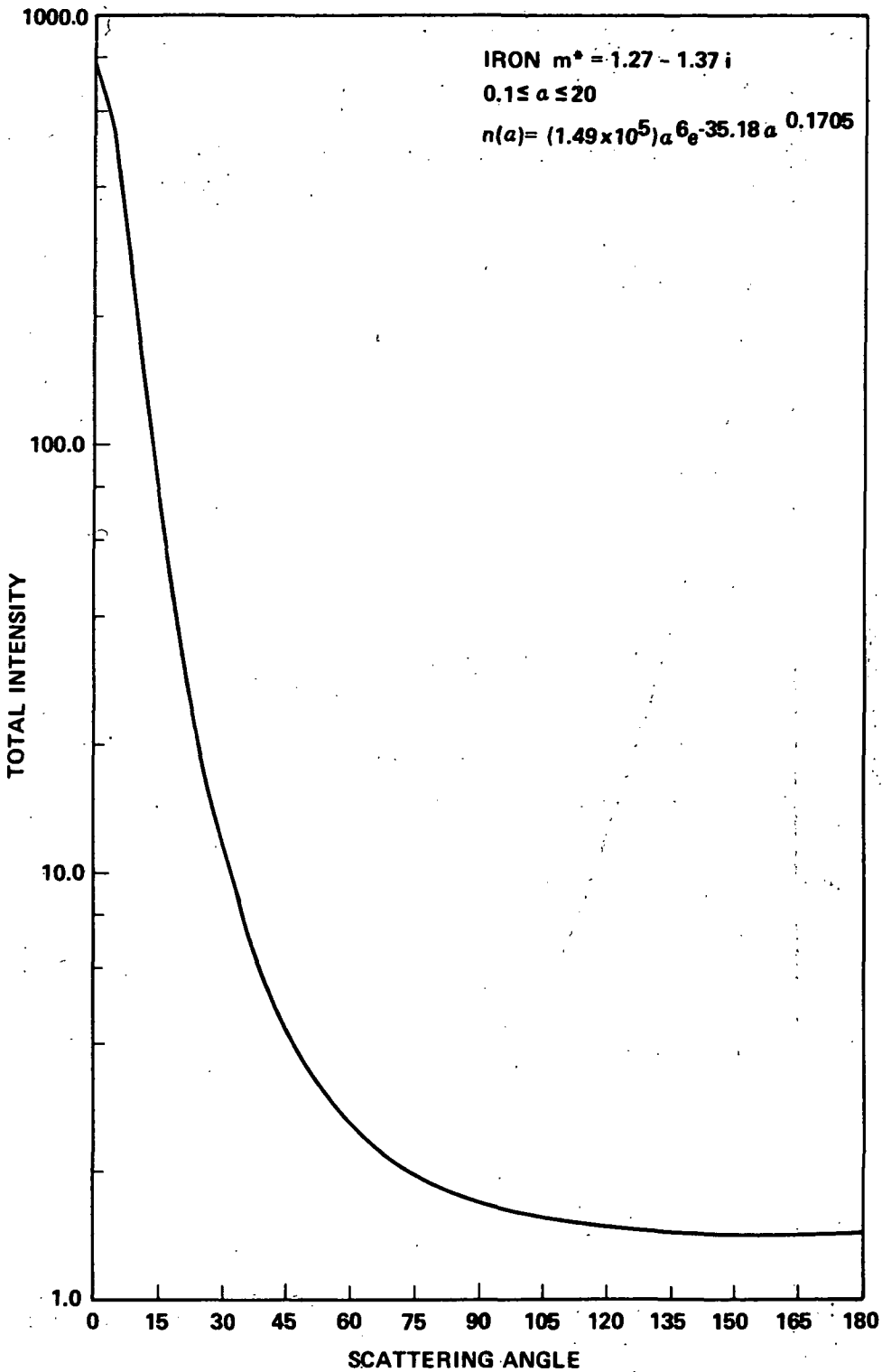

Figure 72a. Normalized scattered intensity versus angle for iron with a modified gamma-size distribution (Category I)

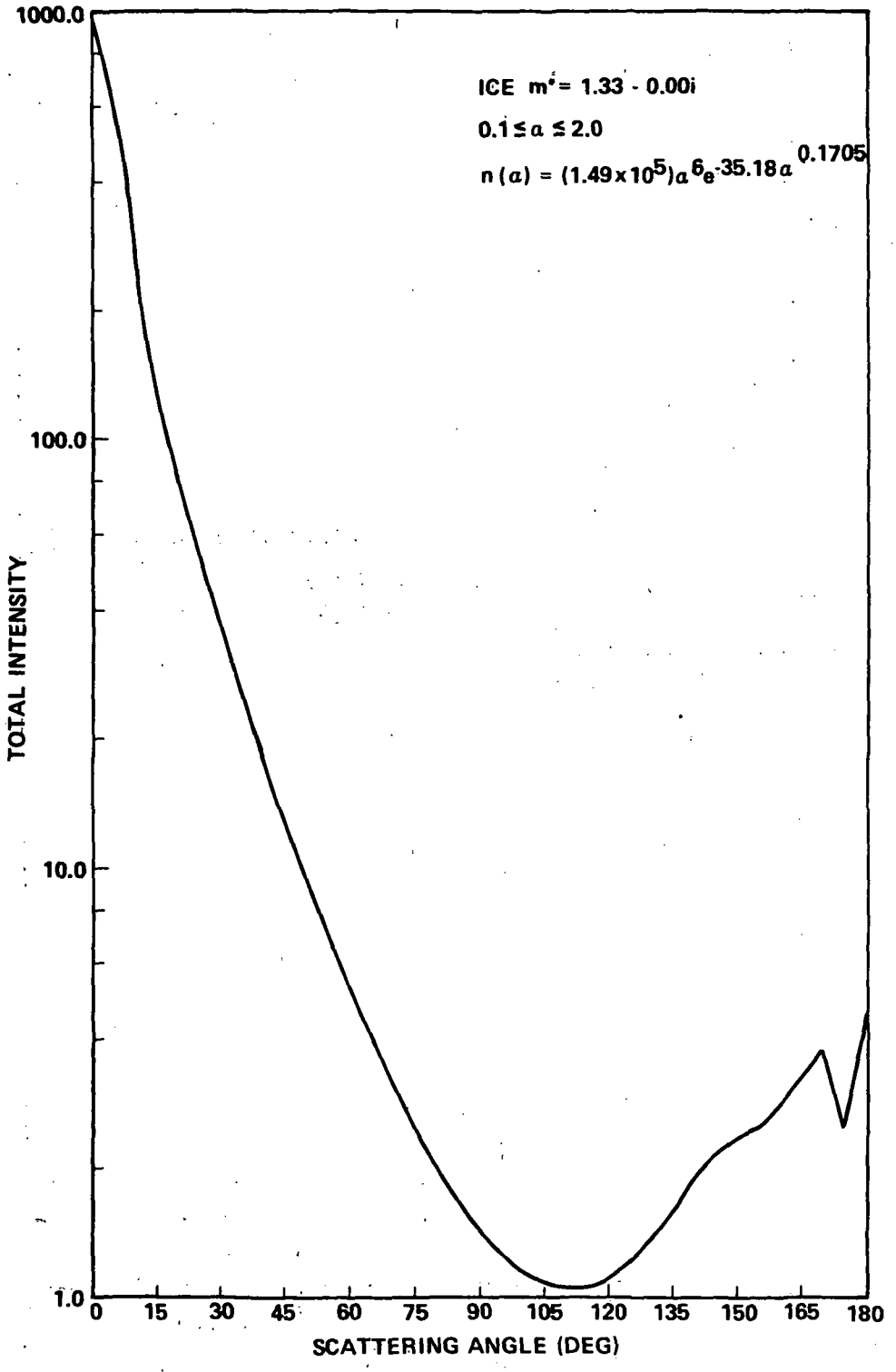

Figure 72b. Normalized scattered intensity versus angle for ice in a modified gamma distribution (Category I).

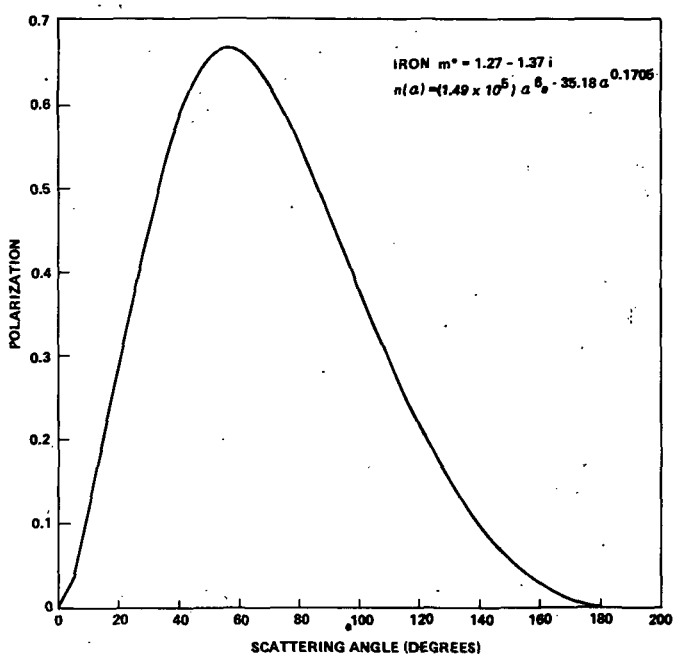

Figure 72c. Degree of polarization of iron in a modified gamma distribution (Category I).

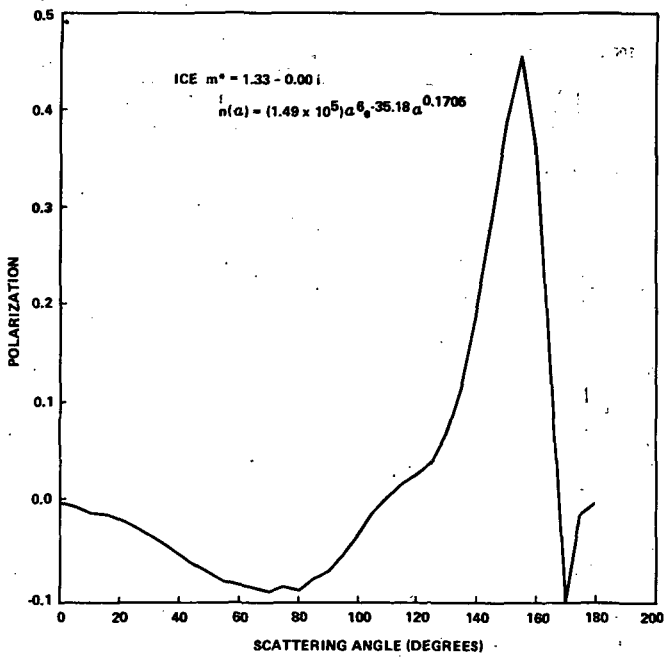

Figure 72d. Degree of polarization for ice in a modified gamma distribution (Category I).

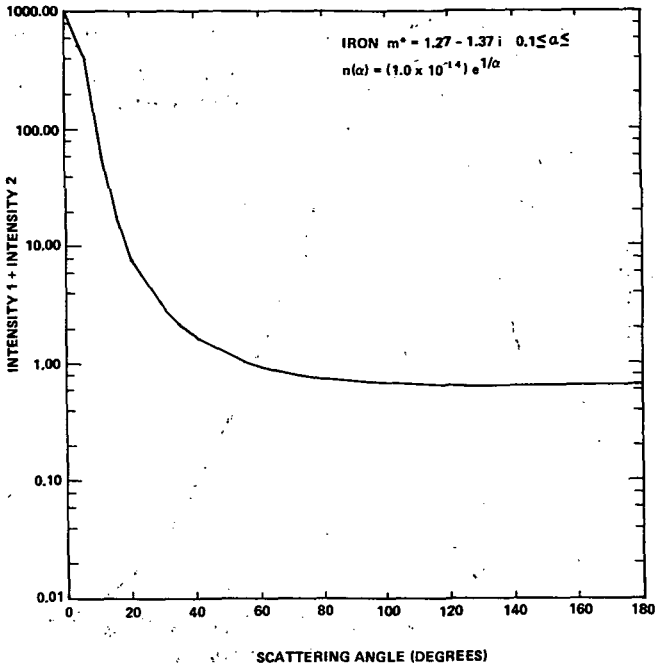

Figure 72e. Normalized scattered intensity versus angle for iron in an exponential size distribution (Category II).

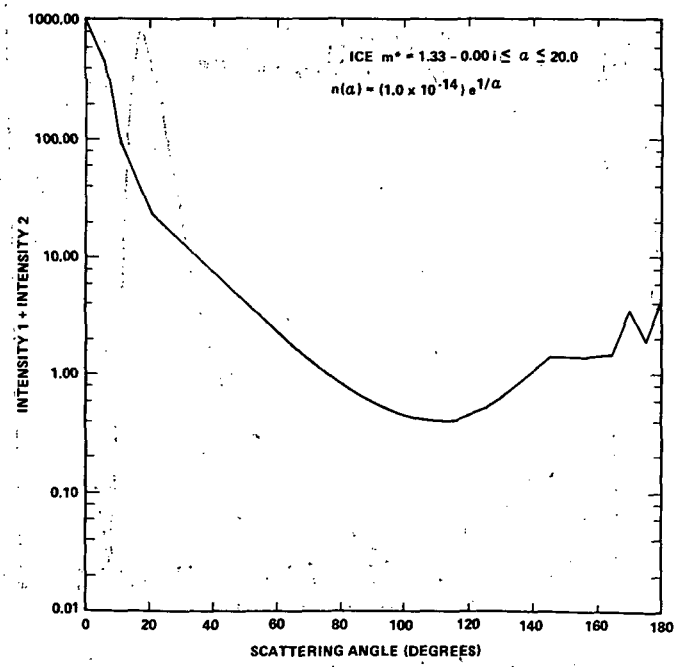

Figure 72f. Normalized scattered intensity versus angle for ice in an exponential size distribution (Category II).

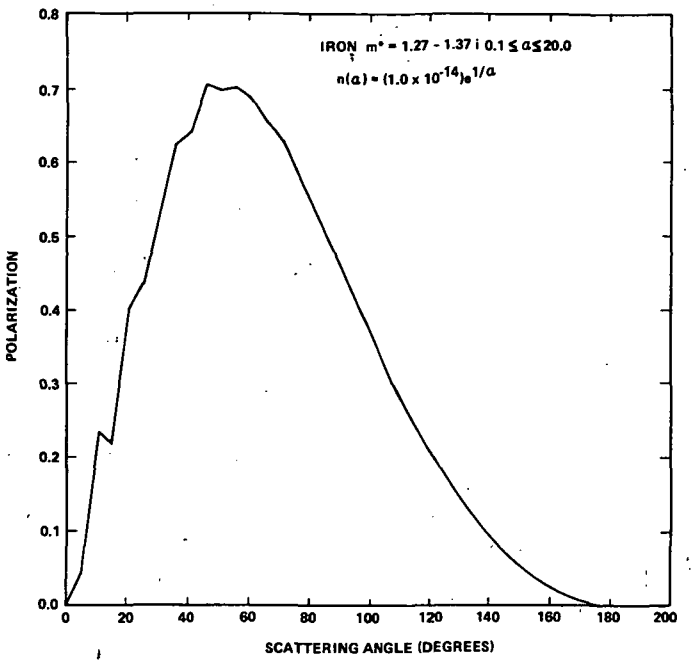

Figure 72g. Degree of polarization of iron in an exponential distribution (Category II).

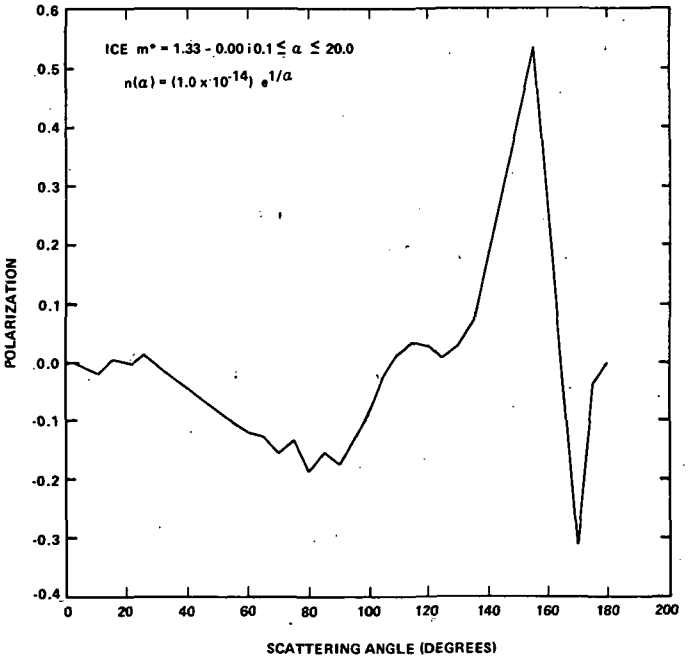

Figure 72h. Degree of polarization for ice in an exponential distribution (Category II).

$$n(\alpha) = 0.7041 \exp - \left(\frac{\ell n\, \alpha}{0.5\sqrt{2}}\right)^2 \quad .$$

A modal size parameter of $\bar{\alpha} = 1.0$ and a distribution width of $\sigma = 0.5$ were assumed. Kerker [24] points out that for a distribution such as this (shape factor m = 0) there is no structure in the radiance curves when σ is as large as used here. For the distributions he considered, a σ of 0.3 is the upper limit. For σ's smaller than this, maximum and minimum peaks did appear. Figures 72i through 72l shows the radiance and polarization as obtained from this distribution. As can be seen from the smooth radiance and polarization curves, the position of the peak values of degree of polarization and the low values of radiance, the smaller particles dominate this distribution. The dip at 175 deg in the radiance curve for ice does not appear. This dip is apparently due to particles with $\alpha > 5$. In this distribution, the number of particles with $\alpha > 5$ is very small.

J. Ecliptic Zodiacal Light Models

Mie theory has been used in models of the zodiacal light to calculate the components of the scattering intensity functions. Although the particles are restricted to spheroids, the models are on much firmer footing than those based on empirical laws. In a series of papers, Giese et al. [16, 26, 32, 35] considered the photometric properties of different models by the use of Mie theory. This section closely follows these papers.

Start with the basic equation for the radiance of the zodiacal light [equation (33)] of the heliocentric model restricting the region of interest to the ecliptic plane.

$$\bar{L}_\lambda = \frac{R\, E_\lambda^e\, \delta_\lambda\, N_o}{\sin^{m+1} \epsilon} \int_\epsilon^\pi \sin^m \Theta \left(\overline{\frac{d\sigma}{d\Omega}}\right) d\Theta \ , \tag{172}$$

where

$$\left(\overline{\frac{d\sigma}{d\Omega}}\right) = \frac{1}{N_o} \int_{a_{min}}^{a_{max}} n_o \left(\frac{a}{a_o}\right)^{-p} \left(\frac{d\sigma}{d\Omega}\right) da$$

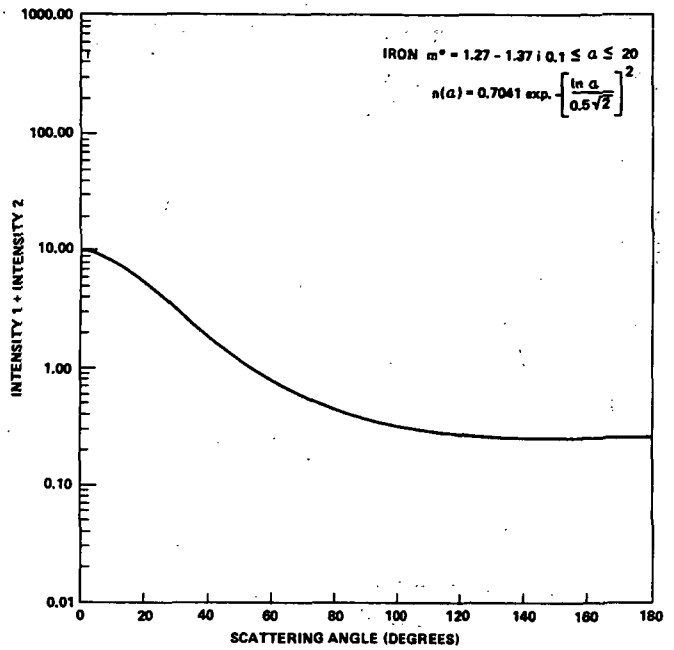

Figure 72i. Normalized scattered intensity versus angle for iron with a logarithmic (shape factor m = 0) size distribution (Category III).

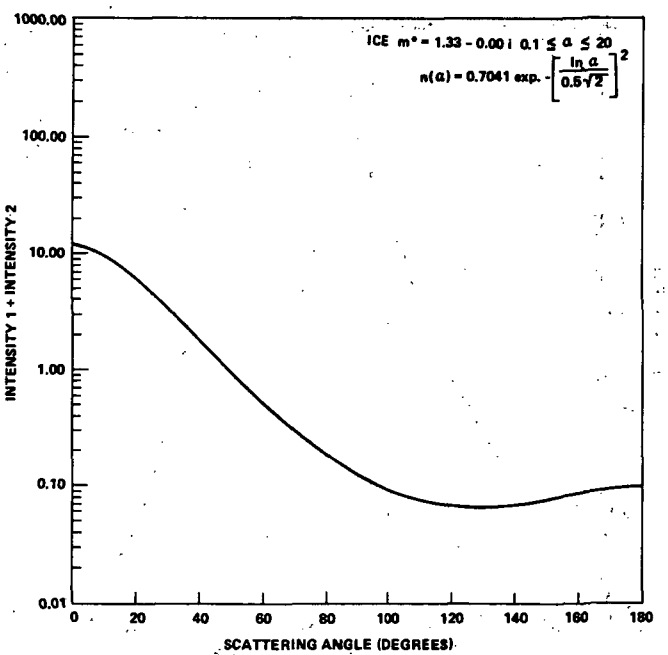

Figure 72j. Normalized scattered intensity versus angle for ice in a logarithmic (shape factor m = 0) size distribution (Category III).

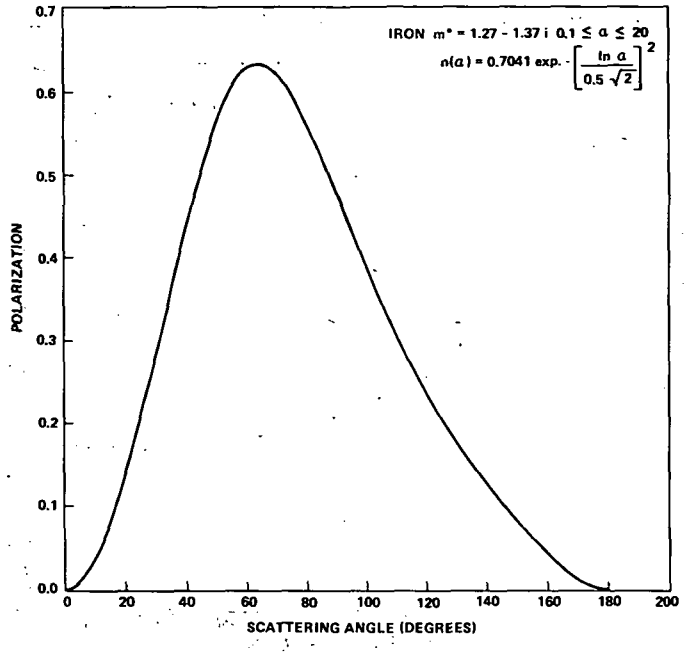

Figure 72k. Degree of polarization of iron in a logarithmic (shape factor m = 0) distribution (Category III).

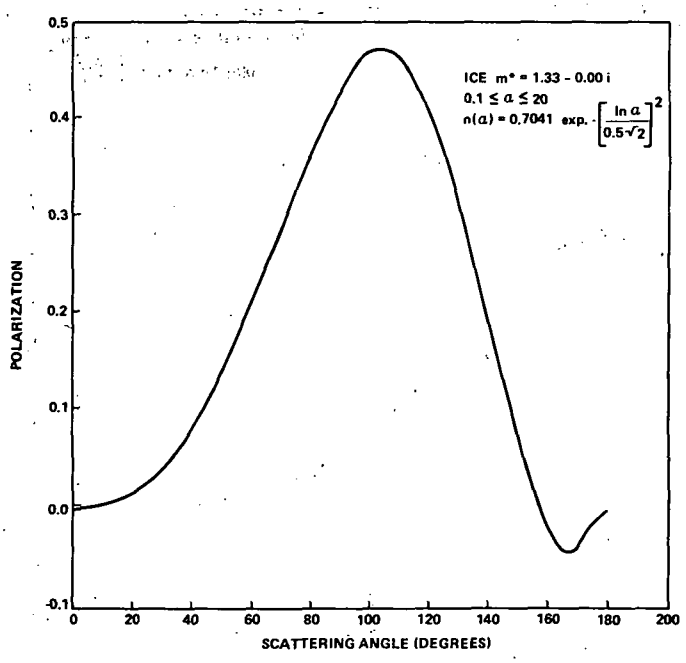

Figure 72l. Degree of polarization for ice in a logarithmic distribution (shape factor m = 0) (Category III).

and

$$N_o = \int_{a_{min}}^{a_{max}} n_o \left(\frac{a}{a_o}\right)^{-p} da \quad .$$

From these equations, one sees that the model parameters are:

n_o = number density parameter.

a_o = size distribution parameter.

a_{max} = maximum particle size.

a_{min} = minimum particle size.

p = size distribution exponent.

m = spatial distribution exponent.

This general model assumes a density distribution of the form

$$\eta(a, r) = n_o r^{-m} a^{-p} \quad .$$

A specific model calculation requires the selection of the refractive indices, or equivalently the selection of the material composition, and the percentages of each material selected. A series of selections and iterations will probably be needed before a model satisfying observations is obtained.

Before considering different compositions, a single material (ice) will be considered and the above parameters varied. N_o is varied to obtain a match to the magnitude of the observed radiance. The parameters a_{min}, a_{max}, p , and m are varied to study their effects on the elongation dependence of the radiance and polarization.

For a_{max} small, all particles will scatter light approximately according to the Rayleigh law. The calculated radiance from a distribution of small particles ($0.01 < \alpha < 0.1$) with m = 1, p = 4.0, and $N_o = 5 \times 10^{-2}$ particles/ cm^3 is shown in Figure 73. The number density

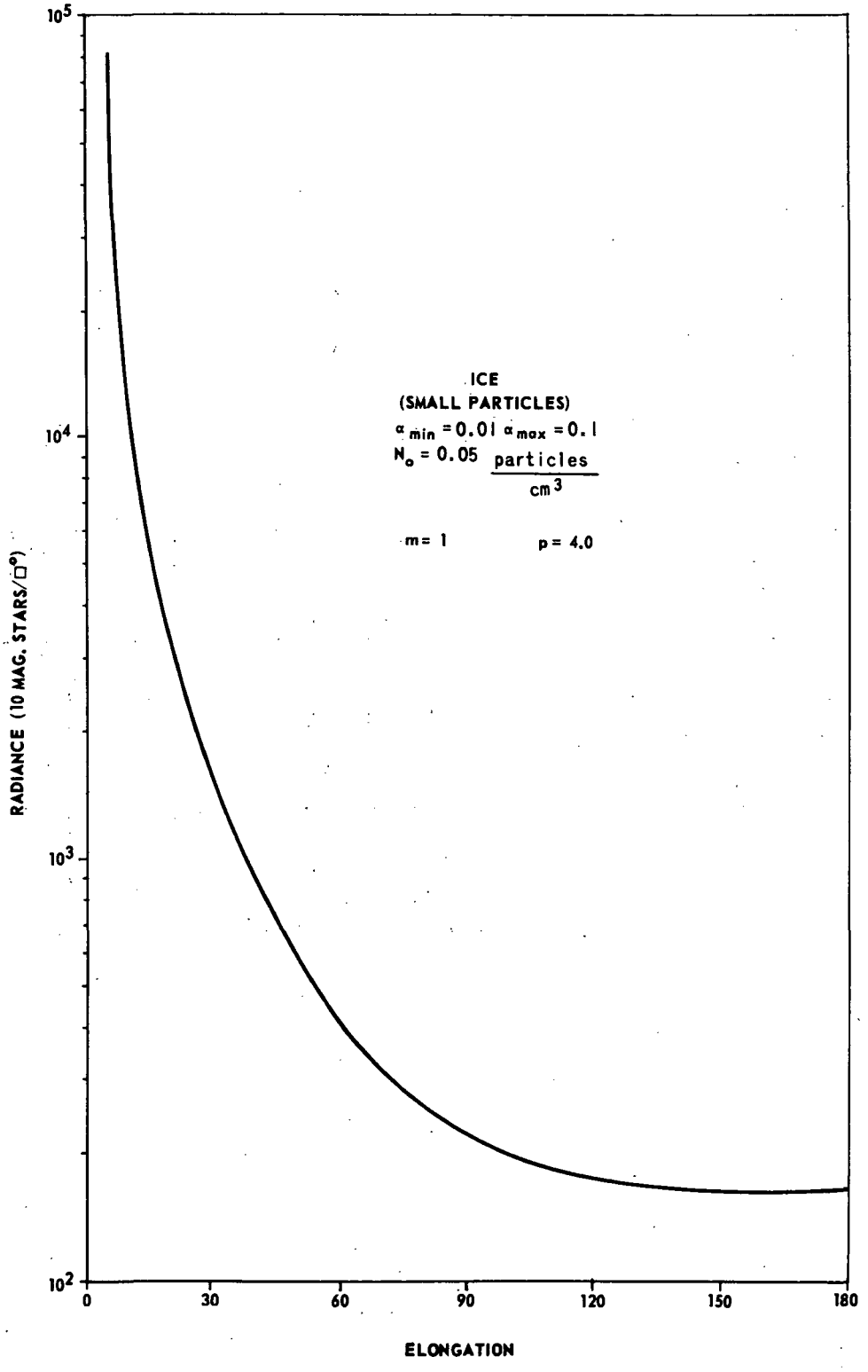

Figure 73. The radiance dependence for very small ($\alpha = 0.01 - 0.1$) ice particles ($N_o = 0.05$ particles/cm^3, m = 1, and p = 4).

$$N_o = \frac{\lambda}{2\pi} \int_{\alpha_{min}}^{\alpha_{max}} n_o \left(\frac{\alpha}{\alpha_o}\right)^{-p} d\alpha \quad , \tag{173}$$

is calculated at a wavelength of $\lambda = 0.5\,\mu m_o$ and α_o is set equal to 1.

The variation of radiance with elongation roughly follows the observed dependence with the obvious discrepancy at $\epsilon = 180$ deg. The polarization is shown in Figure 74. Since the scattering intensity functions for electrons behave according to the Rayleigh theory, this distribution of small particles is equivalent to approximately 1.1×10^3 electrons/cm^3, a value which is too high [57, 58]. The polarization is large for $\epsilon < 90$ deg. It peaks at 60 deg with a value of 0.60 which is three times greater than the observed value.

In Figures 75 and 76, α_{max} is varied while $\alpha_{min} = 1$. For a particle distribution of α^{-p}, the radiance and polarization do not have a strong dependence on particles with α greater than 10 (Part I of this section). In Figure 75, the radiance curve for $\alpha_{max} = 20$ is very close to that for $\alpha_{max} = 10$. The curve labeled "coarse" uses a 16-point Gaussian integration procedure which has been used in most cases in this study to save computer time. Although the coarse integration gives some false features, it is felt that the comparisons made are still valid.

As one would have anticipated from the single particle and distribution results, the variation of α_{min} with α_{max} fixed affects the degree of polarization strongly, as shown in Figures 77 and 78 [22]. The increase of the radiance (Fig. 77) with increasing α_{min} is due to holding N_o a constant and to the greater scattering efficiency per particle for the large particles.

Figures 79 and 80 show the results of varying the spatial dependence parameter m. The radiance increases for $\epsilon \lesssim 50$ deg as m increases and decreases for $\epsilon > 50$ deg as m increases. Polarization increases with m. From the earlier study of

$$I_m(\epsilon) = \frac{1}{\sin^{m+1}\epsilon} \int_{\epsilon}^{\pi} \sin^m(\Theta)\, d\Theta \quad ,$$

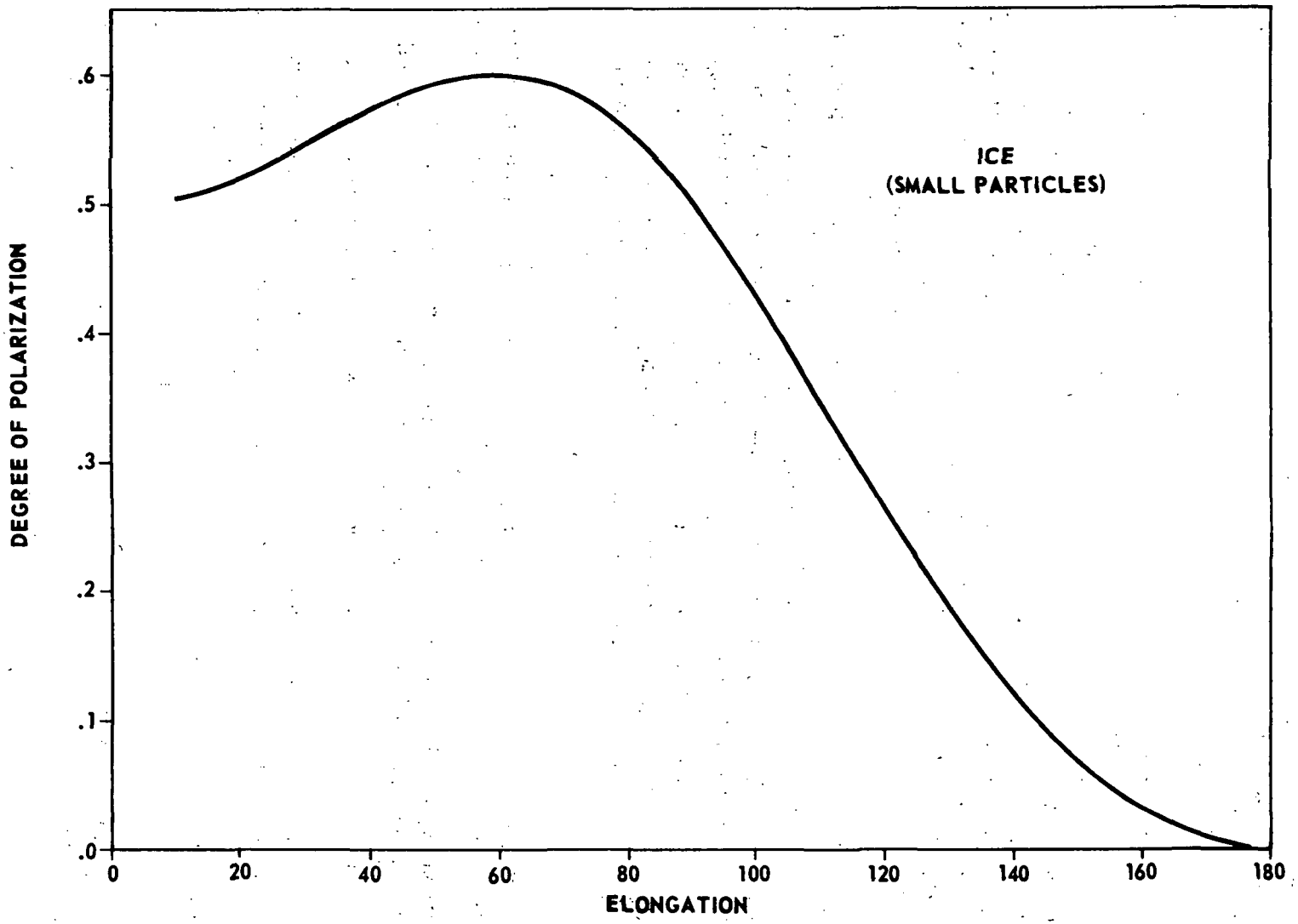

Figure 74. Degree of polarization for very small (α = 0.01 - 0.1) ice particles (N_o = 0.05 particles/cm^3, m = 1, and p = 4).

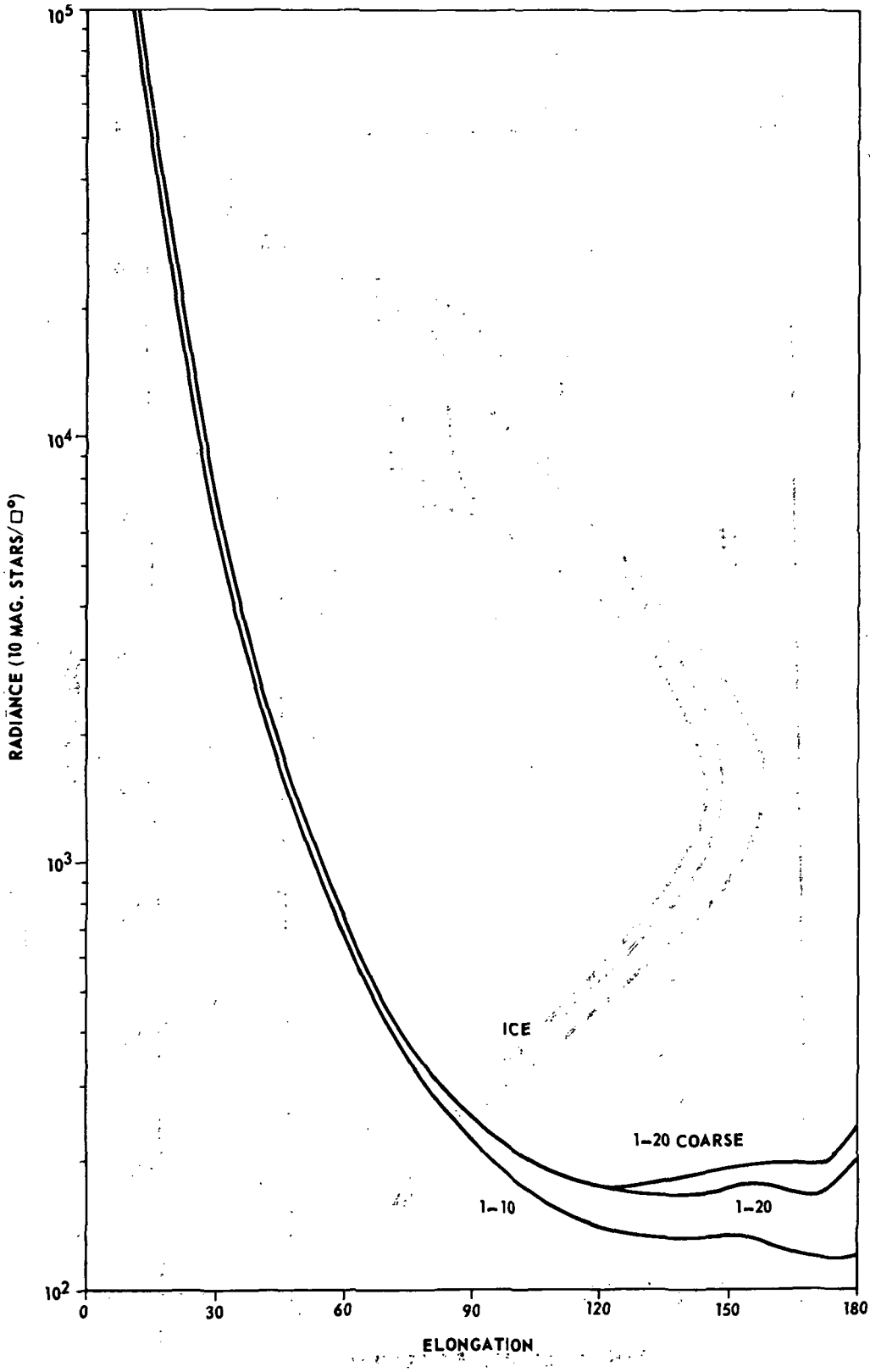

Figure 75. Radiance for a variation of α_{max} by 96-point Gaussian. [Coarse implies a 16-point Gaussian integration ($N_o = 1.5 \times 10^{-11}$ particles/cm^3, m = 1, p = 4, and $\alpha_{min} = 1$).]

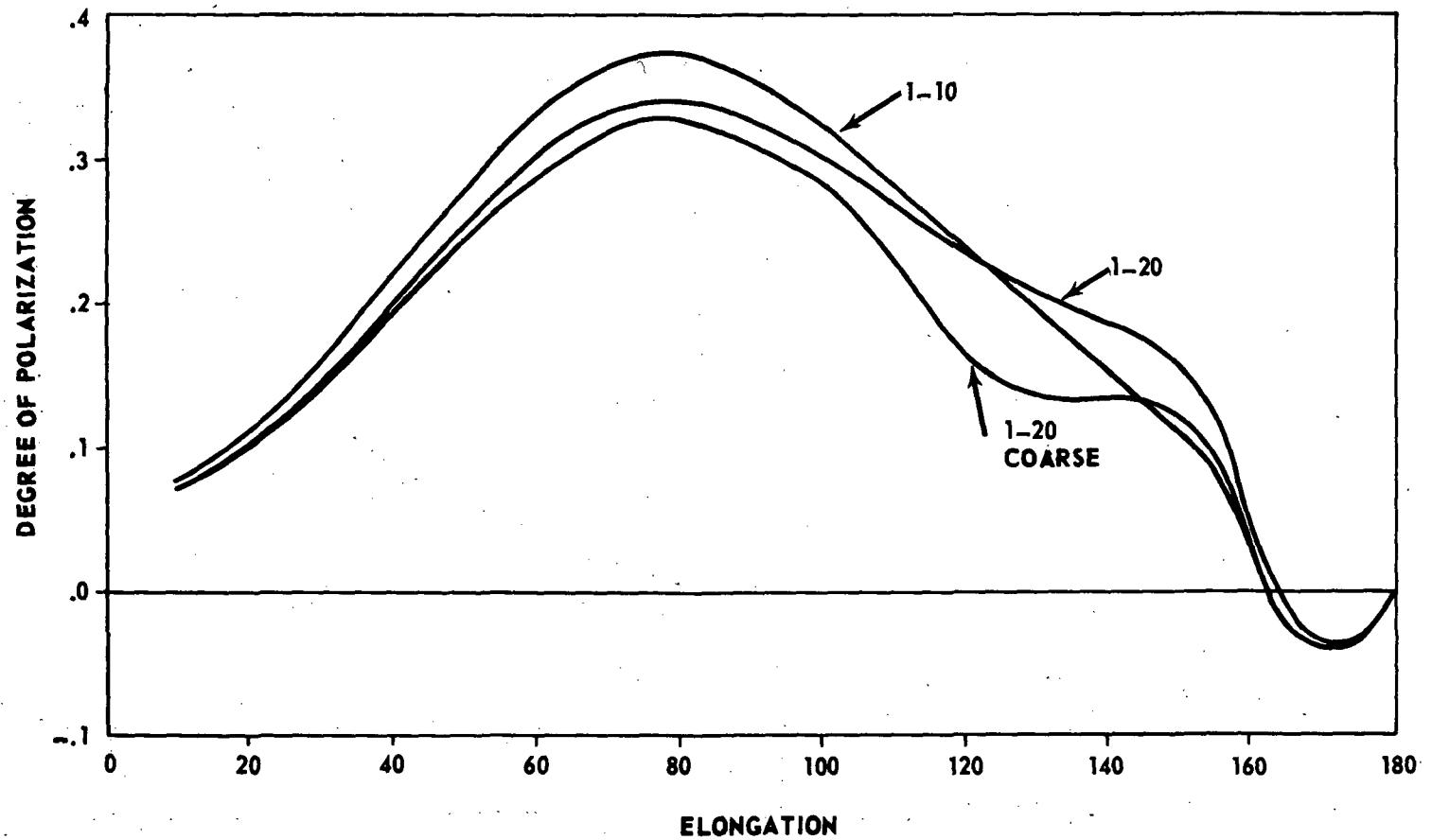

Figure 76. Degree of polarization for a variation of α_{max} for Figure 75.

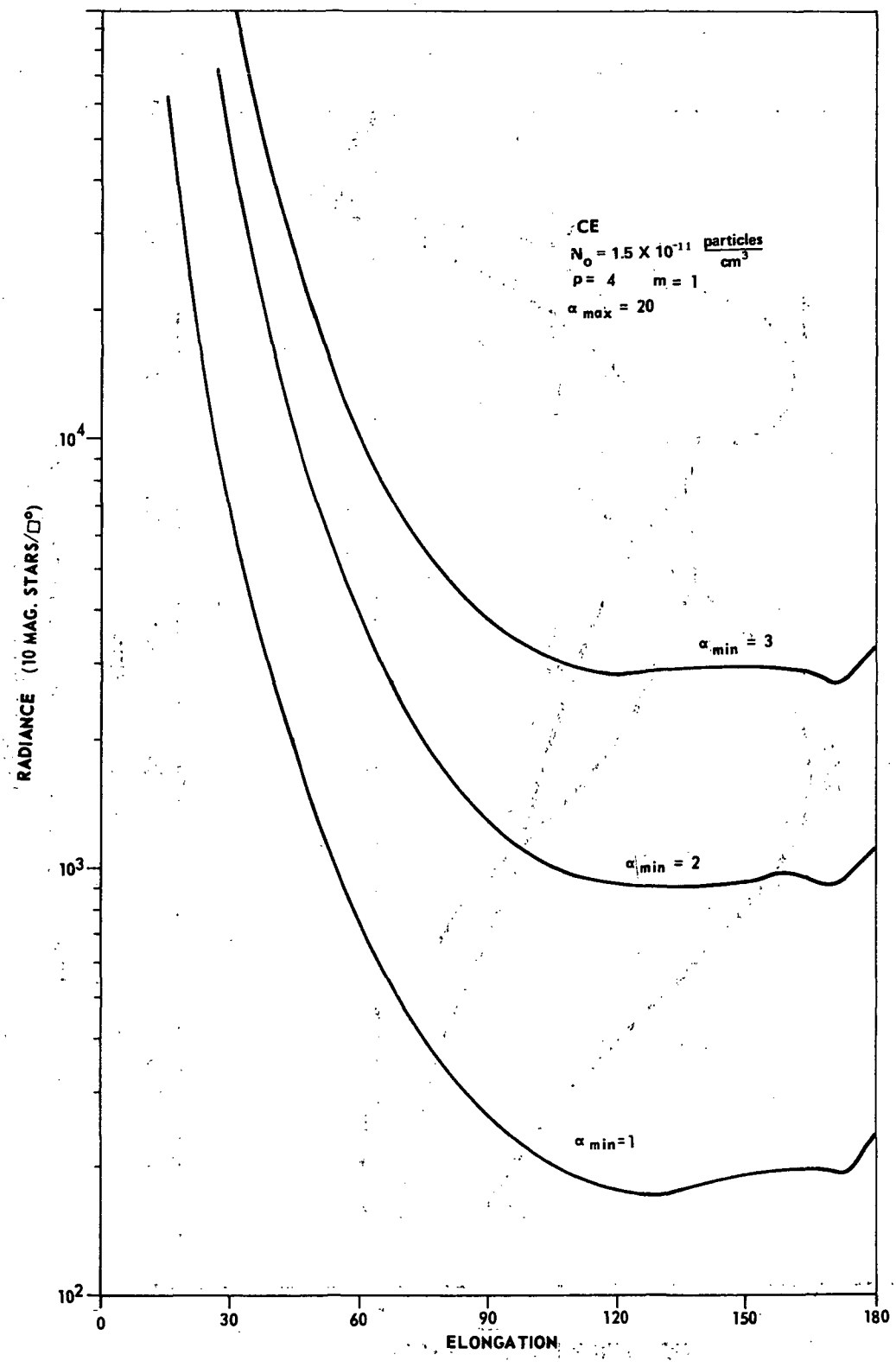

Figure 77. Radiance for a variation of α_{min}.

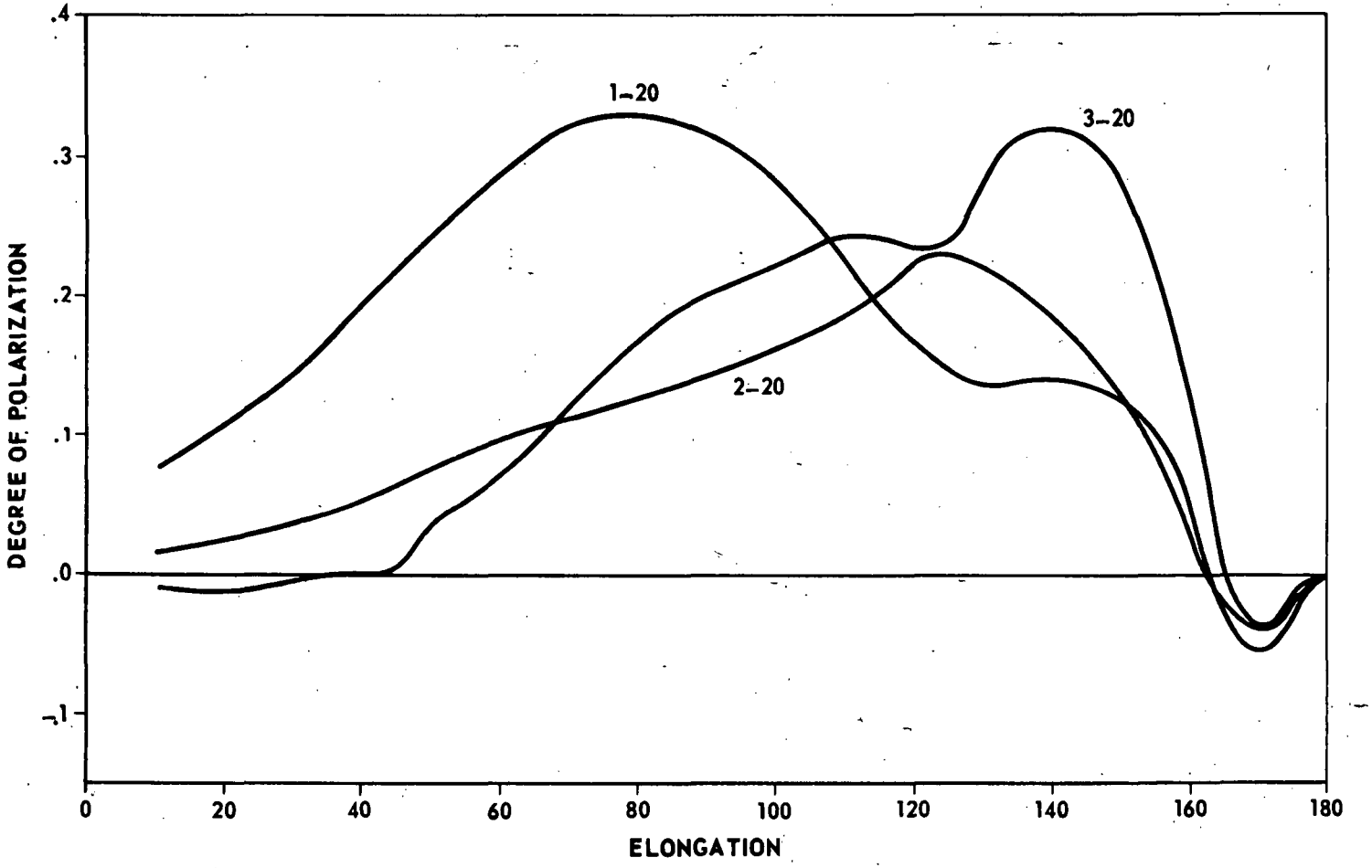

Figure 78. Degree of polarization for variation of α_{min} for Figure 77.

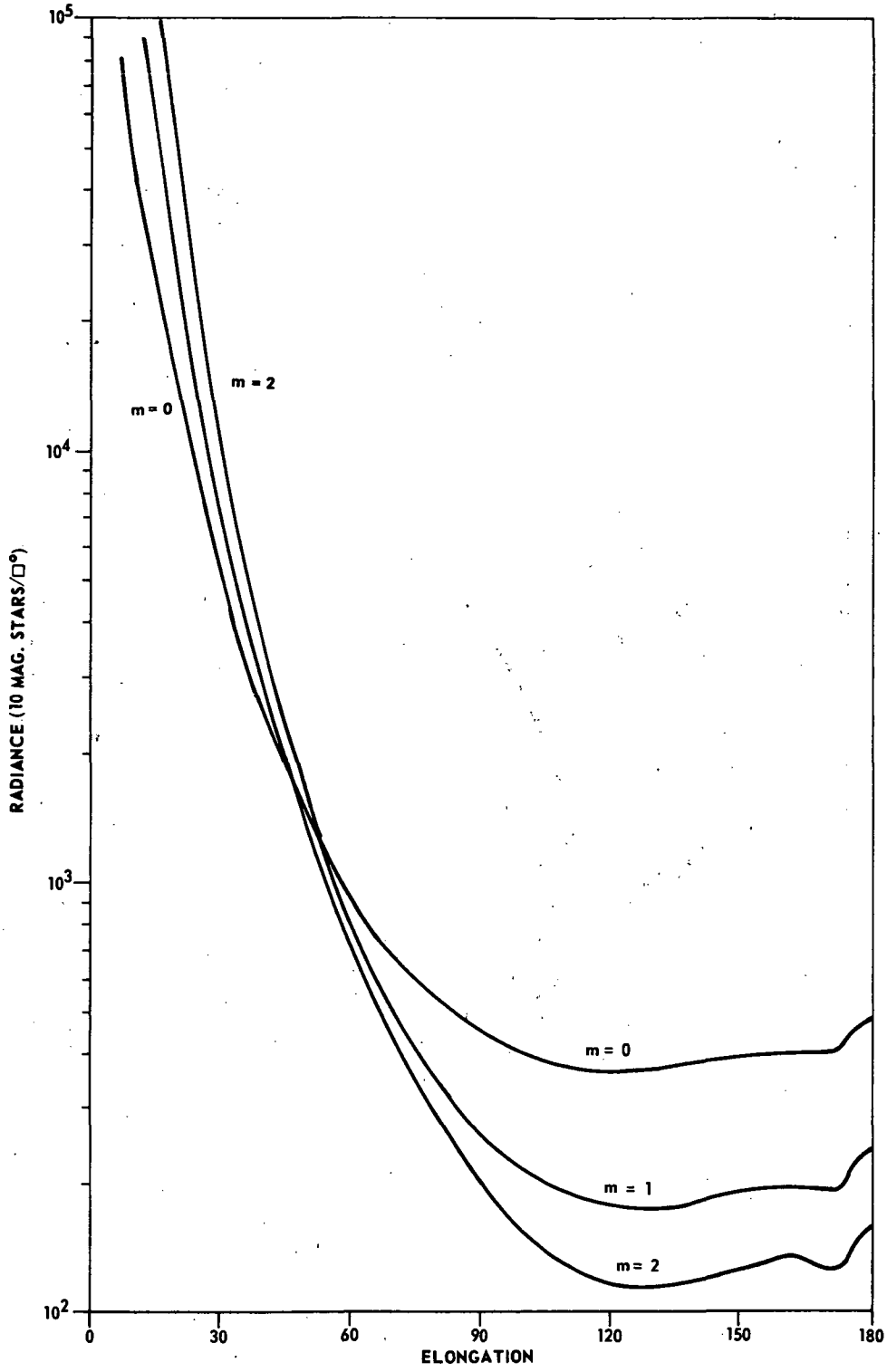

Figure 79. Radiance for a variation of m ($N_o = 1.5 \times 10^{-11}$, p = 4, $\alpha_{min} = 1$, and $\alpha_{max} = 20$).

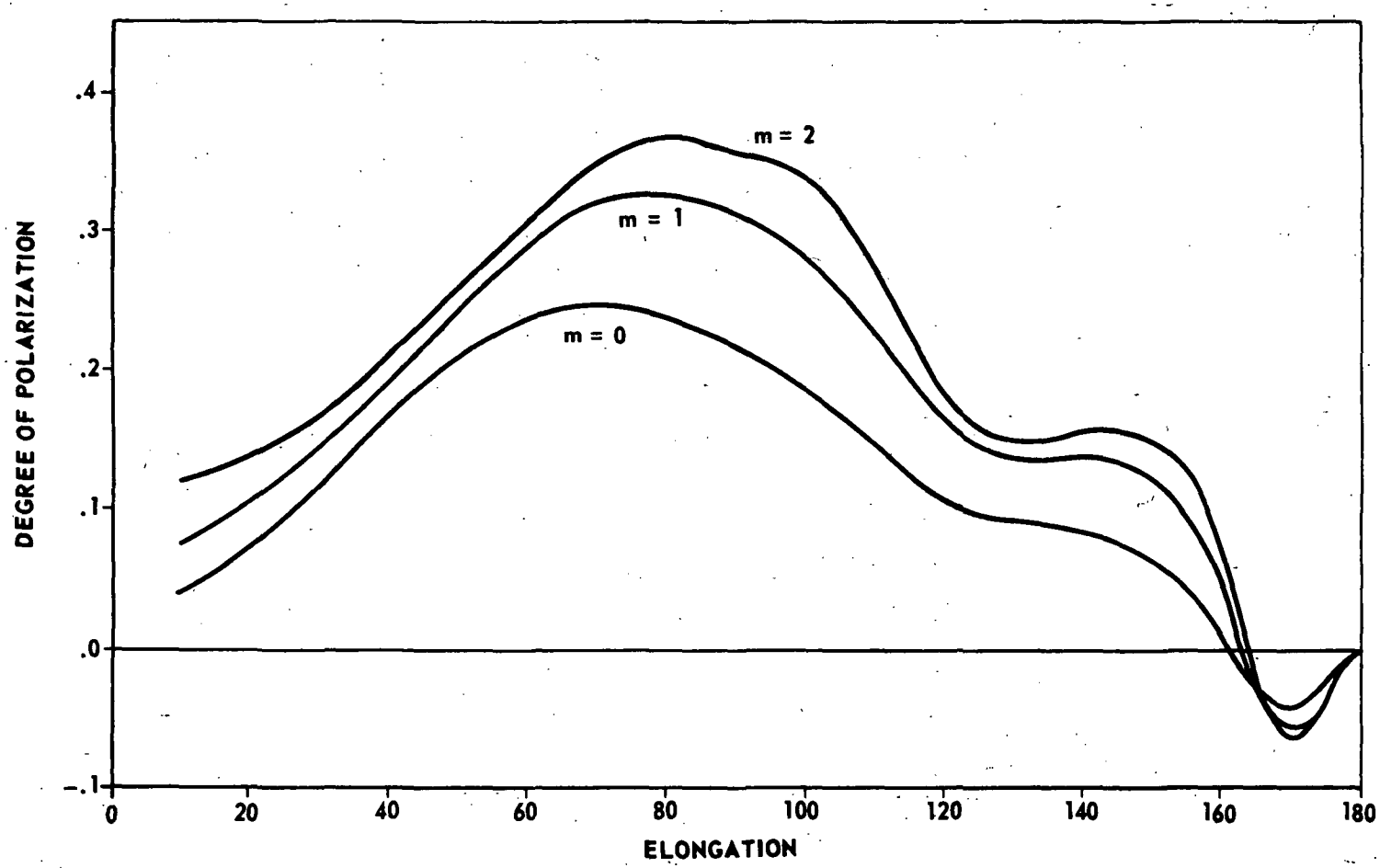

Figure 80. Degree of polarization for a variation of m for Figure 79.

it was noted that

$$I_m(\epsilon = \pi) = \frac{1}{m+1} \quad ,$$

which shows the inverse dependence of the radiance on m at ϵ = 180 deg. The increase of radiance toward the sun is caused by the increase in particle number (i.e., increasing m). The increase of polarization with increasing m results from having less smoothing effects along the line of sight, since for higher m the contribution to the polarization by the larger scattering angles decreases. For comparison purposes, the results of Giese [26] and Giese and Siedentopf [16, 84] for the variation of m are shown in Figure 81. Their calculations are based on particle sizes that go from α = 2 to α = 120; however, the variational dependence is the same as shown in Figures 79 and 80.

Table 24 compares the exponential gradient for the variations of m and p for the range of 30 to 60 deg. κ is directly related to an increase in m and varies weakly with an increase in p. The variation with p is shown in Figures 82 and 83. Increasing p gives more weight to the smaller particle sizes in the distribution. These particles have lower scattering efficiencies and a Rayleigh-like polarization. The decrease in scattering efficiency causes the radiance curves to be lower for higher p. Likewise, the higher p, the polarization peak increases and shifts towards 90 deg when Rayleigh-type particles are included (cf. Ref. 22). Giese's results for varying p are shown in Figure 84. Except for the changes in magnitude of the radiance and polarization, the dependence on p is the same. An explanation for the lack of changes in the shape of Giese's curves for quartz and ice as compared to Figures 82 and 83 is that his distributions, in starting from α = 6 and α = 12, eliminate the particles which contribute most to the change. The structure of the curves for iron does not change because the scattering cross section after $\alpha \simeq 5$ is more stable than that for dielectrics.

TABLE 24. EXPONENTIAL GRADIENT (30 TO 60 DEG) FOR ICE

	κ		κ
m = 0	2.6	p = 3	3.3
1	3.3	4	3.3
2	3.9	5	3.2
p = 4		m = 1	

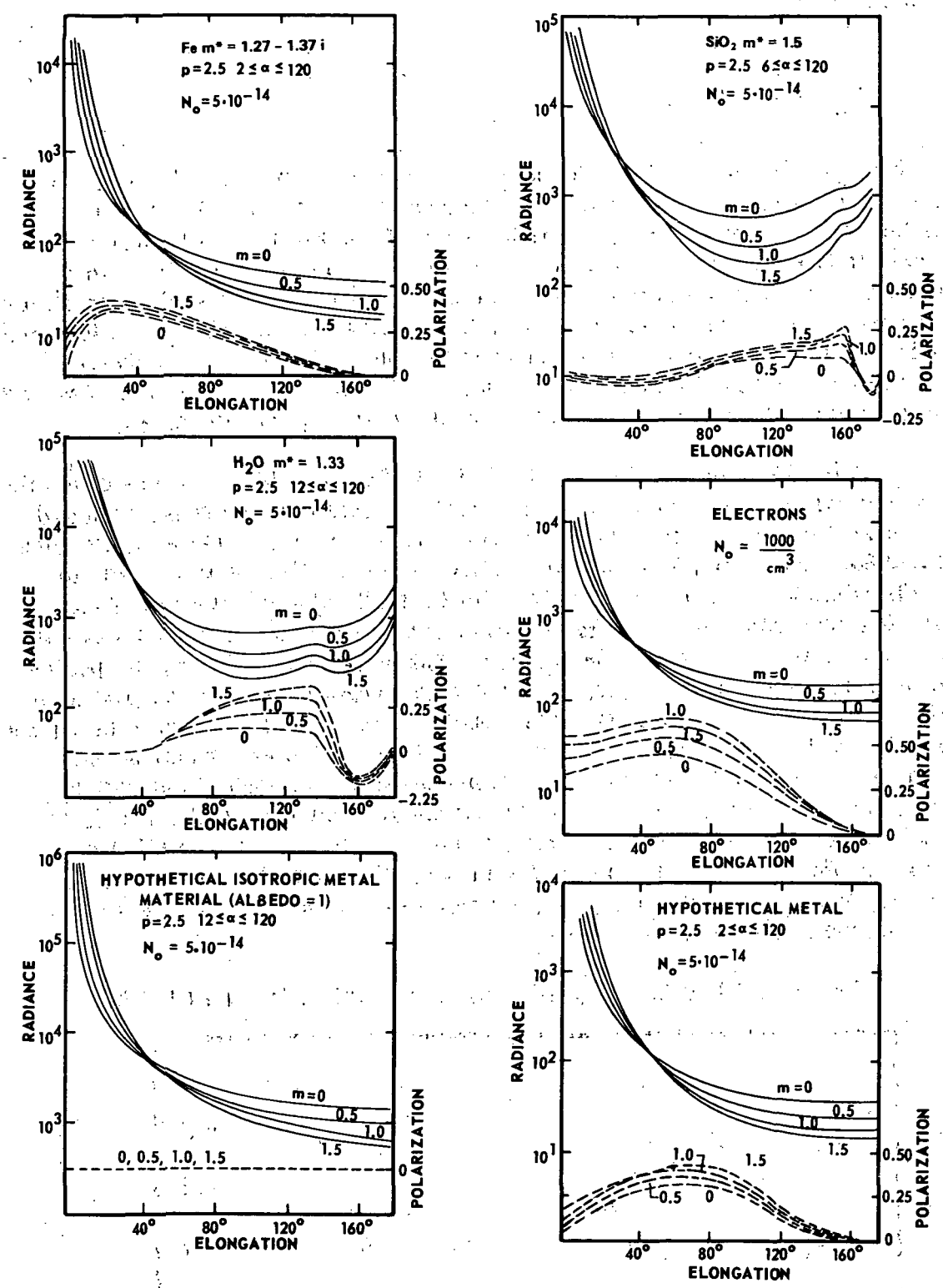

Figure 81. Giese and Siedentopf's results for m variation [16, 84].

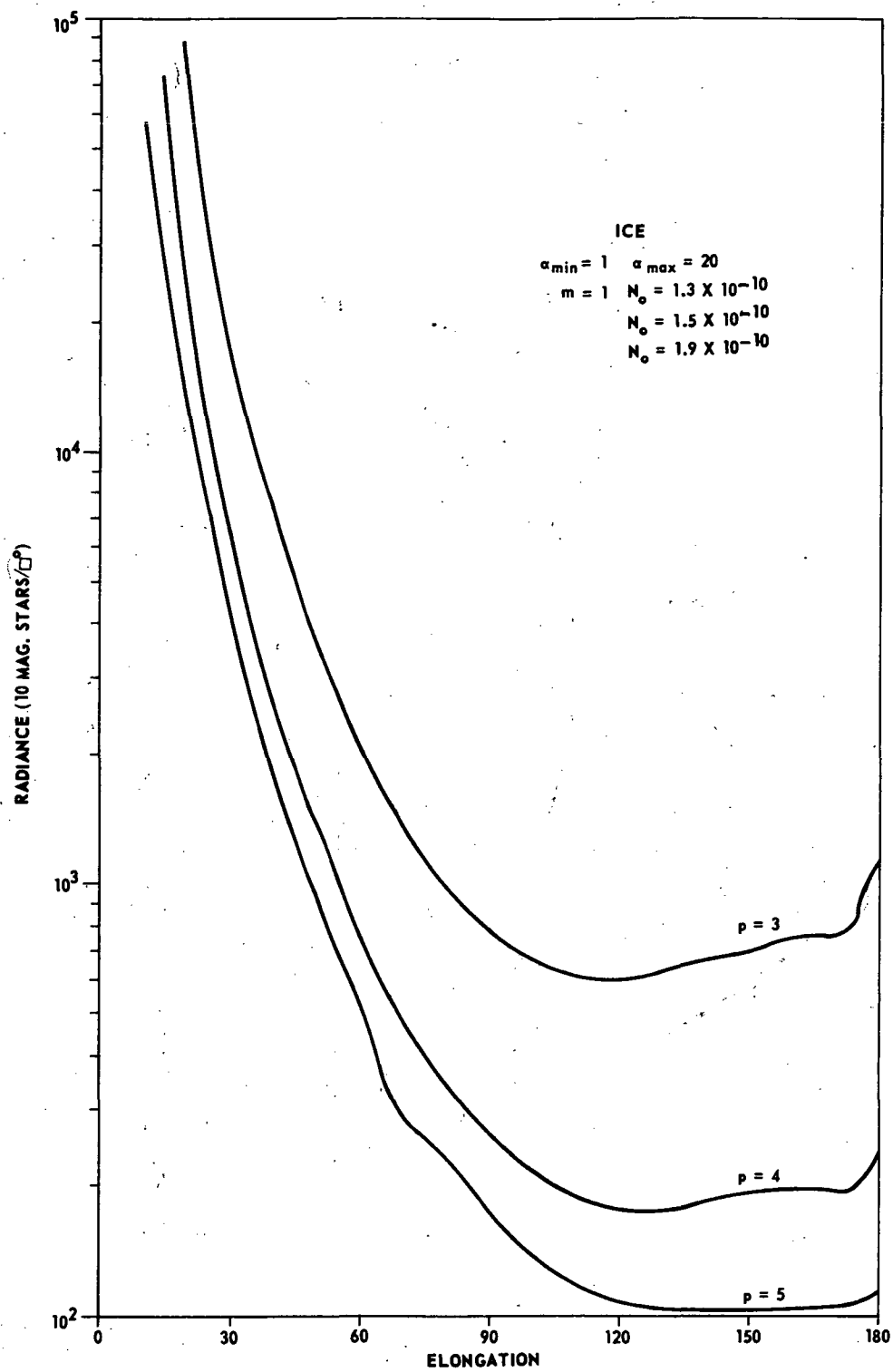

Figure 82. Radiance for a variation of p ($p = 3$, $N_o = 1.3 \times 10^{-10}$, $p = 4$, $N_o = 1.5 \times 10^{-10}$, $p = 5$, $N_o = 1.9 \times 10^{-10}$, $m = 1$, $\alpha_{min} = 1$, $\alpha_{max} = 20$).

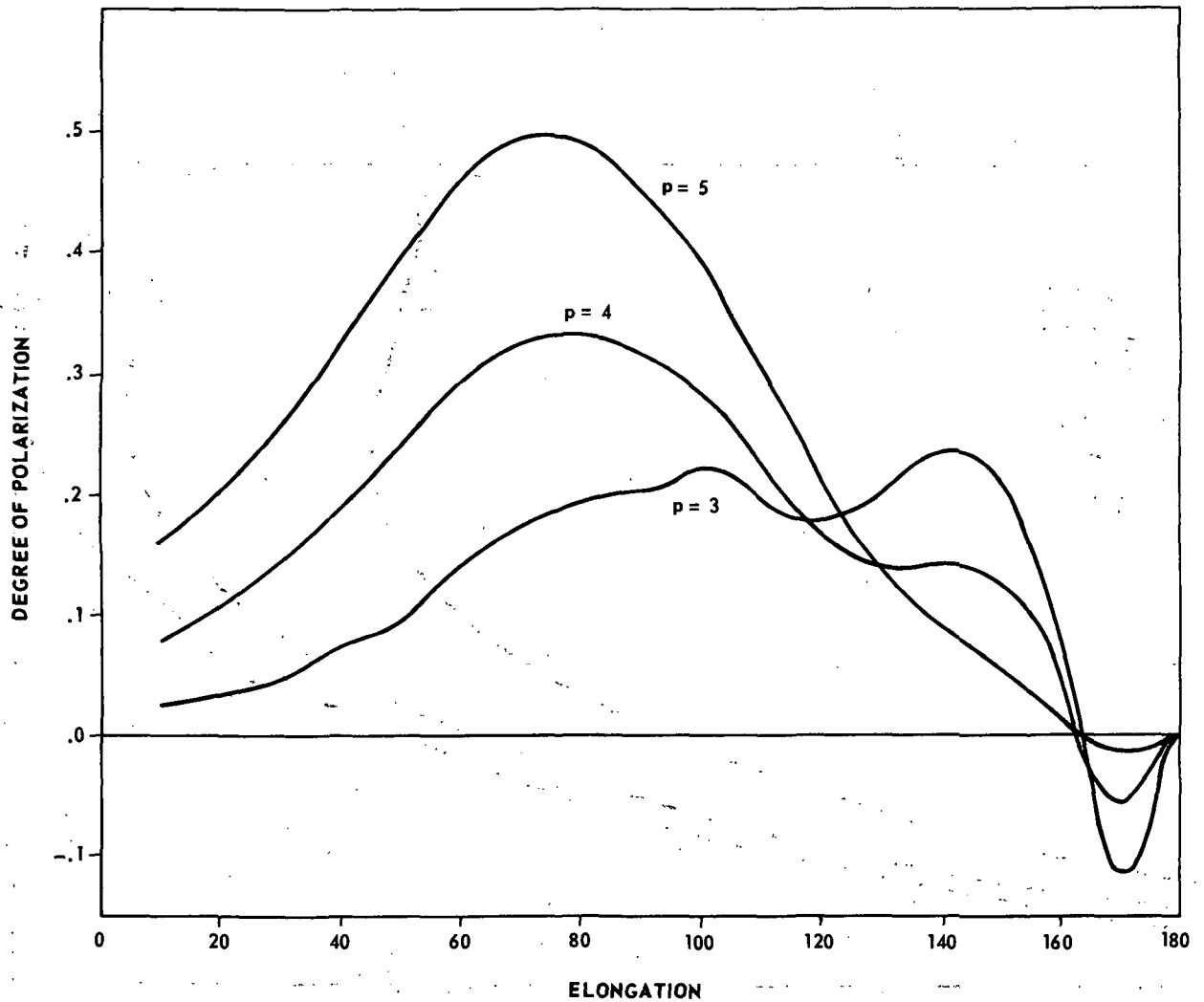

Figure 83. Degree of polarization for a variation of p for Figure 82.

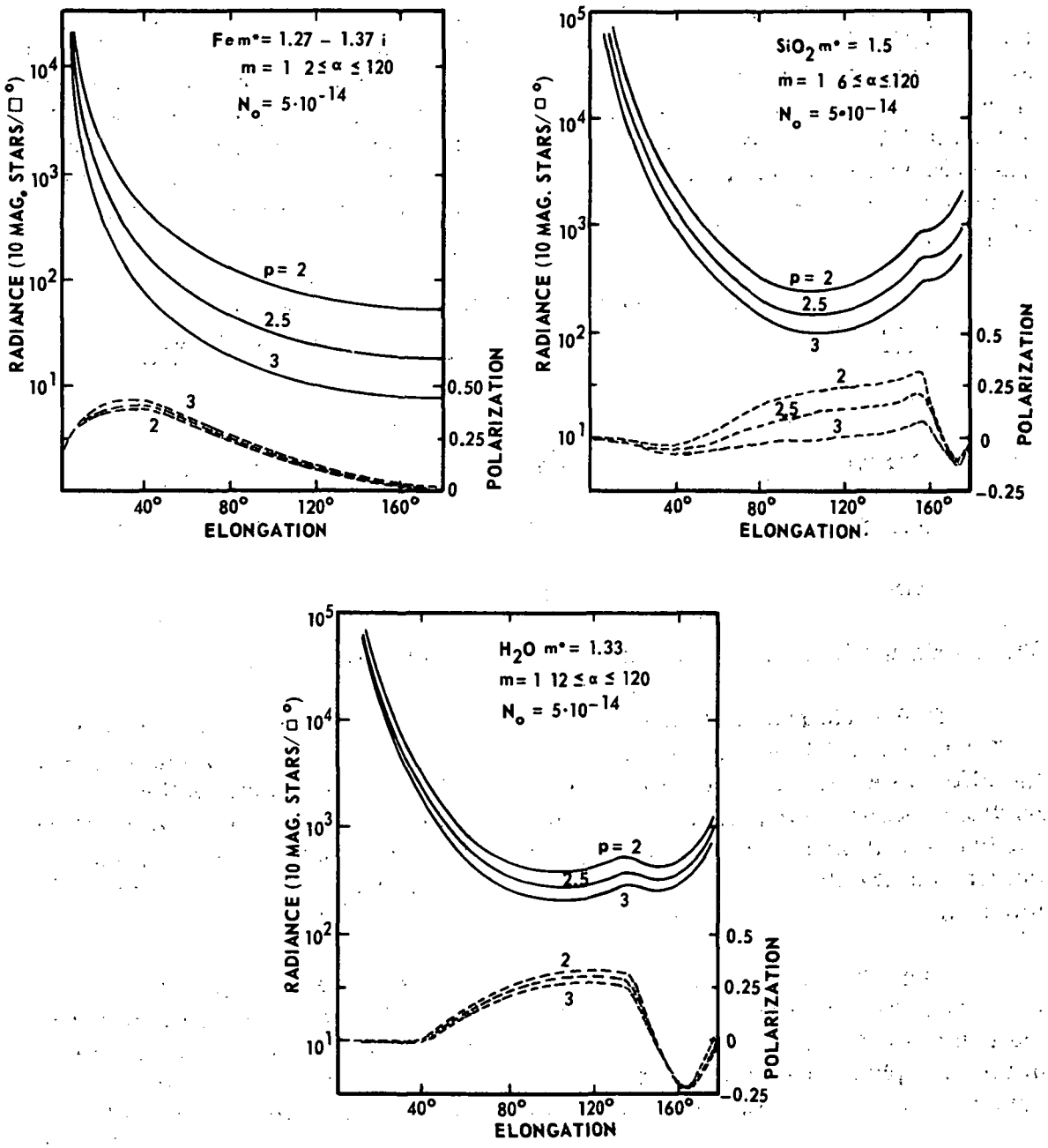

Figure 84. Giese and Siedentopf's results for a variation in p and particle type [16, 84].

For a given m and p, the shape and magnitude of the radiance and polarization curves depend on the material. The results of varying the material while keeping m = 1, and p = 4 fixed are presented below. For these calculations, the particle size range is $1 \leq \alpha \leq 20$.

In Figure 85 the radiance curves for the metallic materials iron ($m^* = 1.27 - 1.31\,i$), carbon ($m^* = 2.45 - 1.42\,i$), nickel ($m^* = 1.46 - 2.68\,i$), and zinc ($m^* = 1.41 - 4.10\,i$) are compared. Polarization and radiance for these metals have similar dependences on elongation, although the numerical values differ. No increase in the antisolar direction is seen in the radiance. The polarization from 130 to 180 deg is very similar for all metals. Position and value of the maximum polarization for each material are given below (Fig. 86):

Material	Maximum Value of Polarization	Position of Maximum (deg)
Iron	0.49	46
Carbon	0.30	48
Nickel	0.31	33
Zinc	0.24	33

The maximum in the polarization occurs in the forward direction.

Dielectric materials are compared in Figure 87. Except for dirty ice ($m^* = 1.33 - 0.5\,i$) which approaches a metallic material, the radiance shows the effect of a gegenschein. The scattering efficiency increases as the particles become hard (i.e., as the refractive index increases). Polarization fluctuates with no general trend (Fig. 88). Ice is dominantly positive, while quartz and titanite are dominantly negative for the range of particles considered.

Table 25 compares the exponential gradient for various materials. Generally the dielectric materials have a higher value of κ than do the metallic materials for the 30- to 60-deg range. No conclusions about the composition of the interplanetary matter can be drawn from this because of the limited number of materials studied and the limited range of particle sizes used.

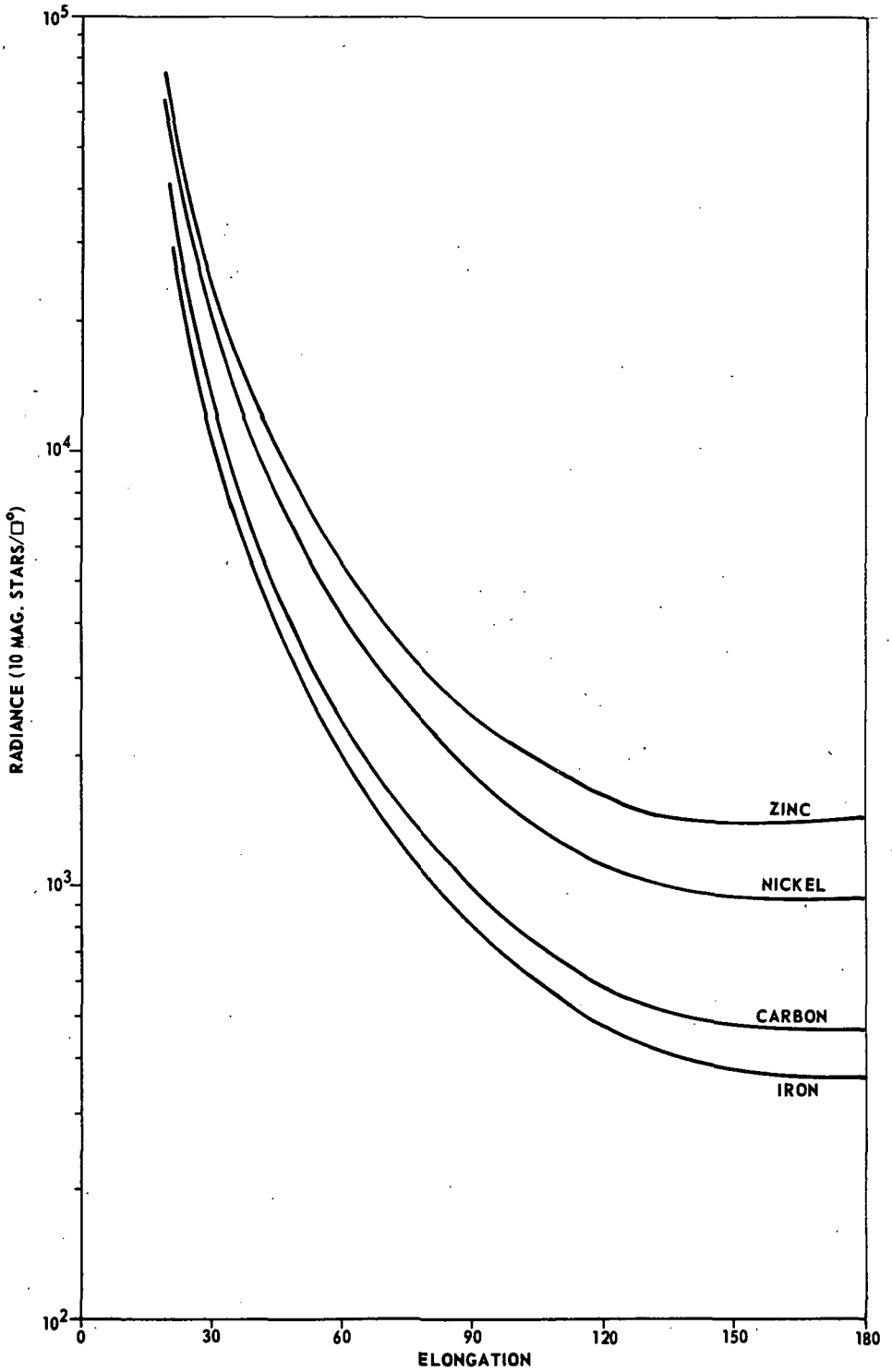

Figure 85. Radiance for a variation of metallic materials ($N_o = 1.5 \times 10^{-10}$, $p = 4$, $m = 1$, $\alpha_{min} = 1$, and $\alpha_{max} = 20$).

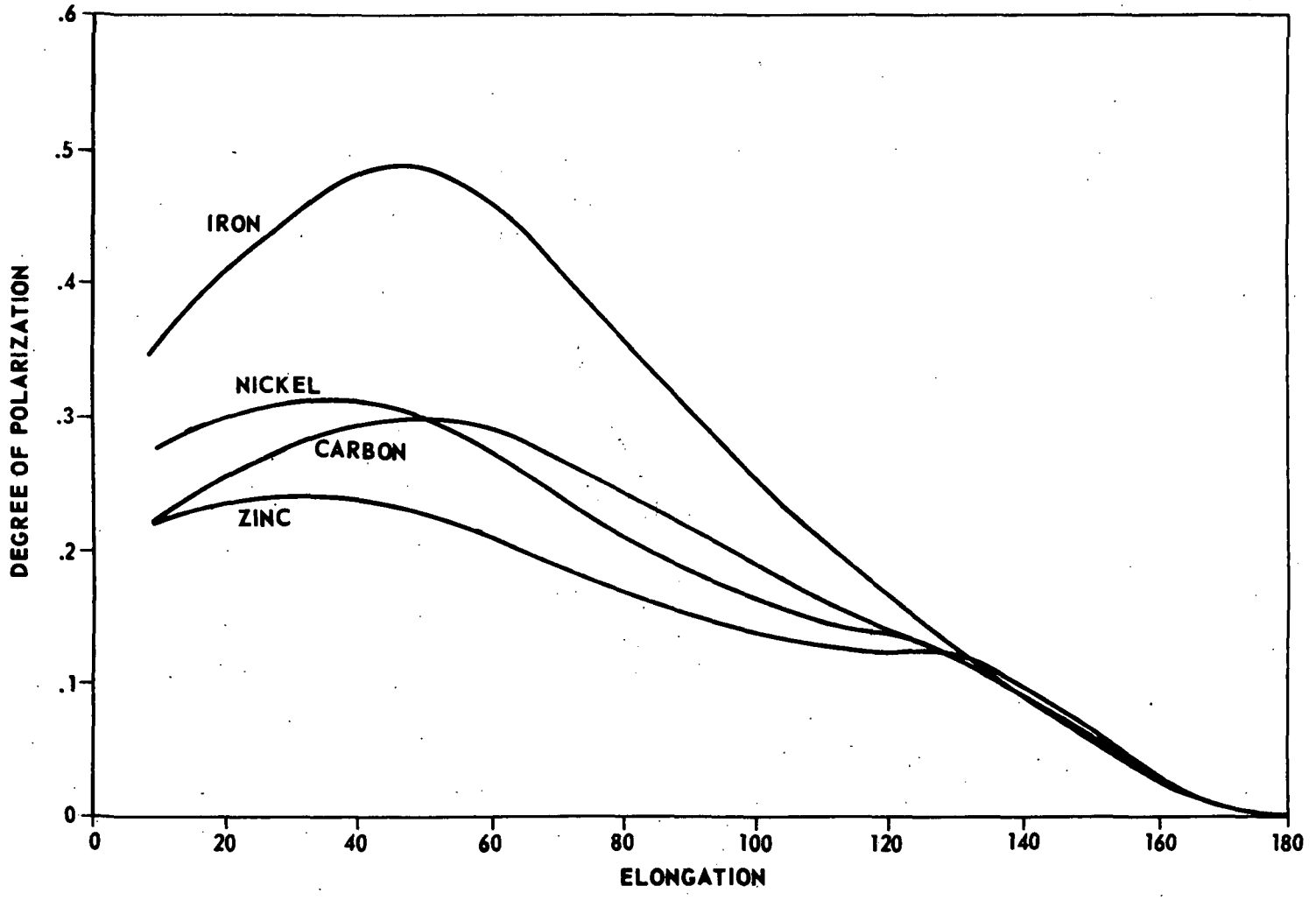

Figure 86. Degree of polarization for a variation of metallic materials.

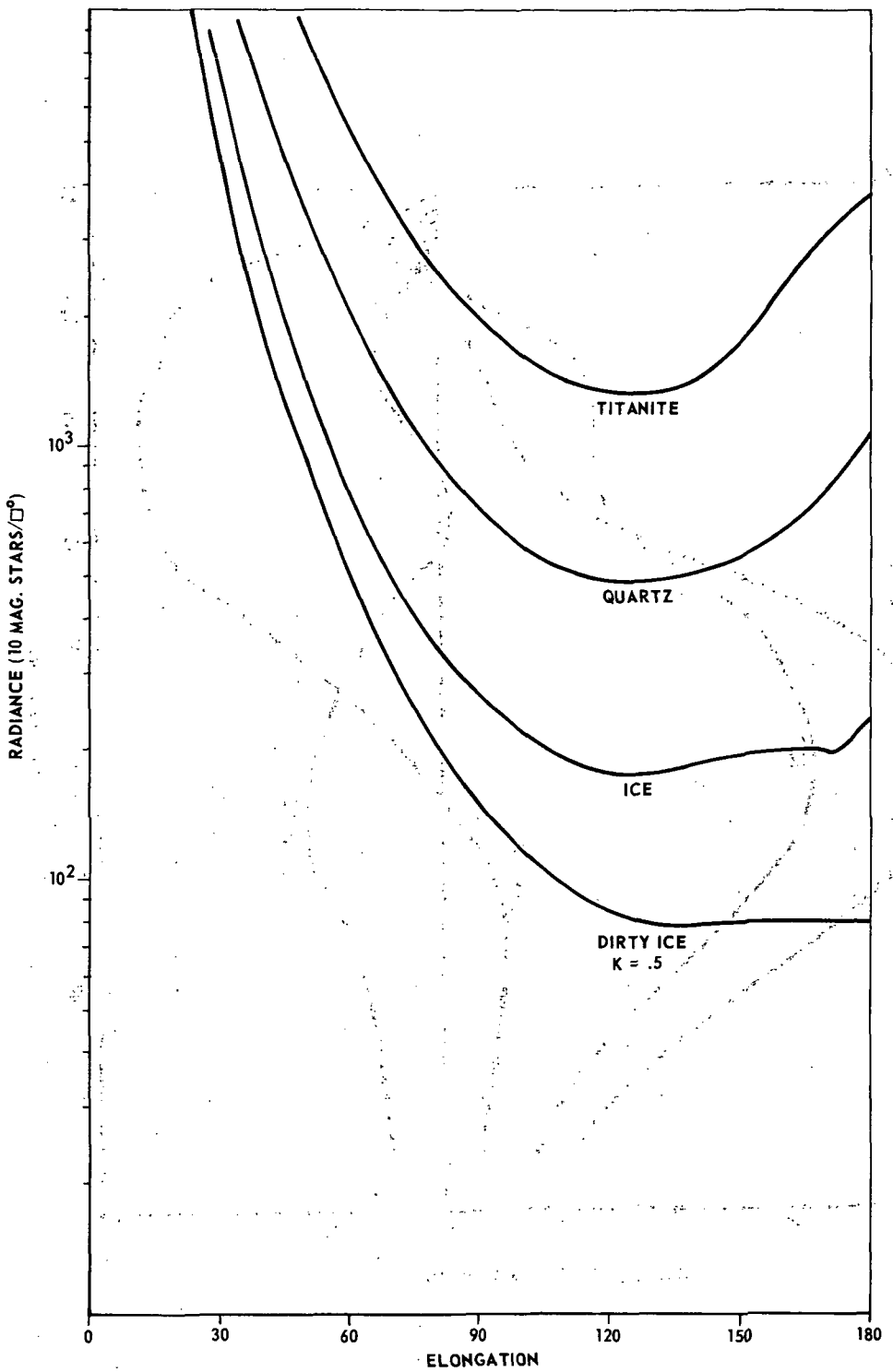

Figure 87. Radiance for a variation of dielectric materials ($N_o = 1.5 \times 10^{-10}$, p = 4, m = 1, $\alpha_{min} = 1$, and $\alpha_{max} = 20$).

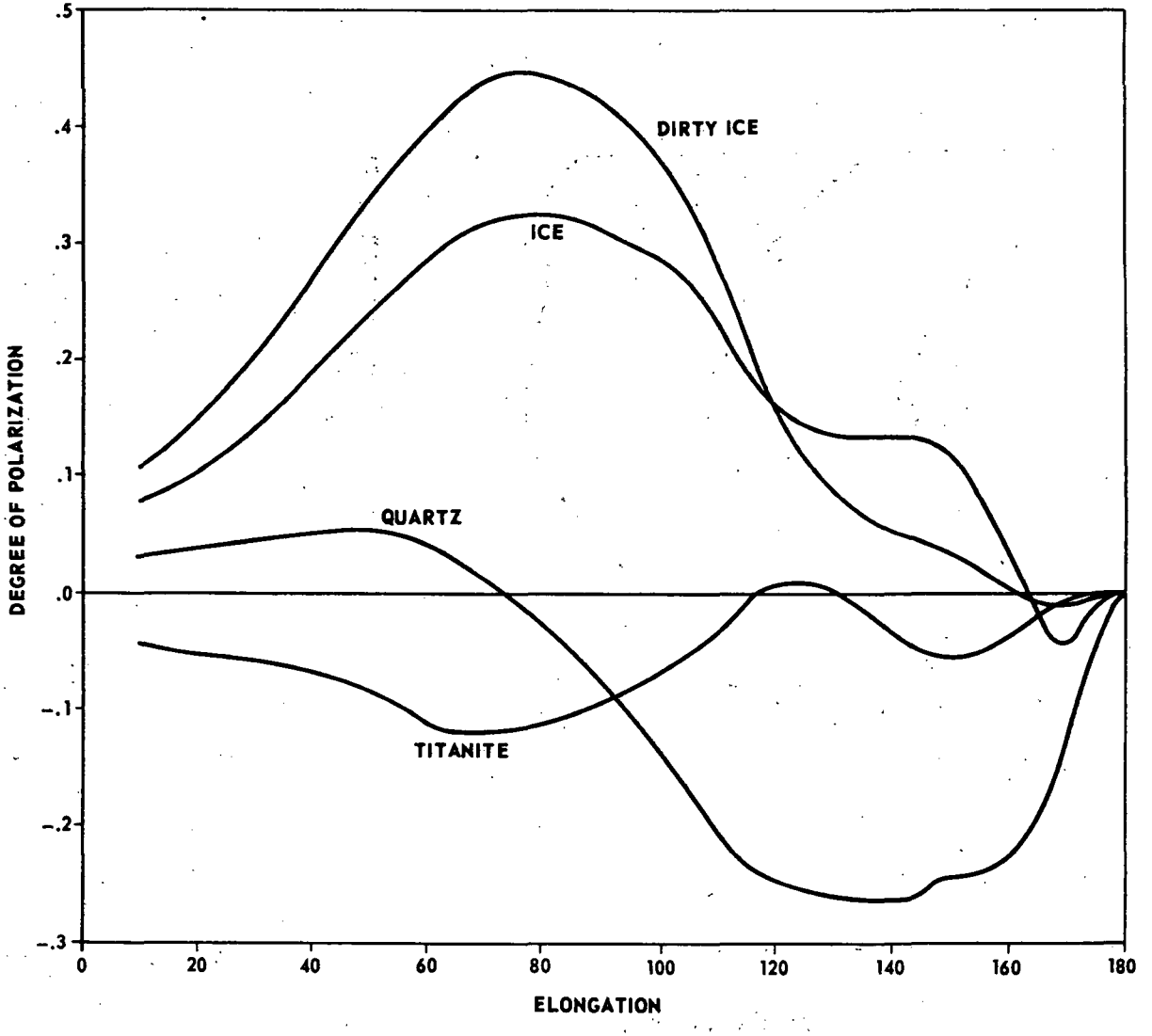

Figure 88. Degree of polarization for a variation of metallic materials.

TABLE 25. EXPONENTIAL GRADIENT FOR VARIOUS MATERIALS BETWEEN 30 to 60 DEG FOR THE MODELS CONSIDERED

	κ		κ
Titanite	2.7	Iron	2.6
Quartz	3.0	Carbon	2.6
Ice	3.3	Nickel	2.4
Dirty Ice	3.4	Zinc	2.3

Since no single component model has resulted in duplicating completely the observed zodiacal light quantities [40], various combinations of materials should be investigated. In general, metals give the correct position of the polarization peak, while dielectrics give the gegenschein effect. To combine these effects, a model should include at least one metallic and one dielectric material.

For a combination of two materials, the radiance expression is

$$\bar{L}_\lambda = \frac{1}{2}\left[L_\lambda^{A(1)} + L_\lambda^{B(1)} + L_\lambda^{A(2)} + L_\lambda^{B(2)}\right] = \bar{L}_\lambda^{A} + \bar{L}_\lambda^{B} , \tag{174}$$

where $L_\lambda^{\alpha\,(j)}$ are the jth component and the α th particle type. The polarization is

$$\bar{P}_\lambda = \frac{L_\lambda^{A(1)} + L_\lambda^{B(1)} - L_\lambda^{A(2)} - L_\lambda^{B(2)}}{L_\lambda^{A(1)} + L_\lambda^{B(1)} + L_\lambda^{A(2)} + L_\lambda^{B(2)}} \tag{175}$$

In general, $\bar{P}_\lambda$ is not equal to $P_\lambda^{B} + P_\lambda^{A}$, but the following statements can be made as a result of the definition above:

(1) if

$$\bar{L}_\lambda^{A} = \bar{L}_\lambda^{B} \text{ then } \bar{P}_\lambda = \frac{1}{2}\left(P_\lambda^{A} + P_\lambda^{B}\right) ; \tag{176}$$

(2) if

$$P_\lambda^A = P_\lambda^B \text{ then } P_\lambda^A = P_\lambda^B = \overline{P}_\lambda \; ; \tag{177}$$

(3) the polarization tends toward the polarization of the material with the larger total radiance.

A method to fit experimental data using a two-component model is as follows (cf. References 16 and 84). From computed values of

$$L_\lambda^{A(1)} \, , \; L_\lambda^{B(1)} \, , \; L_\lambda^{A(2)} \, , \; L_\lambda^{B(2)}$$

(which could be curved fitted), the values of

$$\overline{L}_\lambda^A \, , \; \overline{L}_\lambda^B \, , \; P_\lambda^A \, , \; P_\lambda^B$$

can be calculated for some N_o^A and N_o^B. Variation of N_o^A and N_o^B changes the levels of $\overline{L}_\lambda^A$ and $\overline{L}_\lambda^B$, while P_λ^A and P_λ^B remain unchanged. But from the statements above, the average polarization $\overline{P}$ will follow the material with the larger radiance values. Hence, by varying N_o^A and N_o^B, a best fit for $\overline{L}_\lambda$ and $\overline{P}_\lambda$ can be obtained. For a metallic-dielectric combination, the dependence of both the radiance and polarization is changed by varying N_o^M and N_o^D (i.e., the number densities for each component). The correct polarization peak is obtained from the metallic component, while the dielectric component gives the gegenschein or backscattering peak. Figure 89 illustrates the results that can be obtained by varying N_o^M and N_o^D for a given model. Clearly, almost any result can be obtained. The procedure can be extended to models with several compositions of materials.

As an example, a dielectric-metallic and a dielectric-dielectric model are shown in Figures 90 and 91 along with single-material models. In the combination examples $N_o^A = N_o^B$ (compare with Fig. 89).

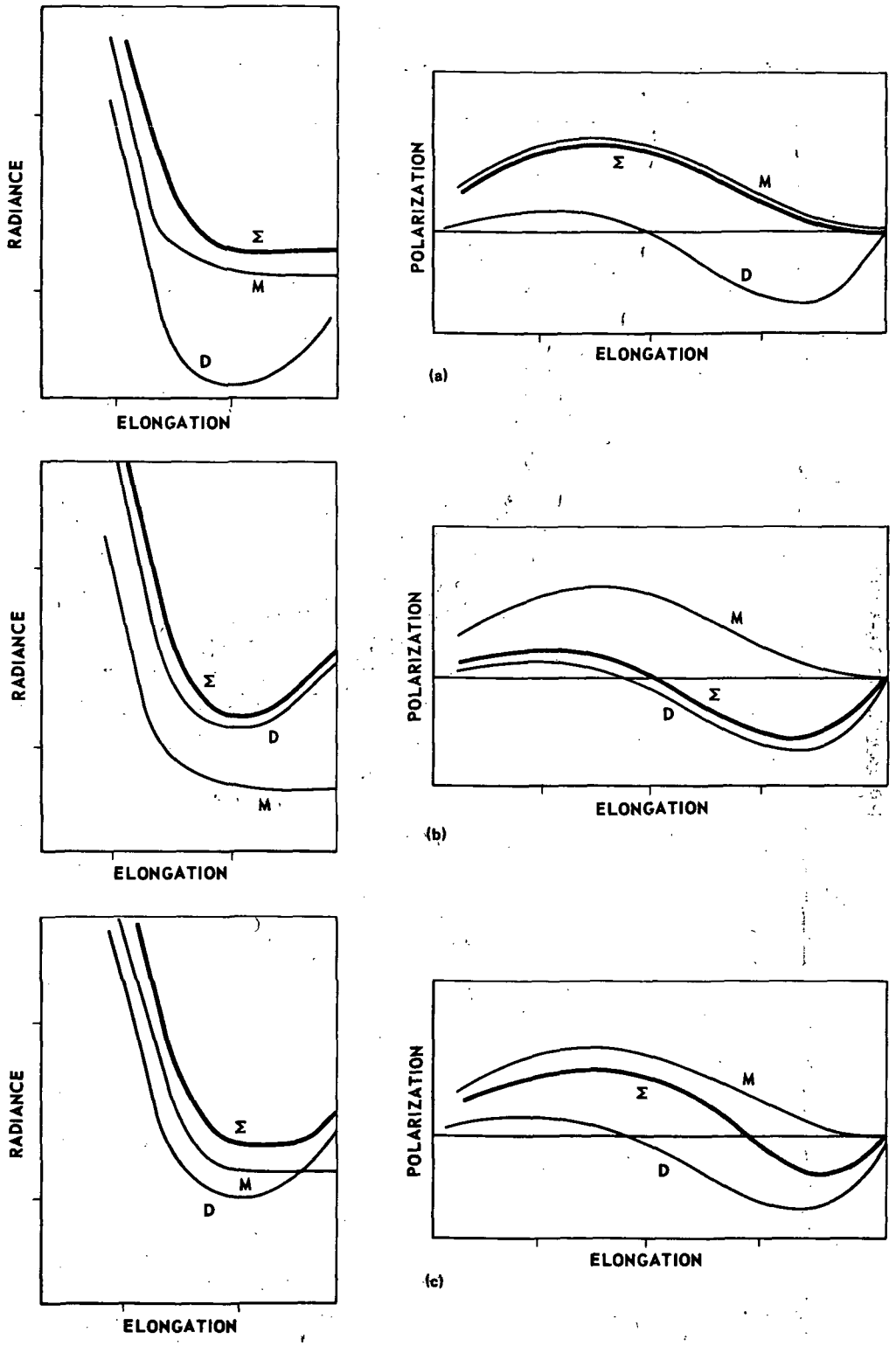

Figure 89. Variation of N_o^M and N_o^D on $\bar{L}_\lambda$ and $\bar{P}_\lambda$: a metal M dominates and sum $\sum$ resembles a metallic model, (b) dielectric D dominates and sum $\sum$ resembles a dielectric model, and (c) a dielectric balanced model.

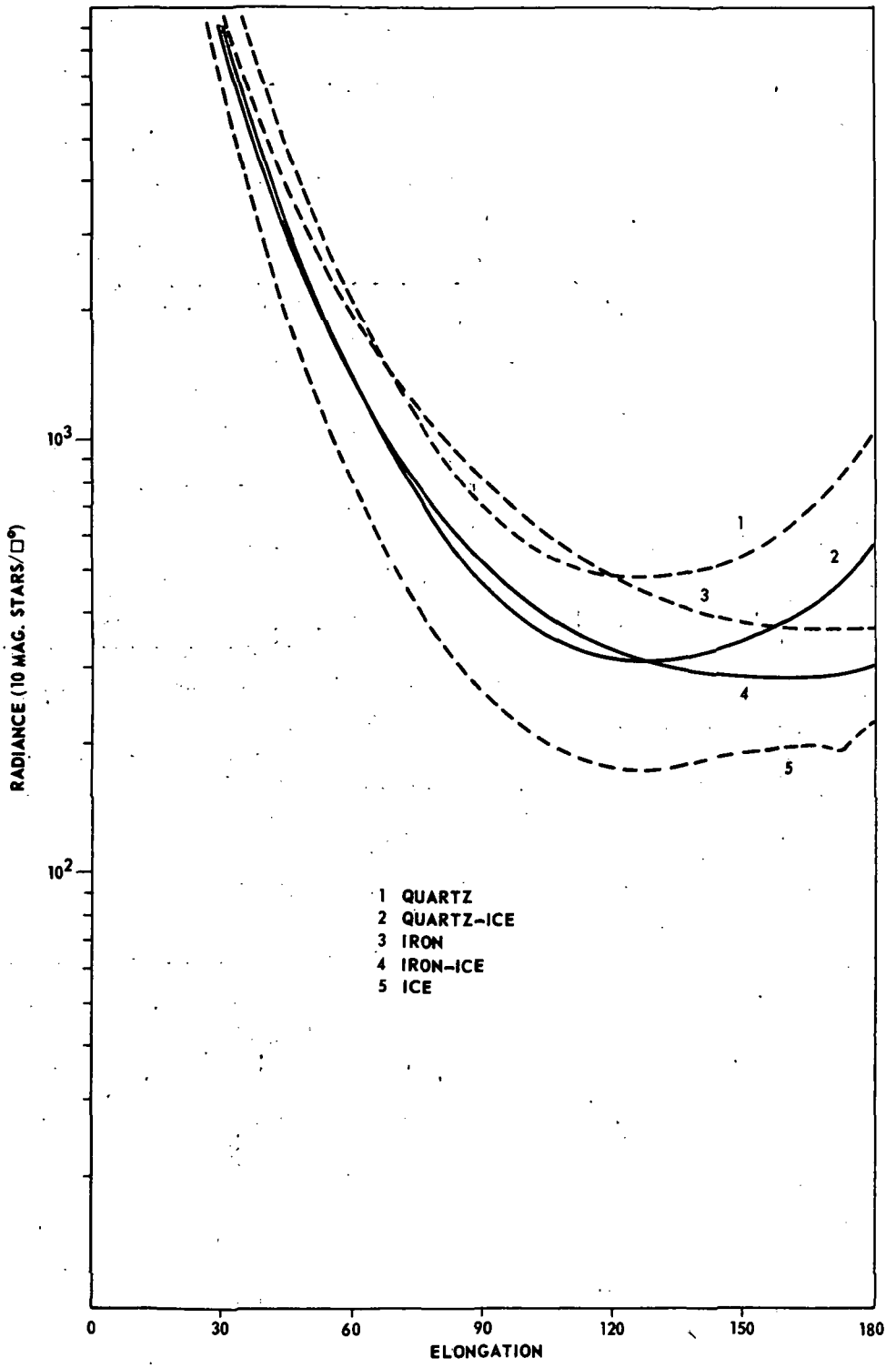

Figure 90. Radiance values for a combination of quartz, ice, and iron ($N_o = 1.5 \times 10^{-10}$, m = 1, p = 4, $\alpha_{min} = 1$, and $\alpha_{max} = 20$).

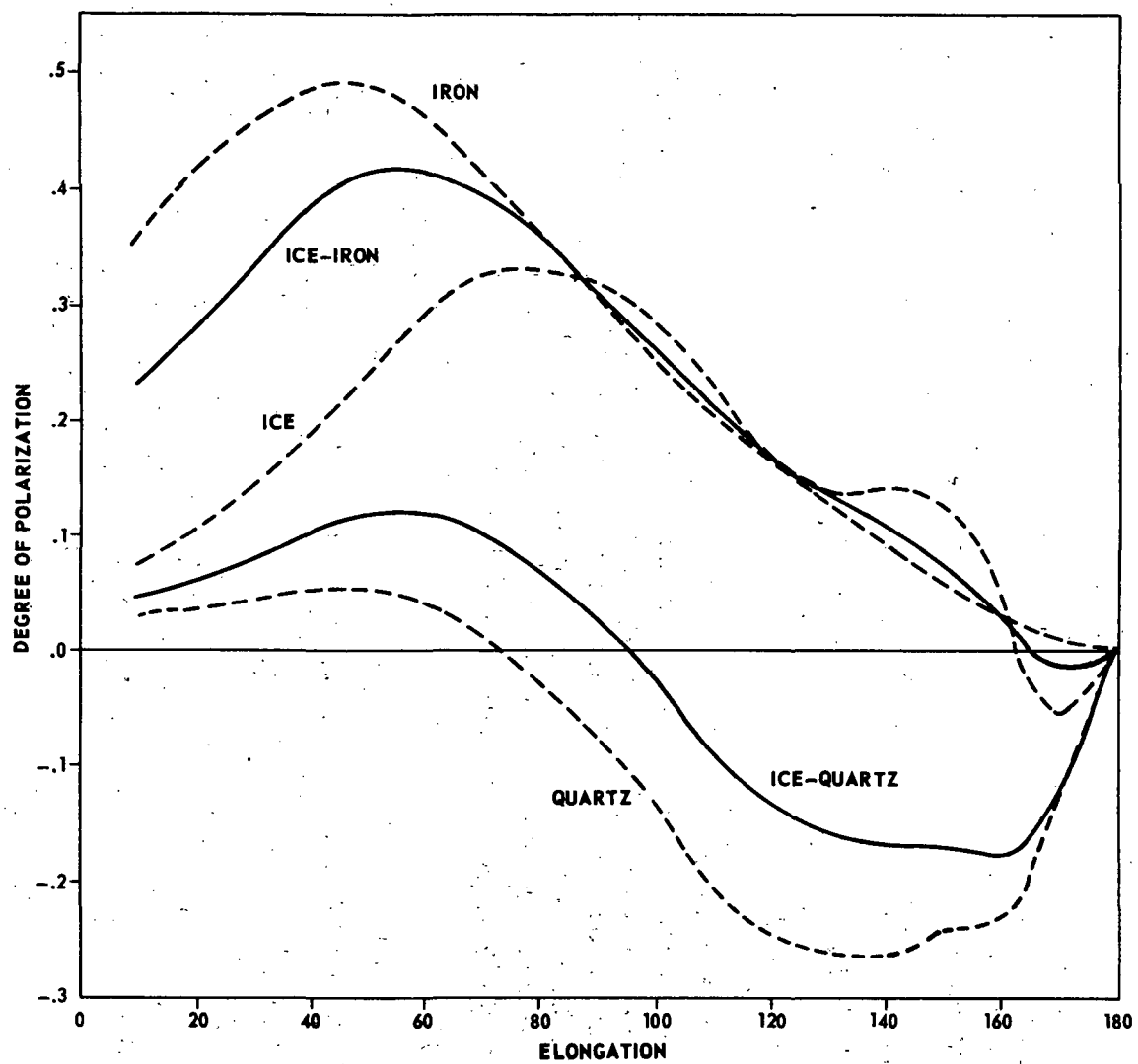

Figure 91. Degree of polarization for combinations of quartz, ice, and iron.

Giese and Siedentopf [16, 84] investigate combinations of electrons and purely dielectric dust; electrons, iron, and dielectric dust; and iron and dielectric without electrons. Their results are shown in Figures 92, 93, and 94. The high electron values of Figures 92 and 93 result from early observations which gave high values for the polarization. (Compare with Figure 74 of electron polarization.)

Figure 95, which summarizes their results, illustrates that several composition models can yield approximately the same results, giving no uniqueness to the models [16, 84]. However spectral dependence was not calculated. Models I and II have too large a value for the electron density. Model III contains small (Rayleigh) scatterers. Weinberg [17, 18] concluded from his observations and the results of Giese and Siedentopf that a major fraction of both the radiance and polarization of the observed zodiacal light can be accounted for by small dielectric particles without resorting to high electron densities.

Other composition models have been considered by other authors. Kovar and Kovar [85] based their compositions on the Apollo 11 lunar sample analysis. Consequently, they include glass in their models in varying amounts. The glass is considered to be in three forms having a refractive index of $m^* = 1.55$, 1.65, and 1.75. Several models were reported which differed in materials and percentages of the constituents. Two models from their preliminary report are shown in Figures 96 and 97. The parameters for the models are:

Model 5	Percent	Refractive Index	m	p
Iron	60	1.27-1.37i	1.5	2.5
Ice	30	1.33	0.0	2.0
Glass	7	1.55	2.0	4.0
	2	1.65	2.0	4.0
	1	1.75	2.0	4.0

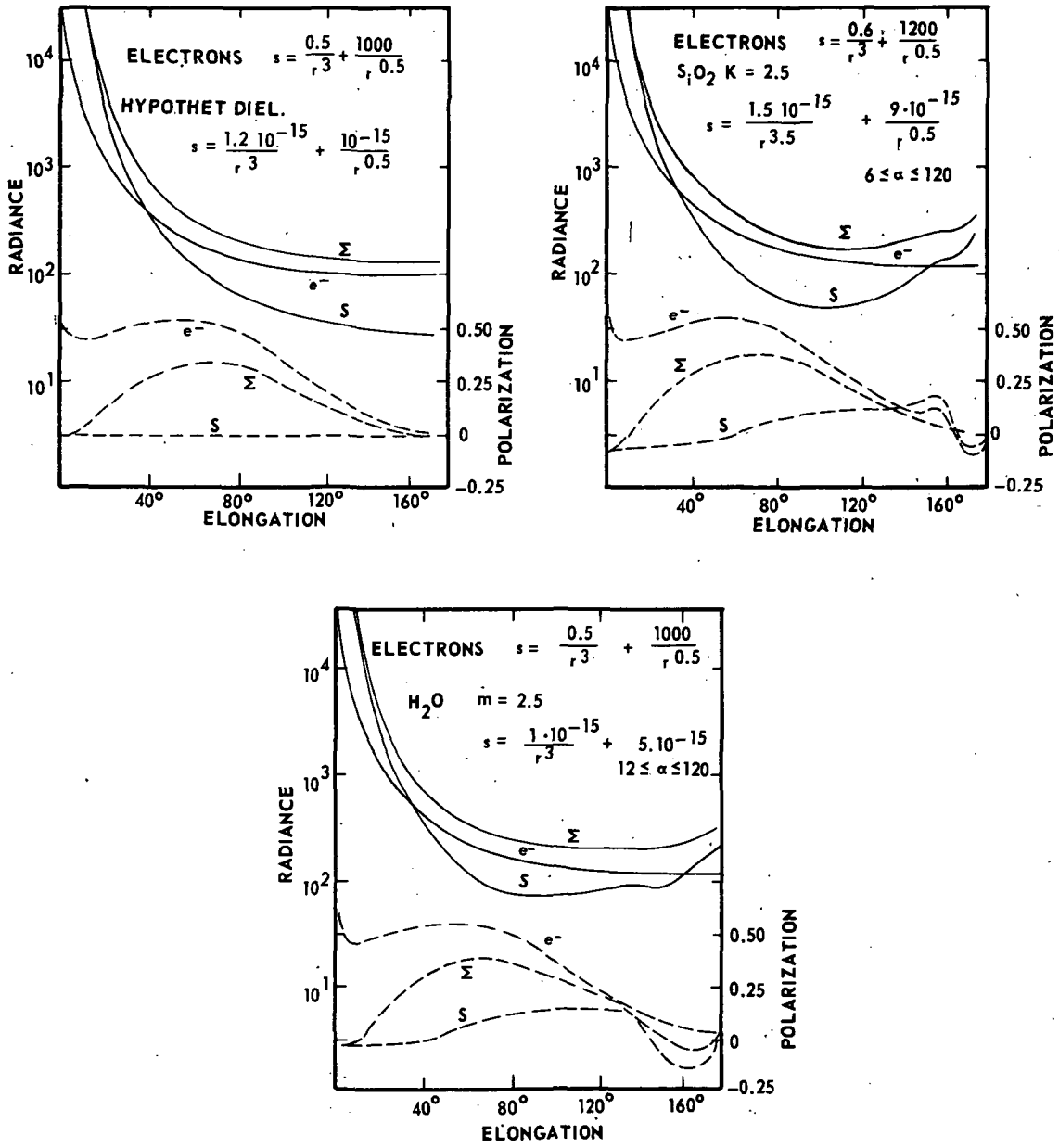

Figure 92. Giese and Siedentopf's [16, 84] results for various electron-dielectric models.

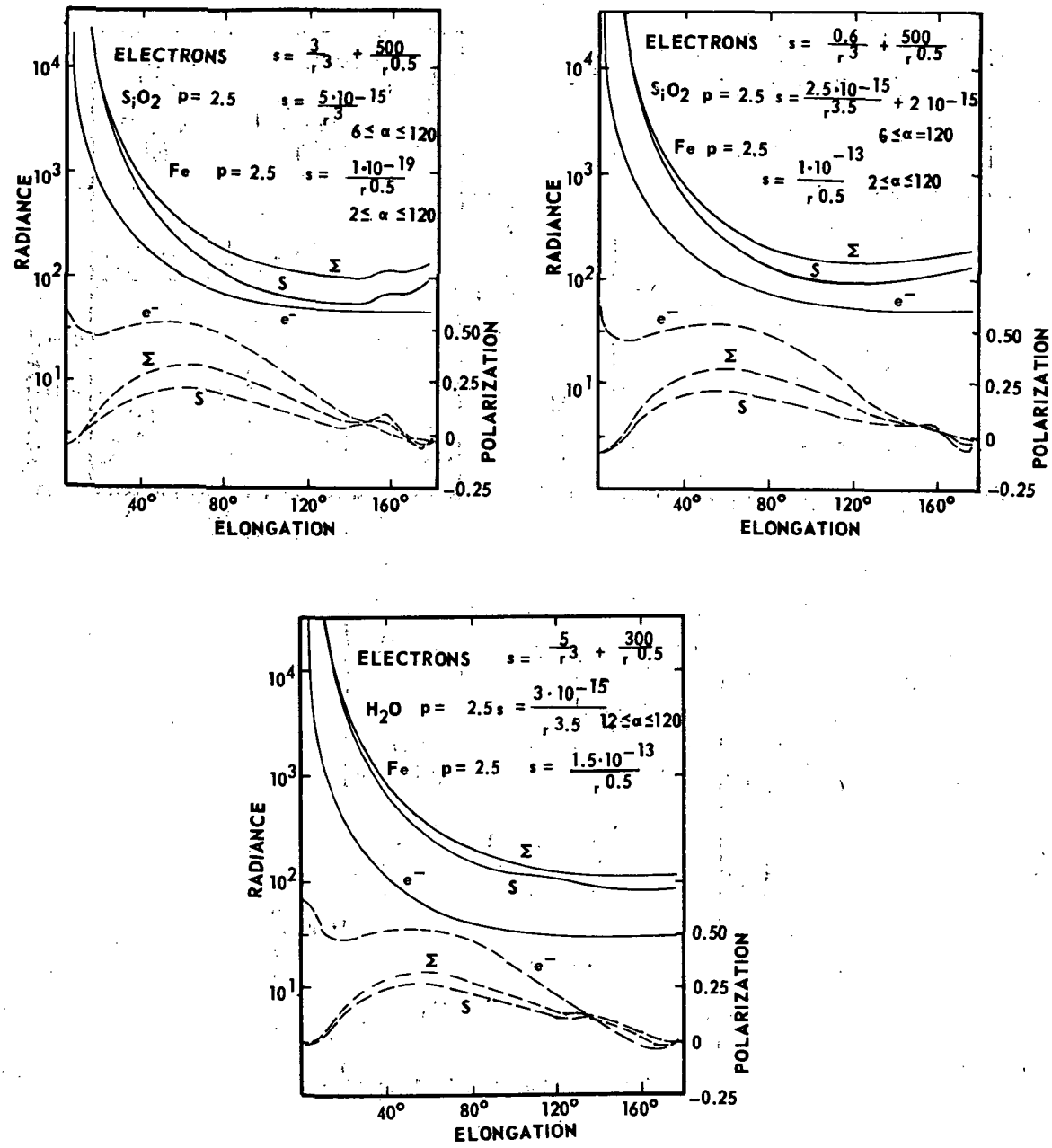

Figure 93. Giese and Siedentopf's results for various metallic-dielectric models [16, 84].

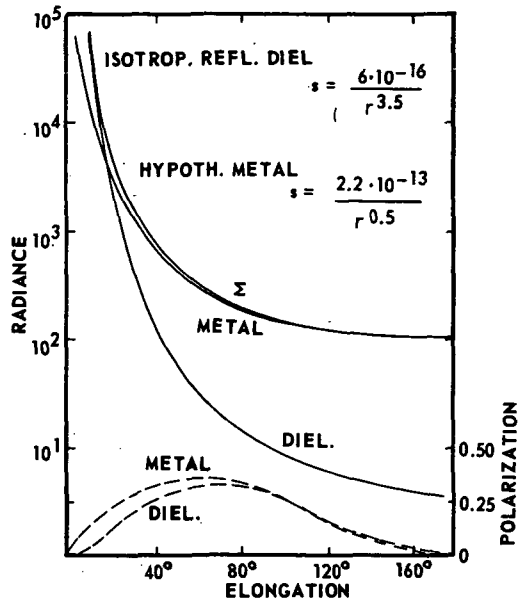

Figure 94. Giese and Siedentopf's results for an isotropic reflecting dielectric and a hypothetical metal having Ingham's polarization function [16].

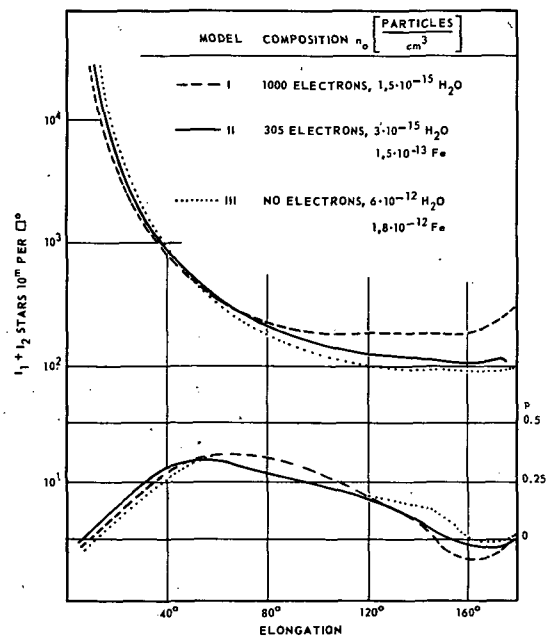

Figure 95. Giese's [26] results for radiance and polarization for three models assuming different electron densities.

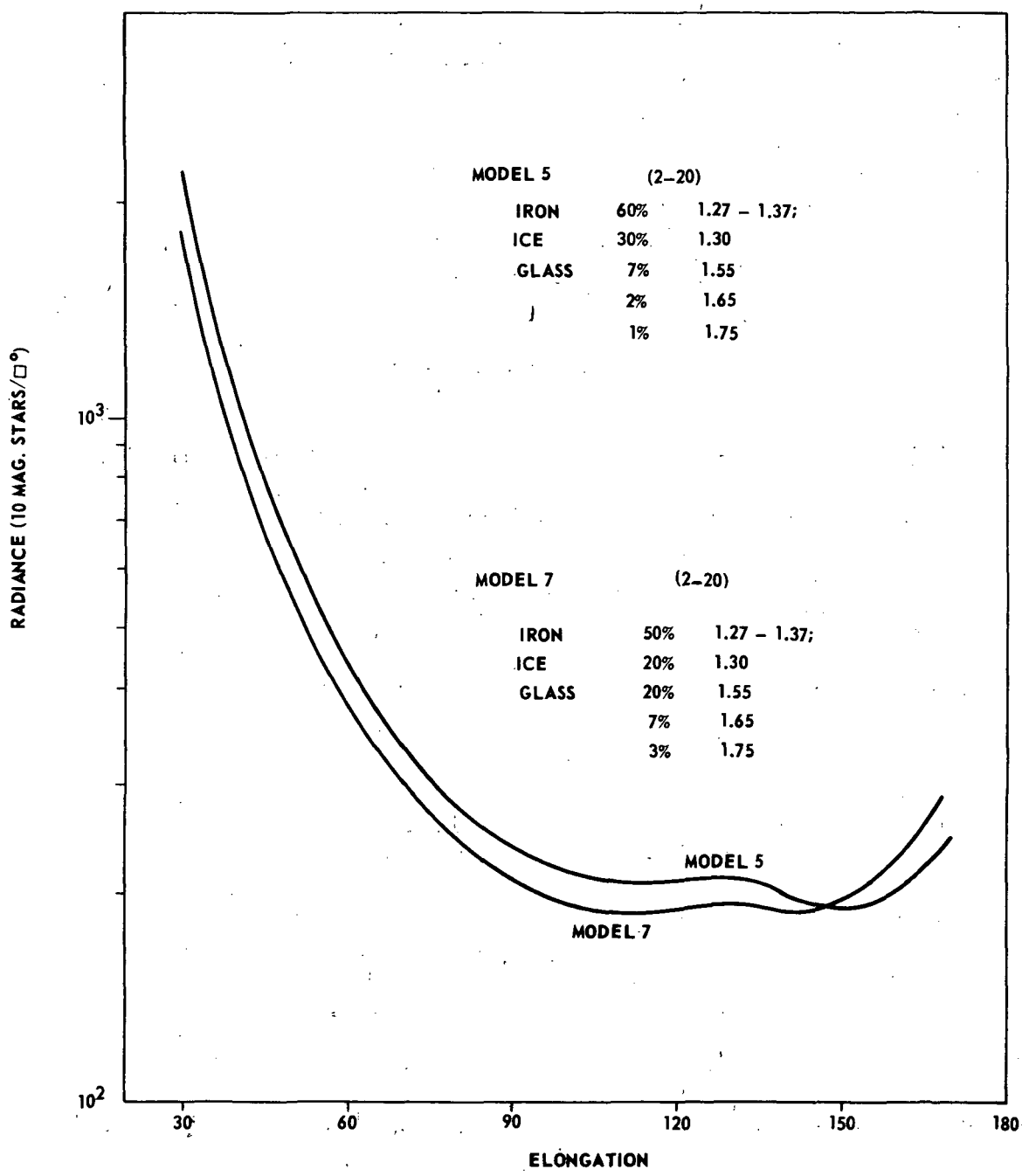

Figure 96. Kovar and Kovar's [85] Models 5 and 7 results for radiance for a combination of iron, ice, and glass.

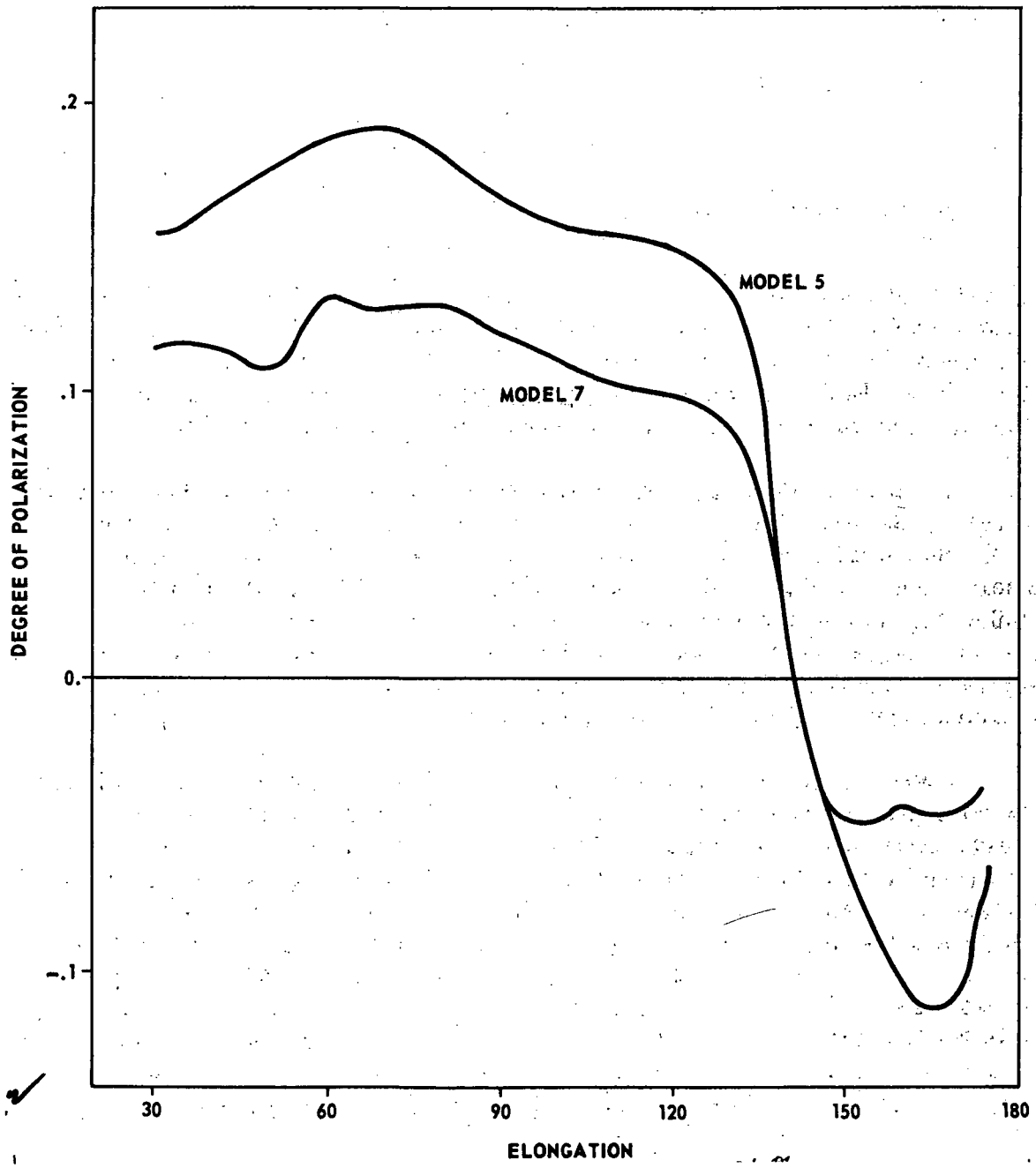

Figure 97. Polarization for Kovar and Kovar's Models 5 and 7.

Model 7	Percent	Refractive Index	m	p
Iron	50	1.27	1.0	2.5
Ice	20	1.30	0.0	2.0
Glass	20	1.55	0.5	3.0
	7	1.65	0.5	4.0
	3	1.75	0.5	3.0

$N_o = 5 \times 10^{-14}$ particles/cm^3

Model 7 has less ice and more glass with a different spatial and size dependence than Model 5. The radiance curves for both Models 5 and 7 are in good agreement with the observed radiances of Weinberg [47] and Wolstencroft and Rose [52]. However, the polarization of these models is somewhat lower than the observed values; for $\epsilon > 160$ deg, the deviation is significant.

Earlier, Little et al. [86] also considered a model with a glass content. Using a model with 97 percent ice ($m^* = 1.33$) and 3-percent pyroxene ($m^* = 1.70$), they were able to obtain moderate agreement with the polarization observations of Ingham and Weinberg. But, for $\epsilon > 160$ deg, their curves exhibit the same behavior as the curves of Kovar and Kovar given above. This is because of the ice content with a particle size range of $1 \leq \alpha \leq 26$ and $p = 4$. Little concluded that for the polarization of this model to agree with observation, m must be greater than 0.6.

Giese and Dziembowski [32, 33], in connection with out-of-the-ecliptic analysis, give an iron-quartz model and an ice-dirty ice model which agree approximately with observations. Their models (Table 26) are based on scattering by absorbing and dielectric particles large enough to produce non-Rayleigh scattering. The different models use the fact that the scattering functions for a distribution are dependent on the imaginary part of the refractive index. For example in the distributions used by Giese and Dziembowski, the polarization for particles with $m^* = 1.0 - 0.01\,i$ peaks at $\simeq 90$ deg; for particles with $m^* = 1.0 - 2.0\,i$ it peaks at $\simeq 40$ deg. Both models used by them have a particle size range of 2 to 120 and a size distribution with $p = 2.5$. They noted [33], models which contain large particles, whose sizes are

TABLE 26. PARTIAL LISTING OF ZODIACAL LIGHT MODELS WHICH ARE IN APPROXIMATE AGREEMENT WITH OBSERVATIONS

Author	Designation	Material	Refractive Index	Alpha Range	p	m	N_o	Comment
Giese [16, 34]	A1	Ice Electrons	1.33	12 to 120	2.5 2.5	3.5 0.0 3.0 0.5	1×10^{-15} 5×10^{-15} 0.5 1000	Model I Electron Model
	A2	Ice Iron Electrons	1.33 1.27 - 1.37i	12 to 120 2 to 120	2.5 2.5 2.5	3.0 0.5 3.0 0.5	3×10^{-15} $1 \times 5 \times 10^{-13}$ 5 300	Model II Partial Electron
	A3	Ice Iron	1.33 1.27 - 1.37i	10 to 40 1 to 25 1 to 25	2.0 4.0 4.0	3.0 0.5 0.5	3×10^{-15} 6×10^{-12} 1.8×10^{-12}	Model III No Electrons Small Particles
Giese-Dziembowski [33]	B1	Quartz Iron	1.5 1.27 - 1.37i	6 to 120 2 to 120	2.5 2.5	3.0 0.1 0.5	2.4% 2.0% 2.195×10^{-13} 95.6%	Model I Metallic
	B2	Ice	1.33 1.33 - 0.1i	12 to 120 2 to 120	2.5 2.5	0.1 0.1	1.1% 7.587×10^{-13} 98.9%	Model II Dielectric
Little-O'Mara-Aller [86]	C	Ice Pyroxene	1.33 1.7	1 to 20 1 to 20	4.0 4.0	1-2 1-2	97% 1.5×10^{-15} 3%	Dielectric
Powell et al. [28]	D	Dielectric	1.6	1 to 19	Deduced from Observations Belt Model			Small Particles
Kovar-Kovar [85]	E1	Iron Ice Glass	1.27 - 1.37i 1.30 1.55 1.65 1.75	2 to 120 2 to 120 2 to 120 2 to 120 2 to 120	2.5 2.0 4.0 4.0 4.0	1.5 0.0 2.0 2.0 2.0	60% 5×10^{-14} 30% 7% 2% 1%	Model 5 Glass Content
	E2	Iron Ice Glass	1.27 - 1.37i 1.30 1.55 1.65 1.75	2 to 120 2 to 120 2 to 120 2 to 120 2 to 120	2.5 2.0 3.0 4.0 3.0	1.0 0.0 0.5 0.5 0.5	50% 5×10^{-14} 20% 20% 7% 3%	Model 7 Glass Content
Aller et al. [22]	F1	Ice	1.33 - 0.01i	1.25 to 5 5 to 25.5	2.0 4.0	1.0 1.0	2.21×10^{-11}	Broken Distribution
	F2	Ice	1.33 - 0.01i	1.25 to 6.3 6.3 to 25.5	2.3 4.0	1.0 1.0	2.21×10^{-11}	B.D.
	F3	Ice	1.33 - 0.01i	1.25 to 7.5 7.5 to 25.5	3.0 4.0	1.0 1.0	2.21×10^{-11}	B.D

distributed according to the inverse power law, allow an increase of the particle sizes to increase the forward portion of the scattering intensity function without seriously altering the polarization of higher scattering angles. This differs from the case with very small particles ($\alpha = 1$) where any considerable increase of particles with a high α value would result in deviations from the Rayleigh-like scattering behavior.

To match observational data, using single material models, Aller et al. [22] had to "break" the power law distribution (Table 26); i.e., for some range,

$$a_{min} \leq a \leq a_B \qquad p = p_L \tag{178}$$

and for

$$a_B < a \leq a_{max} \qquad p = p_M \quad . \tag{179}$$

Any number of breaks could be included, but they employed two break points. Using dirty ice ($m^* = 1.33 - 0.01$), $m = 1$ and

$$1.25 \leq \alpha \leq 25.5,$$

they obtained an approximate agreement with observations in three cases; for

$$a_{min} = 0.01\,\mu \qquad p_M = 4.0$$

and

$$a_B = 0.40 \qquad p_L = 2.0$$

$$a_B = 0.50 \qquad p_L = 2.3$$

$$a_B = 0.60 \qquad p_L = 3.0$$

However, in breaking the distribution, another parameter, the break point radius a_B, is introduced into the calculations, as well as another exponential parameter for the distribution.

The same situation is obtained with the belt models. The belt models increase the versatility of the model but also increase the number of parameters.

Powell et al. [28] matches the observations of Weinberg [46, 47, 48], Blackwell and Ingham [9, 10, 11], Divari and Asaad [64], Robley [45], and Behr and Siedentopf [8] using such models. They conclude that particle sizes are in the range of a = 0.08 to 1.5. The number density of particles in each size range is approximately constant between the orbits of Venus and Mars where dielectric particles ($1.4 < m < 1.8$) dominate. Powell et al. concluded that the density of particles in the region beyond Mars is not sufficient to affect the character of the zodiacal light.

In these models, the size distribution is arbitrarily truncated at some lower limit α_{min}. Although this is within the order of the current models, it is not physically realistic, especially in certain cases (appendix).

In summary, many models can closely match the observational data taken in the ecliptic plane. Although good physical arguments may exist to justify preference of some models over others (e.g., multimaterial versus single-material models), these arguments have no firm basis. Table 26 is a partial listing of zodiacal light models which are in close agreement with observational data.

K. Spectral Dependence and Null Point

An additional step in studying the behavior of the radiance and polarization from models is to study the variation of these quantities with wavelength. Color differences between models is a function of the refractive indices of the material used. Thus, observations of radiance and polarization in several wavelengths would help establish possible compositions of the zodiacal cloud.

Color magnitudes are calculated by

$$M_A = -2.5 \log_{10} (\overline{L}_\lambda) \quad . \tag{180}$$

For two wavelengths, the color excess, with reference to the spectral content of the sun, is calculated from

$$\Delta (M_A - M_B) = (M_A - M_B) + 2.5 \log_{10} \frac{\xi_{\lambda A}}{\xi_{\lambda B}} \quad . \tag{181}$$

$\xi_{\lambda i}$ is the radiant energy flux, at wavelength λ_i, from the sun. Color excesses for Rayleigh scattering are easily calculated. Since the scattered energy flux is ξ_λ/λ^4, the color magnitudes are given by

$$M_A = -2.5 \log_{10} \frac{\xi_\lambda}{\lambda^4} - 2.5 \log_{10} R \quad .$$

All terms common to each calculation are included in R. The color excess is thus

$$\Delta (M_A - M_B) = -2.5 \log_{10} \frac{\xi_{\lambda A}}{\lambda^4} + 2.5 \log_{10} \frac{\xi_{\lambda B}}{\lambda_B^4}$$

$$+ 2.5 \log_{10} \left(\frac{\xi_{\lambda A}}{\xi_{\lambda B}} \right) = 10 \log_{10} \lambda_A - 10 \log_{10} \lambda_B .$$

Using explicit subscripts and the wavelengths $\lambda_V = 380$ Nm, $\lambda_G = 500$ Nm, and $\lambda_R = 650$ Nm, the color excesses

$$\Delta (M_V - M_G) = -1.192$$

and

$$\Delta (M_G - M_R) = -1.139$$

are obtained. Thus, the color enhancement in both cases is bluish. These values represent an upper limit for small particle models. Aller et al. [22] using these same wavelengths, calculated the color excesses from Model F1 of Table 26. Selected values of their results are listed in Table 27. From their Mie theory models they concluded that the zodiacal light is about 0.2 magnitudes bluer than the sun in both V-G and G-R color indices. Powell, et al. [28], using the belt model, also found some color enhancement in the blue in agreement with observations of Tanabe and Huruhata [87]. Blue enhancement indicates submicron-size particles because of Rayleigh scattering. Gindilis and Karyagina [88] find a wavelength dependence of the zodiacal light that goes as $\lambda^{-0.1}$, while for the gegenschein the dependence is $\lambda^{-1.28}$; Peterson [43, 89], on the other hand, finds a $\lambda^{0.065}$ dependence, a reddening effect. (Peterson used a G1 star for his calculations.)

TABLE 27. COLOR EXCESSES FROM ZODIACAL LIGHT MODEL F1 [22]

ϵ	$\Delta(M_V-M_G)$	$\Delta(M_G-M_R)$	Degree of Polarization	Approximate Radiance[a]
20	-0.132	-0.252	0.063	50 000
40	-0.152	-0.061	0.129	6 310
60	-0.148	-0.170	0.218	1 590
80	-0.197	-0.157	0.236	631
100	-0.203	-0.181	0.213	399
120	-0.187	-0.228	0.102	317
140	-0.273	-0.211	-0.061	282
160	-0.054	-0.239	-0.068	317

a. Read from Figure 11 of Reference 22.

The dependence of the neutral point position of polarization on wavelength is not well defined because of a lack of observational data. The dependence found by Weinberg [40] has yet to be predicted by any published model. For ice ($n \sim \alpha^{-4}$), the null point variation is not that which is observed. Figure 31 shows the null point variation for our basic model ($1 \leq \alpha \leq 20$, $n \sim \alpha^{-4}$, r^{-1}, ice). The null points were determined by extrapolating from the values at $\epsilon = 150$ and 160 deg. The tendency is for the null point to move to higher elongations with increasing wavelength rather than to decrease as observed. Greenberg [90, 91] finds this is the behavior of the null point for ice. However, for particles with $m = 1.65$ whose sizes are distributed according to $n(a) \sim e^{-5(4a)^3}$, he finds, over a limited wavelength region, that the null point position moves to lower elongations with increasing wavelength as observed.

Greenberg has observed that mixtures of metallic and dielectric materials (e.g., Giese's models) should be examined. A significant difference between them would be expected because the backscattering from metals differs from that of dielectrics.

L. Out-of-the-Ecliptic Model

The out-of-the-ecliptic models discussed in Chapter III were:

1. Constant thickness model [27].
2. Linear thickness model [27].
3. Ellipsoidal symmetry model [32, 33].
4. Exponential model [22].
5. Meteor model [35, 36].

This section presents the results of radiance and polarization calculations using the models given above. Only those values of the parameters which made the model fit the observations closely will be considered. However, observational results out of the ecliptic are scarce.

Gillett [27] used an empirical formula for the total differential cross section $d\sigma_T/d\Omega$ (Fig. 39) in the constant and linear thickness models. The specific cross sections used and the values obtained for K_i and (2R/W) for the constant thickness model and K_i and $(\omega_o)_i$ for the linear thickness model are given in Table 28. W is the width of the interplanetary cloud, ω_o is a defining cone angle, and K_i is a weighing factor (Fig. 17). The out-of-the-ecliptic polarization obtained by the models was high compared to that observed. Gillett obtained results for the constant thickness model with m = 1/2 or 1 and for the linear thickness model with m = 1/2 which were fairly consistent with observations in the ecliptic. The variation of L (45, i)/L (45, 0) for various values of (2R/W) is shown in Figure 98. The best fit is obtained by having $d\sigma_T/d\Omega$ reproduce L (ϵ, 0) for 30 to 100 deg with L (90, 90) = 0, such that L(90) > L(180) > L(110) with the minimum value L(ϵ) in the range $125 < \epsilon < 155$.

To understand the behavior of Gillett-type models, several simple models and several models using the Mie theory were considered by the authors. The results are shown in Figures 99 through 109. In Figures 99 and 100, the radiance contours for a hemisphere are shown for a simple

TABLE 28. GILLETT'S RESULTS [27]

Spatial Distribution	Total Average Differential Cross Section	Distribution Off of Ecliptic	Ecliptic Pole Radiance S_{10} (Vis)	Ecliptic Pole Polarization
Constant Thickness Model				
m = 0	$\sin^{-2}\frac{\Theta}{2} - \frac{1}{2}\sin\Theta + \begin{cases} 3\cos^2\Theta & \Theta \le \pi/2 \\ 0 & \Theta > \pi/2 \end{cases}$	$\frac{2D}{W} = 7.5$	13	0.61
m = 0.5	$\sin^{-1}\frac{\Theta}{2} - \frac{1}{2}\sin\Theta + \begin{cases} 2.5\cos^2\Theta & \Theta \le \pi/2 \\ 0 & \Theta > \pi/2 \end{cases}$	$1 \times \left(\frac{2D}{W} = 5\right)$ + 0.2 $\left(\frac{2D}{W} = 10\right)$	18	0.59
m = 1	$\sin^{-1}\frac{\Theta}{2} - \frac{1}{2}\sin\Theta + \begin{cases} 0.75\cos^2\Theta & \Theta \le \pi/2 \\ 0 & \Theta > \pi/2 \end{cases}$	$0.5 \times \left(\frac{2D}{W} = 2.5\right)$ + $0.5 \times \left(\frac{2D}{W} = 7.5\right)$	21	0.62
Linear Thickness Model				
m = 0.5	$\sin^{-1}\frac{\Theta}{2} - \frac{1}{2}\sin\Theta + \begin{cases} 2.0\cos^2\Theta & \Theta \le \pi/2 \\ 0 & \Theta > \pi/2 \end{cases}$ + 10 $\begin{cases} \cos^2 2\Theta, & \Theta \le \pi/4 \\ 0, & \Theta > \pi/4 \end{cases}$	$1 \times (\omega_o = 5.7$ deg) + $1.2 \times (\omega_o = 10$ deg) + $1.5 \times (\omega_o = 25$ deg) + $0.3 \times (\omega_o = 45$ deg)	27	0.48
m = 1	$\sin^{-1}\frac{\Theta}{2} - \frac{1}{2}\sin\Theta + \begin{cases} 0.75\cos^2\Theta, & \Theta \le \pi/2 \\ -\cos^2\Theta, & \Theta > \pi/2 \end{cases}$	$1 \times (\omega_o = 5.7$ deg) + $1.2 \times (\omega_o = 10$ deg) + $1 \times (\omega_o = 25$ deg) + $0.9 \times (\omega_o = 45$ deg) + $0.32 \times (\omega_o = 90$ deg)	37	0.47

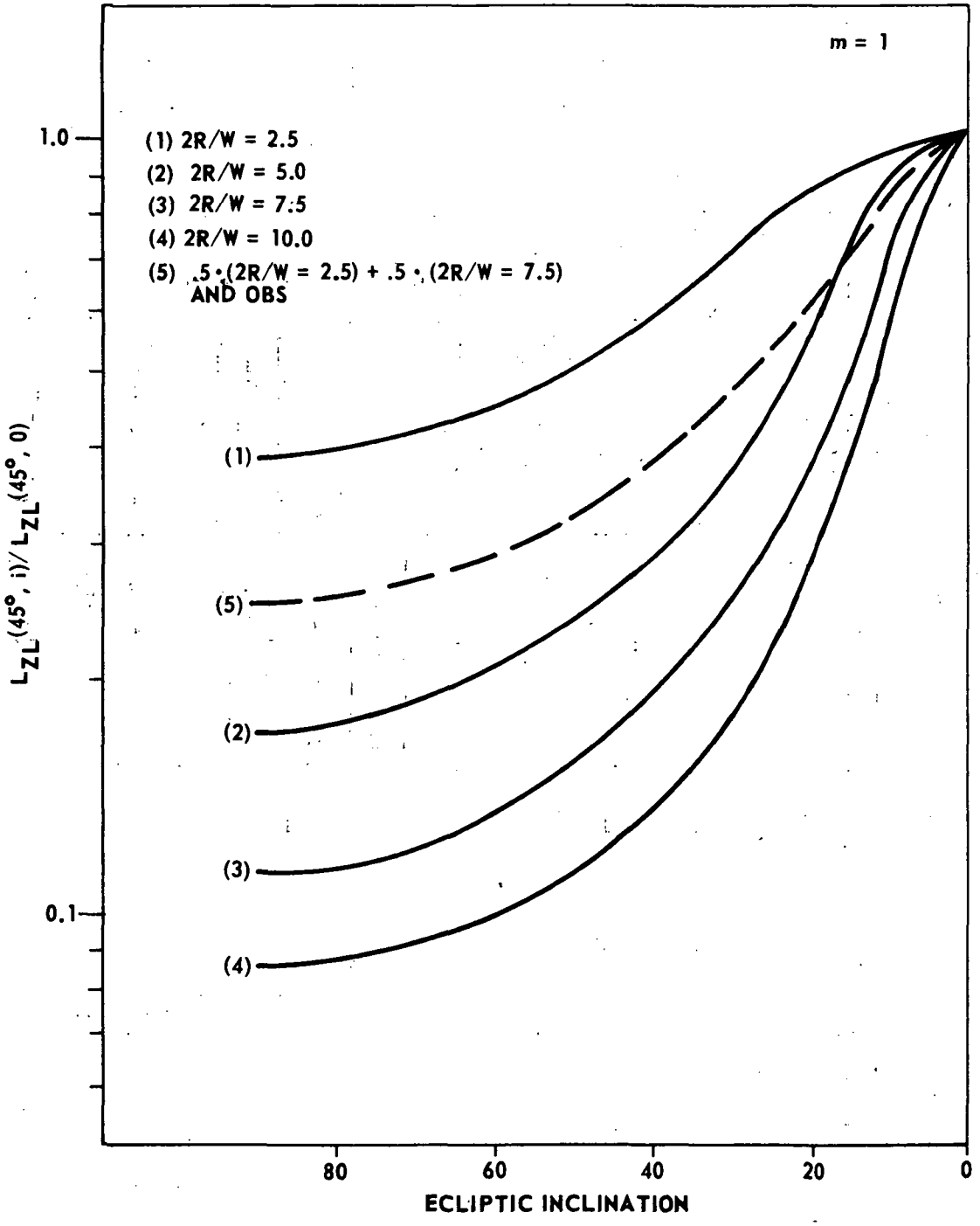

Figure 98. Gillett's [27] results for a constant thickness model. (The variation out of the ecliptic for the radiance is shown for various thickness models.)

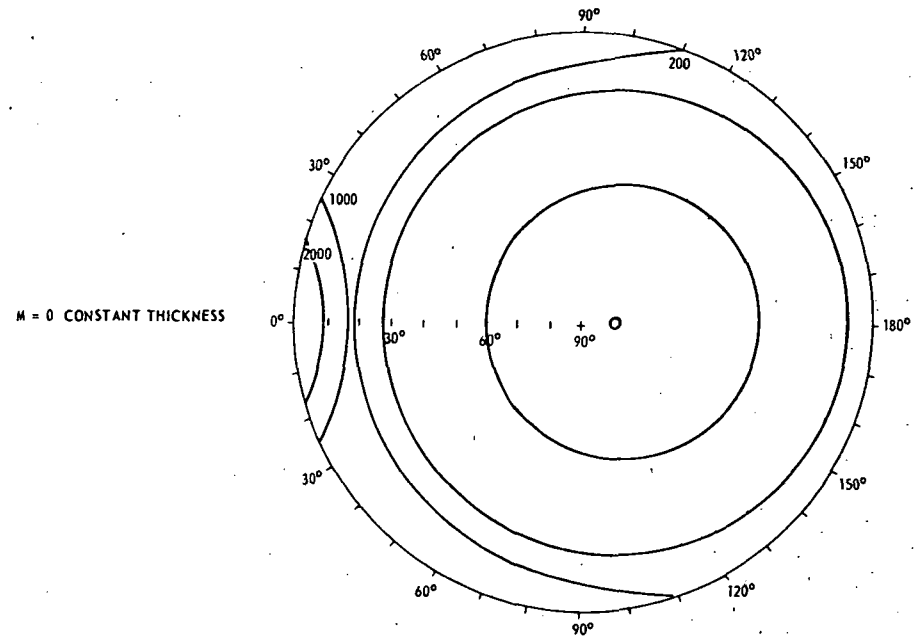

Figure 99. Out-of-the-ecliptic results using the constant thickness model and the basic heliocentric model (R/W = 2.5)

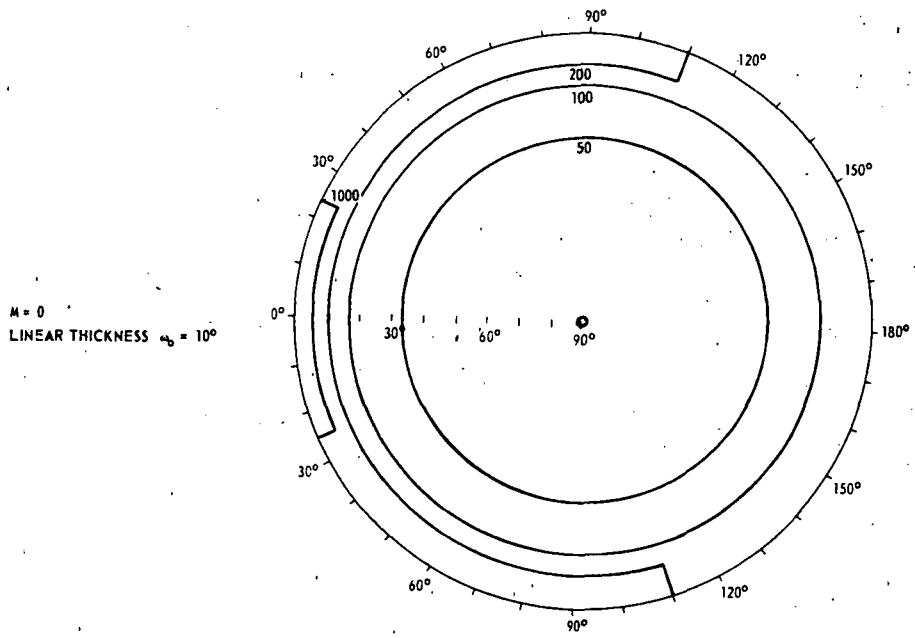

Figure 100. Out-of-the-ecliptic results using the linear thickness model and the basic heliocentric model.

heliocentric model with constant thickness and with linear thickness. The ecliptic pole is at the center of the figure and the ecliptic plane is on the circumference. The difference in the contours is that the linear thickness model is only piece-wise smooth and has a discontinuity in the rate of change of the radiance when the line of sight reaches the defining cone. The constant thickness model has the minimum radiance shifted from the ecliptic pole, whereas it is at the pole for the linear thickness model. Changes in the radiance and polarization of the constant thickness model with a change of R/W (≡ROW) are shown in Figures 101 through 104. Ice ($m = 1.33$) was used as the particle material. As R/W is decreased (i.e., W is increased), the radiance values off the ecliptic increase although the values on the ecliptic remain the same and the minimum value remains in the same region. The value of R/W = 1/10 is the best fit to radiance-observed data. The polarization value increases for $\epsilon < 90$ deg (Fig. 104) and decreases for $\epsilon > 90$ deg. For this figure, the point of observation moves such that $\epsilon = 90$ deg is the ecliptic pole. Figures 105 through 107 show the result of changing the materials. The contours are, in general, established by the distribution scattering functions, as is the effect of changing p (Figs. 108 and 109). Refer to Figure 102 for a comparison.

The ellipsoidal symmetry model [32, 33] adopted a spatial distribution out-of-the-ecliptic mode that is continuous,

$$s = n_o \left(\frac{r}{A}\right)^{-m} \left[1 + \left(\gamma \frac{z}{r}\right)^2\right]^{-m/2}$$

Two of their models (Table 29 and Fig. 110) approximate the out-of-the-ecliptic results of Smith, et al. [19]. In Figure 110, ℓ is the ecliptic latitude and δ is the distance from the sun in ecliptic longitude.

TABLE 29. GIESE-DZIEMBOWSKI MODELS [33]

Model	Refractive Index	Alpha Range	$N_o \left(\frac{\text{particles}}{\text{cm}^3}\right)$	m	γ
I Model	1.5	6 to 120	5.3×10^{-15}	3.0	10
	1.5	6 to 120	4.2×10^{-15}	0.1	10
	1.27 - 1.37 i	2 to 120	2.1×10^{-13}	3.0	10
II Model	1.33	12 to 120	8.7×10^{-15}	0.1	300
	1.33 - 0.1 i	2 to 120	7.5×10^{-13}	0.1	300

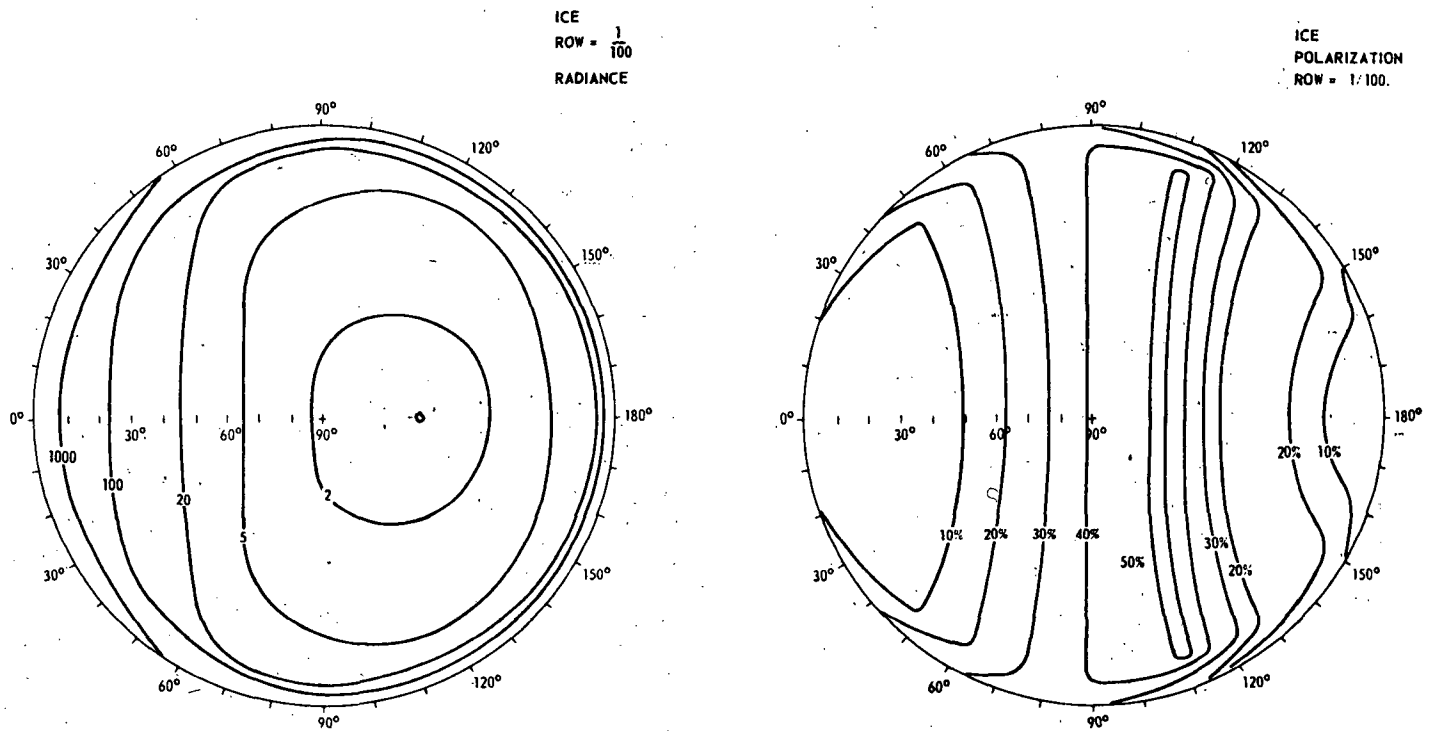

Figure 101. Out-of-the-ecliptic results using the constant thickness model for ice; ROW = 1/100 and p = 4 ($N_o = 1.5 \times 10^{-10}$, m = 1, $\alpha_{min} = 1$, and $\alpha_{max} = 20$).

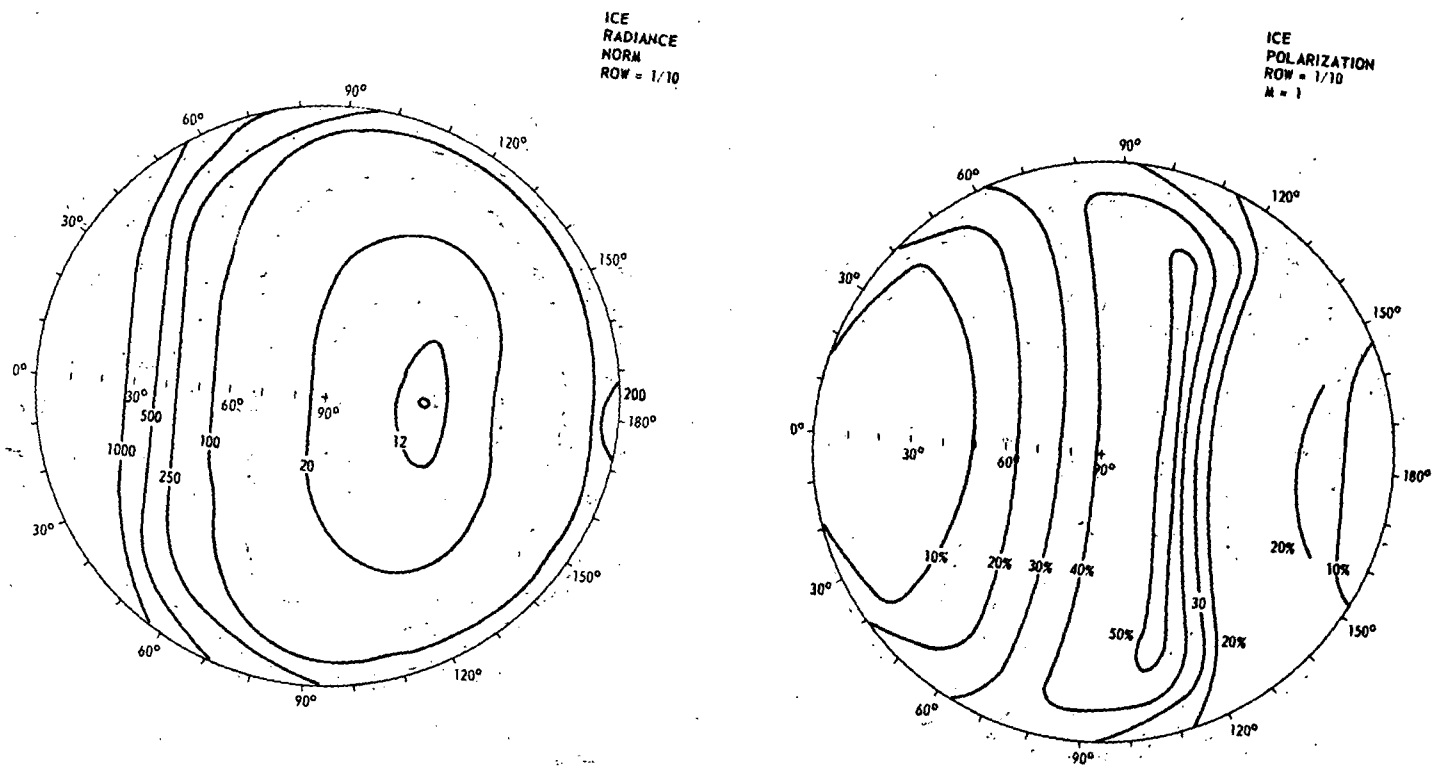

Figure 102. Out-of-the-ecliptic results using the constant thickness model for ice; ROW = 1/10 and p = 4 ($N_o = 1.5 \times 10^{-10}$, m = 1, $\alpha_{min} = 1$, and $\alpha_{max} = 20$).

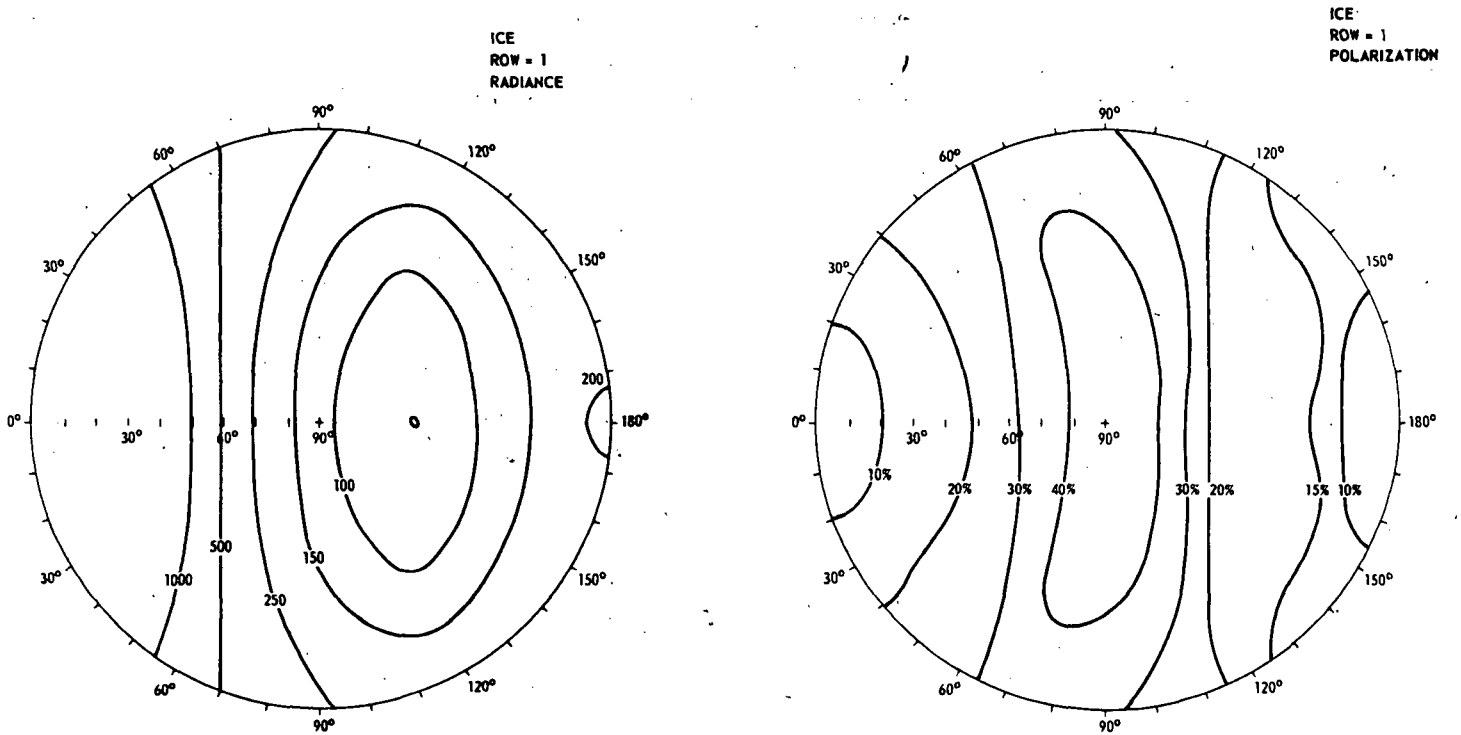

Figure 103. Out-of-the-ecliptic results using the constant thickness model for ice; ROW = 1 and p = 4 ($N_o = 1.5 \times 10^{-10}$, m = 1, $\alpha_{min} = 1$, and $\alpha_{max} = 20$).

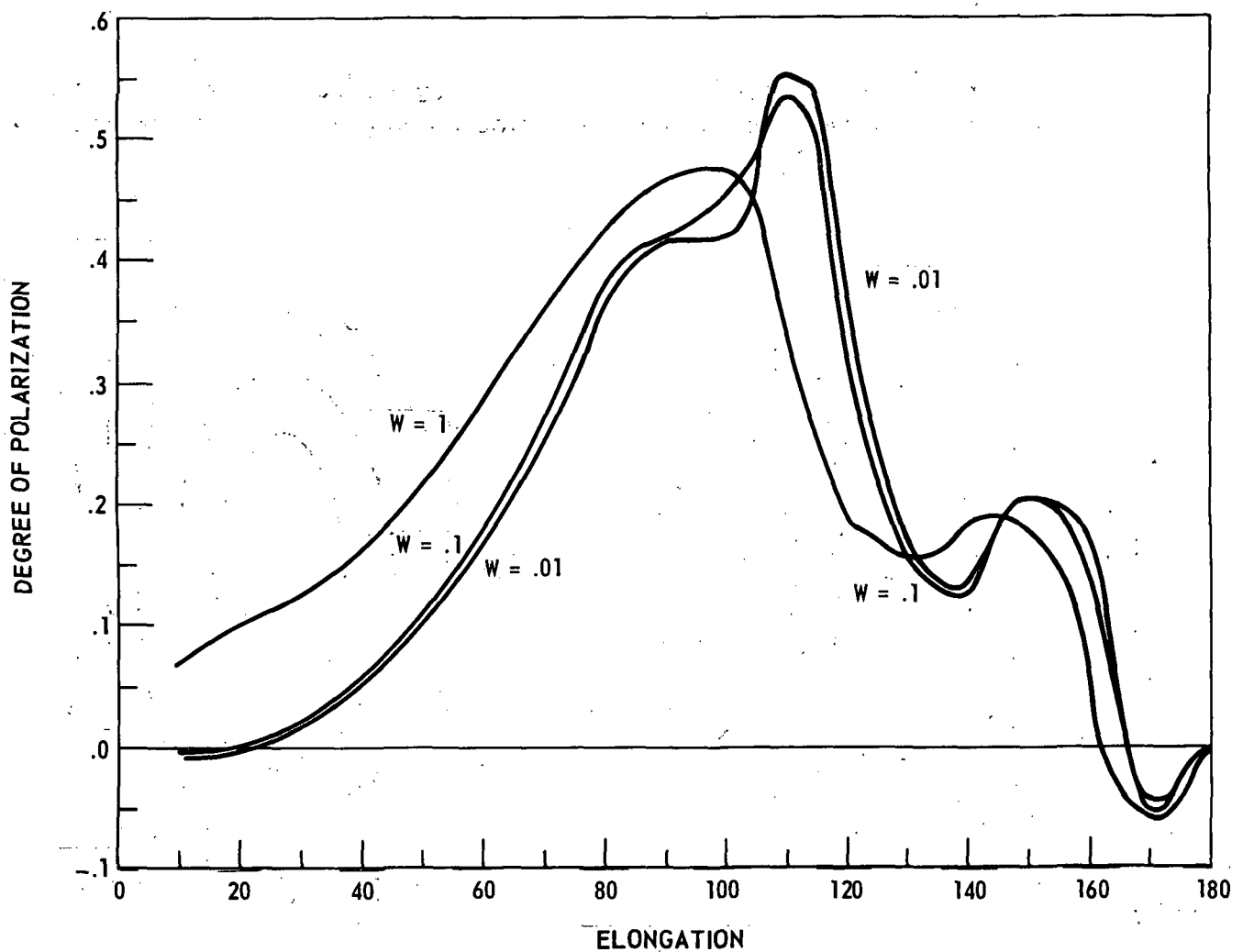

Figure 104. The degree of polarization for the constant thickness models of Figures 101, 102, and 103 for an inclination of 90 deg.

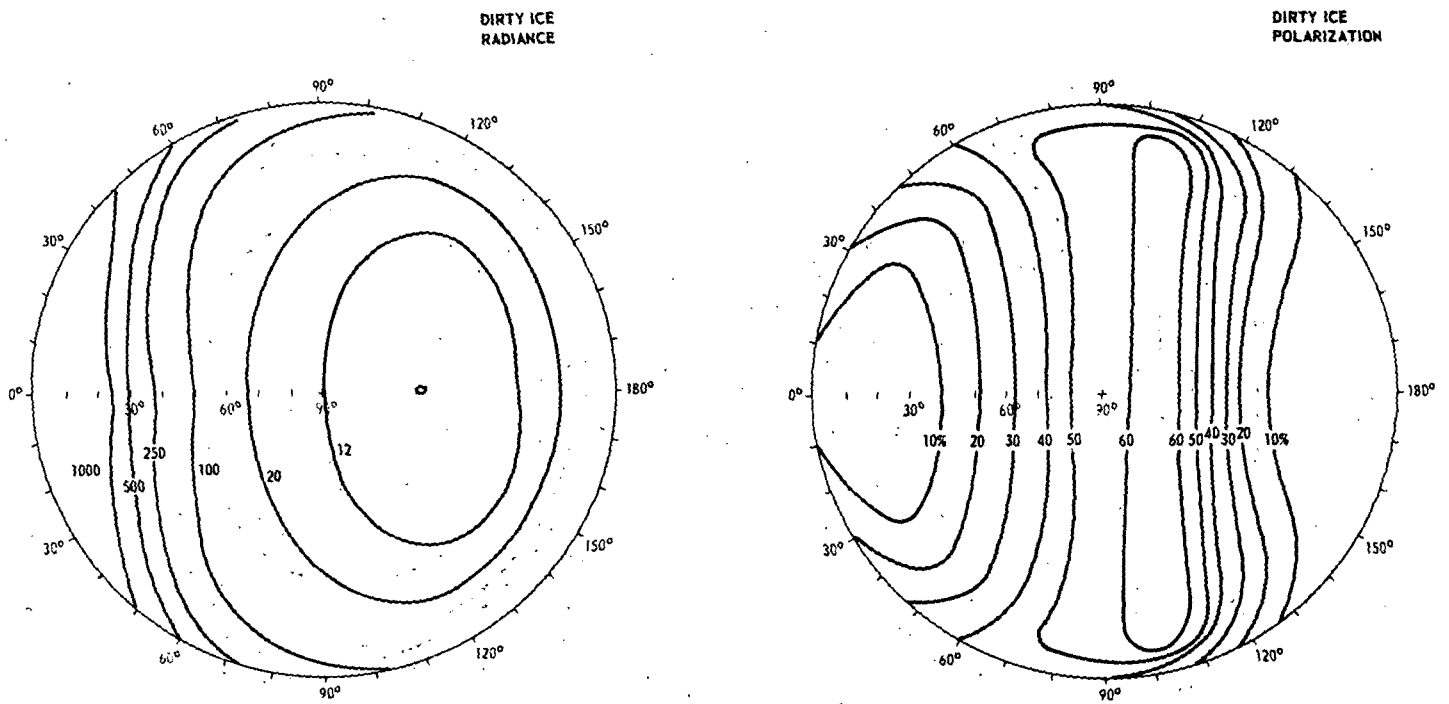

Figure 105. Out-of-the-ecliptic results using the constant thickness model for dirty ice ($k = 0.5$); ROW = 1/10 and $p = 4$ ($N_o = 1.5 \times 10^{-10}$, $m = 1$, $\alpha_{min} = 1$, $\alpha_{max} = 20$).

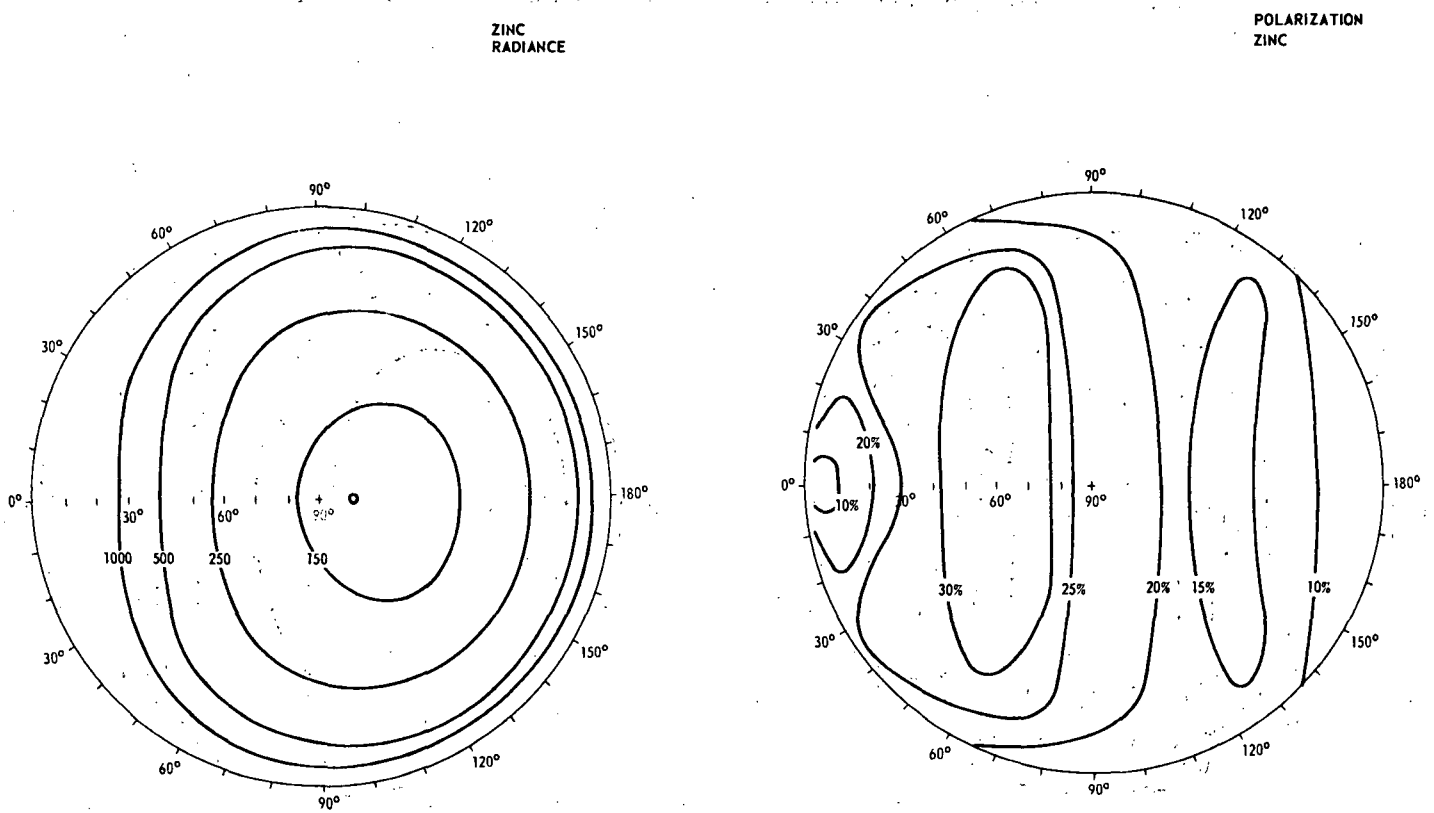

Figure 106. Out-of-the-ecliptic results using the constant thickness model for zinc; ROW = 1/10 and p = 4 ($N_o = 1.5 \times 10^{-10}$, m = 1, $\alpha_{min} = 1$, and $\alpha_{max} = 20$).

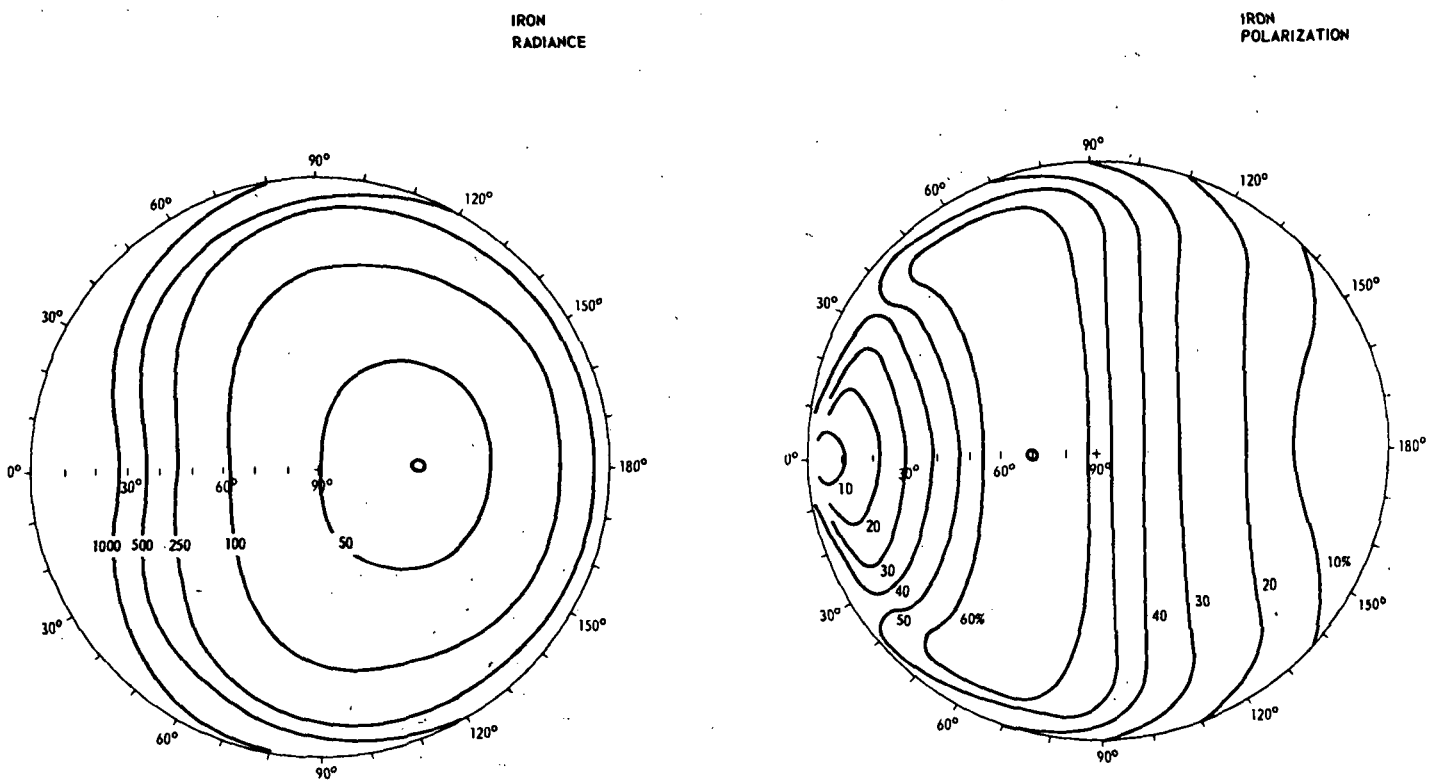

Figure 107. Out-of-the-ecliptic results using the constant thickness model for iron; ROW = 1/10 and p = 4 ($N_o = 1.5 \times 10^{-10}$, m = 1, $\alpha_{min} = 1$, and $\alpha_{max} = 20$).

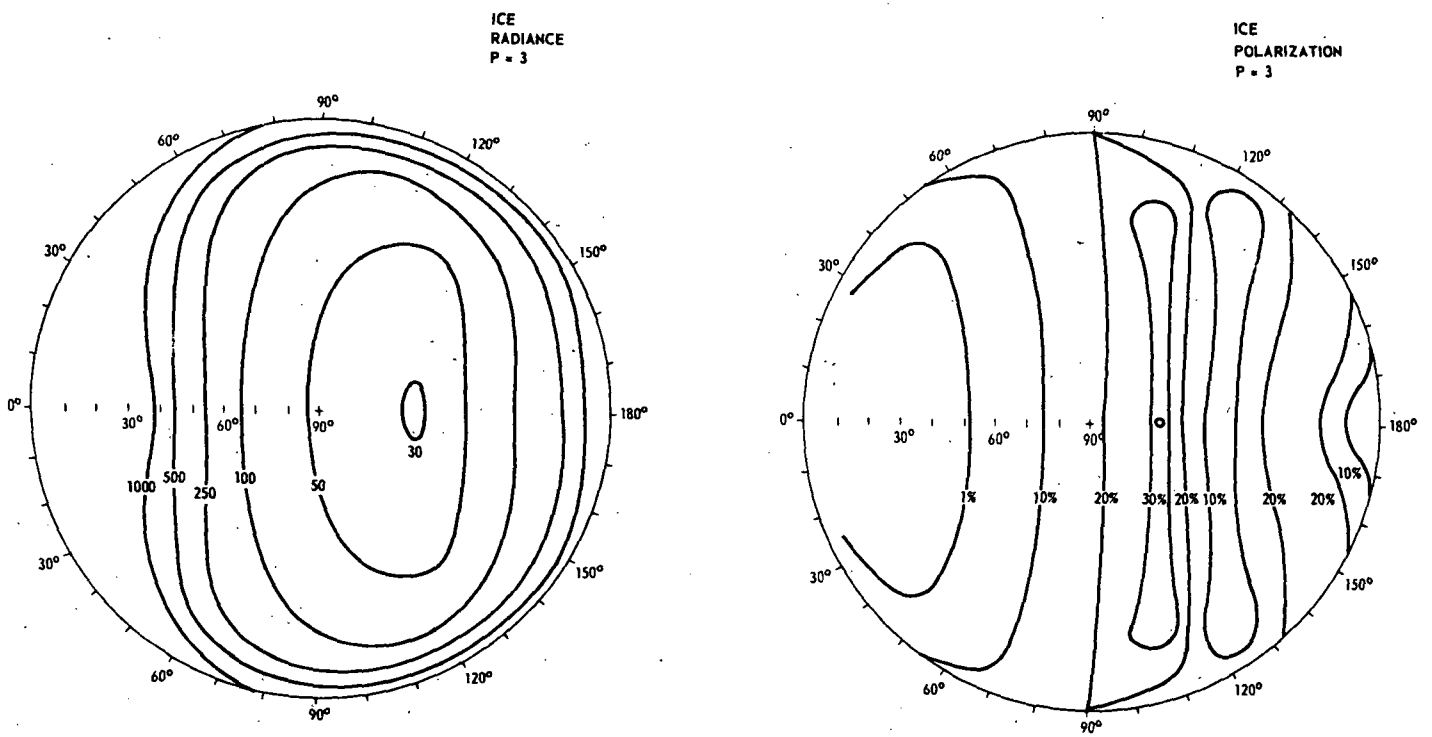

Figure 108. Out-of-the-ecliptic results using the constant thickness model for ice; ROW = 1/10 and p = 3 ($N_o = 1.5 \times 10^{-10}$, m = 1, $\alpha_{min} = 1$, and $\alpha_{max} = 20$).

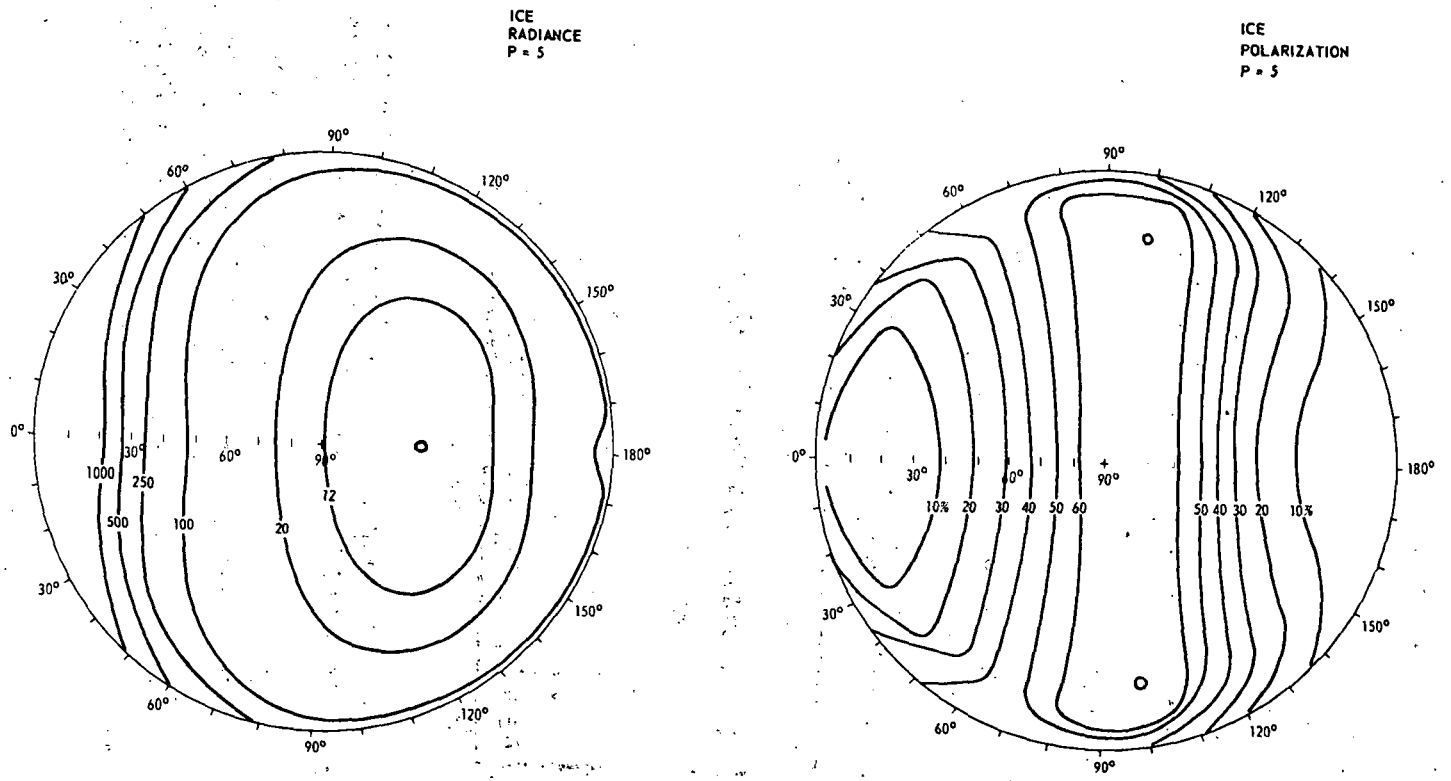

Figure 109. Out-of-the-ecliptic results using the constant thickness model for ice; ROW = 1/10 and p = 5 ($N_o = 1.5 \times 10^{-10}$, m = 1, $\alpha_{min} = 1$, and $\alpha_{max} = 20$).

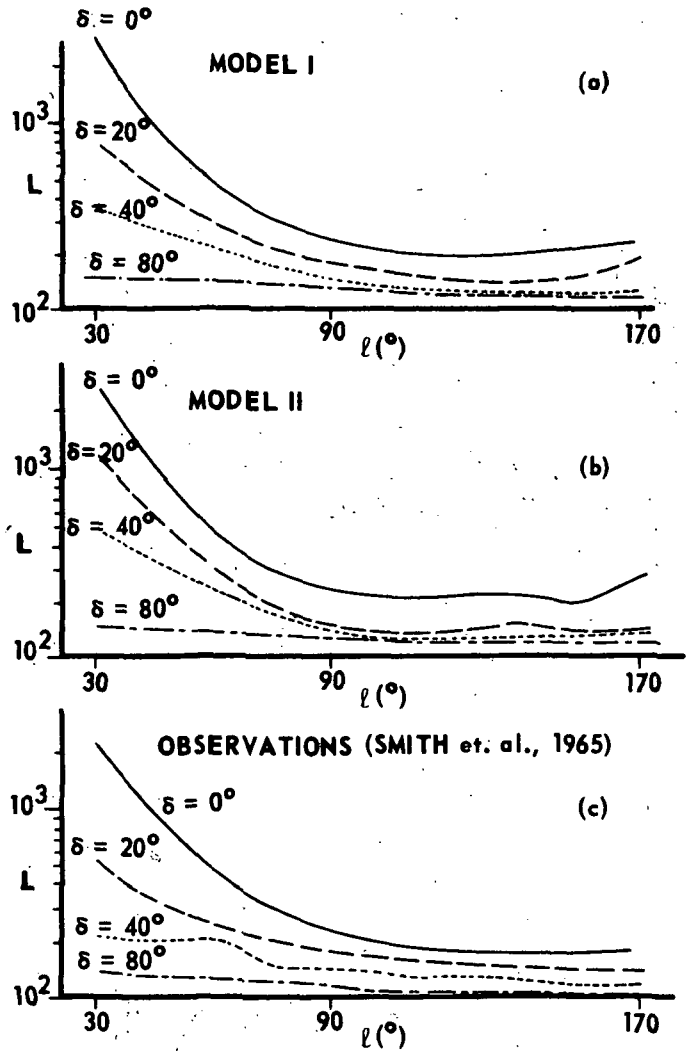

Figure 110. Giese and Dziembowski's [33] results for two ellipsoidal symmetry models compared with Smith et al. [19] observations.

Model I is metallic and Model II is dielectric. Both models have large particles with slowly decreasing ($p = 2.5$) size distribution. By comparing large particle models with Rayleigh models (i.e., smaller size particles) which tend to have a minimum further from the sun than the ecliptic pole, Giese and Dziembowski concluded that the larger particles better fit the observed data.

Van Rhijn used a density distribution of the form

$$n(x, y, z) = N_o \left(1 - a\left(x^2 + y^2\right) - bz^2\right), \tag{182}$$

where x, y, z are heliocentric coordinates for out-of-the-ecliptic calculations [2]. The integral was terminated when

$$n(x, y, z) = 0,$$

and a phase function was assumed; thus,

$$4\pi\, h(\Theta) = 0.655 - 0.711 \sin \Theta - 0.345 \cos \Theta + 0.406 \sin^3 \Theta \qquad (183)$$

for the angular distribution of the scattered light. The values of the parameters a and b were determined from observed radiance to be a = 0.176 and b = 1.406. This gives a ratio of the major-to-minor axis of 2.8. For geocentric longitudes (ecliptic longitudes) of δ = 0, 20, and 60 deg, the values of Van Rhijn are compared with the out-of-the-ecliptic data of Smith et al. [19] in Figure 111. The data points (δ = 0 and ϵ = 80 deg) were used to normalize the data. The agreement is good. Using a particle with an albedo of 0.3 and a 50-cm radius (rocks), Van Rhijn estimated the density of particles at 1 AU to be 10^{-18} g/cm^3.

Fesenkov [34] also used the ellipsoidal model and the scattering functions for aerosols to determine the polarization at the ecliptic pole. The following values resulted:

Eccentricity	Polarization
e = 0 disc model	p = 34.0 percent
e = 0.1	p = 32.8 percent
e = 1 (spherical model)	p = 26.4 percent

Aller et al. [22] used the exponential model to calculate out-of-the-ecliptic contours. However, their polarizations are generally too high compared with observations; cf., Table 13, p. 107. The radiance minimum occurred near ϵ = 130 deg, with i = 90 deg. However, the exponential decay away from the ecliptic varies as $e^{-5z/R}$, which gives an exponential half-width of the cloud of on the order of 10^{-1} AU.

Rouy and Aller [92] make the observation that the distribution of the radiance perpendicular to the ecliptic could be approximated by a Gaussian distribution. For scans orthogonal to the ecliptic plane at a specific elongation ϵ, the radiance could be expressed by

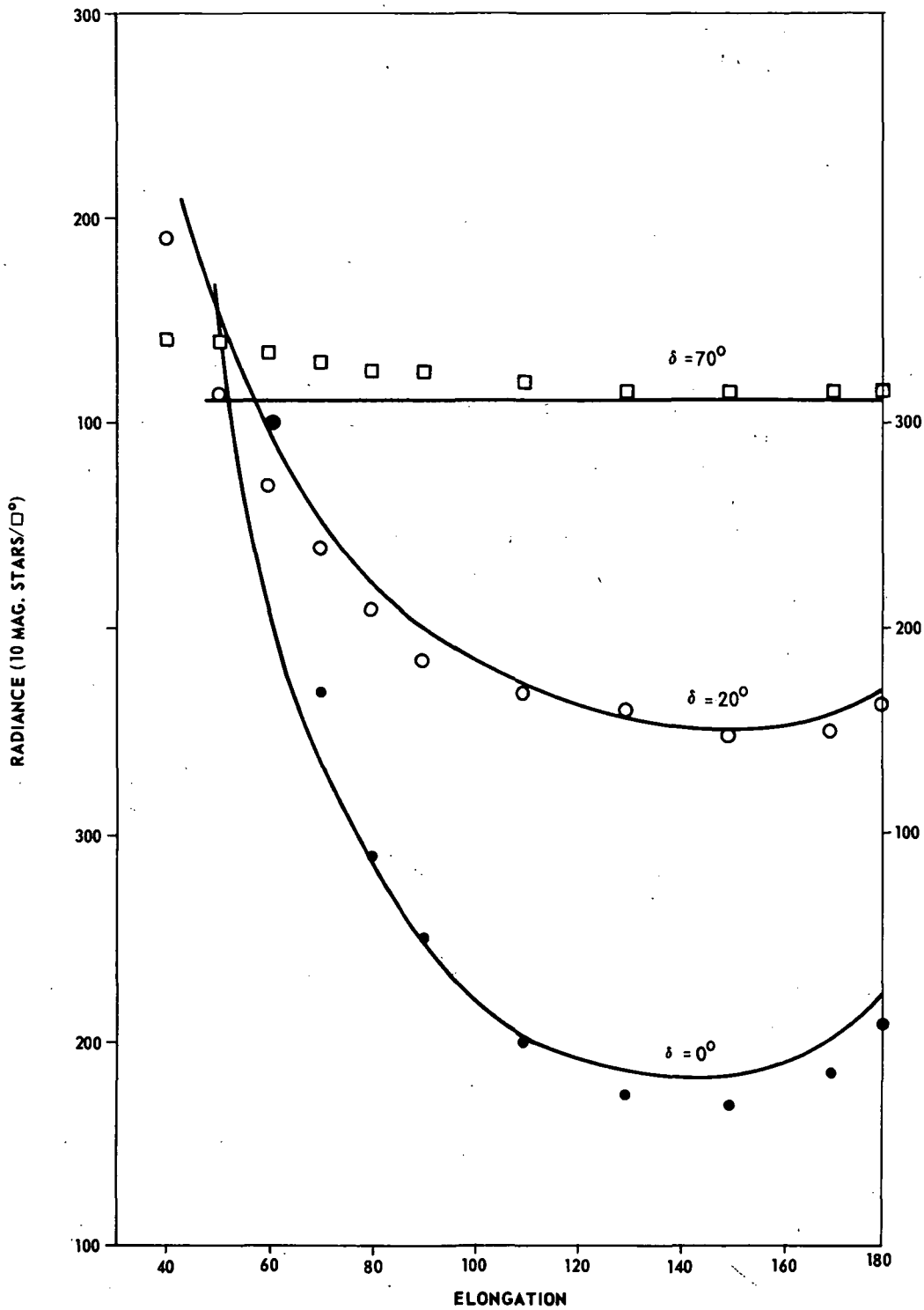

Figure 111. Van Rhijn's [3] ellipsoid results for out-of-the-ecliptic (solid lines) compared with Smith et al. [19] data (● ~ $\delta = 0$ deg, ○ ~ $\delta = 20$ deg, □ ~ $\delta = 70$ deg) normalized at $\delta = 0$ and $\epsilon = 80$ deg.

$$\bar{L}(\omega, \epsilon) = L_{zo}(\epsilon)\, e^{-K\omega^2} + L_B(\epsilon)$$

where

$L_{zo}(\epsilon)$ = the peak radiance of the zodiacal light.

$L_B(\epsilon)$ = the average radiance of the background.

ω = the angular measurement from the ecliptic.

By analysis of the derivatives, various zeroes (Fig. 112) arise which one can use for determining the parameters in the equation. Examining Weinberg's data for a particular scan for total radiance, Rouy and Aller determine that K = 1.182 (Fig. 112). Their calculation should be considered a preliminary one since the accuracy of the approximation has yet to be determined.

Singer and Bandermann [21] used the generalized model with the size distribution given by

$$n(r, \Theta) = \frac{1}{r} \int_{r/2}^{\infty} \int_{|r/a-1|}^{1} \int_{\pi/2-\Theta}^{\pi/2} \frac{a^2 f(a, e, i)\, da\, de\, di}{[e^2 - (r/a-1)^2]\, (\sin^2 i - \cos^2 \Theta)^{1/2}} \tag{184}$$

where

$$f(i) = \sin i\, e^{-bi} \quad . \tag{185}$$

They assumed a scattering intensity function $i(\Theta)$ of the form

$$i_\lambda(\Theta) = \frac{\gamma}{2\pi} \left(\frac{1+\eta^2}{1+e^{\eta\pi}} \right) e^{\eta\Theta} + \frac{1}{2} \frac{\gamma < S >}{< S^2 >} (\Theta\pi)^{-3}, \tag{186}$$

where the first term is the diffraction component, and the second is the reflection component. γ is the albedo of the particle, η is the phase coefficient of of reflection, and $\langle S \rangle$ and $\langle S^2 \rangle$ are the mean and mean-square of the particle size dimension. The values of $\eta = 0.02$, $T = \gamma < S > / < S^2 > = 0.14$, $b = 3$, $\gamma = 0.1$, and $m = 1.5$ fit the observations of Smith et al. [19] best for the functions:

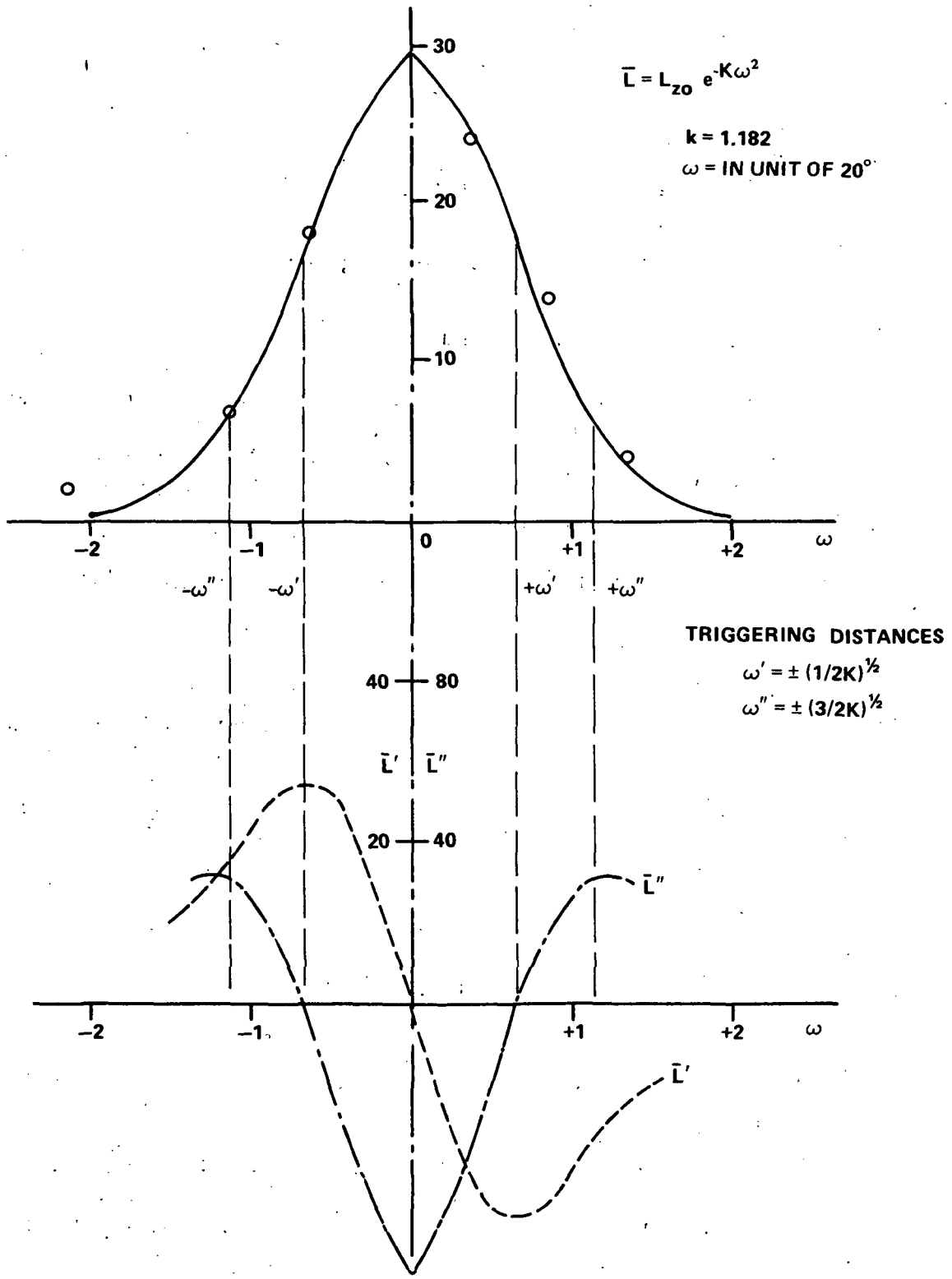

Figure 112. Apparent Gaussian distribution of the zodiacal light and the zeros of the derivatives [92].

$\overline{L}(\epsilon)/\overline{L}(\epsilon = 30 \text{ deg})$, $i = 0$ deg

$\overline{L}(i)/\overline{L}(i = 0 \text{ deg})$, $\epsilon = 90$ deg

and

$\overline{L}(\epsilon, i = 0 \text{ deg})/\overline{L}(\epsilon, i = 90 \text{ deg})$.

$T = 0.14$ indicates a flat size spectrum of large particles and $b = 3$ indicates an average orbital inclination of $i = 30$ deg. The radial dependence is $r^{-1.5}$. Polarization values were not calculated because of the form of the scattering intensity function.

Divari [93] has taken the meteor model with a scattering function of the form

$$f(\Theta) = 0.0549 \left[1 + 11.1 \left(e^{-3\Theta} - 0.009\right) \right] \tag{187}$$

and calculated relative radiance. The isophotes obtained are close to those observed. The polarization was also matched by using an empirical function taken from atmosphere observations. The zodiacal light polarization values obtained are high, even in the ecliptic (e.g., $p(\epsilon = 80) = 40$ percent); hence, due to the values of the parameter used as input by Divari, the results are inconclusive.

It can now be seen that there are several out-of-the-ecliptic models (some using Mie theory, some not) which achieve reasonable agreement with observations. The agreement is not yet close enough to be really satisfactory, but further improvement will probably await the results of measurement made outside the earth's atmosphere.

M. Nonspherical Particles

The Mie-theory models deal only with spherical particles and can show peculiar effects, e.g.; haze bow [32]. Analysis using this theory may give an erroneous interpretation of experimental data, especially in the anti-solar direction where the geometry of the particle plays a more important role [90, 91]. However, Little et al. [86], Napper and Ottewill [94], and Donn and Powell [95] have shown that the radiance, in the $50 < \Theta < 150$ deg range, from a distribution of nonspherical particles of random orientation can be represented approximately by an appropriate distribution of spherical particles. For scattering angles $\Theta \lesssim 60$ deg, the protrusion of irregular structure increases the scattering function by diffraction. Nonspherical particles may prefer a

given orientation, resulting in further differences from Mie theory. Though Powell et al. [28] concluded that the scattering intensity functions at a given wavelength for a distribution of cubes (large-volume shape) could be reproduced by spheres whose distribution is approximately that of the cubes. They also conclude that a size distribution for small-volume shapes may differ markedly from that of equivalent spheres. The difference between small-volume scatterers and spheres can be seen geometrically by considering the ratio of the projected area of rods and disc to that of a sphere. If the rods have a length-to-radius ratio of 10, and the disc has a radius thickness ratio of 10, then, for an equivalent volume, the projected area ratio to a sphere is 1.7 and 5.5, respectively. Hence, small-volume particles, such as flat particles and very elongated particles, are more efficient scatterers than spheres for equivalent volumes.

Only a few scattering problems for finite bodies have been solved {e.g., sphere, prolate spheroid, oblate spheroid, disc and rods [96]} although various perturbation procedures have been applied to other shapes. Recent investigations on finite cylinders might lend themselves to zodiacal light studies [24, 97, 98, 117, 118, 101]. Cylindrical scattering differs from spherical scattering in that there is a loss in the degree of symmetry which introduces anisotropic scattering. A shape factor can give a general characterization of the anisotropic scattering. The anisotropic processes should lead to new results in zodiacal light model parameters, although no model exists employing cylinders to date.

Figure 113 and 114 give the scattering intensity functions and polarization for infinite cylinders whose axes are perpendicular to the incident direction [82, 98]. The polarization for the cylinders is not zero in the forward or backward direction, a marked difference from spheres. For larger α, the diffraction peak (Fig. 113) is observed as an increase in the radiance in the forward direction for all angles of incidence. Kerker et al. [24] give single-size scattering functions for oblique incidence. The functions are strongly dependent on the orientation of the cylinder axis with respect to the incident direction. The scattered intensity functions contain a perpendicular and a parallel component for both perpendicular and parallel polarization of the incident beam.

For a distribution of dielectric cylinders, ($m^* = 1.33$), Hanner [97] observed that with natural light at normal incidence, the total scattering intensity is analogous to dielectric spheres, having a forward diffraction peak and an increase in the back-scattered radiance. However, the polarization differed significantly from that for spheres (Fig. 115).

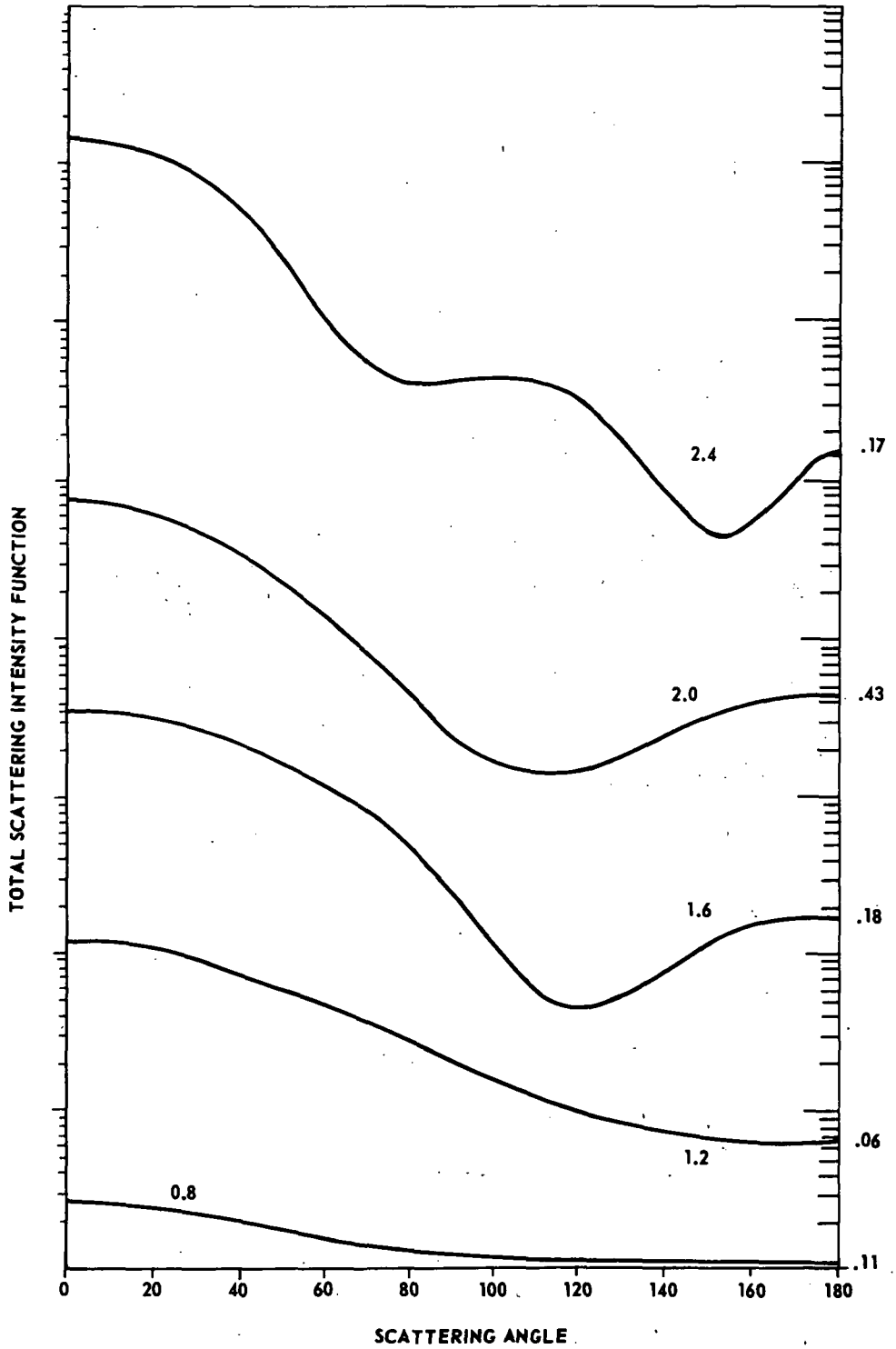

Figure 113. The total scattering intensity functions for cylinders perpendicular to the incident beam [98].

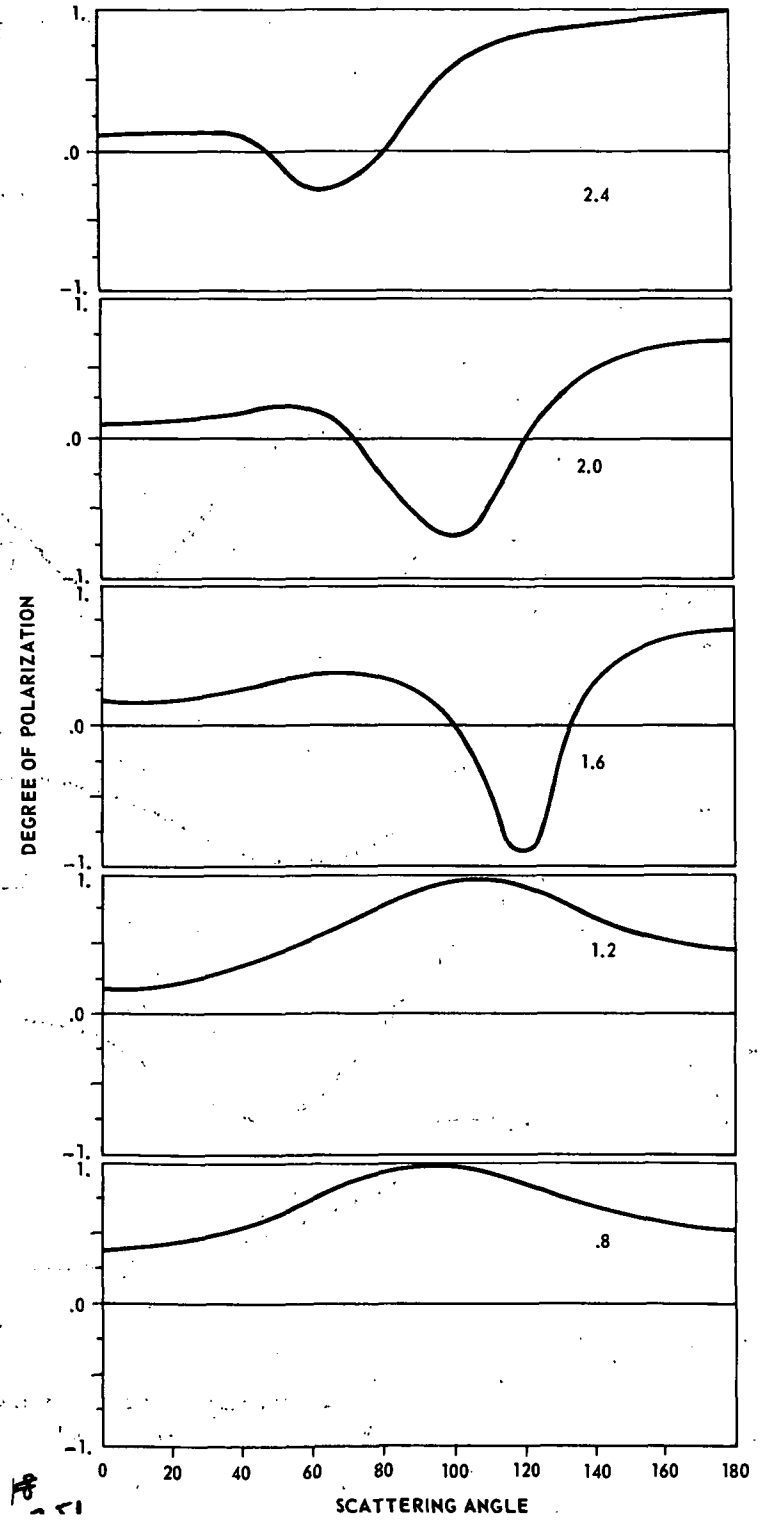

Figure 114. The degree of polarization for cylinders perpendicular to the incident beam [98].

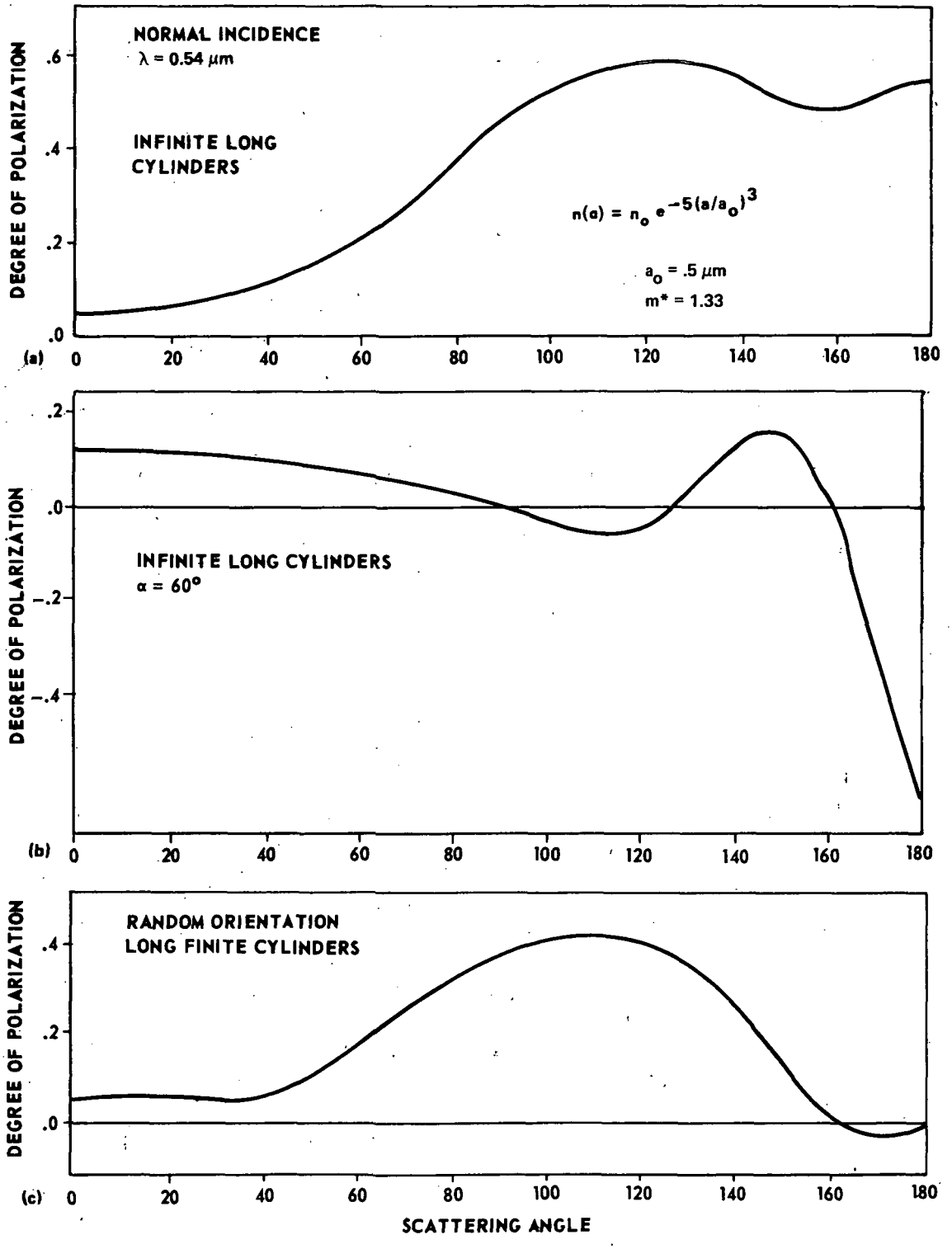

Figure 115. Hanner's [97] results for cylinders with a distribution of the form $n = n_o \exp[-5(a/ao)^3]$, α = tilt angle.

For a distribution of particle sizes, as the tilt angle increases, the total intensity decreases. The tilt angle is the angle in the incident plane between the incident direction and the perpendicular to the cylinder axis. Also, as the tilt angle increases, the polarization in the forward direction does not change much while the polarization in the backward direction oscillates in polarity. Compare Figures 115a and 115b [97]. Making use of an extension given by Lind [99] to the infinite cylinder treatment, Hanner gives results (Fig. 115c) for randomly oriented long, finite dielectric cylinders. The shape of the curve is similar to that for a distribution of dielectric spheres [$m^* = 1.33$, $n(\alpha) = n_0\alpha^{-4}$, $1 \leq \alpha \leq 20$] (cf. Fig. 62). The differences are that the polarization for cylinders is nonzero in the forward direction, less negative in the backward direction, and its peak is at 110 deg instead of 120 deg.

Thus, it is seen that the radiance and polarization from models depend greatly on the shape of the particles. Hence, the Mie theory approach can be considered a first-order approximation. To obtain better models, the effects of irregular shapes on the radiance, polarization, and color of zodiacal light require further investigation, both experimentally and theoretically, and more reliable and consistent observations are needed.

N. Areas for Further Research

Presently, a unique model does not exist which predicts the observed photometric properties of the zodiacal light. However, comparing the various models which are in approximate agreement with the observations (cf. Table 26), one finds that the following properties are representative of the zodiacal light dust cloud:

1. Composition — Largely dielectric particles with a refractive index in the range 1.3 to 1.8 with smaller percentages of metallic particles.

2. Shape structure — An equivalent size distribution of spheres in the range from 0.1 to 1.0 micron or 1.0 to 10 microns. Assuming the smaller size distribution, the exponential power law exponent is on the order of 3-4, while the larger size distribution has a smaller value of, say, 2-3.

3. Spatial structure — The spatial structure of the cloud can be considered to be heliocentric with a decrease in the particle density according to r^{-m} where $0 < m < 3.0$. The out-of-the-ecliptic spatial density models indicate a characteristic half-thickness of 10^{-1} AU for the dust cloud. The number density is on the order of 10^{-13} - 10^{-15} particles/cc.

In conclusion, it can be said that an enormous amount of work has been done in relating light scattering models to the photometric observations of the interplanetary dust cloud; however, a conclusive knowledge of the physical properties of the dust cloud still remains elusive.

The following areas need refinement for model calculations and analysis of the zodiacal light by photometry:

1. The size and spatial distribution needs to be based on experimental data. This is particularly true in the case of particle-size distributions where a lower cut-off limit is assumed. A sharp cut-off seems unlikely.

2. A set of polynomials needs to be created to form $\overline{d\sigma/d\Omega}$.

3. The effects of irregularly shaped particles compared to spheres should be better defined to categorize differences.

4. The methods of inversion of the photometric observations of $\overline{d\sigma/d\Omega}$ to find particle sizes and composition need more definition and study.

5. The complete effects of the physical forces on the dynamics of the interplanetary particles need to be determined.

6. If possible, a Mie theory model which satisfies all the gross properties of the observational data should be found.

APPENDIX. DYNAMICAL FORCES

This appendix considers the physical forces which act on the interplanetary particles, thereby possibly determining the spatial and size distribution and the temporal variation.

1. Radiation Pressure [24]

According to Maxwell's theory of electromagnetic radiation, light carries momentum as well as energy. The direction of the momentum is in the same direction as the energy flow and is given by

$$M = E/c$$

where E is the energy and c is the velocity of light. Electromagnetic momentum produces a radiation pressure on the interplanetary particles. The momentum of the incident field is scattered and absorbed by the scattering center. The total energy per second removed from the incident beam of unit radiance by absorption is equal to the cross section for extinction, C_{ext}. However, of the momentum carried away by the scattered radiation, that part which is associated with the forward component is restored to the incident beam. The time-averaged radiation force is [24]

$$F_r^{\lambda} = \frac{\Sigma^{\lambda}\pi a^2}{c}\left(C_{ext} - \overline{\cos\theta}\, C_{sca}\right) ,$$

where Σ^{λ} is the spectral radiant flux density at the surface of the particle, C_{sca} is the cross section for scattering, and

$$\overline{\cos\theta} = \frac{\frac{\pi}{k^2}\int_{-1}^{+1}(i_1 + i_2)\cos\theta\, d(\cos\theta)}{\frac{\pi}{k^2}\int_{-1}^{+1}(i_1 + i_2)\, d(\cos\theta)}$$

$$= \frac{\pi}{k^2}\int_{-1}^{+1}(i_1 + i_2)\cos\theta\, d(\cos\theta)\,/C_{sca} .$$

The asymmetry factor, $\overline{\cos\theta}$, is the mean of $\cos\theta$ with the scattering intensity functions as the weighting function. The efficiency factor for radiation pressure is defined as

$$Q_{pr}^{\lambda} = Q_{ext}^{\lambda} - \overline{\cos\theta}\, Q_{sca}^{\lambda} = \frac{C_{ext}}{\pi a^2} - \overline{\cos\theta}\,\frac{C_{sca}}{\pi a^2} .$$

The asymmetry function can be expressed as

$$\overline{\cos\theta}\, Q_{sca}^{\lambda} = \frac{4}{\alpha^2} \sum_{n=1}^{\infty} \left[\frac{n(n+2)}{n+1} \operatorname{Re}\left(a_n^* a_{n+1} + b_n^* b_{n+1}\right) + \frac{(2n+1)}{n(n+1)} \operatorname{Re} a_n^* b_n \right] .$$

Hence, for a specific wavelength the pressure exerted on a particle of a cross-sectional area πa^2 is

$$P^{\lambda} = \frac{F_r^{\lambda}}{\pi a^2} = \frac{\Sigma^{\lambda} \pi a^2}{c} Q_{pr}^{\lambda} .$$

2. Gravitational Force Versus Radiation Force

The force of gravity on a particle of radius a, mass density ρ, and distance r from the sun is

$$F_g = \frac{GM_{\odot}}{r^2} \frac{4}{3} \pi \rho a^3 ,$$

where G is the universal gravitational constant (6.670×10^{-11} nt m^2/kg^2) and $M_{\odot}$ is the mass of the sun (1.989×10^{30} kg). For r in AU, ρ in kg/m^3, and a in meters [100]

$$F_g = \frac{2.5 \times 10^{-2}}{r^2} \rho a^3 \quad [\text{nt}] .$$

To compare this to radiation pressure, one sees that the radiation force is

$$F_r = \frac{\pi a^2}{cr^2} \overline{Q_{pr}(a)}\, R^2 \int_{\lambda_1}^{\lambda_2} \Sigma^{\lambda}\, d\lambda = \frac{\pi a^2}{c} \frac{R^2}{r^2} \int_{\lambda_1}^{\lambda_2} Q^{\lambda}(m, \alpha)\, \Sigma^{\lambda}\, d\lambda ,$$

where Σ^{λ} is evaluated at 1 AU. $\overline{Q_{pr}(a)}$ is a function which is on the order of unity for a greater than 0.6×10^{-7} m and which declines approximately as a^4 for smaller a. For r in AU and a in meters,

$$F_r = 1.4 \times 10^{-5} \frac{a^2}{r^2} \overline{Q}_{pr} \quad [\text{nt}] .$$

The quantity of $1 + \mu$, defined as the ratio of the force caused by radiation pressure F_r to the force of gravitational attraction F_g, is independent of the distance r of the particle from the sun and is given by Gindilis et al. [105]

$$1 + \mu = \frac{F_r}{F_g} = \frac{A}{\rho a} \int_{\lambda_1}^{\lambda_2} Q_{pr}^{\lambda} (m, \alpha) \Sigma^{\lambda} \, d\lambda \quad ,$$

where ρ is the density of the dust particle, $A = 3 R^2/4cG M_{\odot}$. They use

$$\Phi (m, a) = \rho (1 + \mu)$$

to represent the ratio of radiation force to the gravitational force per unit density for a given particle with radius a and refractive index m*. This quantity is important in evaluating the relative magnitude of the two forces. Table A-1 gives the values of $Q_{pr} (m, \alpha)$ obtained by them; Table A-2 gives the values $\Phi (m, a)$; Figure A-1 gives the pertinent results for several substances. In the case of quartz and water, the radiation pressure is less than the force caused by gravitational attraction for all particle sizes.

An analogous situation occurs for most dielectrics ($m^* \leq 1.6$ and $\rho \approx 2\text{-}3$ g/cm^3). When m is larger than two, particles of certain sizes will be pushed out of the solar system. For titanite ($m^* = 2$, $\rho = 3.5$ g/cm^3), particles with $0.1 \leq a \leq 0.3 \times 10^{-6}$ m will be ejected. If $\overline{Q_{pr}(a)} = 1$, then the radiation pressure dominates solar gravity for $a \leq 5 \times 10^{-7}$ m. The rapid decline of $\overline{Q_{pr}(a)}$ below 1×10^{-7} m limits the region of radiation pressure.

TABLE A-1. EFFICIENCY FACTOR $\overline{Q_{pr}(m, \alpha)}$ [105]

	m*									
α	1.2	1.3	1.33	1.4	1.5	1.6	2.0	10^4	1.27 - 1.37i Iron	2.455 - 1.25i Graphite
0.001	$4.47.10^{-14}$	$9.51.10^{-14}$	$1.11.10^{-13}$	$1.57.10^{-13}$	$2.31.10^{-13}$	$3.14.10^{-13}$	$6.66.10^{-13}$	$5.95.10^{-12}$	$2.79.10^{-3}$	$9.82.10^{-}$
0.005	$2.74.10^{-11}$	$5.82.10^{-11}$	$6.92.10^{-11}$	$9.79.10^{-11}$	$1.44.10^{-10}$	$1.95.10^{-10}$	$4.17.10^{-10}$	$2.57.10^{-9}$	$1.38.10^{-2}$	$4.91.10^{-}$
0.01	$4.36.10^{-10}$	$9.32.10^{-10}$	$1.11.10^{-9}$	$1.57.10^{-9}$	$2.31.10^{-9}$	$3.11.10^{-9}$	$6.67.10^{-9}$	$4.53.10^{-8}$	$2.76.10^{-2}$	$9.88.10^{-}$
0.05	$2.72.10^{-7}$	$5.82.10^{-7}$	$6.94.10^{-7}$	$9.79.10^{-7}$	$1.44.10^{-5}$	$1.95.10^{-6}$	$4.17.10^{-6}$	$2.94.10^{-6}$	0.138	$4.97.10^{-}$
0.1	$4.35.10^{-6}$	$9.30.10^{-6}$	$1.11.10^{-5}$	$1.56.10^{-5}$	$2.30.10^{-5}$	$3.12.10^{-6}$	$6.68.10^{-3}$	$4.67.10^{-4}$	0.279	0.101
0.2	$6.88.10^{-5}$	$1.47.10^{-4}$	$1.76.10^{-4}$	$2.49.10^{-4}$	$3.67.10^{-4}$	$4.98.10^{-4}$	$1.07.10^{-2}$	$7.47.10^{-3}$	0.576	0.217
0.3	$3.42.10^{-4}$	$7.36.10^{-4}$	$8.78.10^{-4}$	$1.25.10^{-3}$	$1.85.10^{-3}$	$2.57.10^{-3}$	$5.47.10^{-2}$	$3.78.10^{-2}$	0.905	0.367
0.4	$1.05.10^{-3}$	$2.28.10^{-3}$	$2.72.10^{-3}$	$3.87.10^{-3}$	$5.77.10^{-2}$	$7.89.10^{-3}$	$1.74.10^{-2}$	0.120	0.273	0.575
0.5	$2.48.10^{-3}$	$5.40.10^{-3}$	$6.46.10^{-3}$	$9.25.10^{-2}$	$1.39.10^{-2}$	$1.90.10^{-2}$	$4.28.10^{-2}$	0.290	1.669	0.870
0.6	$4.91.10^{-2}$	$1.08.10^{-2}$	$1.29.10^{-2}$	$1.86.10^{-2}$	$2.81.20^{-2}$	$3.88.10^{-2}$	$8.90.10^{-2}$	0.587	2.039	1.270
0.7	$8.60.10^{-2}$	$1.90.10^{-2}$	$2.29.10^{-2}$	$3.31.10^{-2}$	$5.03.10^{-2}$	$7.01.10^{-2}$	0.164	1.025	2.391	1.762
0.8	$1.37.10^{-2}$	$3.06.10^{-2}$	$3.69.10^{-2}$	$5.36.10^{-2}$	$8.19.10^{-2}$	0.115	0.273	1.561	2.620	2.275
0.9	$2.02.10^{-2}$	$4.55.10^{-2}$	$5.50.10^{-2}$	$8.02.10^{-2}$	0.123	0.173	0.415	2.064	2.734	2.686
1.0	$2.81.10^{-2}$	$6.34.10^{-2}$	$7.66.10^{-2}$	0.112	0.172	0.242	0.577	2.420	2.752	2.900
1.2	$4.57.10^{-2}$	0.103	0.125	0.181	0.277	0.385	0.884	2.525	2.641	2.815
1.4	$6.21.10^{-2}$	0.138	0.165	0.237	0.353	0.483	1.822	2.188	2.497	2.536
1.6	$7.26.10^{-2}$	0.157	0.187	0.266	0.400	0.581	2.303	1.836	2.376	2.359
1.8	$7.73.10^{-2}$	0.167	0.201	0.298	0.501	0.827	2.108	1.645	2.267	2.258
2.0	$8.16.10^{-2}$	0.190	0.236	0.376	0.673	1.034	2.359	1.586	2.170	2.156
2.5	0.118	0.295	0.361	0.528	0.785	1.109	1.232	1.442	1.995	1.951
3.0	0.139	0.312	0.380	0.574	0.908	1.265	1.849	1.322	1.859	1.816
3.5	0.150	0.363	0.445	0.661	1.027	1.290	1.531	1.260	1.762	1.720
4.0	0.170	0.401	0.487	0.698	1.012	1.518	1.181	1.211	1.683	1.644
5.0	0.189	0.457	0.555	0.770	1.150	1.266	1.124	1.153	1.569	1.538
6.0	0.209	0.490	0.592	0.840	1.033	1.060	0.889	1.116	1.488	1.465
8.0	0.246	0.540	0.650	0.798	0.973	1.045	1.067	1.076	1.381	1.370
10.0	0.268	0.594	0.634	0.724	0.741	0.645	0.780	1.055	1.312	1.310
15.0	0.313	0.583	0.556	0.520	0.525	0.667	0.810	1.031	1.213	1.224
20.0	0.319	0.464	0.494	0.561	0.589	0.693	0.755	1.021	1.159	1.176
25.0	0.346	0.407	0.364	0.441	0.459	0.601	0.950	1.015	1.125	1.146
30.0	0.262	0.359	0.346	0.456	0.460	0.525	0.697	1.012	1.100	1.125
35.0	0.282	0.302	0.343	0.444	0.494	0.470	0.708	1.009	1.082	1.109
40.0	0.280	0.296	0.318	0.363	0.436	0.498	0.682	1.008	1.057	1.096
45.0	0.184	0.299	0.299	0.430	0.488	0.505	0.700	1.007	0.986	1.086
50.0	0.251	0.300	0.296	0.399	0.437	0.452	0.657	1.006	0.907	1.077
∞	0.132	0.208	0.231	0.277	0.340	0.397	0.576	1.000	0.960	0.979

TABLE A-2. VALUES OF $\Phi(m, \alpha)$ OR $1 + \mu$ WITH $\rho = 1\ g \cdot cm^{-3}$ [105]

	m*											
α	1.2	1.3	1.33	1.4	1.5	1.6	2	10^4	Iron 1.27 - 1.37i	Graphite m* = m*(λ) complex	Water, m* = m*(λ) Real	Water, m* = m*(λ) Complex
0.001	$5.59.10^{-7}$	$1.71.10^{-6}$	$2.04.10^{-6}$	$2.88.10^{-6}$	$4.22.10^{-6}$	$5.72.10^{-6}$	$1.22.10^{-4}$	$8.48.10^{-6}$	15.1	5.58	$2.26.10^{-6}$	$6.90.10^{-6}$
0.005	$6.97.10^{-5}$	$1.57.10^{-4}$	$2.03.10^{-4}$	$2.72.10^{-4}$	$4.28.10^{-4}$	$5.44.10^{-4}$	$1.24.10^{-2}$	$8.69.10^{-2}$	15.2	5.63	$2.16.10^{-4}$	$7.13.10^{-3}$
0.01	$5.53.10^{-4}$	$1.30.10^{-3}$	$1.56.10^{-3}$	$2.19.10^{-3}$	$3.24.10^{-3}$	$4.39.10^{-2}$	$9.46.10^{-2}$	$6.61.10^{-2}$	15.4	5.80	$1.73.10^{-3}$	$8.51.10^{-3}$
0.03	$1.36.10^{-2}$	$3.02.10^{-2}$	$3.61.10^{-2}$	$5.20.10^{-2}$	$7.74.10^{-2}$	0.107	0.239	1.60	17.0	7.87	$4.08.10^{-2}$	$4.65.10^{-2}$
0.04	$2.97.10^{-2}$	$6.63.10^{-2}$	$7.93.10^{-2}$	0.115	0.173	0.242	0.552	3.41	17.6	9.54	$8.97.10^{-2}$	$9.41.10^{-2}$
0.05	$5.04.10^{-2}$	0.116	0.139	0.203	0.307	0.431	1.01	5.44	17.6	11.0	0.156	0.160
0.06	$7.75.10^{-2}$	0.174	0.209	0.304	0.463	0.648	1.56	7.11	17.1	12.1	0.232	0.235
0.07	0.104	0.252	0.280	0.406	0.617	0.867	2.21	8.17	16.2	12.6	0.307	0.309
0.08	0.128	0.285	0.343	0.498	0.761	1.07	2.87	8.66	15.2	12.6	0.375	0.376
0.09	0.148	0.331	0.398	0.579	0.891	1.27	3.46	8.73	14.1	12.2	0.433	0.433
0.1	0.165	0.359	0.445	0.649	1.01	1.45	4.00	8.53	13.0	11.7	0.482	0.482
0.15	0.212	0.485	0.589	0.872	1.38	2.01	5.03	6.49	8.97	8.76	0.633	0.631
0.2	0.230	0.533	0.649	0.960	1.51	2.16	4.59	4.80	6.49	6.46	0.689	0.689
0.25	0.233	0.545	0.664	0.973	1.52	2.09	3.88	3.68	4.94	4.92	0.696	0.697
0.3	0.230	0.538	0.655	0.953	1.45	1.94	3.22	2.91	3.92	3.89	0.680	0.681
0.4	0.217	0.504	0.612	0.873	1.27	1.59	2.26	2.00	2.69	2.66	0.624	0.628
0.5	0.202	0.464	0.558	0.777	1.07	1.29	1.65	1.50	2.01	1.97	0.560	0.568
0.6	0.187	0.425	0.504	0.681	0.903	1.05	1.27	1.19	1.58	1.55	0.499	0.510
0.7	0.175	0.390	0.454	0.595	0.760	0.863	1.00	0.983	1.30	1.27	0.446	0.458
0.8	0.164	0.358	0.408	0.520	0.646	0.716	0.830	0.837	1.09	1.07	0.400	0.411
0.9	0.153	0.328	0.369	0.458	0.554	0.610	0.679	0.728	0.940	0.922	0.361	0.369
1.0	0.144	0.301	0.333	0.405	0.481	0.527	0.597	0.645	0.824	0.809	0.327	0.332
3.0	$5.41.10^{-2}$	$8.02.10^{-2}$	$8.15.10^{-2}$	$9.65.10^{-2}$	0.104	0.116	0.150	0.199	0.219	0.225	$8.52.10^{-2}$	$8.46.10^{-2}$
5.0	$3.03.10^{-2}$	$3.97.10^{-2}$	$3.97.10^{-2}$	$4.92.10^{-2}$	$5.41.10^{-2}$	$5.95.10^{-2}$	$8.30.10^{-2}$	0.118	0.119	0.127	$4.26.10^{-2}$	$4.36.10^{-2}$
10	$1.20.10^{-2}$	$1.68.10^{-2}$	$1.69.10^{-2}$	$2.03.10^{-2}$	$2.38.10^{-2}$	$2.64.10^{-2}$	$3.81.10^{-2}$	$5.89.10^{-2}$	$5.43.10^{-2}$	$4.81.10^{-2}$	$1.77.10^{-2}$	$1.92.10^{-2}$
50	$1.7.10^{-2}$	$3.1.10^{-3}$	$3.2.10^{-3}$	$3.6.10^{-3}$	$4.2.10^{-3}$	$5.0.10^{-3}$	$7.2.10^{-3}$	$1.2.10^{-2}$	$1.0.10^{-2}$		$3.3.10^{-3}$	$3.4.10^{-3}$
100	$8.0.10^{-4}$	$1.6.10^{-3}$	$1.6.10^{-3}$	$1.8.10^{-3}$	$2.1.10^{-3}$	$2.5.10^{-3}$	$3.6.10^{-3}$	$5.8.10^{-3}$	$5.3.10^{-3}$		$1.6.10^{-3}$	$1.7.10^{-3}$
500	$1.6.10^{-4}$	$3.1.10^{-4}$	$3.2.10^{-4}$	$3.6.10^{-3}$	$4.2.10^{-4}$	$5.0.10^{-4}$	$7.2.10^{-4}$	$1.2.10^{-3}$	$1.0.10^{-3}$	*	$3.3.10^{-4}$	*
1000	$7.7.10^{-5}$	$1.6.10^{-4}$	$1.6.10^{-4}$	$1.8.10^{-4}$	$2.1.10^{-4}$	$2.5.10^{-4}$	$3.6.10^{-4}$	$5.8.10^{-4}$	$5.3.10^{-4}$	*	$1.6.10^{-4}$	*
10000	$7.7.10^{-6}$	$1.6.10^{-5}$	$1.6.10^{-6}$	$1.8.10^{-6}$	$2.1.10^{-6}$	$2.5.10^{-6}$	$3.6.10^{-6}$	$5.8.10^{-6}$	$5.3.10^{-6}$	*	$1.6.10^{-6}$	*

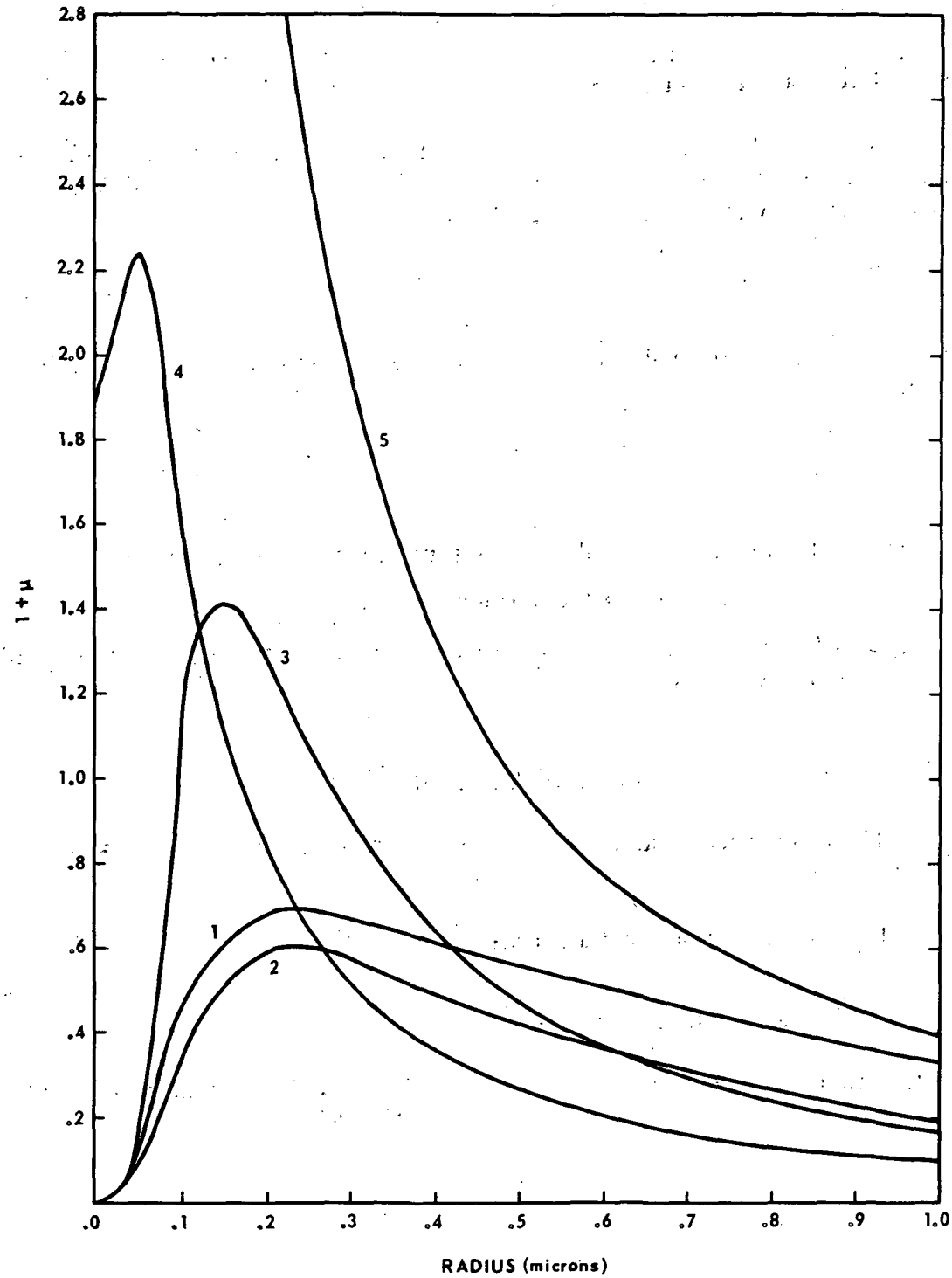

Figure A-1. The magnitude of $1 + \mu$ as a function of the particle radius: 1 = water, 2 = quartz ($m^* = 1.5$, $\rho = 2.5$), 3 = titanite ($m^* = 2.0$, $\rho = 3.5$), 4 = iron ($\rho = 7.8$), 5 = graphite ($\rho = 2.0$) [105].

3. Lorentz Force

The processes which are important in determining the electric charge q on an interplanetary dust particle are shown in Figure A-2.

Because of magnetic fields carried in the solar wind, the particle can experience the Lorentz force which is exerted by the magnetic field $\vec{B}$ on the particle moving with a velocity $\vec{v}$ and is given by

$$\vec{F}_L = -q\vec{v} \times \vec{B} \quad .$$

For $|\vec{v}| = 400$ km/s and $|\vec{B}| = 3 \times 10^{-5}$ gauss at 1 AU, then with a in meters [99]

$$F_L \approx 10^{-14} \quad a[nt] .$$

The Lorentz force F_L is caused by the interaction with the interplanetary magnetic field alone, whereas the convective force $F_{con} = q\vec{w} \times \vec{B}$ depends on the fact that the solar wind carries the magnetic field along at a speed w, which is large compared with v.

4. Corpuscular Drag

The drag forces caused by collisions with solar wind particles can be calculated by:

$$F_{cd} = \text{rate of momentum transfer}$$

$$= \text{proton flux} \times \text{momentum} \times \text{area of particle.}$$

An estimate of the total drag force is 6.3×10^{-19} a^2 [nt]. The component of drag parallel to the velocity is 4×10^{-20} a^2 [nt] [77].

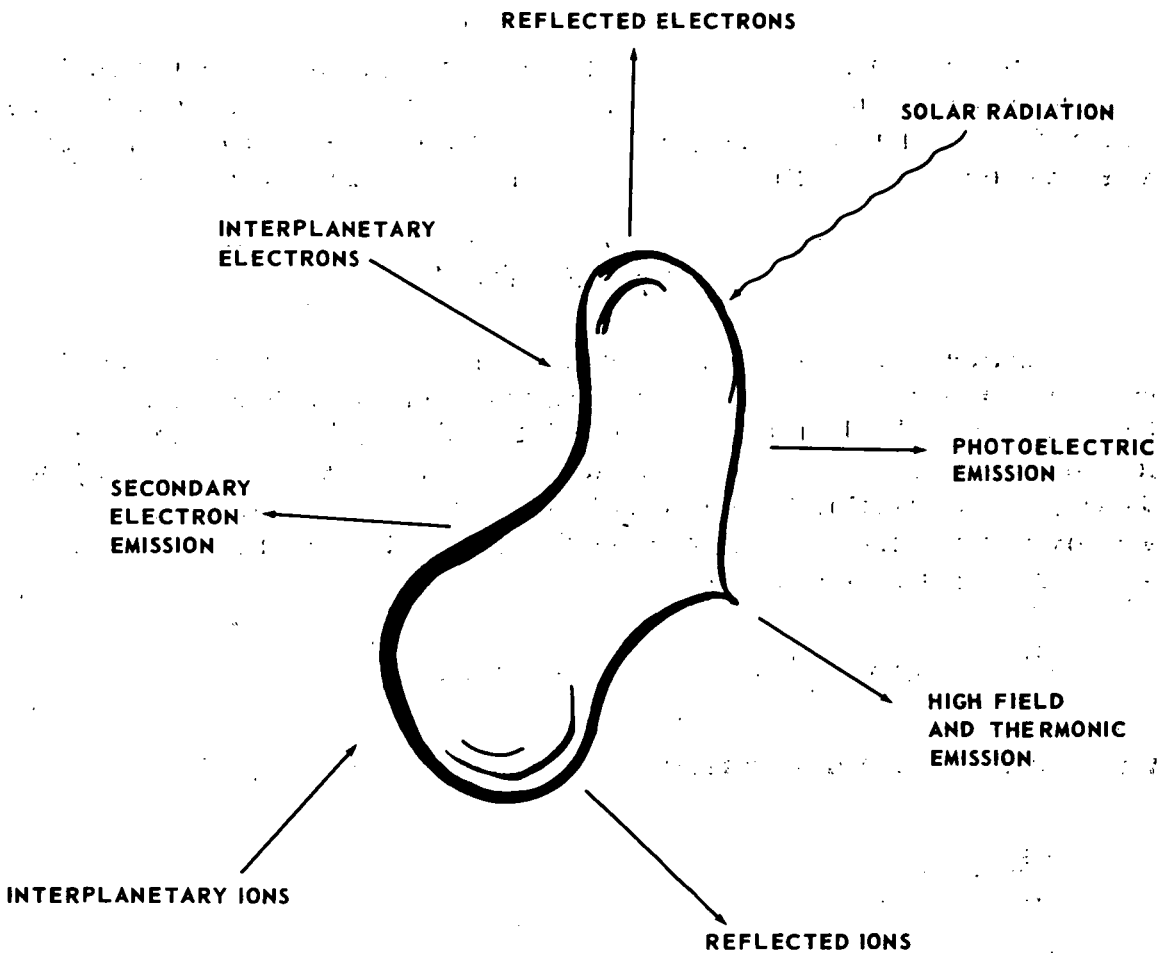

Figure A-2. Processes which determine the electric charge on an interplanetary dust particle [102].

5. Coulomb Drag

An equilibrium charge q on a dust particle can be approximately calculated if the charging process is the photoelectric effect and the discharging process is the collection of electrons from the solar wind. An estimate of the equilibrium potential is $\simeq$ 2 volts [103]. If the charged particle sees an electric Field, then the particle will experience a Coulomb drag force, $F_q = qE$. An estimate of this force is 10^{-19} a^2 [nt] and the drag component parallel to the particle velocity is 6.6×10^{-21} a^2 [nt] [27].

6. Mass Loss Effects

The solar wind will cause a radial sputtering erosion. Solar radiation will cause evaporation or sublimation. Both of these effects contribute to mass loss of the interplanetary particles and are more important closer to the sun. Mass loss effects will affect the dynamics through the equation of motion.

7. Physical Process

Sputtering by protons and alpha particles is most effective at kilovolt energies. The threshold energy for sputtering of metals by ions has been found to be given by the requirement that the product of the momentum transferred at threshold from an ion to the target atom and of the sound velocity in the target be proportional to the heat of sublimation of the target [36]. The erosion rate of a dust particle is proportional to the flux of ions in the solar wind. The mass rate loss is

$$\frac{dm}{dt} = -4\pi a^2 \left(\frac{da}{dt}\right) , \qquad a = \text{radius}$$

where da/dt is the shrinkage rate:

$$\frac{da}{dt} = c\, m_t \sum_i F_i Y_i ,$$

and m_t is the atomic mass of the target, F_i represents the various fluxes, and Y_i the corresponding yields (atomic/ion).

To estimate the temperature, the solar irradiance blackbody equilibrium temperature is calculated from the equilibrium equation; energy received is energy radiated:

$$\frac{\alpha S}{r^2} A_\pi = e\sigma T^4 A_t$$

(Stefan-Boltzmann Law) where

α = absorptivity

S = solar constant [1390 watts $(AU)^2/m^2$]

r = solar distance ($1\ AU = 1.496 \times 10^{11}$ m)

A = projected area (solar-oriented) = πa^2 (sphere)

e = emissivity

σ = Stefan-Boltzmann constant,

T = equilibrium temperature,

A_t = total area = $4\pi r^2$ (sphere)

and heat loss from vaporization is neglected.

Assuming that (1) the sphere is rotating or the sphere is small enough that equilibrium temperature has meaning and (2) $\alpha = e$; then for interplanetary spherical blackbody particles the equation for the equilibrium temperature for various solar distance is

$$T^2 r = 0.785 \times 10^5\ [°K^2\ AU] \quad .$$

8. Poynting-Robertson Effect

Because light has momentum, its reradiation or general reflection from a particle in orbit about the sun produces a retarding force on the motion of the particle. While the process of absorption and re-emission produces no net force when one chooses to work with a stationary frame referred to the particle, it is found when the solar reference frame is used that a resisting force is introduced on the particle which is proportional to its velocity [104]. Assuming (1) spherical particles of radius a and uniform density, (2) gravitational forces are dominant over the radiation pressure, (3) diffraction is not considered, and (4) the particles absorb all incident radiation over a cross section πa^2 and re-emit the radiation isotropically at the same rate, then the equations of motion are

$$\ddot{r} - r\dot{\theta}^2 = -\frac{\mu}{r^2} - \frac{2\alpha \dot{r}}{r^2}$$

$$\frac{1}{r}\frac{d}{dt}(r^2\theta) = \frac{\alpha\dot{\theta}}{r^2} \quad ,$$

where

$$\mu = G M_{\odot} - \alpha c \quad ,$$

$$\alpha = 3 E'_{\odot} / 16 \pi c^2 a \rho$$

$E'_{\odot}$ = total energy emitted by the sun per second (3.79×10^{33} erg/s).

The resultant equations for the semimajor axis b and the eccentricity e are

$$\frac{db}{dt} = - \frac{\alpha (2 + 3 e^2)}{b (1 - e^2)^{3/2}}$$

$$\frac{de}{dt} = - \frac{5 \alpha e}{2 b^2 (1 - e^2)^{1/2}} \quad .$$

For circular orbits, the total time of fall for a particle of radius a, density ρ — at an initial distance r in AU is [119]

$$t = \frac{b^2}{4\alpha} = 7.0 \times 10^6 \, a \, \rho r^2 \qquad \text{[years]} \quad .$$

George C. Marshall Space Flight Center
National Aeronautics and Space Administration
Marshall Space Flight Center, Alabama 35812, March 30, 1972

REFERENCES

1. Searle, A.: Researches on the Zodiacal Light. Harvard V. Astron. Obs. Annals., Part II, 19, 1893, pp. 165-245.

2. Schoenberg, E.: Theoretische Photometrie Handbuch der Astrophysik. Verlag Julius Springer, Berlin, NASA TT, F-11, 044, X67-21261, vol. II/1, 1929, pp. 1-280.

3. Van Rhijn, R. J.: On the Brightness of the Sky at Night and the Total Amount of Starlight. Pub. of the Astron. Lab. at Groningen, No. 31, 1921.

4. Dufay, J.: La Polarization de la Lumière Zodiacale. Compt. Rend. 181 pp. 399-

5. Elvey, C. T., and Roach, F. E.: A Photoelectric Study of the Light from the Night Sky. Astrophys. J. 85, 1937, pp. 213-241.

6. Hoffmeister, C.: Beitrag Zur Photometrie der Südlichen Milchstrasse und des Zodiakallichts. Vero Univer. Steruw Berlin-Babelsberg, 8, 1930, pp. 1-60.

7. Hoffmeister, C.: Untersuchungen Über das Zodiakallicht. Veröff. Univ.-Sternw., Berling-Babelsberg X H.1, 1932, pp. 1-111.

8. Behr, A., and Siedentopf, H.: Untersuchungen Über Zodiakallicht and Gegenschein Nach Lichtelektrischer Messungen auf dem Jungfraujoch. Zeits. f. Astrophys. 32, 1953, pp. 19-50.

9. Blackwell, D. E. and Ingham, M. F.: Observations of the Zodiacal Light from a Very High Altitude, Stn. I. M.N.R.A.S. 122, 1961, pp. 113-127.

10. Blackwell, D. E., and Ingham, M. F.: Observations of the Zodiacal Light from a Very High Altitude, Stn. II. M.N.R.A.S. 122, 1961, pp. 129-141.

11. Blackwell, D. E., and Ingham, M. F.: Observations of the Zodiacal Light from a Very High Altitude, Stn. III, M.N.R.A.S. 122, 1961, pp. 143-155.

REFERENCES (Continued)

12. Allen, C. W.: The Spectrum of the Corona at the Eclipse of 1940 October 1. M.N.R.A.S. 106, 1946, pp. 137-150.

13. van de Hulst, H. C.: Zodiacal Light in the Solar Corona, Astrophys. J. 105, 1947, pp. 471-488.

14. Richter, N.: Experimentelle Untersuchungen zur Beleuchtung Staubförmiger Wolken, I. Teil: Partikel Grobe, Ver Öffentlichungen der Sternwarte in Sonneberg, 2, No. 6, 1956, pp. 369-389.

15. Walter, H.: Theoretische Deutung des Gegenscheins durch Lichtstreuung and sparischen Partikeln, Zeits. f. Astrophys. 46, 1958, pp. 9-16.

16. Giese, R. H., and Siedentopf, H.: Optical Characteristics of Models of Interplanetary Matter. Zeit. Astrophys. 54, 1962, pp. 200-216.

17. Weinberg, J. L.: Photoelectric Polarimetry of the Zodiacal Light at 5300. Ph. D. Thesis, University of Colorado, 1963.

18. Weinberg, J. L.: White-Light vs. Narrow Band Observations of the Polarization of the Zodiacal Light. Nature, 198, 1963, pp. 842-844.

19. Smith, L. L., Roach, F. E., and Owen, R. W.: The Absolute Photometry of the Zodiacal Light. Planet Space Science, 13, 1965, pp. 207-217.

20. Cassini, J. D.: Découerte de la lumière céleste qui paroist dans le zodiaque, Mem. Acad. Roy. des. Sci. Paris (1660-1699), 1685, p. 121.

21. Singer, S. F., and Bandermann, L. W.: Nature and Origin of Zodiacal Dust. The Zodiacal Light and the Interplanetary Medium (Ed. J. L. Weinberg), NASA SP-150, U. S. Government Printing Office, 1967, pp. 379-397.

22. Aller, L. H., Duffner, G., Dworetsky, M., Gudenus, D., Kilston, S., Leckrone, D., Montgomery, J., Oliver, J., and Zimmerman, E.: Some Models of the Zodiacal Light. The Zodiacal Light and the Interplanetary Medium (Ed. J. L. Weinberg) NASA SP-150, U. S. Government Printing Office, 1967, pp. 243-256.

23. Mie, G.: Beiträge zur Optik trüber Medien, spezielle Kolloidaler Metallösungen. Ann. Physik, 25, 1908, pp. 377-445.

24. Kerker, M.: The Scattering of Light and Other Electromagnetic Radiation. Academic Press, N. Y., 1969.

25. McCracken, C. W., Alexander, W. M., and Dubin, M.: Direct Measurements of the Mass Distribution and Time Variations in the Flux of Small Dust Particles in Meteor Orbits and Dust. Ed. G. S. Hawkins, NASA SP-135, U. S. Government Printing Office, 1965.

26. Giese, R. H.: Light Scattering by Small Particles and Models of Interplanetary Matter Derived from the Zodiacal Light. Space Sci. Reviews, 1, 1963, pp. 589-611.

27. Gillett, F. C.: Zodiacal Light and Interplanetary Dust. Ph. D. Thesis, University of Minnesota, 1966.

28. Powell, R. S., Woodson, P. E., III, Alexander, M. A., Circle, R. R., Konheim, A. G., Vogel, D. C., and McElfresh, T. W.: Analysis of All Available Zodiacal Light Observations. The Zodiacal Light and the Interplanetary Medium (Ed. J. L. Weinberg), NASA SP-150, U. S. Government Printing Office, 1967, pp. 225-240.

29. Anderson, D., et. al.: Preliminary Examinations of Lunar Samples from Apollo II. Science 165, The Lunar Sample Examination Team, 1969, pp. 1211-1227.

30. Powell, Robert Stephen: Analysis of Polydisperse Particle Ensembles by Light Scattering Techniques. Ph. D. Thesis, The Catholic University of America, 1967.

31. Roosen, R. G.: The Gegenschein and Interplanetary Dust Outside the Earth's Orbit. Icarus, vol. 13, 1970, p. 184-201.

32. Giese, R. H., and Dziembowski, C. V.: On Optical Models Approximating Observations of the Zodiacal Light Outside the Ecliptic. The Zodiacal Light and the Interplanetary Medium (Ed. J. L. Weinberg), NASA SP-150, U. S. Government Printing Office, 1967, pp. 271-276.

33. Giese, R. H., and Dziembowski, C. V.: Suggested Zodiacal Light Measurements from Space Probes Planet. Space Sci., 17, 1969, pp. 949-956.

34. Fesenkov, V. G.: Isophotes of Zodiacal Light from Observations made in Egypt during the Autumn of 1957. Sov. Astron., AJ 7, 1964, pp. 829-834.

35. Fesenkov, V. G.: Meteoric Matter in Interplanetary Space, Academy of Sciences Press, Moscow, 1947.

36. Bandermann, L. W.: Physical Properties and Dynamics of Interplanetary Dust. Ph. D. Dissertation, University of Maryland, 1968.

37. Hildebrand, F. B.: Methods of Applied Mathematics. Prentice-Hall, Englewood Cliffs, N. Y., 1952, p. 381 ff.

38. Southworth, R. B.: Phase Function of the Zodiacal Light. The Zodiacal Light and the Interplanetary Medium (Ed. J. L. Weinberg), NASA SP-150, U. S. Government Printing Office, 1967, pp. 257-270.

39. Powell, R. S., and Circle, R. R.: Analysis of the F-Corona According to the Mie Theory Mathematical Formulation and Uniqueness of the Derived Theoretical Models. Melpar, Inc. Report/under NASw-1206, 1965.

40. Weinberg, J. L.: Current Problems in the Zodiacal Light. COSPAR, 12th Plenary Mtg. Prague, 1969, pp. 1-12.

41. Dumont, R., and Martinez, F.: Polarization du Ciel Nocturne et Polarization de La Lumière Zodiacale Vers 5000 Å Sur L'Ensemble de la Sphere Céleste. Ann. d'Astrophys. 29, 1966, pp. 113-118.

42. Divari, N. B.: Zodiacal Light. Usp. Fiz. Nauk, 84, 1964, pp. 75-98.

43. Peterson, A. W.: Multicolor Photometry of the Zodiacal Light. The Zodiacal Light and the Interplanetary Medium (Ed. J. L. Weinberg), NASA SP-150, U. S. Government Printing Office, 1967, pp. 23-31.

44. Divari, N. B., and Kyrlova, S. N.: Results of Photoelectric Observations of Zodiacal Light. Geomagnetism and Aeronomy 5, 1966, pp. 605-608.

45. Robley, R.: Photometric des Lumieres Zodiacale et Anti-Solaire, Ann. de. Geophys, 18, 1962, pp. 341-350.

46. Weinberg, J. L.: On the Use of a Pile-of-Plates Polarizer- The Transmit. Comp. Applied Optics, 3, 1964, pp. 1057-1061.

47. Weinberg, J. L.: The Zodiacal Light at 5300 Å. Annales d'Astrophysique, 27, 1964, pp. 718-738.

48. Weinberg, J. L.: Summary Report on Zodiacal Light. Hawaii Inst. for Geophys., HIG-64-11, University of Hawaii, 1964.

49. Peterson, A. W.: Three-color Photometry of the Zodiacal Light. Astrophys. J. 133, 1961, pp. 668-674.

50. Divari, N. B., and Krylova, S. N.: Photoelectric Observations of Zodiacal Light from a High-Altitude Observatory. Odessa Polytech. Inst., Trans. Astronomicheskii Zhurnal, 40, 1963, pp. 514-522.

51. Elsasser, H.: Neue Helligkeits- and Polarisationsmessungen am Zodiakallicht und ihre Interpretation. Die Sterne 9-10, 1958, pp. 166-169.

52. Regener, V. H., and Van de Noord, E. L.: Observations of the Zodiacal Light by Means of Telemetry from Balloons. The Zodiacal Light and the Interplanetary Medium (Ed. J. L. Weinberg), NASA SP-150, U. S. Government Printing Office, 1967, pp. 45-47.

53. Ingham, M. F.: Observations of the Zodiacal Light from a Very High Altitude Station, IV. M.N.R.A.S. 122, 1961, pp. 157-176.

54. Weinberg, J. L.: Zodiacal Light at the Celestial Pole. Planet. Space Sci. 13, 1965, pp. 1311-1312.

55. Weinberg, J. L.: Zodiacal Light as an Indicator of the Nature of the Interplan. Matt; - Past, Present and Prospective Results. Meteor Orbits and Dust (Ed. G. S. Hawkins), NASA SP-135, U. S. Government Printing Office, 1965, pp. 203-211.

56. Dumont, R.: Photometry of Zodiacal Light and Atmospheric Continuum by H-M Method and Barbier Correlations and Tenerite Results about the Shape of the Zodiacal Cloud. The Zodiacal Light and the Interplanetary Medium (Ed. J. L. Weinberg) NASA SP-150, U. S. Government Printing Office, 1967, pp. 63-69.

57. Beggs, D. W., Blackwell, D. E., Dewhirst, D. W., and Wolstencroft, R. D.: Further Observations of the Zodiacal Light from a High Altitude Station and Investigation of the Interplanetary Plasma. M.N.R.A.S., 127, 1964, pp. 319-328.

58. Beggs, D. W., Blackwell, D. E., and Dewhirst, D. W.: Further Observations of the Zodiacal Light from a High Altitude Sta. and Investigation of Interplanetary Plasma. M.N.R.A.S. 127, 1964, pp. 319-328.

59. Wolstencroft, R. D., and Roach, F. E.: The Zodiacal Light at the North Ecliptic Pole. The Astrophysical Journal, 158, 1969, pp. 365-369.

60. Sparrow, J. G., and Ney, E. P.: OSO-B2 Satellite Observations of Zodiacal Light. The Astrophys. J., 154, 1968, pp. 783-787.

61. Dumont, R.: Separation des Composantes Atmosphérique, Interplanétaire et Stellaire du ciel nocturne a 5000 Å. Application à la Photométrie de la Lumière Zodiacale et du Gegenschein. Ann. d'Astrophy. 1965, pp. 265-319.

62. Wolstencroft, R. D., and Rose, L. J.: Zodiacal Light Observations from a Sounding Rocket. The Zodiacal Light and the Interplanetary Medium (ed. J. L. Weinberg), NASA SP-150, U. S. Government Printing Office, 1967, pp. 49-56.

63. Gillett, F. C.: Measurement of the Brightness and Polarization of Zodiacal Light from Balloons and Satellites. The Zodiacal Light and the Interplanetary Medium (Ed. J. L. Weinberg), NASA SP-150, U. S. Government Printing Office, 1967, pp. 9-15.

64. Divari, N. B., and Asaad, A. S.: Photoelectric Observations of the Zodiacal Light in Egypt. Soviet Astron. AJ, 3, 1960, pp. 832-838.

65. Blackwell, D. E., Dewhirst, D. W., and Ingham, M. F.: The Zodiacal Light. Advances in Astronomy and Astrophys. 5, 1967.

66. Roosen, R. G.: The Gegenschein. Ph. D. Thesis, University of Texas, Austin, Texas, 1969.

67. Roosen, R. G.: Are the Libration Clouds Real? Nature, vol. 224. November 8, 1969, p. 571.

68. Wolstencroft, R. D., and Rose, L. J.: Observations of the Zodiacal Light from a Sounding Rocket. Astrophys. J. 147, 1967, pp. 271-292.

69. Allen, C. W.: Astrophysical Quantities. University of London, The Athlone Press, London, 1963.

70. Shifrin, K. S.: Scattering of Light in a Turbid Medium. Trans. of "Rasseyaniye Sveta v Mutnoy Srede," Teoreticheskoy Literatury, Moscow, Leningrad (NASA TT F-477), 1951.

71. Divari, N. B.: The Cosmic Dust Cloud Around the Earth. Soviet Astron. AJ 10, 1967, pp. 1017-1030.

72. Hunt, G. E.: The Generation of Angular Distribution Coefficients for Radiation Scattered by a Spherical Particle. J. Quant. Spectrose. Radiat. Trans. vol. 10, 1970, pp. 857-864.

73. Kloverstrom, F. A., and Rense, W. A.: Reflection from Meteoritic Surfaces. Astrophys. J., 115, 1952, pp. 495-500.

74. Richter, N. B.: The Photometric Properties of Interpl. Matter. Quart. Journ. Roy. Astron., 3, 1962, pp. 179-186.

75. Richter, N. B.: Experimentelle Untersuchungen zur Beleuchtung Interplanetarer Materie I. Teil. Veröffentlichungen der Sternwarte in Sonneburg, 5, No. 3, 1962, pp. 157-189.

76. Giese, R. H.: Scattering of EM Waves by Absorptive and Dielectric Spherical Particles and by Mixtures of Such Particles. Zeitschrift für Astrophysik, 51, 1961, pp. 119-147.

77. Watson, G. N.: Bessel Functions. Cambridge University Press, Cambridge, 1944, p. 389.

78. Gehrels, Thomas: Wavelength Dependence of Polariz. IX. Interstellar Particles. Ast. J. 72, 1967, pp. 1-23.

79. Rosen, James M.: Stratospheric Dust and its Relationship to the Meteoric Influx. Space Science Reviews, 9, 1969, pp. 58-89.

80. Richter, N. B.: Experimentelle Untersuchungen zur Beleuchtung Interplanetarer Materie II. Teil. Veröffentlichungen der Sternwarte in Sonneburg, 5, No. 4, 1962, pp. 199-224.

81. Dollfus, A.: Polarization of the Light Reflected by Solid Bodies and Natural Clouds. Annales d'Astrophysque, 19, 1956, pp. 83-113.

82. van de Hulst, H. C.: Light Scattering by Small Particles. John Wiley & Sons, Inc., New York, London, 1957.

83. Bicket, N. A., and Gary, G. A.: Mie Scattering: A Computer Program and an Atlas. NASA Technical Memorandum Report No. 53951, Marshall Space Flight Center, 1969.

84. Giese, R. H., and Siedentopf, H.: Eih Modellversuch zue Bestimmung der Streufunktionen nicht Kugelförmiger Teilchen mit 3 cm-Wellen. (Notizen) Z. Naturforschg., 17a, 1962, pp. 817-819.

85. Kovar, N. S., and Kovar, R. P.: Zodiacal Light Models based on Apollo 11 Lunar Sample Anal. Paper presented at the Amer. Astronom. Soc. Mtg., New York, 1969.

86. Little, S. J., O'Mara, B. J., and Aller, L. H.: Light Scattering by Small Particles in the Zodiacal Cloud. Astronomical Journal, 70, 1965, pp. 346-352.

87. Tanabe, H., and Huruhata, M.: Rocket Observations of the Brightness of the Zodiacal Light. The Zodiacal Light and the Interplanetary Medium (ed. J. L. Weinberg) NASA SP-150, U.S. Government Printing Office, 1967, pp. 37-43.

88. Gindilis, L. M., and Karyagina, E. V.: Energy Distribution in the Counterglow (Gegenschein) Spectrum in the Region $\lambda = 3900\text{-}6500$ Å. Soviet Astr. -AJ 8, 1964, pp. 86-90.

89. Peterson, A. W.: Experimental Detection of Thermal Radiation from Interplanetary Dust. Astrophys. J. 148, 1967, pp. L37-L39.

90. Greenberg, J. M.: Models of Zodiacal Light. COSPAR, Plenary Meeting, 12th, Prague, Czechslovaka, 1969.

91. Greenberg, J. M.: A Possible Inter-Relation Between Interstellar and Interplanetary Cosmic Dust. Space Research IX, 1969, pp. 111-115.

92. Rouy, Auguste L., and Aller, Lawrence H.: A Feasibility Study of a Radiation Analyzer for the Zodiacal Light. NASA Project NaG-550, 5, 1964.

93. Divari, N. B.: A Meteor Model for Zodiacal Cloud. Soviet Phys-Astron. II, 1968, pp. 1048-1052.

94. Napper, D. H., and Ottewill, R. H.: Light Scattering Studies on Monodisperse Silver Bromide Sols. ICES Electromagnetic Scattering (Ed. M. Kerker), Pergamon Press, N. Y., 1963, pp. 377-386.

95. Donn, B., and Powell, R. S.: Angular Scattering from Irregularly Shaped Particles with Application to Astronomy. ICES Electromagnetic Scattering, (Ed. M. Kerker), Pergamon Press, N. Y., 1963, pp. 151-158.

96. Bowman, J. J., Senior, T. B. A., and Uslenghi, P. L. E.: Electromagnetic and Acoustic Scattering by Simple Shapes. North-Holland Publishing Co., Amsterdam (John Wiley & Sons, Inc., N.Y.), 1969.

97. Hanner, M. S.: Light Scattering in Reflection Nebulae. Ph. D. Thesis, Rensselaer Polytechnic Institute, 1969.

98. Lind, A. C.: Resonance Electromagnetic Scattering by Finite Circular Cylinders. Ph. D. Dissertation, Rensselaer Polytechnic Institute, 1966.

99. Rayleigh, Lord: On the Dispersal of Light by a Dielectric Cylinder. Scientific Papers 434, 1918, pp. 554-563.

100. Schmidt, T., and Elsasser, H.: Dynamics of Submicron Particles (a 10^{-5} cm) in Interplanetary Space. The Zodiacal Light and the Interplanetary Medium (ed. J. L. Weinberg), NASA SP-150, U. S. Government Printing Office, 1967, pp. 287-289.

101. Lind, A. C., Wang, R. T., and Greenberg, J. M.: Microwave Scattering by Nonspherical Particles. Applied Optics, 4, 1965, pp. 1555-1561.

102. Belton, Michael J. S.: Dynamics of Interplanetary Dust, Science, 151, 1966, pp. 35-44.

103. Whipple, F. L.: On Maintaining the Meteoritic Complex. The Zodiacal Light and the Interplanetary Medium (Ed. J. L. Weinberg), NASA SP-150, U. S. Government Printing Office, 1967, pp. 409-426.

104. Robertson, H. P.: Dynamical Effects of Radiation in the Solar System. M.N.R.A.S. 97, 1937, pp. 423-438.

105. Gindilis, L. M., Divari, N. B., and Reznova, L. V.: Solar Radiation Pressure on Particles of Interplanetary Dust. Astronomicheskii Zhurnal, 46, 1969, pp. 152-158.

106. Fessenkoff, V.: La Lumiere Zodiacale. Doctoral Dissertation, University of Paris, 1914.

107. Whipple, F., and Gossner, J.: Astrophysical Journal. 109 (3), p. 380, 1949.

108. Fath, E. A.: Lick Obs. Bull. 5, 141, 1909.

109. Brorsen, T. J. C. A.: Concerning a New Phenomenon in the Zodiacal Light. Unterhalten fur Dilettanten und Freunde der Astronomie, Geographie und Witterungskunde, 8, 156, 1854.

110. Born, M., and Wolf, E.: Principles of Optics. Pergamon Press, N. Y., 1964, pp. 633-664.

111. Espenschied, W. F.: A Light Scattering Study of Aerosols Consisting of Solid Spherical Particles in the Submicron Range. Ph. D. Thesis, Clarkson College of Technology, Potsdam, New York, 1965.

112. Divari, N. B., Krylova, S. N., and Moroz, V. I.: Polarization Measurements of Zodiacal Light. Geomagnetism and Aeronomy, 4, 1964, pp. 684-687.

113. Ivanov, A. I., Livshits, G. S., Pavlov, V. Y., Tashenov, B. T., and Teyfel', Y. A.: Light Scattering in the Atmosphere. Part 2, NASA Technical Translation, NASA TT F-553, 1969, p. 36.

114. Chandrasekhar, S.: Radiative Transfer. Dover Publications, Inc., New York, New York, 1963, p. 7.

115. Deirmendjian, D.: Electromagnetic Scattering on Spherical Polydispersions. American Elsevier Publishing Company, Inc., New York, 1969.

116. Rouy, A., Carroll, B., Aller, L. H., Roach, F. E., and Smith, L.: Measurements of the Gegenschein from Space. Nature, 232, 1971, pp. 323-324.

117. Lind, A. C., and Greenberg, J. M.: Electromagnetic Scattering by Obliquely Oriented Cylinders. Journal of Applied Physics, 37, 1966, pp. 3195-3203.

118. Greenberg, J. M., Lind, A. C., Wang, R. T., and Libelo, L. F.: Scattering by Nonspherical Systems. ICES Electromagnetic Scattering (Eds. R. L. Rowell and R. S. Stein), Gordon and Breach, New York, 1967, pp. 3-53.

119. Wyatt, S. P., Jr., and Whipple, F. L.: The Poynting Robertson Effect on Meteor Orbits. Astrophysical Journal, 111, 1950, pp. 134-141.

REFERENCES (Concluded)

120. Van de Hulst, H. C.: Light Scattering by Small Particles. John Wiley & Sons, Inc., New York, 1957.

121. Weinberg, J. L.: Summary Report II on Zodiacal Light. Hawaii Inst. of Geophysics, HIG-67-13, University of Hawaii, 1967.

BIBLIOGRAPHY

Abramowitz, M., and Stegun, I. A.: Handbook of Mathematical Functions with Formulas, Graphs, and Mathematical Tables. National Bureau of Standards, Applied Mathematics Series 55, U. S. Government Printing Office, 1964.

Alexander, W. M., McCracken, C. W., Secretan, L., and Berg, O. E.: Review of Direct Measurements. Space Research III, 1963, pp. 891-917.

Arvesen, J. C., Griffin, R. N. Jr., and Pearson, B. D. Jr.: Determination of Extraterrestrial Solar Spectral Irradiance from a Research Aircraft. Applied Optics, 8, 1969, pp. 2215-2232.

Barbier: Sur les variations d' intensité de la lumière zodiacale. Mem. Soc. Roy. Sci. Liege 15, 1955, pp. 55-71.

Beard, David B.: Interplanetary Dust Distribution and Erosion Effects. Advances in Astronaut. Sci., 3, 1958, pp. 23-1 - 23-6.

Beard, David B.: Interplanetary Dust Distribution. Astrophys. J., 129, 1959, pp. 496-506.

Bicket, N. A., and Gary, G. A.: Celestial Coordinate Transformation. NASA TMX-53943, Government Printing Office, 1969.

Biermann, L.: Theoretical Considerations of Small Particles in Interplanetary Space. The Zodiacal Light and the Interplanetary Medium (Ed. J. L. Weinberg), NASA SP-150, U.S. Government Printing Office, 1967, pp. 279-286.

Blackwell, D. E.: Observations from an Aircraft of the Zodiacal Light at Small Elongations. M.N.R.A.S. 116, 1956, pp. 365-379.

Blackwell, D. E., and Ingham, M. F.: Toward a Unification of Eclipse and Zodiacal-Light Data. The Zodiacal Light and the Interplanetary Medium (Ed. J. L. Weinberg), NASA SP-150, U.S. Government Printing Office, 1967, pp. 17-21.

Borg, Kenneth: Computations on Interstellar Extinction. Acta Univ. Lund, II, 1967, 35 pp.

BIBLIOGRAPHY (Continued)

Born, M., and Wolf, E.: Principles of Optics, Pergamon Press, N.Y., 1964.

Borngen, F., and Richter, N.: Exper. Untersuchungen zur Bcleuchtunginterplan. Materie II. Teil. Veröff. Sternw. Sonneberg, 5, 1962, pp. 197-224.

Briesemeister, W.: A New Oblique Equal-Area Projection, Geog. Rev. 43, 1953, pp. 260-261.

Briggs, Robert E.: Steady-State Space Distr. of Meteor, Particles under the Operation of the Poynting-Robertson Effect. Astronom. J., 67, 1962, pp. 710-723.

Chapman, S.: The Interplanetary Gas and the Earth's Outermost Atmos. Agard Advan. In Upper Atmosphere, 1963, p. 7-10.

Coyne, G. V., and Gehrels, T.: Wavelength Dependence of Polarization VIII. Astronomical J., 71, 1966, pp. 355-363.

Deetz, C. H., and Adams, O. S.: Elements of Map Projection, Special Publication No. 68. U. S. Dept. of Commerce Coast and Geodetic Survey, U. S. Government Printing Office, 1944.

Deirmendjian, D.: Electromagnetic Scattering on Spherical Polydispersions. American Elsevier Publishing Co., Inc. N. Y., 1969.

Dietze, Von G., and Seidel, H.: Ein teilautomatisches Gerät zum Messen der Himmelslicht-Polarization bei Tage und in der Dämmerung. Zs. F. Meteorologie, 20, 1969, pp. 253-258.

Divari, N. B.: Contribution of the Dust Cloud Near the Earth to the Brightness of the Zodiacal Light and of the F-Corona. Soviet Astron. AJ 9, 1965, pp. 493-499.

Divari, N. B.: Charged Dust Particles in Interplanetary Space. Soviet Astron. AJ 10, 1966, pp. 151-155.

Divari, N. B.: On Some Models of Zodiacal Cloud. Astronomicheskiy Vestnik, Tom. 1, No. 2, Izdute'stzvo "NAUKA," 1967, pp. 103-109.

BIBLIOGRAPHY (Continued)

Divari, N. B.: Light Scattered by the Earth's Dust Cloud. The Zodiacal Light and the Interplanetary Medium (Ed. J. L. Weinberg) NASA SP-150, U. S. Government Printing Office, 1967, pp. 321-331.

Divari, N. B.: Photometric Study of the Zodiacal Light. Ast. Zhur 29, Translation ATIC-235224 F-TS-8698/III, AD 105070, 1952, pp. 49-56.

Divari, N. B., and Krylova, S. N.: Photoelectric Observations of Zodiacal Light from a High-Altitude Observatory, Soviet Astron. AJ 7, 1963, pp. 391-398.

Divari, N. B., Krylova, S. N., and Moroz, V. I.: Polarization Measurements of the Zodiacal Light. Geomagnetism and Aeronomy 4, 1964, pp. 684-687.

Divari, N. B., Komarnitskaia, N. I., and Krylova, S. N.: Isophotes of the Zodiacal Light and its Near-Earth Component. Astronomicheskij Vestnik, 2, 1968, pp. 102-107.

Donn, Bertram: The Origin and Nature of Solid Particles in Space. Annals New York Academy of Sciences, 119, 1964, pp. 5-16.

Donn, B., and Krishnaswamy, K. S.: Extinction by Interstellar Grains, Mie Particles and Polycyclic Aromatic Molecules. Physica, 41, 1969, pp. 144-150.

Dumont, R.: L'élimination de la luminescence atmosphérique dans la photométrie photoélectrique de la lumière zodiacale. Compt. Rend. 254, 1962, pp. 4428-4430.

Dumont, R.: Separation des composantes extraterrestre et atmosphérique de la lumière du ciel nocturne au pole et en différents points du ciel. Compt. Rend. 256, 1963, pp. 1447-1449.

Dumont, R.: Mésures photométriques de la lumière zodiacale et du gegenschein corriges de la luminescence atmosphérique. Compt. Rend. 257, 1963, pp. 2242-2245.

M-454

BIBLIOGRAPHY (Continued)

Elsasser, H.: The Zodiacal Light. Planet. Space Sci. 11, 1963, pp. 1015-1033.

Elsasser, H., and Siedentopf, H.: Die Helligkeit des Gegenscheins nach lichtelektrischen Messungen an der Boyden-Station. Zeits. f. Astrophys. 43, 1957, pp. 132-143.

Evans, D. C., and Dunkelman, L.: Airglow and Star Photographs in the Daytime from a Rocket. Science 164, 1969, pp. 1391-1393.

Farone, W. A., and Querfeld, C. W.: Electromagnetic Scattering from an Infinite Circular Cylinder at Oblique Incidence. U. S. Army Electronics Research and Development Activity, White Sands Missile Range, New Mexico, ERDA-287 (AD-461156), 1965.

Fesenkov, V. G.: Optical Properties of the Dust Cloud Surrounding Earth. Sov. Astron. -AJ 8, 1965, pp. 803-807.

Fesenkov, V. G.: Interplanetary Dust Matter and Methods for its Investigation. Sov. Astron. -AJ 10, 1966, pp. 474-478.

Fesenkov, V. G.: The Conditions of Observation of the Zodiacal Light during a Solar Eclipse. Akademiia Nauk Kazakhskoi SSR, 1968, pp. 1-9.

Fesenkov-Pyaskovaskaya, E. V.: Tr. Astrofizich Inst., AN KazSSR, 3, Alma-Ata, 1962, p. 133.

Fracassini, M., and Pasinetti, L. E.: The Brightness of Zodiacal Light and Anti-Solar Light and of Airglow in Relation to the Solar and Lunar Cycle. Ricera Scientifica Series 2, 8, 1965, pp. 665-675.

Fracassini, M., and Pasinetti, L. E.: Remarks and Hypothesis about the Variations of the Zodiacal Light Brightness and of the Airglow Emissions. Mem. Soc. Astro. Ital., [N.S.] 36, 1965, p. 199.

Giese, R. H.: Light Scattering by Spherical Metal Particles. Notizen-Z. Naturforschg. 14a, 1959, pp. 1085-1088.

BIBLIOGRAPHY (Continued)

Giese, R. H. (Ruhr-Universitat Bochum): The Significance of Zodiacal Light Measurements by Deep Space Probes. Scientific Note ESRO SN-41, 1968.

Gillett, F. C., Stein, W. A., and Ney, E. P.: Observations of the Solar Corona from the Limb of the Sun to the Zodiacal Light. Astrophy. J. 140, 1964, pp. 292-305.

Gindilis, L. M.: The Gegenschein as an Effect Produced by the Scattering of Light from Particles of Interpl. Dust. Soviet Astron. -AJ 6, 1963, pp. 540-548.

Gindilis, L. M., Divari, N. B., and Reznova, L. V.: Solar Rad. Press. on Particles of Interplanet. Dust. Astronomicheskii Zhurnal, 46, 1969, pp. 152-158.

Gordon, M. A.: Night Sky Photometry of [OI] λ 5377 and λ 6300 Inside the Southern Auroral Zone. Planet. Space Sci. 16, 1968, pp. 297-308.

Greenberg, J., Libelo, L., Lind, A., Wang, R.: Scattering by Nonspherical Particles Whose Size is on the Order of the Wavelength, Symposium on Electromagnetic Theory and Antennas, Copenhagen, June 25-30, 1962, Pergamon Press, 1963, pp. 81-92.

Greenberg, J. M.: Small Particles in Space. The Zodiacal Light and the Interplanetary Medium (Ed. J. L. Weinberg), NASA SP-150, U. S. Government Printing Office, 1967, pp. 215-223.

Greenberg, J. M.: Interstellar Grains, Stars and Stellar Systems, Vol. VII: Nebulae and Interstellar Matter, (eds. B. M. Middlehurst and L. H. Aller) University of Chicago, 1968, Chapter 6.

Hall, J. S., and Serkowski, K.: Polarization of Starlight. Stars and Stellar Systems, Vol. III, Basic Astronomical Data, 1963, pp. 293-319.

Hapke, B.: A Theoretical Photometric Function for the Lunar Surface. J. Geophys. Res. 68, 1963, p. 4571.

Hapke, B.: An Improved Theoretical Lunar Photometric Function. Astron. J. 71, 1966, p. 333.

BIBLIOGRAPHY (Continued)

Hardie, R. H.: Photoelectric Reductions. Astrophysical Techniques (Ed. Hiltner), Stars and Stellar Systems, Vol. II, The University of Chicago Press, Chicago, 1962.

Harwit, Martin: Origins of the Zodiacal Dust Cloud. J. of Geophysical Research, 68, 1963, pp. 2171-2180.

Heiles, Carl: Temperatures and OH Optical Depths in Dust Clouds. The Astrophys. J., 157, 1969, pp. 123-134.

Hodge, P. W., and Wright, F. W.: Elemental Abundances in Interplanetary Dust. The Zodiacal Light and the Interplanetary Medium (ed. J. L. Weinberg), NASA SP-150, 1967, pp. 173-176.

Hopfield, J. J.: Science. 151, 1966, pp. 1380-1381.

Huruhata, M.: Photoelectric Study of the Zodiacal Light. Publ. Astron. Soc. Japan 2, 1951, pp. 156-171.

Ingham, M. F.: The Nightglow Spectrum. M.N.R.A.S. 124, 1962, I: 505-522, II: 523-532.

Ingham, M. F.: Scattering by Interplanetary and Cislunar Dust Particles. ICES Electromagnetic Scattering (Ed. M. Kerker), Pergamon Press, N. Y., 1963, pp. 135-149.

Ingham, M. F., and Jameson, R. F.: Observations of the Polariz. of the Night Sky and a Model of the Zodiacal Cloud Normal to the Ecliptic Plane. M.N.R.A.S. 140, 1968, pp. 473-482.

Ireland, J. G., Nandy, K., Seldon, H., and Wolstencroft, R. D.: Role of Impurities in Interstellar Graphite Grains. Nature 215, 1967, pp. 377-378.

Jackson, J. D.: Classical Electrodynamics. John Wiley and Sons, Inc. N. Y., 1962.

James, J. F.: Theoretical Fraunhofer Line Profiles in the Spectrum of the Zodiacal Light. M.N.R.A.S. 142, 1969, pp. 45-52.

Janke, E., and Emde, F.: Tables of Functions. Dover Publications, New York, 1945.

BIBLIOGRAPHY (Continued)

Jones, D. S.: The Theory of Electromagnetism. The Macmillan Co., N. Y., 1964.

Kaiser, T. R.: The Interplanetary Dust Cloud. (Kresak and Millman, Eds.) Phys. and Dynam. of Meteors at I.A.U., 1968, pp. 323-342.

Karyagina, Z. V.: The Energy Distribution in the Spectrum of Zodiacal Light. Soviet Astron. AJ. 4, 1961, pp. 828-832.

Kerker, M., Cooke, D., Farone, W. A., and Jacobsen, R. A.: Electromagnetic Scattering from Infinite Circular Cylinder at Oblique Incidence I. Radiance Functions for m = 1.46. J. Optical Soc. of Amer., vol. 56, no. 4, 1966, pp. 487-491.

Leinert, Christoph: Das Zodiakallichtexperiment der Sonnensonde. Sterne und Weltraum 5, 1969, pp. 100-104.

Leinert, C.: Planung und Vorbereitung von extraterrestrischen Experimenten zur Messung des Zodiakallichts. Bundesministerium fur Wissenschaft liche Forschung, BMwF-FB W69-18, 1969.

Loden, L. O.: Some Ideas on the Distribution of Interstellar Dust. Physica, 41, 1969, pp. 137-138.

Lyot, B.: Ann. Obs. Paris 8, Fasc. 1, 1929.

Lynds, B. T., and Wickramsinghe: Interstellar Dust. Annual Review of Astronomy and Astrophys. 6, 1968, pp. 215-248.

Maucherat, Andre-Jean: Études sur la Diffusion Interplanetaire. Ph. D. Dissertation, Universite d'Aix Marseille, 1969.

McCracken, C. W., and Alexander, W. M.: The Distribution of Small Interplanetary Dust Particles in the Vicinity of the Earth. NASA-Langley, G-200, 1962.

Meyer, Arendt J. R.: Radiometry and Photometry: Units and Conversion Factors. Applied Optics 7, 1968, pp. 2081-2084.

Millman, P. M.: Meteor Showers and Interplanetary Dust. 12th Plenary Meeting COSPAR, Prague, Czechoslovakia, 1969.

BIBLIOGRAPHY (Continued)

Ness, Norman, F.: The Magnetic Structure of Interplanetary Space, NASA-GSFC-X-616-69-334, 1969.

Ney, E. P., and Huch, W. F.: Gemini V Experiments on Zodiacal Light and Gegenschein. Science 150, 1965, pp. 53-56.

Parker, E. N.: The Perturbation of Interplan. Dust Grains by Solar Wind. Astrophys. J. 139, 1964, pp. 951-958.

Radzievskii, V. V.: Gravitational Capture of Cosmic Dust by the Sun and Planets and Evolution of the Circumterrestrial Cloud. Soviet Astron. -AJ 11, 1967, 128-136.

Regener, V. H.: Recordings of the Zodiacal Light. Astrophys. J. 122, 1955, pp. 520-529.

Regener, Victor H.: Design Study for Zodiacal Light Observations from an Orbiting Solar Observatory. NASA Grant No. Ns G-666, 1965.

Rense, W. A.: The Origins of Zodiacal Light. Astrophys. J. 115, 1952, pp. 501-505.

Rhee, John W.: Density of Zodiacal Dust in Interplanetary Space. Technical Rept. No. 581, University of Maryland, Dept. Phys. and Astron., 1966, pp. 1-6.

Rhee, J. W.: Electrostatic Potential of a Cosmic Dust Particle. The Zodiacal Light and the Interplanetary Medium (Ed. J. L. Weinberg), NASA SP-150, U. S. Government Printing Office, 1967, pp. 291-298.

Rhee, John W.: Density of Zodiacal Dust in Interplanetary Space, UNESCO, Intl. Series of Monographs in Earth Sci. 30, 1968, pp. 543-546.

Roach, F. E., and Megill, L. R.: Integrated Starlight over the Sky. Astrophys. J. 133, 1961, pp. 228-242.

Roach, F. E., Pettit, H. B., Tandberg-Hanssen, E., and Davis, D. N.: Observations of the Zodiacal Light, Astrophysical Journal, 1954, pp. 253-273.

Roach, F. E., and Rees, M. H.: The Absolute Photometry of the Gegenschein. The Airglow and the Aurorae, (Eds. E. B. Armstrong and A. Palgarno), N. Y., 1956, pp. 142-155.

BIBLIOGRAPHY (Continued)

Roach, F. E., and Smith, L. L.: Absolute Photometry of the Light of the Night Sky. NRS Technical Note No. 214, 1964.

Rougier, G.: Ann. Obs. Stasbourg, 2, 1933, p. 205.

Sanchez, F. Martinez: Recent Polarization Measurements Over the Sky at Tenerife Island. The Zodiacal Light and the Interplanetary Medium (Ed. J. L. Weinberg), NASA SP-150, U. S. Government Printing Office, 1967, pp. 71-73.

Scheffler, Elsasser: Brightness/Unit Area of the Integrated Starlight. Landolt-Bornstein, Numerical Data and Functional Relationships in Science and Technology, Group VI, vol. 1, Ed. H. H. Voight, Springer-Verlag, N. Y., 1965, pp. 603-604.

Scheffler, Elsasser: Star Counts and Surveys. Landolt-Bornstein, Num. Data and Funct. Rel. in Sci. and Tech., Group VI, vol. 1, Ed. H. H. Voight, Springer-Verlag, N. Y., 1965, pp. 603-606.

Schmidt, Karl-Heinz, Jena: Development of Interstellar Dust Particles. Astronomische Nachrichten, 287, 1963, pp. 215-239.

Seeliger, H. V.: Ueber Kosmische Staubmassen und dug Zodiacallicht. Akad. der Wiss Bel. Sitz. ber., 31, 1901, pp. 265-292.

Serkowski, K., Gehrels, T., and Wisniewski, W.: Wavelength Depend. of Polariz XIII, Interstellar Extinction and Polariz. Correlations. Astronom. J. 74, 1969, pp. 85-90.

Sexl, R., Burkhard, D. G., Draxler, K., Folk, R., Lawrence, J., and Sexl, H.: Radiative Aspects of Lunar Materials. PEC Research Assoc. Inc. Report, under NAS8-21044, Final Report, 1969.

Shah, G. A.: Models of Interstellar Grains. Ph. D. Thesis, Rensselaer Polytechnic Institute, 1967.

Shemyakin, M. M.: Arrangement of Galaxies in Coma Berenices. Vestnik, 1, 2, 1967, pp. 126-127.

Sodek, B. A., and Chou, C. Y.: Debris Cloud Brightness: Mie and Rayleigh Scattering. Brown Eng. Report RL-SSL-408, NAS8-20166, 1966.

BIBLIOGRAPHY (Continued)

Southworth, Richard B.: The Size Distribution of the Zodiacal Particles. Annals, New York Acad. of Sciences 119, 1964, pp. 54-67.

Southworth, R. B.: Space Density of Radio Meteors. The Zodiacal Light and the Interplanetary Medium (ed. J. L. Weinberg), NASA SP-150, U. S. Government Printing Office, 1967, pp. 179-188.

Stratton, J. A.: Electromagnetic Theory. McGraw-Hill Book Co., Inc., N. Y., 1941.

Thom, A.: The Zodiacal Light. J. of the British Astro. Assoc., 49, 1939, p. 103.

USA Standard Nomenclature and Definitions for Illuminating Engineering, RP-16, United States of America Standards Institute, USAS Z7.1-1967, 1967.

van de Hulst, H. C.: The Amount of Polarization by Interstellar Grains. The Astrophys. J. 112, 1950, pp. 1-5.

Wait, J. R.: Some Solutions for Electromagnetic Problems Involving Spheroidal, Spherical, and Cylindrical Bodies, Journal of Research of the National Bureau of Standards - B. Mathematics and Mathematical Physics, Vol. 64B, No. 1, January - March, 1960, pp. 15-32.

Walter, H.: Streulichtintensität gro Ber sphärischer Partikel. Optik, 14, 1957, pp. 130-142.

Walter, H.: Streulichtintensität gro Ber sphärischer Partikel, II. Optik, 16, 1959, pp. 401-408.

Weinberg, J. L.: A Photoelectric Study of the Nightglow (Final Report). NASA Grant NsG-676, 1968.

Weinberg, J. L.: Negative Polarization in the Zodiacal Light. The Astrophys. J. 152, 1968, pp. 665-666.

Weinberg, J. L.: Summary Report II On Zodical Light. Hawaii Inst. of Geophysics, HIG-67-13, University of Hawaii, 1967.

BIBLIOGRAPHY (Concluded)

Weinberg, J. L., and Mann, H. M.: A Program of Ground-Base Studies of the Zodiacal Light. The Zodiacal Light and the Interplanetary Medium (Ed. J. L. Weinberg), NASA SP-150, U. S. Government Printing Office, 1967, pp. 3-8.

Weinberg, J. L., Mann, H. M., and Hutchison, P. B.: Polarization of the Nightglow: Line vs. Continuum. Planet Space Sci. 16, 1968, pp. 1291-1296.

Whipple, F. L.: A Comet Model III. The Zodiacal Light. Astrophys. J. 121, 1955, pp. 750-770.

Wickramasinghe, N. C.: Interstellar Dust & Diamonds. Nature, 222, 1969, pp. 154-155.

Wickramasinghe, N. C.: On Graphite Particles as Interstellar Grains. II, M. N. R. A. S. 126, 1963, pp. 99-114.

Witt, A. N.: Scattering Properties of Interstellar Particles. Astrophys. J., 152, 1968, pp. 59-76.

Wolstencroft, R. D.: On the Location in Space of the Zodiacal Dust Particles. Planet. Space Sci., 15, 1967, pp. 1081-1089.

Wolstencroft, R. D., and Brandt, J. C.: A Five-Color Photometry and Polarimetry of the Zodiacal Light: A Preliminary Report. The Zodiacal Light and the Interplanetary Medium (Ed. J. L. Weinberg), NASA SP-150, U. S. Government Printing Office, 1967, pp. 57-62.

Yamamoto, I.: Report of the Sub-Commission on Zodiacal Light. Trans. Int. Astron. Union, Stockholm, 1938, VI, 1939, pp. 172-175.

Zanoni, C. A., and Hill, H. A.: Reduction of Diffracted Light for Astrometry Near the Sun. J. of the Optical Soc. of Amer. 55, 1965, pp. 1608-1611.

☆U.S. GOVERNMENT PRINTING OFFICE: 1973-739-028/45

NATIONAL AERONAUTICS AND SPACE ADMINISTRATION
WASHINGTON, D.C. 20546

OFFICIAL BUSINESS
PENALTY FOR PRIVATE USE $300

SPECIAL FOURTH-CLASS RATE
BOOK

POSTAGE AND FEES PAID
NATIONAL AERONAUTICS AND
SPACE ADMINISTRATION
451

U.S.MAIL

POSTMASTER: If Undeliverable (Section 158 Postal Manual) Do Not Return

"The aeronautical and space activities of the United States shall be conducted so as to contribute . . . to the expansion of human knowledge of phenomena in the atmosphere and space. The Administration shall provide for the widest practicable and appropriate dissemination of information concerning its activities and the results thereof."

—NATIONAL AERONAUTICS AND SPACE ACT OF 1958

NASA SCIENTIFIC AND TECHNICAL PUBLICATIONS

TECHNICAL REPORTS: Scientific and technical information considered important, complete, and a lasting contribution to existing knowledge.

TECHNICAL NOTES: Information less broad in scope but nevertheless of importance as a contribution to existing knowledge.

TECHNICAL MEMORANDUMS: Information receiving limited distribution because of preliminary data, security classification, or other reasons. Also includes conference proceedings with either limited or unlimited distribution.

CONTRACTOR REPORTS: Scientific and technical information generated under a NASA contract or grant and considered an important contribution to existing knowledge.

TECHNICAL TRANSLATIONS: Information published in a foreign language considered to merit NASA distribution in English.

SPECIAL PUBLICATIONS: Information derived from or of value to NASA activities. Publications include final reports of major projects, monographs, data compilations, handbooks, sourcebooks, and special bibliographies.

TECHNOLOGY UTILIZATION PUBLICATIONS: Information on technology used by NASA that may be of particular interest in commercial and other non-aerospace applications. Publications include Tech Briefs, Technology Utilization Reports and Technology Surveys.

Details on the availability of these publications may be obtained from:

SCIENTIFIC AND TECHNICAL INFORMATION OFFICE

NATIONAL AERONAUTICS AND SPACE ADMINISTRATION

Washington, D.C. 20546